DUST DISKS AROUND HOT WHITE DWARFS AND CENTRAL STARS OF PLANETARY NEBULAE

BY

JANA BILIKOVA

DISSERTATION

Submitted in partial fulfillment of the requirements
for the degree of Doctor of Philosophy in Astronomy
in the Graduate College of the
University of Illinois at Urbana-Champaign, 2012

Urbana, Illinois

Doctoral Committee:

Professor You-Hua Chu, Chair, Director of Research
Professor Charles F. Gammie
Dr. Kate Y.-L. Su, University of Arizona
Professor Laird A. Thompson
Associate Professor Leslie W. Looney
Professor Emeritus Ronald F. Webbink

Abstract

Two types of dust disks have been discovered around white dwarfs (WDs): small dust disks within the Roche limits of their WDs, and a large dust disk around the hot central WD of the Helix planetary nebula (PN), possibly produced by collisions among Kuiper Belt-like objects.To search for more dust disks of the latter type, we have carried out a *Spitzer* MIPS 24 μm survey of 71 hot WDs or pre-WDs, and found nine WDs with excess 24 μm emission, seven of which are still central stars of planetary nebulae (CSPNs). We have therefore used archival *Spitzer* IRAC and MIPS observations of PNe to search for CSPNs with excess IR emission, and found five additional IR excesses likely originating from dust disks. For some of these CSPNs, we have acquired follow-up *Spitzer* MIPS images and IRS spectra, and Gemini NIRI and Michelle spectroscopic observations.

The spectral energy distributions show great diversity in the emission characteristics of the IR excesses, which may imply different mechanisms responsible for the excess emission. The two most likely dust production mechanisms are: (1) breakup of bodies in planetesimal belts through collisions, (2) formation of circumstellar dust disks through binary interactions. In addition, we have derived basic dust disk parameters using simple blackbody approximations, or optically thin dust disk models with realistic grain and disk properties. The dust disk physical parameters for CSPNs without near-IR excesses appear consistent with the origin as collisionally disrupted planetesimals. The dust disks around CSPNs with near-IR excesses are likely optically thick, and possibly descended from binary post-AGB stars. The Helix Nebula's CSPN is also associated with a hard X-ray point source, whose origin is not known. We have correlated the Galactic WD catalog with the *XMM-Newton* and *ROSAT*

point source catalogs to search for more single WDs with hard X-ray emission. Apart from the central WD of the Helix Nebula, none of the single WDs with hard X-ray emission are known to have excess IR emission.

A better understanding of post-AGB binary evolution as well as debris disk evolution along with its parent star is needed to distinguish between these different origins.Future observations to better establish the physical parameters of the dust disks and the presence of companions are needed for models to discern between the possible dust production mechanisms.

In memory of my grandparents.

Acknowledgments

Graduate school has not been a smooth ride for me, and it took a team of experts to get me to the finish line without losing my sanity. I am glad to have the opportunity to acknowledge the people that have helped me along the way to my PhD.

First of all, I would like to thank my thesis commitee, You-Hua Chu, Kate Su, Leslie Looney, Laird Thompson, Ron Webbink and Charles Gammie for their helpful comments and the feedback during my preliminary and PhD examination.

I want to thank my advisor You-Hua Chu for all the opportunities and guidance that she has given me throughout the years. The education I got from her was broad; the astronomical observations were intermingled with observations of viral videos, and my scientific writing was balanced out by increasing knowledge of the urban dictionary. I don't think that any student got to laugh more with their advisor than I did, as we photographed the double rainbows of Slovakia, observed more than just Mozart's statue in Vienna, or walked the Ulmenweg and Ahornweg in Germany. You-Hua is one of the most generous people that I know, with all the delicious food that she brings in daily, or the upgrades and airplane tickets that she gives away. We have broken the barrier between the professional and personal life, and I am glad to be graduating not only with a great advisor, but also a good friend.

I might never have graduated if it wasn't for Robert Gruendl. Almost everything that I have learned about data, I have learned from him. I appreciate his patience in answering my "quick questions", his help with data reduction, observation preparation or IRAF problems. His scripts have saved me days of work on many occasions. All this knowledge is wrapped up in a modest and kind person that I am lucky to have learned from.

I also want to thank Kate Su, for her help with *Spitzer* data and dust disk modeling, journal articles and many proposals. Her work ethic is something that I aspire to. I am also grateful to her for hosting me in Tuscon, introducing me to her dogs, bringing spicy squid to Kitt Peak and for good beer and good conversations at conferences and observing runs.

I cannot go without mentioning Rosa Williams, my academic sister, for her help with my first paper, and for pulling me out of a slump at the beginning of the research portion of my PhD. Her success is an encouragement to me whenever self-doubt creeps in.

I would like to thank the Astronomy Department Staff, Jeri Cochran, Sandie Osterbur, Mary Margaret O'Connor and Bryan Dunne for always reminding me to register for classes, send in grant reports, or renew paperwork, and for being so nice and friendly. Their kindness makes it easy to feel at home in the department. I am also thankful to Kevin Pointer for tech support and reminders to copy my data to directories that will not be erased.

I also want to thank Leslie Looney, whose classes are no doubt the most entertaining ones, where even innocent passerbys get chalk-attacked into participation. Thanksgivings at the Leslies' are the best, and both me and my stomach are happy to have been included.

I am lucky that my peers in Astronomy were such a great bunch of people who like their integrals with a side of late-night chinese takeout and a hackysack, who work and play hard and who were the best part of the grad school experience.

I would especially like to thank my officemates of few years and dear friends Hsin-Fang Chiang and Amy Lien, brilliant, hard-working, kind and generous women that I am lucky to know. It's been great doing research and schoolwork alongside them. I am thankful for all the fun times - sharing bread pudding, fabric and yarn store expeditions, cheering me on at my races, drawing diamonds in the sky above Einstein, owlies, chats about school and life, and all those wonderful small things that made everyday life in Astro 128 so enjoyable.

I also want to thank Jonathan Seale for making living on Elm street the opposite of nightmare with our Oscar parties, grocery store runs, evenings sewing snuggies and MJ costumes, and alleged waltzing at Crane Alley; Hsin-Lun Kuo for all the good talks and

laughs, for our study times at coffee shops, for hot-pot dinners and all the nights we danced away in our early grad years; Brett Hayes for his great generosity and willingness to always help anyone, for bringing me food and proofreading the last chapters of my thesis at a moment's notice, for his parties, and for putting my bad sleeping habits in perspective; Nick Indriolo for parties and the great laughs during the movie nights, for stopping by the office to chat on the way home, and for always being fashionably on time to every event; Nick Hakobian for chat breaks, movie nights and gettogethers at his place, for all the great naps I took on his floor during movie nights, and for his attempts to explain interferometry to me; Britt Lundgren for enduring our first year together and for her friendship ever since, for the good times in Fiesta, and for always thinking that I am smarter that I think I am; Jessica Evans for bringing me coffee in my most stressed stages of thesis-writing, and for her delicious cookies that I am sure have put my thesis committee into favorable mood for my defense; and all my grad school astronomy friends that have made life in and out of the office so fun: Alfredo Zenteno, Ashley Ross, Chao-Chin Yang, Dominique Segura-Cox, Gary Foreman, Ian Stephens, Jeeseon Song, Jerry Shiao, Karen Yang, Nachiketa Chakraborthy, Rosie Chen, Rukmani Vijayaraghavan, Scott Bain, Tijana Prodanovic, and everyone else.

I also want to thank Lesa Scharnett for the 5:30 "happy hours" at the gym, which have kept me fit and sane in the past two years. Of all the classes I took in grad school, hers were by far my favorite.

I thank Sara Knaack, for being my first and longest friend here in Urbana, for our movie nights, Ribollita dinners and carrot cake, and all the fun, friendship and gourmet food we shared in the past few years. I also want to thank my friend Suzanne Levine Donnelly, for all the laughs, deep conversations and extremely ridiculous inside jokes, for lessons in slang, but above all, for being someone I can always lean on, no matter how far apart we live.

I want to say a special thank you to Jeri Cochran who has seen me through the entire grad school rollercoaster, encouraging me to "hang on to the vine" in the roughest of times, and crowning me "the lady of cool dusty rings" to celebrate my success. I want to thank her

for all of the small chats in the front office that always brighten up my day, for sharing food and drinks at Crane Alley, for my beautiful shawl and all the good times knitting. Above all, I thank her for giving me the feeling of home away from home where I can hide from scary neighbors, forget about stress, and just play with Bob and Mia. I am grateful to Jeri's family too - Becherovka tastes better when Gary drinks with me, and sewing is much more fun with Jeri, Jane and Ann around. It is a relief to know that wherever I end up, I will have a home and a friend for life here in Urbana.

During my time at U of I, I was fortunate to meet my boyfriend Shankar Rao. Shankar has been an incredible inspiration, and a source of love, strength and knowledge for me in the past four years. His tech support has been invaluable to me on more occasions than I should probably admit to, and I could always turn to him with both math- and writing-related questions. But there is much more than the academic support that I have to thank him for. I am also grateful for the daily wake-up calls, for all the visits, for so patiently dealing with my stress and moodiness, for his empathy and constant encouragement. I thank him for flying across US just to be there for my defense, for the home-brewed beer, thoughtful gifts, simply, for being my best friend. All my success is so much better when I can share it with him. I also want to thank Shankar's family for being kind and welcoming to me, for their encouragement, and for the fun Christmas celebrations and other visits that I got to spend with them in recent years.

I want to thank my professors at Franklin and Marshall College, especially Andrea Lommen, Dana Backman, and Elizabeth Praton, for making astronomy classes so fun that I could not help but take more of them, and for my first research and observing experiences. Life abroad has been fun thanks to all my friends from F & M, especially Uyanga Turmunkh, Dina Bash Gabitov, Kajri Sheth, and Ruth Misir. All my best memories from college are tied to them, and even homework or all-nighters in Hackman were enjoyable with my friends around. I am also greatful to my Lancaster moms Mary-Jane Ferretti and Anna Marie Sohonyay, for the fun working at ASFC, the outlet trips, Easter celebrations, and the sweet

gifts that I still use to this day.

Even though after so many years US feels like a second home to me, my true home is back in Slovakia. Very soon after I left to study abroad, I learned to value the friends and family that wait for me back home. I want to thank Naďa Nagyová for her lifelong friendship and all the fun we have every time I go home, and for being able to share all the ups and downs of my life with her. I thank Ľubica Černá, Lenka Dávidová and Tatiana Puhová for their unchanging friendship, and for being able to pick up right where we left off even after a long absence.

I want to thank Mrs. Mikulová, for teaching me and my brother most of the english that I know today, for believing in us and being proud of us. She is greatly missed.

I want to thank, Zdeno Kardoš, Jana Kovářová, Jaroslav Kardoš, Ivan Kardoš, Sandra Kardošová, and Jarmila Kardošová, and all my family for their support, care, and all the great times we had growing up, laughing, playing, and celebrating together. I thank my brother, Pavol Bilík, for being so fun to be around, for taking joy in the small things in life, and his enthusiasm for NASA goodies. I am inspired by his hard work, and his resolve in pursuing work that he enjoys doing. Being around him, and my family, is a great relief from the strains of academic life.

My biggest thanks has to go to my parents, Vladimír Bilík and Maria Bilíková. It is because of their love and support that I am able to do anything in life. I will always be inspired by their hard work, determination and tenacity with which they built up their life, so that they could provide for me the opportunities that they did not have. I am grateful that they have encouraged me to pursue education, but never pressured me about grades, field of study, or the time it took to accomplish. Above all, I am happy that I always have a warm home to come to, where I get to enjoy the companionship of the family, because time spent with loved ones is what matters most in life to me.

Table of Contents

List of Tables

List of Figures

List of Abbreviations

2MASS	Two Micron All Sky Survey
AGB	Asymptotic Giant Branch
BCD	Basic Calibrated Data
CSPN	Central Star of Planetary Nebula
DSS2	Digitized Sky Survey
EPIC	European Photon Imaging Camera
FUSE	Far Ultraviolet Spectroscopic Explorer
FWHM	Full Width at Half Maximum
HR	Hertzsprung-Russel
HST	Hubble Space Telescope
IR	InfraRed
IRAC	Infra-Red Array Camera
IRS	Infra-Red Spectrograph
KBO	Kuiper Belt-like Object
KPNO	Kitt Peak National Observatory
MIPS	Multi-Band Imaging Photometer for *Spitzer*
NIRI	Near Infrared Imager and Spectrometer
PSF	Point Spread Function
PN	Planetary Nebula
PR	Poynting-Robertson

R CrB	R Coronae Borealis
RGB	Red Giant Branch
ROSAT	Roentgensatellit
ROSPSPC	Rosat Position Sensitive proportional Counter
ROSPSPSPCF	Rosat Position Sensitive proportional Counter with Boron Filter
SDSS	Sloan digital Sky Survey
SED	Spectral Energy Distribution
TMAP	Tuebingen non-Local Thermodynamic Equilibrium Model Atmosphere Package
UV	Ultraviolet
WGACAT	WGA Point Source Catalog
WD	White Dwarf
XMM	X-ray Multi-mirror Mission
XMMSSC	XMM-Newton's Serendipitous Source Catalog

Chapter 1

Introduction

1.1 Search for Planets around Main-sequence and Evolved Stars

The search for planets or planetary systems around stars other than our Sun is an integral part of the scientific quest for life's origin. It has been found that planets commonly exist around solar-type stars (Butler et al. 2006; Borucki et al. 2011). The evolution of planetary systems through post-main-sequence stages of their parent star's life has been investigated by many groups (e.g., Villaver & Livio 2007; Debes & Sigurdsson 2002; Duncan & Lissauer 1998; Sackmann et al. 1993). The general consensus is that planets within $\sim$1 AU will be engulfed in the stellar envelope during the Red Giant Branch (RGB) and the Asymptotic Giant Branch (AGB) phases. Beyond 1 AU, some planets may spiral into the stellar envelope, depending on simulation details, such as the strength of stellar wind. Planets beyond $\sim$5 AU are expected to survive and migrate outwards in response to the mass loss of their parent star. As the star ejects its envelope and forms a planetary nebula (PN), the planets can undergo evaporation due to photoionization by stellar UV flux, ram pressure stripping by the stellar winds, and heating in the PN interior (Villaver & Livio 2007). Overall, if a planet is massive and distant enough, it is expected to survive the post-main-sequence evolution.

Observations support planets' survival through at least some post-main-sequence stages of their parent stars. Radial velocity measurements have been used to find massive planets around evolved intermediate-mass red giants (Setiawan et al. 2005; Sato et al. 2007; Hatzes

et al. 2005; Johnson et al. 2007; Lovis & Mayor 2007; Niedzielski et al. 2007; Liu et al. 2008). However, planets around WDs, the final products of stellar evolution, cannot be detected with the radial velocity technique, as WDs have few spectral lines and the lines are highly pressure-broadened, precluding high-precision measurements of radial velocities.

1.2 Infrared Excesses of White Dwarfs

Infrared (IR) observations with ground-based telescopes offer an alternative way to detect planetary systems around WDs. Single WDs with effective temperatures ($T_{\rm eff}$) greater than a few 10^3 K have well-behaved and understandable spectral properties, and their spectra at IR wavelengths can be approximated by the Rayleigh-Jeans tail of blackbody radiation at the stellar $T_{\rm eff}$. If the observed IR flux from a WD exceeds its expected photospheric emission, the WD possesses an "IR excess", which indicates the presence of an external body that is cooler and dimmer/undetectable at optical wavelengths, such as a low-mass companion, a planet, or a dust disk.

The emission from late-type stellar and substellar companions, such as MLT dwarfs, peaks in the near-IR ($\sim$ 1–3 μm). Even though these late-type stars, at $T_{\rm eff}\sim$ 1,000–3,000 K, are cooler than WDs, their radii are $\sim$10–30 times larger, and thus they may outshine the WDs at IR wavelengths.

Near-IR observations have been commonly used to diagnose late-type companions of WDs and to search for planets, either through direct detection of common-proper-motion companions (Hogan et al. 2009; Farihi et al. 2005), or through IR excesses (Farihi et al. 2005; Hoard et al. 2007). While these searches found many late-type stellar companions, mostly with M4-5 spectral types, only a few ($<$0.5%) brown dwarfs were found, and no planets were discovered. However, an L8 dwarf substellar companion was found through spectroscopic analysis of the IR excess of WD SDSS J121209.31+013627.7 (Farihi et al. 2008).

1.3 Spitzer Space Telescope and Planet Searches.

The *Spitzer Space Telescope* (Werner et al. 2004) has provided a new opportunity to search for stellar and substellar companions around WDs, thanks to its unprecedented $\sim\mu$Jy-level sensitivity and coverage at longer wavelengths, which are more challenging or impossible to observe from the ground. *Spitzer* has three instruments, the Infra-Red Array Camera (IRAC, Fazio et al. 2004), the Multi-Band Imaging Photometer for *Spitzer* (MIPS, Rieke et al. 2004), and the Infrared Spectrograph (IRS, Houck et al. 2004). The IRAC camera is a near- to mid-IR imager at 3.6, 4.5, 5.8, and 8.0 μm; MIPS provides imaging at 24, 70, and 160 μm; and IRS takes $\sim$5–40 μm spectra with low or high spectral resolution.

IRAC is well-suited for finding IR excesses of WDs due to unresolved low-mass late-type stars, brown dwarfs, and planets. I have computed the IR excess expected from these WDs, expressed as the companion-to-WD flux density ratio at different wavelength bands, and summarized the results in Table 1. To derive these expected IR excesses, I use the WD flux densities calculated for three different temperatures (100,000 K, 50,000 K, and 10,000 K), approximating the WD with an Earth-sized blackbody. For the companion's emission, I use the JHK and IRAC photometry of M and L dwarfs from Patten et al. (2006). $P_{0.5}$ and $P_{1.0}$ in the first column of the table denote Jupiter-sized planets at orbital radii of 0.5 and 1.0 AU; their emission approximated by blackbodies at their corresponding equilibrium temperatures. These approximate planet flux densities should be treated as lower limits, as planets often emit more energy than the amount incident from their parent stars. From Table 1, I conclude:

1. IR excesses are larger in IRAC bands than in JHK, and thus IRAC observations are ideal for searches of M and L dwarf companions and planets around WDs.

2. M and L dwarf companions produce more IR excesses for cool WDs than hot WDs, and thus are easier to detect around cool WDs.

3. Planets produce negligible IR excesses, unless heated by the hottest WDs at small

orbital radii. Note, however, that more sophisticated models that evolve a planet's spectrum to Gyr-order ages predict detections of M>5–10 $M_{\rm Jupiter}$ planets around WDs (Baraffe et al. 2003; Kilic et al. 2010).

A number of *Spitzer* surveys for brown dwarf companions and planets around WDs have been carried out (e.g., Farihi et al. 2008; Kilic et al. 2009; Mullally et al. 2007; Kilic et al. 2010; Burleigh et al. 2008; Mullally et al. 2009). These surveys find the detection rate for L and T-type dwarf companions to be very low (<0.6%). No planets have been found, although, if present, planets with masses >5–10$M_{\rm Jupiter}$ should have been detected. Such low detection rates may imply that the planets or brown dwarfs have been altered or destroyed during post-main-sequence evolution, or are too cold for detection with current facilities. Efforts to search for planets around WDs using the timing of pulsating WDs and time-series *Spitzer* IRAC photometry have also been carried out, but with only a controversial detection to date (Mullally et al. 2008, 2009).

1.4 Debris Disks

Even though planets were not found directly around WDs, the detection of debris disks provide strong indirect evidence for the survival of planetary systems into the latest stages of stellar evolution. Debris disks, produced by collisions of small bodies in a planetary system, are composed of all sub-planetary objects, from μm-sized dust grains to km-sized planetesimals. As their emitting surface areas are generally much larger than those of their host WDs, the IR emission of debris disk can be several orders of magnitude brighter than the WDs' photospheric emission, and thus easily detectable.

Debris disks are detected around low- and intermediate-mass main sequence stars, but their dust content dissipates and IR luminosities decline with time (Rieke et al. 2005; Su et al. 2006; Carpenter et al. 2009; Trilling et al. 2008). By the time a star evolves into a WD, the dust grains in its debris disk have been removed by gas drag, Poynting-Robertson drag,

radiation pressure, stellar wind, etc.

Nevertheless, dust around WDs has been detected. The first two WDs with dust disks found through their IR excess emission were G29-38 and GD 362 (Becklin et al. 2005; Kilic et al. 2005; Reach et al. 2005a; Zuckerman & Becklin 1987). The excess emission around the first one, G29-38, was initially attributed to an unresolved brown dwarf companion, but subsequent studies provided evidence that the IR emitter is a dust disk. The lack of absorption lines in the IR spectrum's continuum, the significant 10 μm emission, the echoing of stellar optical pulsations in the IR are all properties inconsistent with a brown dwarf emitter (Farihi 2011, and references therein). Furthermore, the spectrum of this cool, ($\sim$11,500 K) WD was found to exhibit metal absorption lines. These are not expected for such a cool, old ($\sim$Gyr) WD, as the gravitational settling of heavy elements occurs rapidly (days to 10^4 yrs), unless material is being accreted onto the WD photosphere.

All of the above facts point to the presence of a dust disk around G29-38. The results of main-sequence debris disk studies suggest that the dust in this system cannot be the remnant of main-sequence evolution. The dust around such old WDs must have been recently replenished. Jura (2003) has suggested that an asteroid entering within the WD's Roche limit would be tidally disrupted, and generate dust around the WD, as well as pollute its atmosphere with metals. The subsequent *Spitzer* spectrum of G29-38 has also revealed a dusty 10 μm silicate feature that is similar to that seen in the zodiacal dust of our Solar System (Reach et al. 2005a), further supporting this disrupted-asteroid scenario.

The general mechanism that propels the asteroids within the WD's Roche limit is presumedly the following: as a star evolves into a WD and loses a significant fraction of its initial mass, the orbits of surviving planets can become unstable due to planet-planet perturbations, and close encounters between planets can lead to new stable orbits, ejection out of the system, or planet collisions (Debes & Sigurdsson 2002). Likewise, close encounters and orbital resonances between planets and sub-planetary objects dynamically rejuvenate the planetary system, leading to orbital eccentricity increases and frequent collisions among

sub-planetary objects, such as the Kuiper Belt-like Objects (KBOs, Debes & Sigurdsson 2002). The small sub-planetary bodies can be scattered into the inner system. If an asteroid is scattered within the Roche limit, it will generate dust that can be observed as an IR excess.

1.5 Surveys of WDs for Dust Disks

Several surveys have been made to search for similar dust disks around WDs. A *Spitzer Space Telescope* IRAC 4.5 and 8.0 μm survey of 124 WDs found only one additional dust disk, around WD 2115−560 (Mullally et al. 2007; von Hippel et al. 2007). Surveys targeting WDs with atmospheric absorption lines of heavy elements, i.e., DAZ/DBZ WDs, have had better success: Kilic et al.'s (2006) near-IR spectroscopic survey of 20 DAZ WDs confirmed the dust disks around G29-38 and GD 362, and found an additional disk around GD 56; Kilic & Redfield (2007) predicted and confirmed the presence of a dust disk around the metal-rich DAZ WD 1150−153, which has a calcium abundance too high for its effective temperature; Jura et al. (2007) analyzed *Spitzer* photometric observations of 11 DAZ/DBZ WDs and discovered dust disks around GD 40, GD 133, and PG 1015+161. Similar dust disks have been discovered at an increasing rate: 14 were discovered before 2010 (Farihi et al. 2009), and another 14 were discovered in 2010–2011 alone, as summarized in Table 1 of Xu & Jura (2011). Yet more are being discovered, e.g., PG 1541+651 (Kilic et al. 2011), and 52 dust disk candidates around WDs from the *Wide-field Infrared Survey Explorer* survey of WDs (Debes et al. 2011).

All these dust disks lie within <0.01 AU from their central WDs, which are all relatively cool (< 24,000 K) and have anomalously high metal content in their atmospheres (when high-quality spectroscopic data are available). The dust disks' being within their central WDs' Roche limits fully supports their origin as tidally crushed asteroids and the metal enrichments in the WD atmospheres are also consistent with accretion of material from

the disrupted asteroids (e.g., Jura et al. 2007; Farihi et al. 2010a,b). Three dust disks are accompanied by metal-rich gaseous debris (Gänsicke et al. 2008; Brinkworth et al. 2009; Farihi et al. 2010b; Melis et al. 2010). These dust disks provide the best indirect evidence to date for the presence of surviving sub-planetary bodies around stellar corpses.

Figure 1.1a demonstrates why these dust disks are found only around relatively cool WDs. The temperature of the dust depends on the luminosity of the WD and the dust's orbital radius. Since the range of WD radii is relatively small, the main parameter determining the WD luminosity is the stellar $T_{\rm eff}$. For purposes of this calculation, we assume a WD radius of 1 $R_{\oplus}$. The figure shows the curves of constant dust temperature as a function of orbital radius and stellar effective temperature, where the dust equilibrium temperature ($T_{\rm dust}$) is calculated via

$$T_{\rm dust} = (1-a)^{\frac{1}{4}} \sqrt{\frac{R_\star}{2D}}\, T_\star \ , \tag{1.1}$$

where D is the orbital distance of the dust, a is the dust's albedo, $R_\star$ is the stellar radius, and $T_\star$ is the stellar effective temperature. The inner edge of the dust disk is limited by dust's sublimation temperature, typically ∼1,500 K, so ultimately, the stellar effective temperature ($\rm T_\star$) determines the inner sublimation radius, assuming a constant stellar radius of 1 $R_{\oplus}$. The outer edge of the dust disk is determined by the Roche limit, given by

$$r \approx 2.456 \left(\frac{\bar{\rho}_\star}{\bar{\rho}_{\rm a}}\right)^{\frac{1}{3}} R_\star, \tag{1.2}$$

where $\bar{\rho}_\star$ and $\bar{\rho}_{\rm a}$ are the average densities of the star and the asteroid, respectively.

The region of the parameter space in Figure 1.1a inside which these dust disks can be detected is bounded by the Roche limit on the top and dust sublimation temperature to the right. It is evident that these dust disks can only be present around cool WDs, because all of the dust inside the Roche limit will sublimate for WDs hotter than ∼30,000 K. The permitted disk radii and stellar temperatures derived from our analysis are consistent with observed disk properties. Furthermore, the similarity of abundances in these dust disks

and in asteroidal material found in our inner solar system reinforces this scenario, and thus provides the best indirect evidence to date for the presence of surviving planetary bodies around stellar corpses.

1.6 Dust Disk around the Helix CSPN

An entirely different kind of dust disk has been discovered around the central star of the Helix Nebula (Figure 1.2a), WD 2226−210, a hot WD with an effective temperature of 110,000 K (Su et al. 2007). *Spitzer* MIPS images reveal a bright compact source coincident with the star at 24 and 70 μm. A follow-up IRS spectrum of the point source, after the nebular background subtraction, has verified that the mid-IR emission originates from dust continuum (Figure 1.2b). The spectral energy distribution (SED) of this IR-emitter (Figure 1.2c) indicates a temperature of 90 – 130 K, too cold to be a star. The luminosity of this IR source, 5 – 11×10^{31} ergs s^{-1}, requires an emitting area of 4 – 40 AU^2, too large for planets. Only an extended object, such as a dust disk, can explain these properties.

The location of the disk, $\sim$ 40 – 100 AU from the star, corresponds to that of the Kuiper Belt in the solar system. Any primordial circumstellar gas and dust at such radial distances would have been blown away by the stellar wind; thus, the dust in this disk must also be freshly generated. The dust was suggested to be produced by collisions among Kuiper-Belt-like objects (KBOs) that were dynamically rejuvenated in AGB and post-AGB phases (Su et al. 2007).

This origin of the Helix dust disk is in line with that of small dust disks around cool WDs. Due to enhanced collisions, some of the remaining asteroids' orbits may be perturbed such that their periastron passages are within the Roche limit, leading to their tidal destruction. The reservoirs of these asteroids around the cool, old WDs would not be heated sufficiently to be detected in IR. If the dust around the central star of planetary nebula (CSPN) Helix is indeed generated by collisions of KBOs or comets, and if KBOs and comets orbiting at

40 – 100 AU are common among intermediate- and low-mass stars, dust disks around WDs could also be common.

Figure 1.1b shows curves of constant dust temperature similar to Figure 1.1a except over a larger range of orbital distances and stellar temperatures. Based on the distances of KBOs in the Solar System (30 – 50 AU) and the expected expansion of orbits due to mass loss of the central star, KBOs may orbit around WDs at greater distances. Therefore, I have plotted the curves for orbital distances up to 100 AU and stellar temperatures up to 200,000 K. The dust temperature and the corresponding wavelength for blackbody emission peaks are labeled. The figure demonstrates that only the hottest WDs' dust disks can be heated to temperatures high enough for their SEDs to peak in the mid- to far-IR wavelength range. As the WDs cool, the dust temperatures drop, shifting the emission peaks out of the *Spitzer* wavelength range. Thus, such dust disks may be detectable only for a limited period of time. Furthermore, as the KBOs and comets expand away from the central star, the collisional rate drops, and the dust disk will dissipate below the detection limit.

1.7 Hard X-ray Emission of the Helix CSPN

The central star of the Helix Nebula presents a surprise at X-ray wavelengths as well. *ROSAT* observations of this WD show not only a soft ($\ll$0.5 keV) X-ray emission component, as expected from its photosphere, but also an additional unexpected harder component peaking at 0.8–0.9 keV (Leahy et al. 1996). *Chandra* observations with $\sim$50 times better resolution than *ROSAT* confirmed this hard X-ray emission, and further showed it to be a point source (Guerrero et al. 2001). This emission cannot be due to stellar wind shocks as in the case of massive O stars because *Far Ultraviolet Spectroscopic Explorer (FUSE)* observations of WD 2226−210 do not show P Cygni line profiles that are indicative of the presence of a fast stellar wind (Chu et al. 2004b). Hard X-ray emission from WDs is usually produced externally by the corona of a late-type companion or the accretion of a companion's material

onto the WD's surface. Based on the hard X-ray luminosity and variations, as well as the variations in the stellar Hα line prole, it has been suggested that WD 2226−210 has a late-type companion (Guerrero et al. 2001; Gruendl et al. 2001). WD 2226−210 is, however, not known to have a binary companion. A sensitive search using *HST* images has ruled out any companion with a spectral type earlier than M5, and 2MASS JHK and *Spitzer* IRAC photometry have ruled out even T-type companions (Ciardullo et al. 1999; O'Dwyer et al. 2003; Su et al. 2007). The 1 keV emission from WD 2226−210 thus remains puzzling.

It is possible that KBOs collide with one another to produce dust and some may have gone astray and hit WD 2226−210; the impact would shock-heat gas to X-ray-emitting temperatures. Alternatively, it is possible that CSPN Helix possesses a very low-mass companion that has escaped detection. If the WD's progenitor is in a close binary system, as the primary evolves into the hot WD, some of the stellar envelope material forms a circumstellar or a circum-binary disk. The companion may accrete material and gain angular momentum, and the faster rotation leads to a more active X-ray-emitting corona, similar to that suggested for common envelope binaries (Soker & Kastner 2002). The two stars may even have undergone a merger, a scenario suggested to explain the hard X-ray emission of another single WD, KPD 0005+5106 (=WD 0005+511, Wassermann et al. 2010).

However, no observational evidence gives strong support for either of these two scenarios explaining the hard X-rays of the Helix CSPN, and further study of hard X-ray and mid-IR emission of WDs is needed to understand the physical processes responsible for these phenomena.

1.8 Thesis Outline

This thesis addresses the exciting new phenomenon of dust disks detected around hot WDs and CSPNs. Chapter 2 describes a *Spitzer* MIPS 24 μm survey of hot WDs to search for dust disks similar to that of the Helix CSPN. This work has been published (Chu et al.

2011) and portions of it are reproduced by permission of the AAS. As most of the WDs with dust disks found in this survey were still surrounded by PNe, I have also searched the *Spitzer* archive for CSPNs with IR excesses indicative of dust disks. This archival search is described in Chapter 3, and its results are presented in Chapter 4, in which I also discuss the possible physical origins of these disks. This work is published by Bilíková et al. (2012), and is reproduced by permission of the AAS. In Chapter 5, I present refined modeling of some of the dust disks from these two surveys. Chapter 6 describes my search for additional WDs with hard X-ray emission in the *XMM* and *ROSAT* archives, which has been published in Bilíková et al. (2010), and is reproduced by permission of the AAS. In Chapter 7, I present the summary and conclusions, and discuss the future directions of this research.

Table 1.1. Expected IR Excesses Due to Low-Mass Companions or Planets

Spec. Type	WD $T_{\rm eff}$ (K)	J 1.2 μm	H 1.66 μm	K 2.16 μm	IRAC1 3.6 μm	IRAC2 4.5 μm	IRAC3 5.8 μm	IRAC4 8.0 μm
M5	100,000	0.98	2.04	3.00	5.09	5.07	5.64	6.25
M8	100,000	0.26	0.56	0.93	1.74	1.64	1.96	2.16
L1	100,000	0.11	0.25	0.43	0.93	0.87	1.01	1.26
L5	100,000	0.03	0.08	0.14	0.45	0.60	0.51	0.63
L8	100,000	0.01	0.04	0.07	0.30	0.32	0.47	0.58
$P_{0.5}$	100,000	0.00	0.00	0.00	0.01	0.03	0.07	0.15
$P_{1.0}$	100,000	0.00	0.00	0.00	0.00	0.00	0.01	0.05
M5	50,000	2.09	4.26	6.21	10.	10.30	11.43	12.61
M8	50,000	0.55	1.16	1.92	3.55	3.33	3.96	4.37
L1	50,000	0.24	0.53	0.89	1.89	1.78	2.04	2.54
L5	50,000	0.06	0.16	0.29	0.92	1.22	1.02	1.27
L8	50,000	0.02	0.07	0.14	0.61	0.64	0.95	1.16
$P_{0.5}$	50,000	0.00	0.00	0.00	0.00	0.00	0.00	0.02
$P_{1.0}$	50,000	0.00	0.00	0.00	0.00	0.00	0.00	0.00
M5	10,000	17.58	31.02	41.29	61.31	58.74	63.27	67.85
M8	10,000	4.64	8.49	12.75	20.95	18.99	21.92	23.51
L1	10,000	2.02	3.82	5.92	11.19	10.14	11.28	13.64
L5	10,000	0.51	1.17	1.96	5.41	6.97	5.67	6.82
L8	10,000	0.21	0.54	0.92	3.58	3.67	5.26	6.25
$P_{0.5}$	10,000	0.00	0.00	0.00	0.00	0.00	0.00	0.00
$P_{1.0}$	10,000	0.00	0.00	0.00	0.00	0.00	0.00	0.00

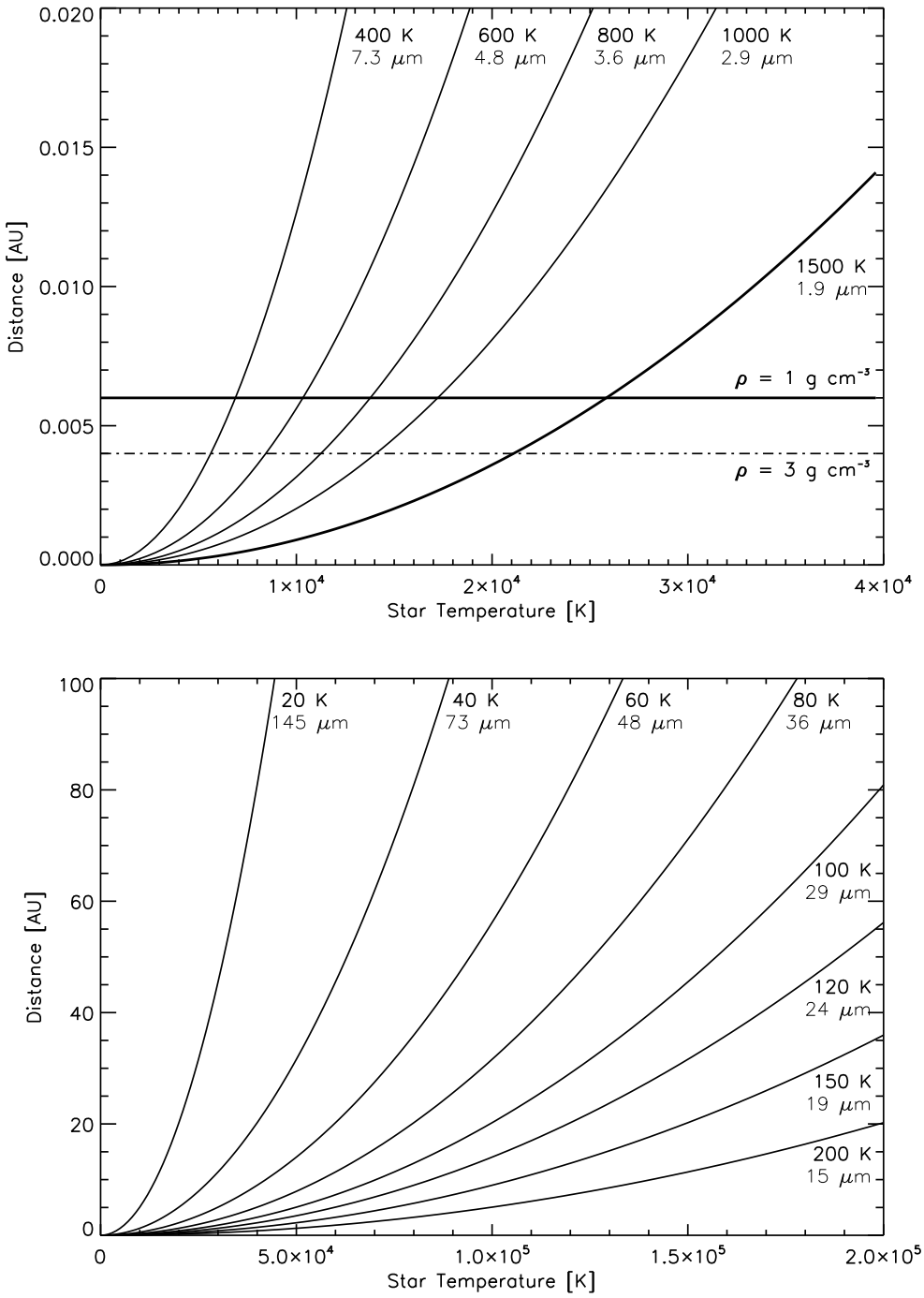

Figure 1.1: Curves of constant dust temperature in the $D - T_\star$ (distance - effective temperature) parameter space, assuming an albedo of 0.1. The dust temperatures and corresponding blackbody peak wavelengths are labelled. (a) Dust disks formed by tidal disruption of asteroids. The horizontal lines at 0.006 and 0.004 AU mark Roche limits for a WD with a mass of $\sim$0.6 $M_\odot$ and a radius of $\sim$1 $R_\oplus$, and asteroid densities of 1 and 3 g cm^{-3}, respectively (range of most Solar System asteroids, (Britt et al. 2005). These represent rough upper limits to the outer extent of the disk. The curve for the dust sublimation temperature of 1,500 K marks the inner boundary of the orbital distance for dust to survive. (b) Curves of constant dust temperature, but over a larger range of orbital distances and stellar temperatures. The dust at distances of 30-100 AU from the star will peak in mid-IR (24-70 μm) only if its central star is very hot (>80,000 K).

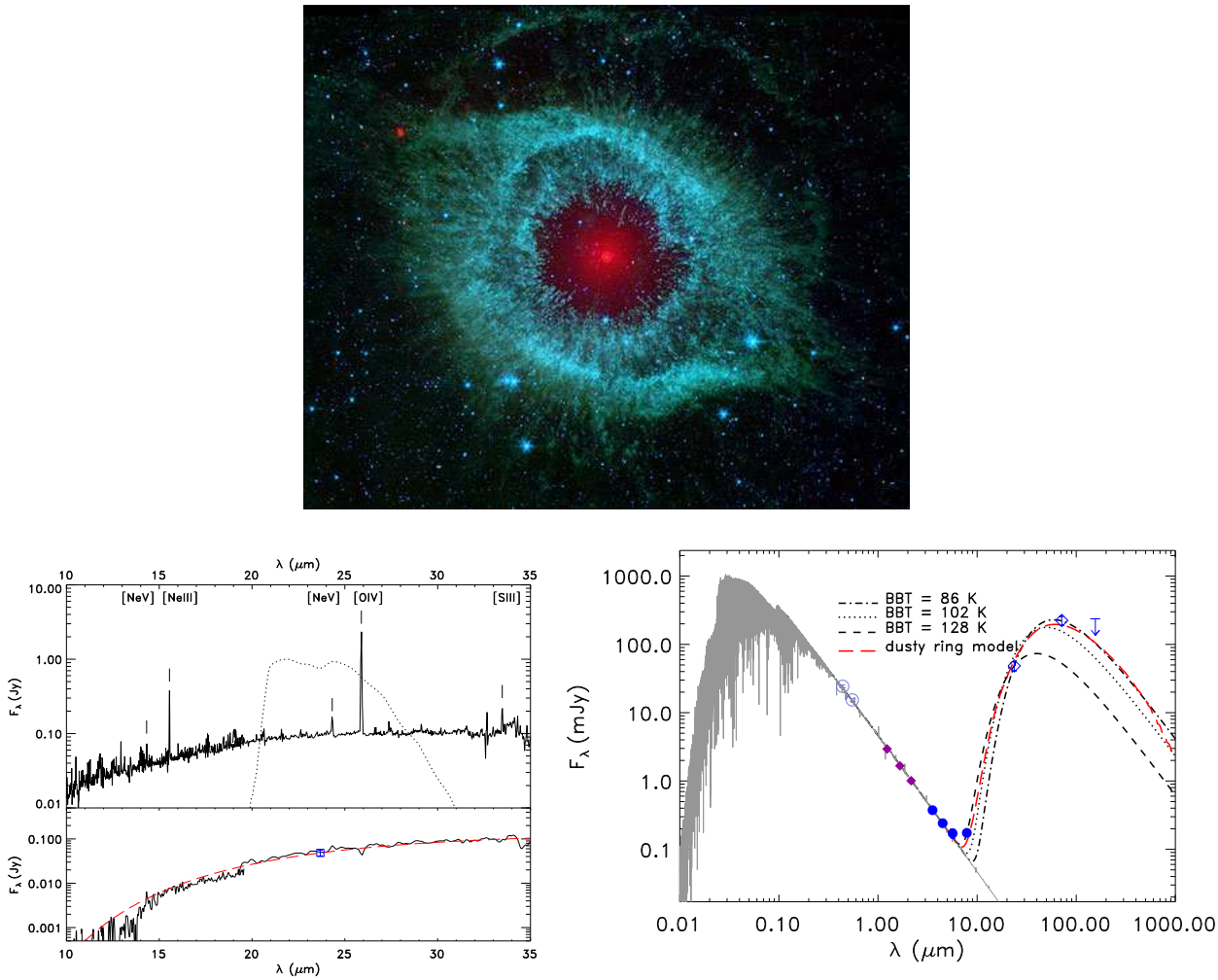

Figure 1.2: The image, IR spectrum and the SED of the Helix CSPN from Su et al. (2007). **(a)** A color composite of *Spitzer* images of the Helix Nebula with 3.6-4.5 μm in blue, 5.8-8.0 μm in green, and 24 μm in red (FOV = $31\farcm5 \times 23\farcm7$). The central diffuse emission in the 24 μm band is dominated by the [O IV] 25.89 μm line with some contribution from the [Ne V] 24.32 μm line. The central point-like source, coincident with WD 2226−210, is dominated by dust continuum in the 24 μm band. **(b)** Spectral energy distribution of the Helix central star. The WD photospheric model is plotted in gray. The excess mid-IR emission is consistent with a blackbody emission for a temperature (BBT) ranging from 86 K to 128 K. The spectral energy distribution of a dusty ring (35-150 AU) is plotted in a red long-dashed line. **(c)** *Spitzer* IRS spectrum of the Helix central star before (top panel) and after (bottom panel) the nebular background subtraction. The MIPS 24 μm bandpass is plotted with a dotted line in the upper panel, and the MIPS 24 μm photometry is shown as a blue square in the bottom panel. A 102 K blackbody curve is plotted in red dashed line in the bottom panel. See Su et al. (2007) for a detailed explanation of this figure.

Chapter 2

Spitzer 24 μm Survey of White Dwarfs for Dust Disks

2.1 Introduction

Spitzer MIPS 24 and 70 μm observations of the Helix Nebula show a compact source coincident with its CSPN, WD 2226−210. This IR emission originates from a 90 – 130 K dust continuum with an emitting area of $\sim$ 4 – 40 AU^2. This dust is likely located in a disk, as opposed to a cloud, because the extinction towards the CSPN is very low (Su et al. 2007). A simple optically thin model of the dust disk places it between 35 and 150 AU, and yields a dust mass of $\sim$0.13 $M_\oplus$. The dust must have been generated recently, because any remnant dust from the main-sequence evolution has been blown out by the stellar wind in the AGB and post-AGB stages. Since the location of the disk is similar to that of the Kuiper Belt in the Solar System, the dust was suggested to be produced by collisions among KBOs or break-up of comets (Su et al. 2007).

Theoretical simulations of debris disk evolution past the main sequence (e.g., Bonsor & Wyatt 2010; Dong et al. 2010) were able to produce similar amount of dust through KBO collisions. If the dust around the Helix CSPN was indeed produced by this mechanism, other WDs should also possess similar dust disks. Therefore, to assess the frequency of occurrence of these dust disks, we have conducted a *Spitzer* MIPS 24 μm survey of hot WDs and pre-WDs for IR excesses indicative of circumstellar dust (Chu et al. 2011). In this chapter, I report the results of this survey, with emphasis on my contributions to the project: the SED modeling and the reduction and analysis of follow-up spectroscopic observations.

2.2 Observations and Data Reduction

In order to detect a dust disk at a distance of few tens of AU, the central WD must be sufficiently luminous. In general, stellar luminosity is a function of both radius and effective temperature. However, the range of WD radii is small, and thus stellar effective temperature is the main factor in determining the luminosity of a WD, and, consequently, the detectability of a Helix-like dust disk around it (see Fig. 1.1). Therefore, the 24 μm survey target list included 71 hot WDs and pre-WDs with $T_{\rm eff}\sim$100,000 K; of these, 36 were still surrounded by a planetary nebula (PN).

The 24 μm survey was carried out in *Spitzer* Program 40953 (PI: Chu). For some of the WDs in this survey, we have also obtained follow-up IRAC and MIPS images, and IRS spectroscopic observations in Program 50629 (PI: Chu). These observations are described below. Note that only a brief summary is given for the imaging observations; for full details, see Chu et al. (2011).

2.2.1 MIPS Observations

The 71 WDs in the *Spitzer* MIPS 24 μm survey were imaged in the small-field photometry mode with a total exposure time of 420 s. The depth of the survey reached a 1-σ point-source sensitivity of 33.6 μJy in typical background conditions. The data were reduced with the Data Analysis Tool (Gordon et al. 2007), and the final images were constructed with a pixel size of $1\farcs245$, half the original resolution.

Nine WDs/pre-WDs were detected at 24 μm. Both aperture photometry and point spread function (PSF) fitting were used to measure the 24 μm flux densities for detected sources, and when the measurements with these two different methods differed, the best appropriate method was selected. We have adopted the results from PSF photometry for all detections except for WD 0439+466, for which the result from aperture photometry was adopted. The final flux densities are listed in Table 2.1.

For three objects, CSPN K 1-22, WD 0103+732, and WD 0439+466, we have obtained *Spitzer* MIPS 70 μm observations, each with a total effective integration time of 960 s. The detailed description of these observations is given in Chu et al. (2011). The images of these three observed objects are shown in Figure 2.1, along with their 24 μm counterparts.

Two of the WDs, WD 0103+732 and WD 0439+466 were detected at 70 μm. The measured 70 μm flux densities and upper limits are listed in Table 2.1. Note that WD 0103+732 is superposed on a diffuse nebular emission. Since this emission may significantly contaminate the measured 70 μm point source flux density, we list our photometric measurement as an upper limit.

2.2.2 IRAC observations

For CSPN K 1-22, WD 0103+732, and WD 0127+581, we have obtained IRAC 3.6, 4.5, 5.8 and 8.0 μm observations with a total integration time of 150 s. Three additional objects, WD 0439+466, WD 0726+133, and CSPN NGC 2438, have IRAC observations in the *Spitzer* archive, in Programs 30432 (PI: Burleigh), 30285 (PI: Fazio), and 68 (PI: Fazio), respectively. The data from all these observations were reduced with the MOPEX package. Aperture photometry was carried out using the IRAF task phot, and appropriate aperture corrections from the IRAC Data Handbook (ver 3.0) were applied. The measured IRAC flux densities are listed in Table 2.1.

2.2.3 IRS Observations

We have also obtained follow-up spectroscopic observations of CSPN K 1-22, WD 0103+732, WD 0127+581, and WD 0439+466 in our Program 50629, using the IRS instrument on *Spitzer* (Houck et al. 2004). All sources were observed using the low-resolution modules SL1 (7.4–14.5 μm), SL2 (5.2–7.7 μm), LL1 (19.5–38.0 μm), and LL2 (14.0–21.3 μm). CSPN K 1-22 and WD 0103+732 were observed in the IRS staring mode.WD 0127+581, the faintest

target, was observed in mapping mode where the target was sequentially stepped along the slit to facilitate an improved background subtraction. The SL1 and SL2 observations of WD 0127+581 used 8 pointings spaced by 3″ while the LL1 and LL2 observations used 12 pointings spaced by 6″. The observations of WD 0439+466 were also made in the mapping mode, with slit positions centered on the WD and sequentially offset in the direction perpendicular to the slit. Nine pointings separated by 3.″6 were taken in SL1 and SL2 modules, and 5 pointings spaced by 10.″6 were obtained in LL1 and LL2 modules. The IRS observations are summarized in Table 2.2.

All spectra were reduced using the CUBISM software (Smith et al. 2007) with the latest pipeline processing of the data and most recent calibration set (irs_2009_05_20-pb-pfc-trim-omeg-lhllbiasfork.cal). Each low-resolution module contains two subslits that are exposed at the same time, e.g., SL1 on-source and SL2 off-source, and vice versa. I examine the off-source frames, select the ones free of any source contamination, trim the maxima and minima, and use the average to produce a background frame. This 2D background frame is then subtracted from all on-source frames in the corresponding module to remove astrophysical background and to alleviate bad pixels contaminating the IRS data. After 2D background subtraction, I flag global and record-level bad pixels first using the default CUBISM parameters for automatic bad pixel detection, and then through manual inspection of each BCD record, as well as by backtracking pixels that contribute to a given cube pixel.

The spectra are extracted with aperture sizes large enough to enclose the 24 μm source. See Table 2.3 for the aperture sizes used for the spectral extractions. For the LL orders, two local background spectra on either side of the source are extracted and averaged for a 1D subtraction of the local background. For the SL orders, a single background spectrum is used for the local 1D background subtraction.

Special notes for spectral reduction of individual objects are given below:

WD 0103+732. The frames used for the construction of LL1 background contain a very faint point source. As the WD is bright and the point source is practically removed in the

min/max trimming and averaging process, I choose to ignore this faint source so that I can perform the 2D background subtraction to maximize the quality of the final data cube. In addition, the frames used for the construction of the LL2 background show a small knot of H_2 line emission at 17 μm. This H_2 emission knot is near the center of one slit position, and at the edge of the other slit position. I therefore use only the latter slit position for background subtraction. Pixels of the on-source BCD frames affected by over-subtraction of the emission knot are flagged as record-level bad pixels, and not used for cube construction. Furthermore, this H_2 knot is far enough from the WD position that both a target spectrum and a local background spectrum can be extracted outside the position of the H_2 emission knot in the slit. The spectrum of WD 0103+732 is not detected in the SL2 observations.

WD 0127+581. This WD is faint, with $F_{24} = 0.34$ mJy. The orientation of the IRS slit, determined by the roll angle of the spacecraft, was such that a very bright neighboring star was included in the slit. Consequently, the weak emission of WD 0127+581 was overwhelmed by the elevated background from the neighboring star. The spectrum of the WD is not unambiguously detected in the background-subtracted frame; the signal-to-noise ratio is too low for meaningful spectral extraction.

WD 0439+466. In its SL2 order, the BCD frames from the three final mapping positions show an abrupt jump in brightness across the center of each frame. Since these slit positions do not contain the target WD, I do not use them for the SL2 cube construction or the SL1 background construction.

2.2.4 Echelle Spectroscopic Observations

For WD 0950+139, I have obtained high-dispersion (R$\sim$30,000) spectra with the echelle spectrograph on the Mayall 4 m telescope at Kitt Peak National Observatory (KPNO) on 2010 January 3. The observations were carried out with the red long-focus camera and the T2KB CCD. We used the 79 lines mm^{-1} (79-63) echelle grating in the multi-order configuration, with the GG-420 filter and the 226 lines mm^{-1} (226-1) cross-disperser. We chose a slit length

of 10″ to include adequate coverage of the extended PN and sky for background subtraction, while avoiding overlap between adjacent orders. The spectral dispersion and wavelength were calibrated with a Th-Ar lamp exposure taken after the target observation. The 24 μm CCD pixel size corresponds to $\sim$0.078 Å and $\sim$0.254″ along the dispersion and spatial axes, respectively. The instrumental profile had a FWHM of 0.275 $\pm$ 0.036 Å measured from the telluric lines. The exposure time for each frame was 1800 s.

Bias subtraction and bad pixel removal were carried out using standard tasks within IRAF. Multiple exposures of WD 0950+139 were compared to eliminate cosmic ray hits. The spectra were calibrated and extracted with the task doecslit. The observing conditions were not photometric; however, we calibrated the relative fluxes between orders using a 600 s exposure of the standard star Feige 34 from the following night.

2.3 Results

Nine out of the 71 objects from our *Spitzer* MIPS survey show a source coincident with the WD at 24 μm. To assess whether the detected emission is in excess of the expected photospheric emission, we have collected optical and near-IR photometric measurements for each WD, using the McCook and Sion WD catalog, the SIMBAD database, the Sloan Digital Sky Survey (SDSS) and the 2MASS Point Source Catalog (Skrutskie et al. 2006). Since the effective temperatures of our program WDs are very high, it is reasonable to approximate their photospheric emission in the IR with the Rayleigh-Jeans blackbody tail. The amounts of extinction toward most of these WDs are unknown, but will have smaller impact at longer wavelengths. We therefore extrapolate the flux density in the 24 μm band from the photometric measurement at the longest wavelength, using the Rayleigh-Jeans blackbody tail and no extinction correction.

All nine detections are at least two orders of magnitude higher than the expected photospheric emission, and thus represent IR excesses. Note that even for non-detections, the 3-σ

upper limits are one to two orders of magnitude above the expected photospheric emission; thus, it is possible that some of these objects also possess a low-level IR excesses.

We have combined all available photometric measurements of the nine WDs and pre-WDs with 24 μm excesses to produce the SEDs plotted in Figure 2.2. The *Spitzer* IRAC and MIPS photometric measurements of these nine hot WDs are listed in Table 2.1. The data points in the SEDs are corrected for interstellar extinction, using values found in the literature, and listed in Table 2.4.

Table 2.4 also lists basic physical parameters of the hot WDs and their IR excesses. The effective temperatures and distances are from the literature, and the references for these are given in the last column. The radius of the WD, $R_\star$, is calculated from the distance and the blackbody fit to the optical flux densities. Note that all values are within the range expected for WDs. The luminosity fraction, $L_{\rm IR}/L_*$, is calculated from the blackbody fits to the optical and IR SEDs. For WDs without excesses in IRAC bands, or WDs without IRAC data, we approximate the IR emitter with a 150 K blackbody, normalized to the 24 μm flux density. For WDs with IRAC excesses, the IRAC flux densities are used to constrain the temperature of the blackbody emitter. Where necessary, an additional blackbody component is used to fit the IR flux density measurements. Below we individually describe the nine hot WDs and pre-WDs with 24 μm excesses.

2.3.1 CSPN K 1-22

Figure 2.3 shows images of CSPN K 1-22 at optical and IR wavelengths. The field of view towards K 1-22 is crowded. A red source is seen 2″ north of the CSPN in the DSS2 Red image, but not in any other images; the origin of this red source is unclear. Ciardullo et al. (1999) have resolved a red ∼K2 V companion to the CSPN in the *Hubble Space Telescope* (*HST*) observations. A source coincident with this pair of stars is seen in 2MASS, IRAC and MIPS images, but the resolution is not sufficient to separate these two sources in the IR images.

The SED in Figure 2.2 shows the V and I magnitudes for the two stars separately; the remaining flux densities in the 1 – 24 μm range are for the two stars combined. The downward arrow at 70 μm indicates the upper flux density limit. The optical and near-IR flux densities in the SED plot have been corrected for extinction using $E(B-V) = 0.076$ (Ciardullo et al. 1999). The physical parameters used to model the WD and IR emission of CSPN K1-22 and the other WDs with IR excesses are listed in Table 2.4. The WD emission of CSPN K1-22 is approximated by a 141,000 K blackbody; for its red companion, we use Kurucz atmospheric model for a K2 V star's. The IRAC and MIPS flux densities are above the combined atmospheric emission from these two stars. Two blackbody components, at 700 and 150 K, are needed to approximate the excess IR emission in the IRAC and MIPS 24 μm bands. The sum of all emission components, the two stars and the two blackbody IR emitters, is shown in Figure 2.2 as a thin solid line.

The IRS spectra of CSPN K 1-22 and local background are shown in Figure 2.4. The plots were made with two different scales to show the relative contribution of line emission and continuum. The spectra of CSPN K 1-22 and the local background both show [Ne III] 15.55 μm, [S III] 18.71 μm, [O IV] 25.89 μm, and [S III] 33.48 μm line emission. After background subtraction, the IRS spectrum of CSPN K 1-22 shows a weak continuum component and residual line emission, especially in the [O IV] line.

To assess whether the residual line emission is associated with an unresolved source, or whether it is a result of incomplete background subtraction, I construct the surface brightness profiles along the slit, extracted from the spectral *Spitzer* IRS data cube. The surface brightness profile is extracted at the wavelength of the high-ionization [O IV] 25.89 μm line, the lower-ionization [S III] 18.71 μm line and the continuum emission in the LL module. The surface brightness profiles, and a raw spectral image are shown in Figure 2.5. It is evident that the continuum originates from a point source, the CSPN, while the line emission from the PN is extended.

The [S III] 18.71 μm line is a lower-excitation line and its profile is extended and relatively

flat, whereas the [O IV] 25.89 μmline, a high-excitation line, shows a centrally peaked surface brightness profile. Such surface brightness distribution agrees with the expected ionization stratification in a PN. Since the spectrum for local background subtraction is extracted $\pm 20''$ away from the CSPN, the [O IV] 25.89 μm emission in the background spectrum is $\sim$1/3 weaker than that at the CSPN. Indeed, the residual [O IV] emission is about a 1/3 of the peak emission in the [O IV] line prior to local background subtraction. Therefore, the [O IV] emission in the background-subtracted spectrum of CSPN K 1-22 is due to imperfect background subtraction.

The open diamonds in Figure 2.4 display the IRAC and MIPS photometric measurements. While the IRAC data points agree with the spectrum within the error bars, the MIPS 24 μm measurement is above the error bars. This discrepancy is likely due to [O IV] contamination in the MIPS 24 μm band.

The raw spectral image, as well as the extracted background-subtracted spectrum of CSPN K1-22 show continuum emission; this emission is well above the expected combined photospheric emission of the CSPN and its red companion ($\sim$0.011 mJy). CSPN K1-22 clearly has an IR excess due to dust emission; however, it is unclear whether this dust emission is associated with the CSPN or its red companion. High-resolution mid-IR imaging is necessary to resolve the two stars.

2.3.2 CSPN NGC 2438

CSPN NGC 2438 (Figure 4.9) shows bright 24 μm emission more than four orders of magnitude above the expected photospheric emission. In addition, IR excess is found in *Spitzer* IRAC bands (see Chapter 4). I have obtained the *Spitzer* IRS $\sim$5 – 15 μm spectrum of CSPN NGC 2438 in Program 50793 (PI: Bilikova). The background-subtracted spectrum of the CSPN shows weak but rising continuum emission. The SED of CSPN NGC 2438 is displayed in Figure 2.2. The IR excesses in the IRAC bands and the MIPS 24 μm band is approximated by two blackbody emitters at temperatures of 1200 K and 150 K, respectively.

A more detailed discussion of the SED and IRS spectrum of CSPN NGC 2438 is given in chapters 3 and 4.

2.3.3 WD 0103+732 (CSPN EGB 1)

WD 0103+732 is the central star of the PN EGB 1. Its optical and IR images are shown in Figure 2.7. Ciardullo et al. (1999) have used the *HST* to search for resolved companions of CSPNs, but no companion has been found for WD 0103+732

The SED of CSPN EGB 1 is displayed in Figure 2.2. The flux densities at optical wavelengths follow the blackbody curve closely. However, the I and J band flux densities, as well as the H band upper limit from 2MASS are below the expected photospheric emission. Note also that the light curve of WD 0103+732 exhibits sinusoidal variations in the BVR bands, but the nature of these variations is not yet known (Hillwig et al. 2012, in preparation). The IRAC fluxes at 3.6, 4.5 and 5.8 μm are close, but slightly below the expected photospheric emission. The 8 μm flux is above the blackbody curve, and a bright excess $\sim$3 orders of magnitude above the expected WD's photospheric emission is seen at 24 μm. A source coincident with the CSPN is also seen at 70 μm, but due to the bright nebulosity and lower angular resolution of the MIPS 70 μm camera, there may be a significant nebular contamination in our 70 μm photometric measurement; we therefore consider the measured value to be the 70 μm flux density upper limit.

The 24 μm point source coincident with WD 0103+732 is superposed on diffuse emission (Chu et al. 2009, see Figure 2.7). The IRS spectrum extracted at the CSPN and adjacent local background is shown in Figure 2.8. The spectrum of the background is dominated by line emission, but a weak rising continuum is seen at wavelengths longer than $\sim$ 20 μm. Both the CSPN and the background spectrum show weak molecular hydrogen (H_2) emission features at 17 and 28 μm; this emission is extended and uniform across the slit, and is removed after the local background subtraction. The background-subtracted spectrum of the CSPN is dominated by continuum emission, but some residual line emission is seen

in [O IV] 25.89 μm line, and a deficit is seen at the [Ne III] 15.55 μm and [S III] 18.31 and 33.48 μm lines. These features are caused by imperfect background subtraction. The raw spectral images, as well as a surface brightness profile extracted in [O IV] and [S III] lines and the continuum from the IRS data cube are shown in Figure 2.9. From the raw spectral images, it is evident that the line emission is extended compared to the continuum. The surface brightness profiles of emission lines are also more extended than that of the continuum emission. Furthermore, the surface brightness profiles are consistent with the ionization stratification of the PN, with the higher-excitation [O IV] line concentrated closer to the CSPN and the lower-excitation [S III] line more extended. The variations of these lines along the slit are responsible for the over- and under-subtractions of background for these emission lines.

The SED and the IRS spectrum of CSPN EGB 1 are similar to those of the Helix CSPN, but the effective temperature of WD 0103+732, $\sim$150,000 K, is higher than that of the Helix CSPN. Therefore, the physical properties of the dust disk around CSPN EGB 1 may differ from those of the disk around the Helix CSPN. A more detailed dust disk model is presented in Chapter 5.

2.3.4 WD 0109+111

Unlike most of the WDs with 24 μm excesses, WD 0109+111 (Figure 2.10) is not surrounded by a PN. There is a good (1-2$''$) positional coincidence for the WD in optical, near-IR and 24 μm images. The MIPS 24 μm image contains a number of faint background sources, likely associated with background galaxies. We find that the chance of random superposition of one of these sources within 2$''$ of WD 0109+111 is very low, $\sim 4 \times 10^{-4}$.

The SED of WD 0109+111 is shown in Figure 2.2. The optical and near-IR flux densities follow the blackbody curve closely, but a clear excess is seen at 24 μm. Unfortunately, no IRS spectra were obtained to determine the nature of the excess 24 μm emission.

2.3.5 WD 0127+581 (CSPN Sh 2-188)

WD 0127+581 (Figure 2.11) is the CSPN Sh 2-188. This WD is faint, and is not detected in 2MASS. The $J = 17.03 \pm 0.13$ and $K_s = 16.18 \pm 0.13$ magnitudes were obtained using the FLAMINGOS detector on the KPNO 2.1 m telescope. The CSPN is faint and superposed on a bright background in IRAC images; therefore, the photometric errors are large; in fact, the 5.8 and 8.0 μm band detections are not very convincing. The IRS spectrum of this WD is compromised by the presence of a very bright source in the slit. Only an extremely weak continuum is seen at the position of the WD; no meaningful spectrum can be extracted.

The SED of WD 0127+581 (Figure 2.2) shows excess emission in all IR wavelength bands, from 1 to 24 μm, but the excess SED is not continuous. The J and K_s excesses may indicate a low-mass companion. Two temperature components, 900 and 150 K, are needed to approximate the excess emission in the IRAC and MIPS bands, respectively.

2.3.6 WD 0439+466 (CSPN Sh 2-216)

Sh 2-216, at a distance of 129±6 pc (Harris et al. 2007), is the nearest PN. The optical and IR images of its CSPN, WD 0439+466, are shown in Figure 2.12. A point source coincident with the central WD, surrounded by diffuse emission, is seen in the MIPS 24 μm image. The optical and IR flux densities in the SED of this WD (Figure 2.2) follow the blackbody curve up to 8 μm, but the 24 μm flux density is ~ 2 orders of magnitude above the expected photospheric emission of the WD.

Figure 2.13 displays the raw IRS spectral image, and the extracted spectra of WD 0439+466 and its local background. The spectrum extracted at the CSPN shows rising continuum emission, and [O IV] 25.89 μm and the H_2 17 μm emission lines. These emission lines originate from the local nebular background, and they are removed after the local background subtraction. The background-subtracted spectrum is dominated by continuum emission, and the flux densities in the spectrum are in good agreement with *Spitzer* IRAC and MIPS pho-

tometric measurements, plotted as open diamonds. This spectrum is very similar to that of the Helix CSPN.

2.3.7 WD 0726+133 (CSPN Abell 21)

WD 0726+133 is the central star of the PN Abell 21. Its optical and IR images are presented in Figure 2.14. At 24 μm, a point source coincident with the CSPN is seen superposed on a diffuse emission (Chu et al. 2009). The SED in Figure 2.2 shows that the flux densities in the optical, 2MASS JHK and IRAC bands follow the blackbody curve expected from the photospheric emission of the WD. At 24 μm, a significant excess, $\sim$3 orders of magnitude above the expected photospheric emission, is seen. For this CSPN, high-resolution *HST* images are available, but no companion of CSPN A21 is found (Ciardullo et al. 1999). The SED for this CSPN is similar to that of the Helix CSPN, but no IRS spectrum is available to assess the nature of the excess 24 μm emission.

2.3.8 WD 0950+139 (CSPN EGB 6)

WD 0950+139 is the central star of PN EGB 6. Optical observations of this CSPN showed an unresolved emission line source in [O III] and [Ne III] lines (Liebert et al. 1989), and the CSPN also exhibits a near-IR excess (Fulbright & Liebert 1993).

High-resolution *HST* Faint Object Camera emission-line images revealed that the emission actually originates from a point-like source that is offset from the PN nucleus by 0.″18, and subsequent continuum images confirmed the presence of a dM companion (Bond 1994, 2009). It has been suggested that the dM companion has accreted material from the progenitor of WD 0950+139 and that this accretion disk is responsible for the excess IR emission as well as the nebular line emission (Bond 1994). Optical and IR images of WD 0950+139 are presented in Figure 2.15.

Using high-resolution echelle spectroscopic observations of WD 0950+139, we detect the

emission-line source in a number of lines: He I 7065 Å, Hα 6563 Å, He I 5875 Å, [N II] 5754 Å, [O III] 5007 Å, [O III] 4959 Å, and Hβ 4861 Å. The full width at half maximum (FWHM) of these lines are 30–50 km s^{-1}, and their base extends between -50 km s^{-1} and 50 km s^{-1}. The profiles of some of these lines are shown in Figure 2.16. The [O III] 4959 and 5007 lines exhibit a double-peaked profile, which is consistent with a rotating gaseous disk. The raw spectral image of the [O III] 5007 emission line can be seen in Figure 2.16. Fitting the [O III] line profiles with two Gaussian components yields the separation between the two peaks of $\sim$22 km s^{-1}, or $\pm$11 km s^{-1}. Assuming Keplerian rotation, such velocity corresponds to an orbital radius 0.5 AU around a 0.06 $M_{\odot}$ star, and 1.5 AU around a 0.2 $M_{\odot}$ star (Su et al. 2011).

The 24 μm image of EGB 6 shows a bright point source coincident with WD 0950+139. The SED (Figure 2.2) demonstrates that emission in excess of the expected WD photospheric emission can be seen starting from the J-band to longer wavelengths. A dM (T$\sim$2000 K) companion can account for the near-IR excess, but not the IRAC and MIPS excesses. The SED in the IRAC and MIPS 24 μm bands is approximated by two blackbody emitters at temperatures of 500 and 150 K. A *Spitzer* IRS spectrum of WD 0950+139, obtained through Guaranteed Time Observations, shows that the excess IR emission originates from a dust continuum (Su et al. 2012, in preparation). Unfortunately, it is unclear whether the dust emission seen at 24 μm is associated with WD 0950+139, or its low-mass companion.

2.3.9 WD 1342+443

WD 1342+443 is a faint WD discovered in the SDSS. Its optical and IR images are presented in Figure 2.17. Its SED in Figure 2.2 displays the photometric measurements from the SDSS; the WD was not detected in 2MASS. The flux densities follow the blackbody approximation of the WD's photospheric emission, but the 24 μm flux density is more than 2 orders of magnitude higher than the expected photospheric emission of the WD. The 24 μm excess of this WD is the weakest among the nine WDs with IR excesses. No IRS spectrum is available

to investigate the nature of this excess 24 μm emission.

2.4 Discussion

2.4.1 Statistical Properties

Nine out of the 71 hot WDs and pre-WDs from our sample exhibit excess 24 μm emission, corresponding to a detection rate of $\sim$13%. Correlation of the 24 μm excess and the J-band magnitudes, indicative of WD distances, shows that the detection of 24 μm excesses in more distant objects is limited by the sensitivity of the MIPS 24 μm survey, and thus, the true percentage of WDs with 24 μm excesses is likely higher than 13% (Chu et al. 2011). Interestingly, seven out nine hot WDs/pre-WDs with 24 μm excesses are still surrounded by PNe: CSPN K 1-22, CSPN NGC 2438, WD 0103+732 in EGB 1, WD 0127+581 in Sh 2-188, WD 0439+466 in Sh 2-216, WD 0726+133 in Abell 21 (YM 29), and WD 0950+139 in EGB 6. The two WDs not surrounded by PNe, WD 0109+111 and WD 1342+443, have the faintest 24 μm emission and the lowest 24 μm excesses. While the detection rate of 24 μm excesses among CSPNs in our sample is 20%, the detection rate of 24 μm excesses among hot WDs not surrounded by PNe is much lower, 5–6%. The higher incidence rate of 24 μm excesses among CSPNs, which are less evolved than bare WDs, could indicate an evolutionary effect of excess diminishing with age. Such evolutionary effect is however not seen among PNe, if the PN size is assumed to reflect its evolutionary status (Chu et al. 2009). On the other hand, the sample size is too small to see a clear evolutionary trend.

2.4.2 Nature of the 24 μm Excesses

The SEDs of hot WDs with 24 μm excesses fall into two broad categories, those without near-IR excess, and those with near-IR excess.

The SEDs of three WDs, WD 0103+732 (CSPN EGB 1), WD 0439+466 (CSPN Sh 2-

216) and WD 0726+133 (CSPN Abell 21), show only 8 and 24 μm excesses and are therefore similar to the SED of the Helix CSPN. Their SEDs, lacking near-IR excesses, do not indicate the presence of a late-type companion. Four hot WDs with 24 μm excesses also exhibit excess emission in the IRAC bands: CSPN K 1-22, CSPN NGC 2438, WD 0127+581 (CSPN Sh 2-188), and WD 0950+139 (CSPN EGB 6). Their IRS spectra indicate that the origin of the excess emission is a continuum, and the emitting areas required to account for the excess emission are too large for the emission to originate from a brown dwarf companion. The IR emitters in these cases are most likely dust disks. Two out of these CSPNs, CSPN K 1-22 and WD 0950+139, have known late-type companions (Ciardullo et al. 1999; Bond 2009). It may be possible that the IR excesses of these CSPNs is associated with a companion. Two WDs with 24 μm excesses lack IRAC observations, therefore, it is not known whether an IR excess at these wavelengths is present.

Even though the IR emission is very likely to originate from dust disks, it is not certain that these dust disks are all produced by collisions among KBOs, as proposed for the Helix CSPN by Su et al. (2007). It is possible that some of these dust disks have formed through binary interactions. Keplerian-rotating dust disks around post-AGB binaries are common, and since the CSPN stage immediately follows that of post-AGB stars, the dust disks around some of the CSPNs may be connected to those of post-AGB binaries. The covering fractions listed in Table 2.4 and those of post-AGB binaries of de Ruyter et al. (2006) are very different; however, and it is not known whether this is due to a different physical origins, or evolutionary effects. For further discussion of the origin of dust disks around these hot WDs and CSPNs, see Chu et al. (2011) and Chapter 4.

2.5 Summary

Inspired by the discovery of a dust disk around the CSPN of the Helix Nebula, we have carried out a 24 μm *Spitzer* MIPS survey of hot WDs and pre-WDs for similar dust disks.

We find nine cases of 24 μm excesses; in seven of these, the hot star is still surrounded by a PN. The detection rate $\sim$13% is likely a lower limit to the true fraction of hot WDs with dust disks, since the detection of more distant disks is precluded by inadequate sensitivity. The detection rate of 24 μm excesses, 20%, is much higher than that of hot WDs not surrounded by PNe, 5%.

In four cases, the 24 μm excess is accompanied by JHK or IRAC excess as well. In two of these cases, the excess JHK emission is caused by a known companion, but the IRAC excesses are still above the expected emission from both these components.

Spitzer IRS spectra are available for 6 of the hot WDs/pre-WDs. In five cases, the spectra clearly show that the IR excesses originate from a dust continuum. In one case, an extremely faint continuum is seen, but the contamination from a nearby very bright source precludes any spectral extraction. Blackbody fits of the IR excesses indicate that the IR emitters must have large emitting areas, which can only be provided by dust disks.

The dust around the Helix CSPN was suggested to be produced by collisions among KBOs objects in the surviving planetesimal belts. The near-IR excesses, as well as known companions for some of these sources, may indicate another physical origin for these dust disks. These dust disks could have been produced in binary interactions, and correspond to remnants of the commonly-observed disks around post-AGB binaries. The luminosity fractions, $L_{\rm IR}/L_*$, are similar to those of dust disks around main-sequence stars and lower than those of dust disks around post-AGB stars, but this may be due to evolutionary effects.

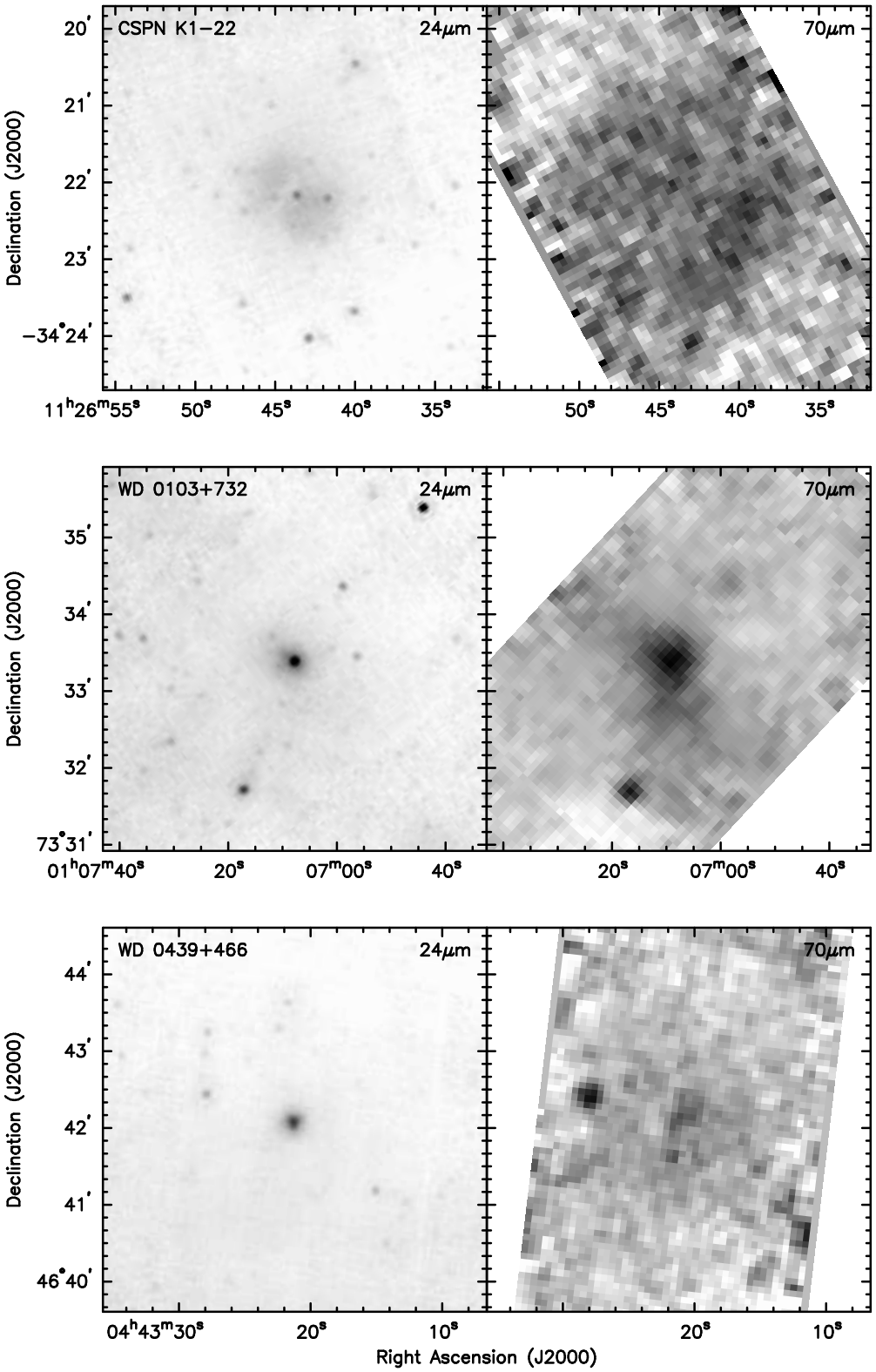

Figure 2.1: *Spitzer* MIPS 24 and 70 μm images of CSPN K 1-22, WD 0103+732 (CSPN EGB 1), and WD 0439+466 (CSPN Sh 2-216).

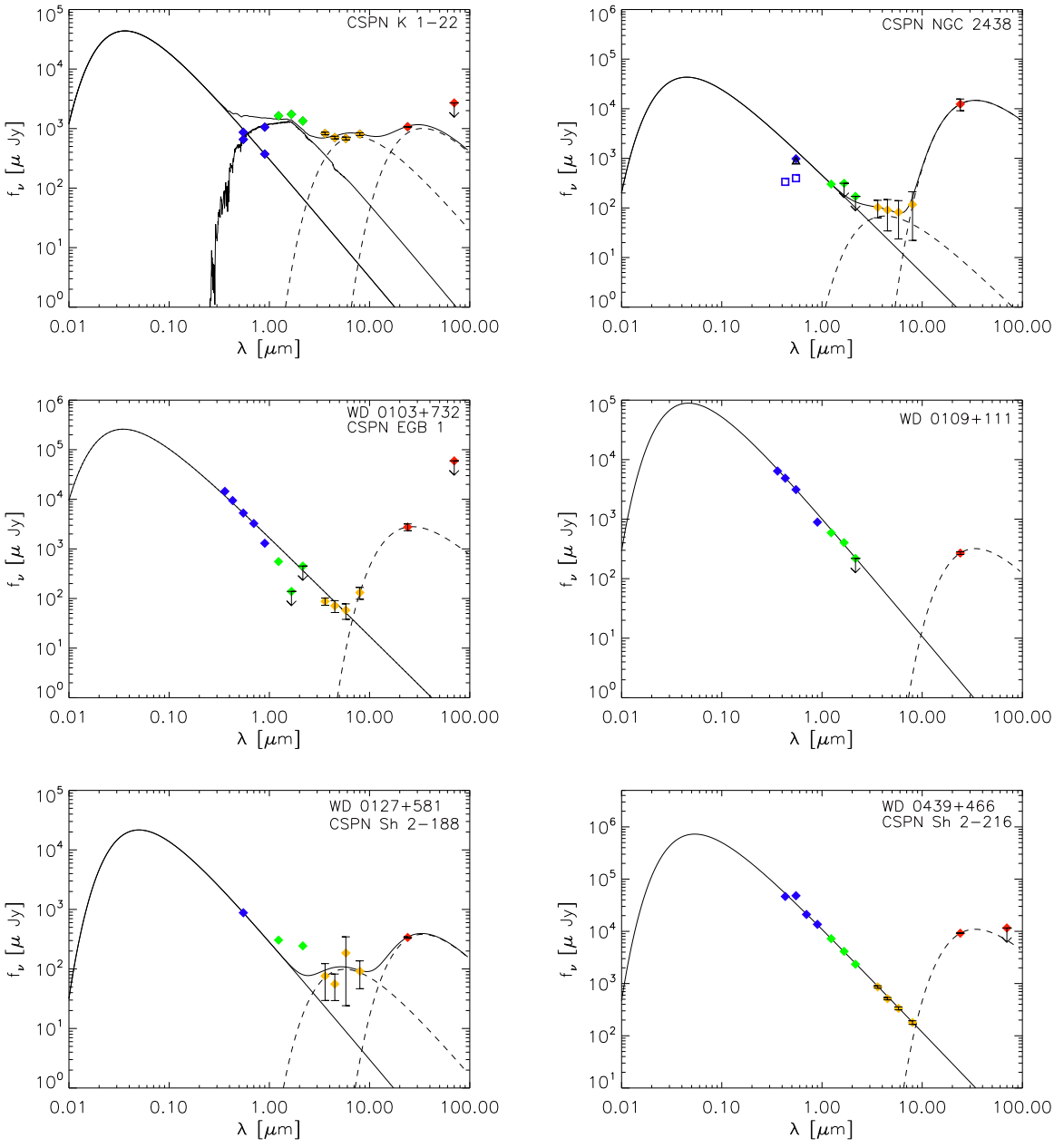

Figure 2.2: cont. on next page

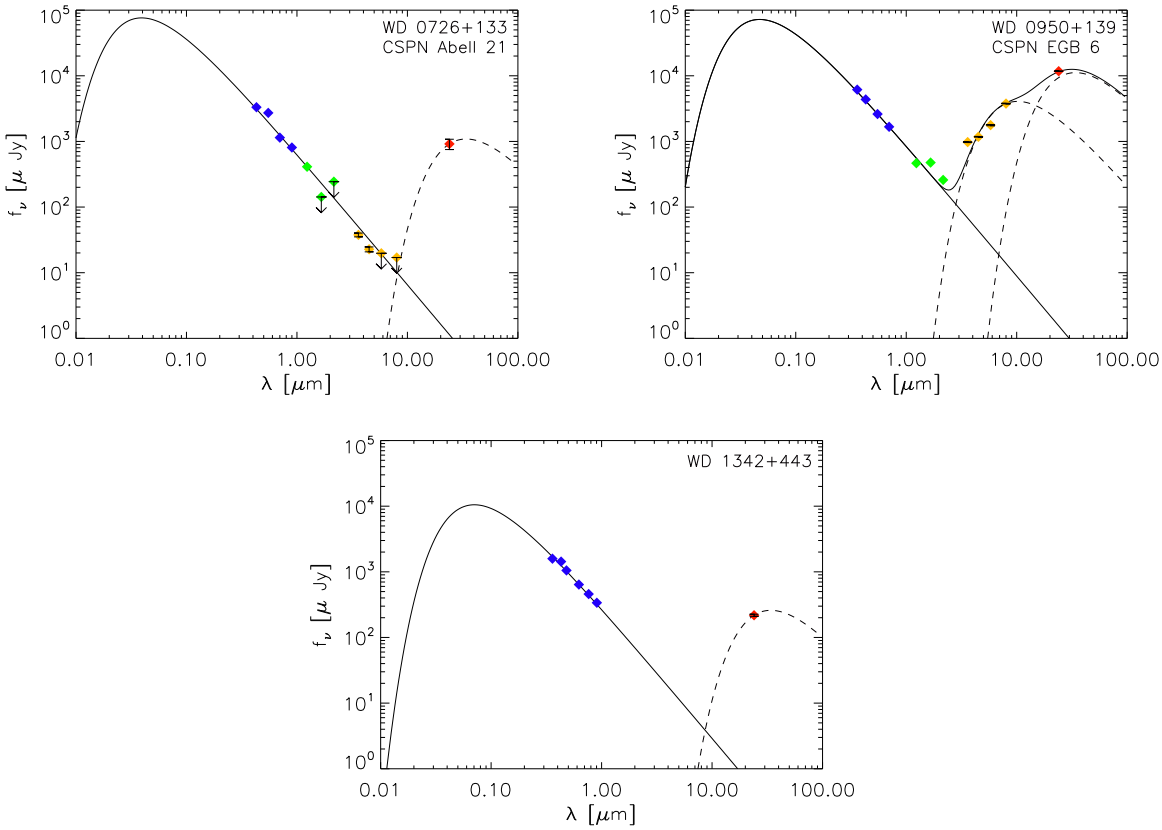

Figure 2.2: Spectral energy distribution plots for WDs detected in the MIPS 24 μm band. The photometric measurements include published optical magnitudes (blue diamonds), 2MASS JHK (green diamonds), *Spitzer* IRAC bands (yellow diamonds), and MIPS 24 and 70 μm bands (red diamonds). Solid blackbody lines in the optical wavelengths represent the WD photospheric emission, while dashed lines represent the blackbody-like excess emission with the best-fit dust temperatures (see Table 2.4). For the four objects with excess emission in the IRAC bands, the sum of the stellar emission and two blackbody components is plotted in thin black line.

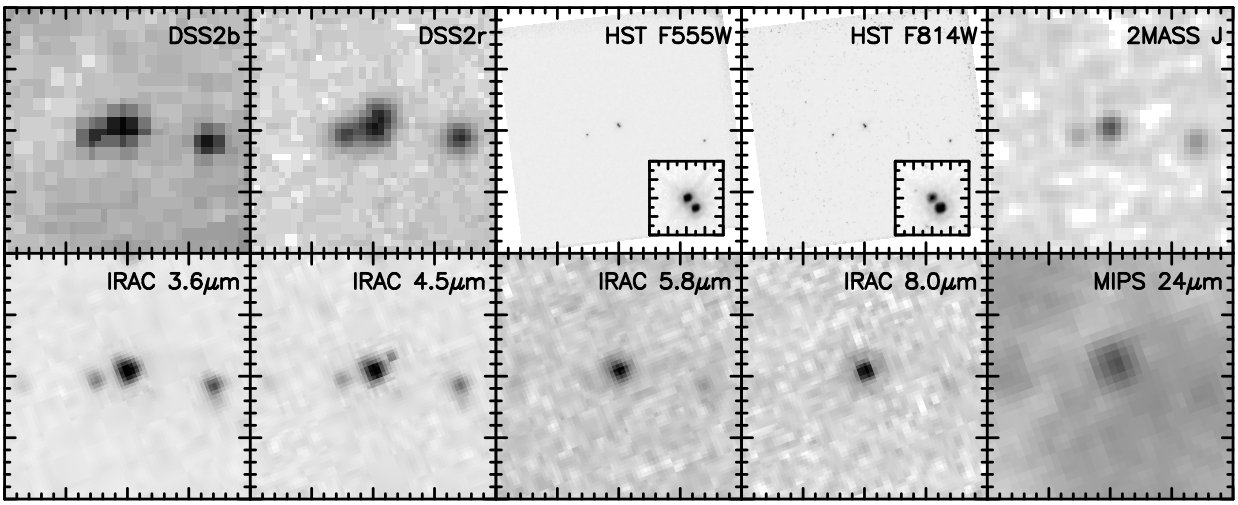

Figure 2.3: Optical and IR images of CSPN K 1-22. The field of view of each panel is $40'' \times 40''$. The inset in the *HST* images is $2'' \times 2''$.

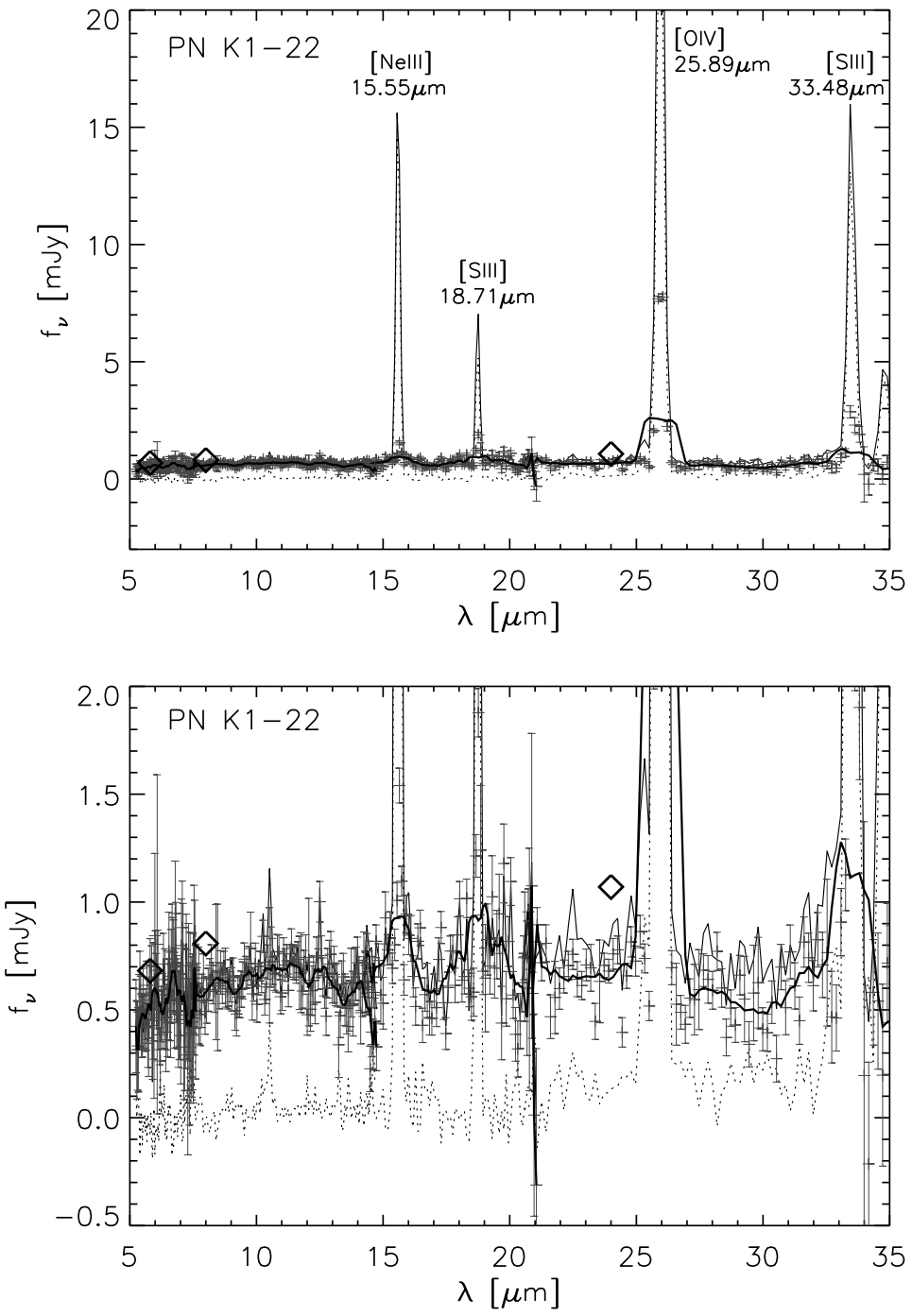

Figure 2.4: *Spitzer* IRS spectrum of CSPN K 1-22 plotted with different stretches to illustrate the relative intensity of lines and continuum. The spectrum extracted at CSPN K 1-22 is plotted in a thin solid line, the local background spectrum in a dotted line, the background-subtracted spectrum of CSPN K 1-22 in pixels with error bars, and the smoothed background-subtracted spectrum in a thick line.

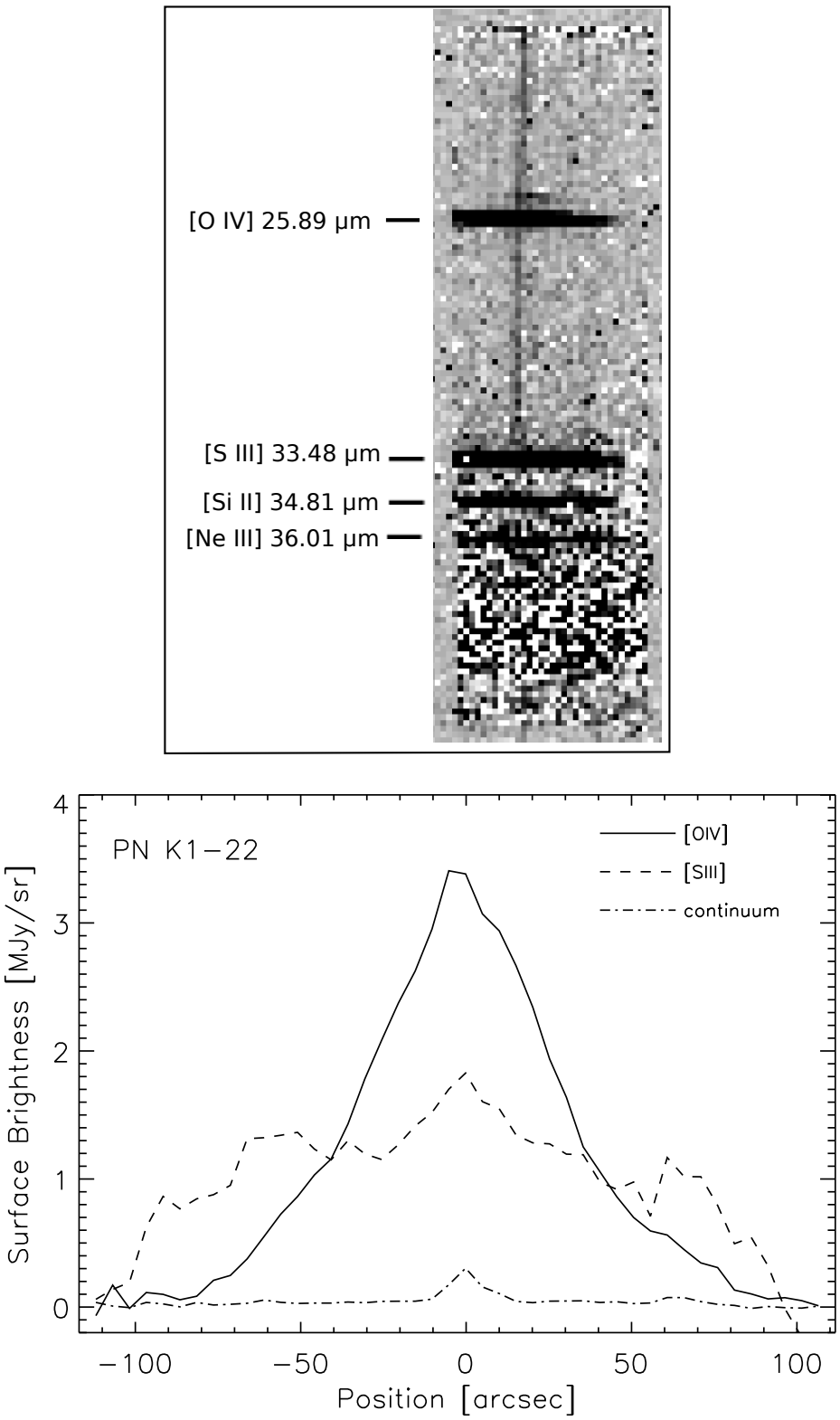

Figure 2.5: Raw spectral image (top) and surface brightness profile plots (bottom) of CSPN K 1-22 extracted from the *Spitzer* IRS data cube in the continuum (dash-dotted curve), [O IV] 25.89 μm line (solid curve), and [S III] 18.71 μm line (dashed curve).

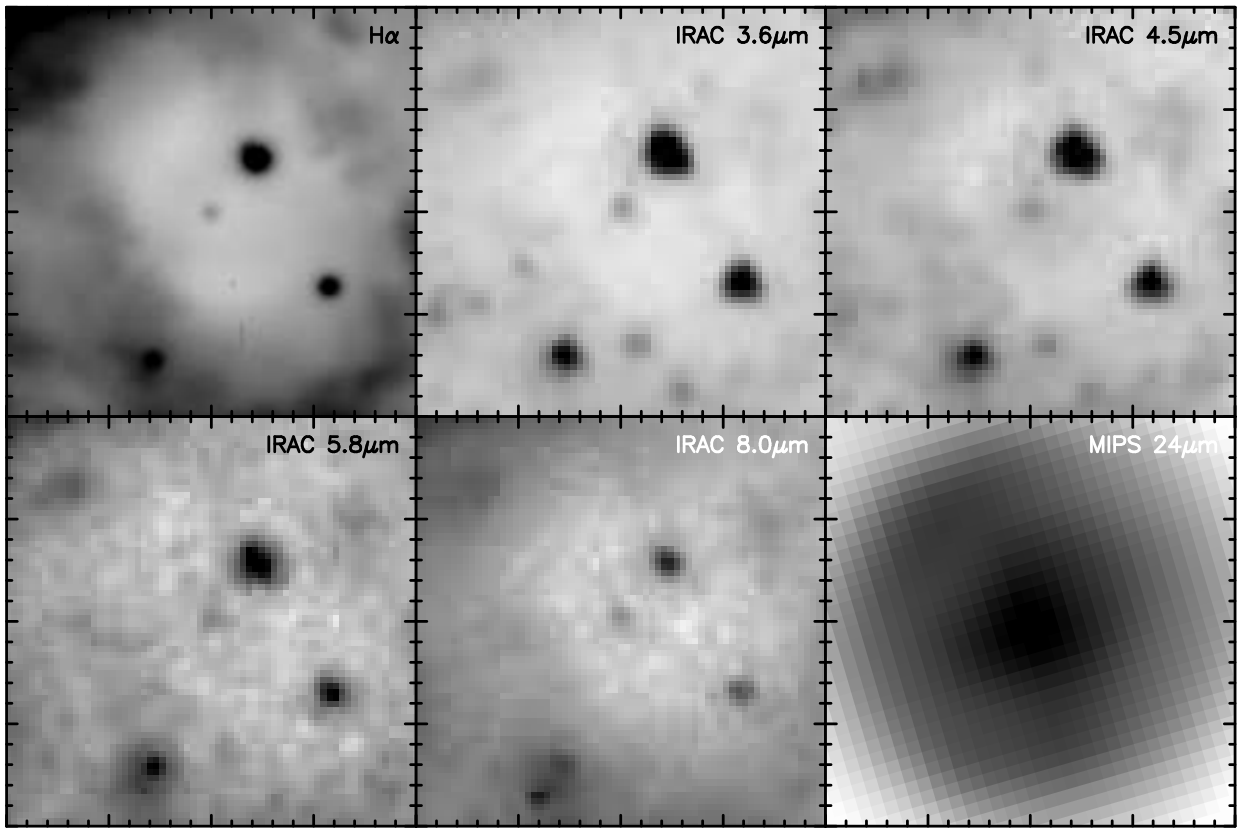

Figure 2.6: Hα and IR images of NGC 2438. The field of view of each panel is 40″×40″.

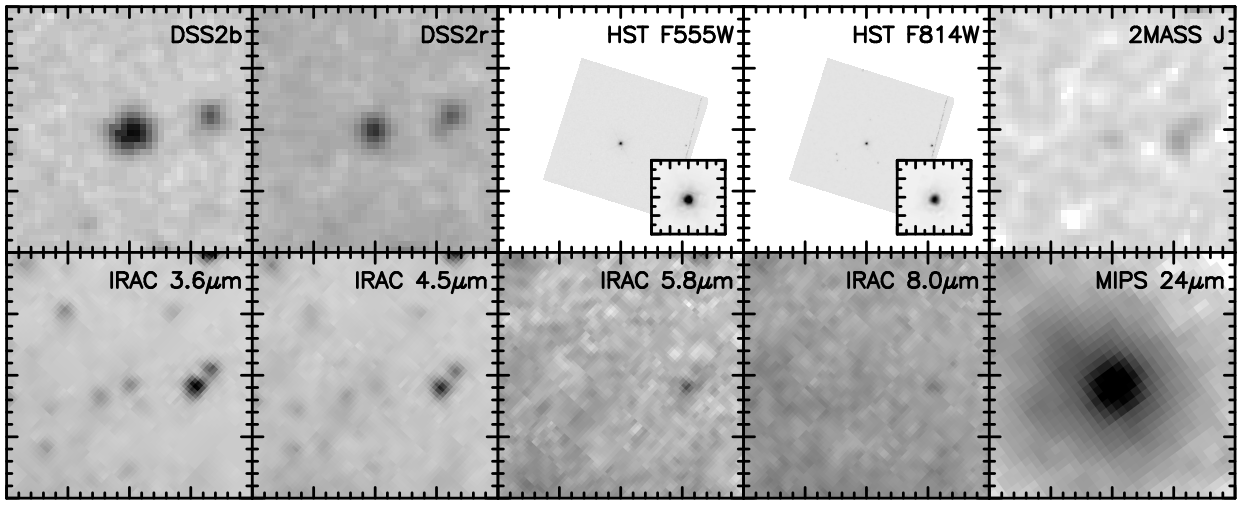

Figure 2.7: Optical and IR mages of WD 0103+732. The field of view of each panel is $40'' \times 40''$. The inset in the *HST* images is $2'' \times 2''$.

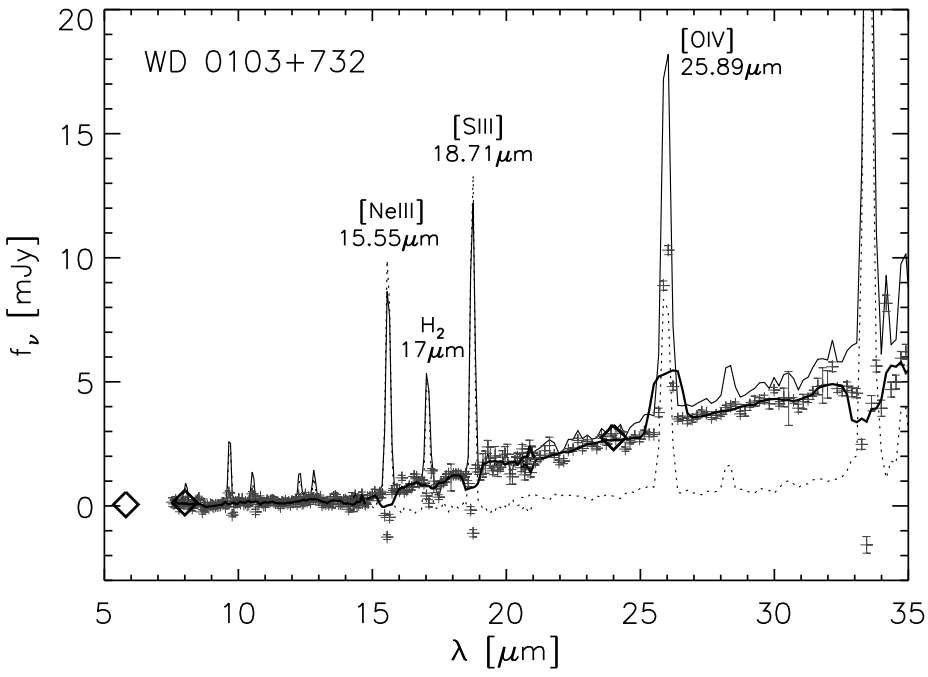

Figure 2.8: *Spitzer* IRS spectrum of WD 0103+732. The spectrum extracted at WD 0103+732 is plotted in a thin solid line, the local background spectrum in a dotted line, the background-subtracted spectrum of WD 0103+732 in pixels with error bars, and the smoothed background-subtracted spectrum in a thick line.

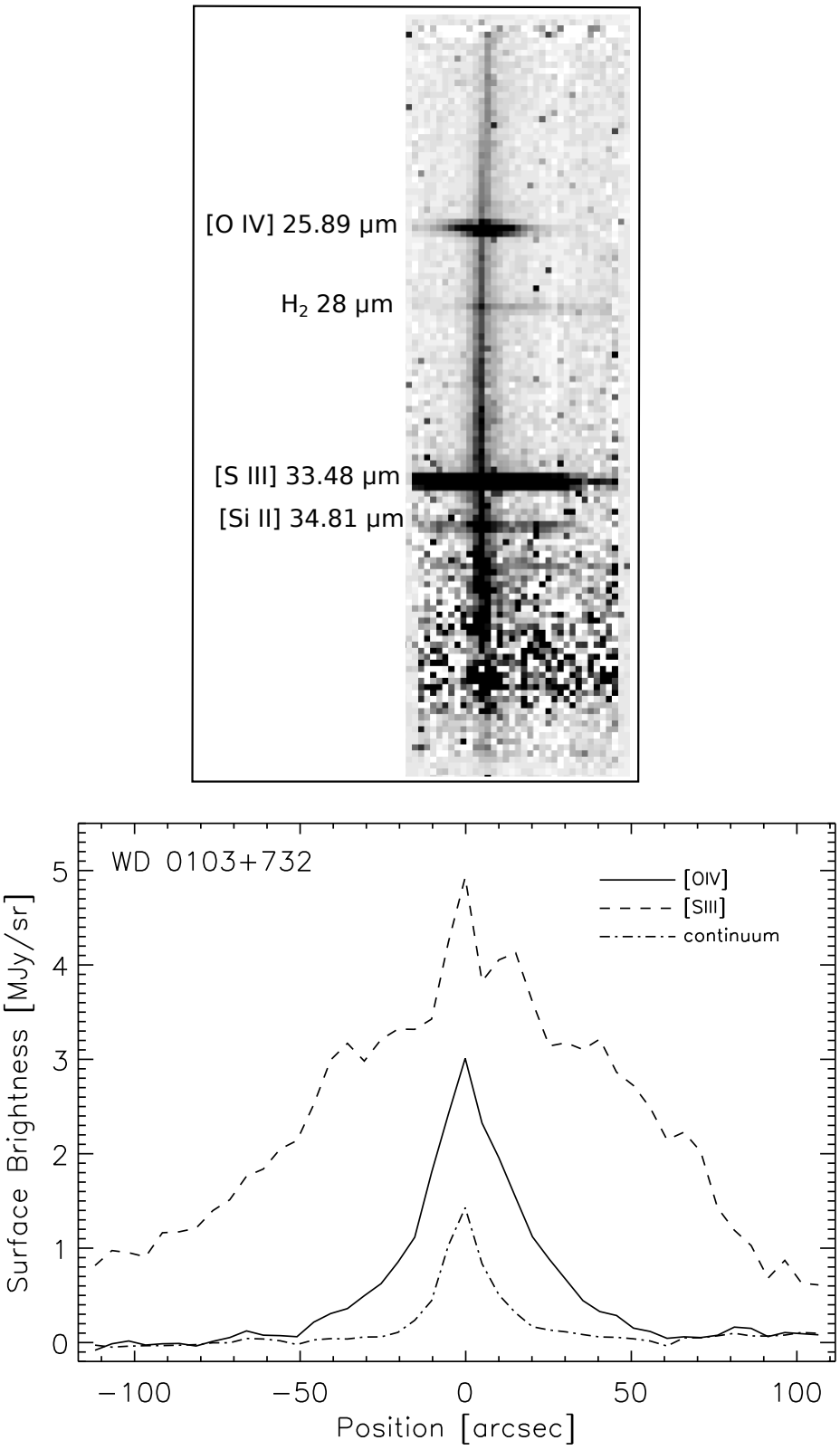

Figure 2.9: Raw spectral image (top) and surface brightness profile plots (bottom) of WD 0103+732 extracted from the *Spitzer* IRS data cube in the continuum (dash-dotted curve), [O IV] 25.89 μm line (solid curve), and [S III] 18.71 μm line (dashed curve).

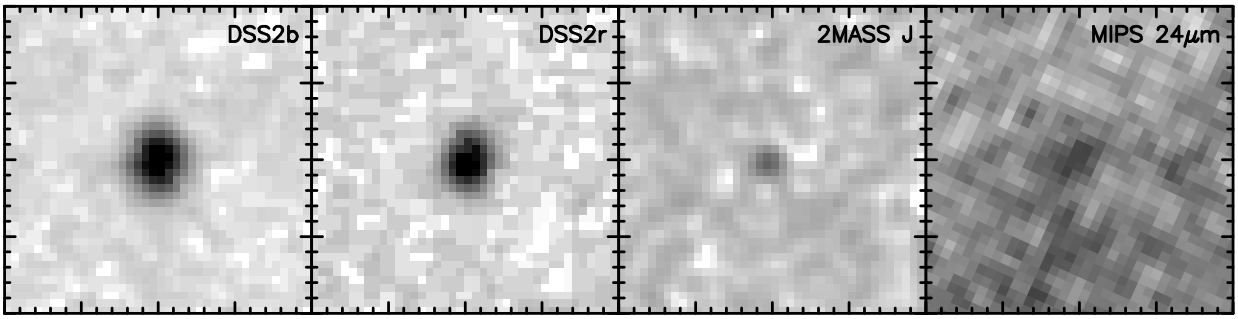

Figure 2.10: Optical and IR images of WD 0109+111. The field of view of each panel is $40'' \times 40''$.

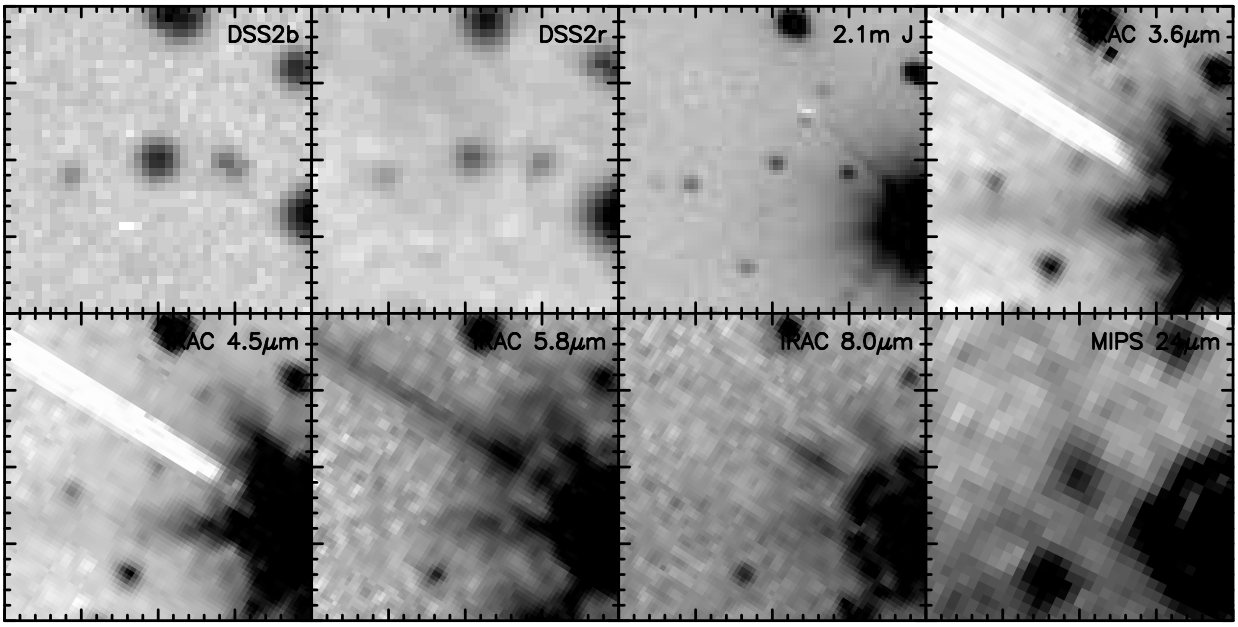

Figure 2.11: Optical and IR images of WD 0127+581. The field of view of each panel is $40'' \times 40''$.

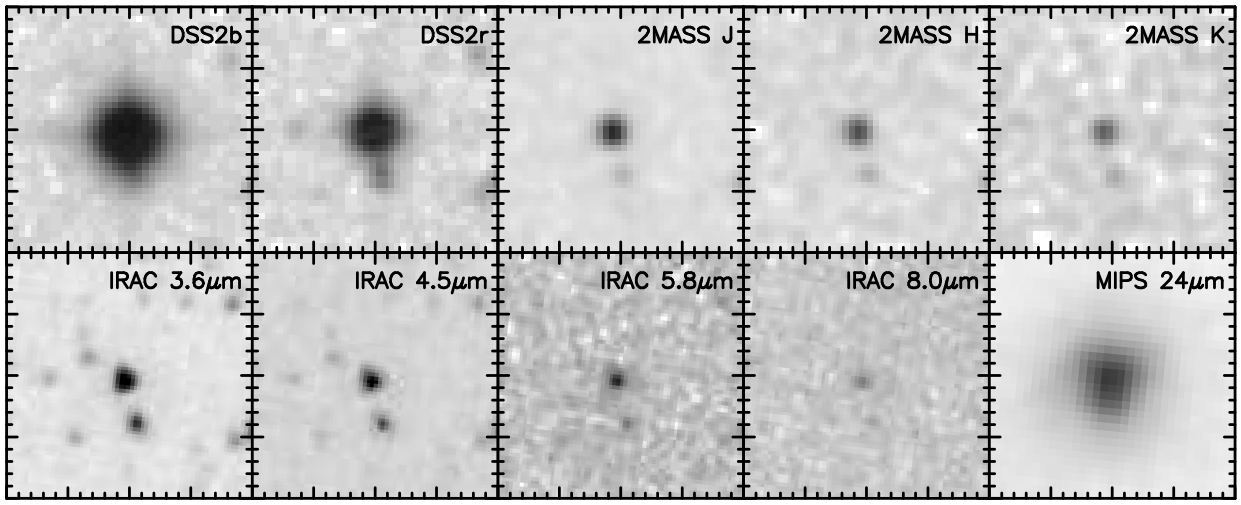

Figure 2.12: Optical and IR images of WD 0439+466. The field of view of each panel is $40'' \times 40''$.

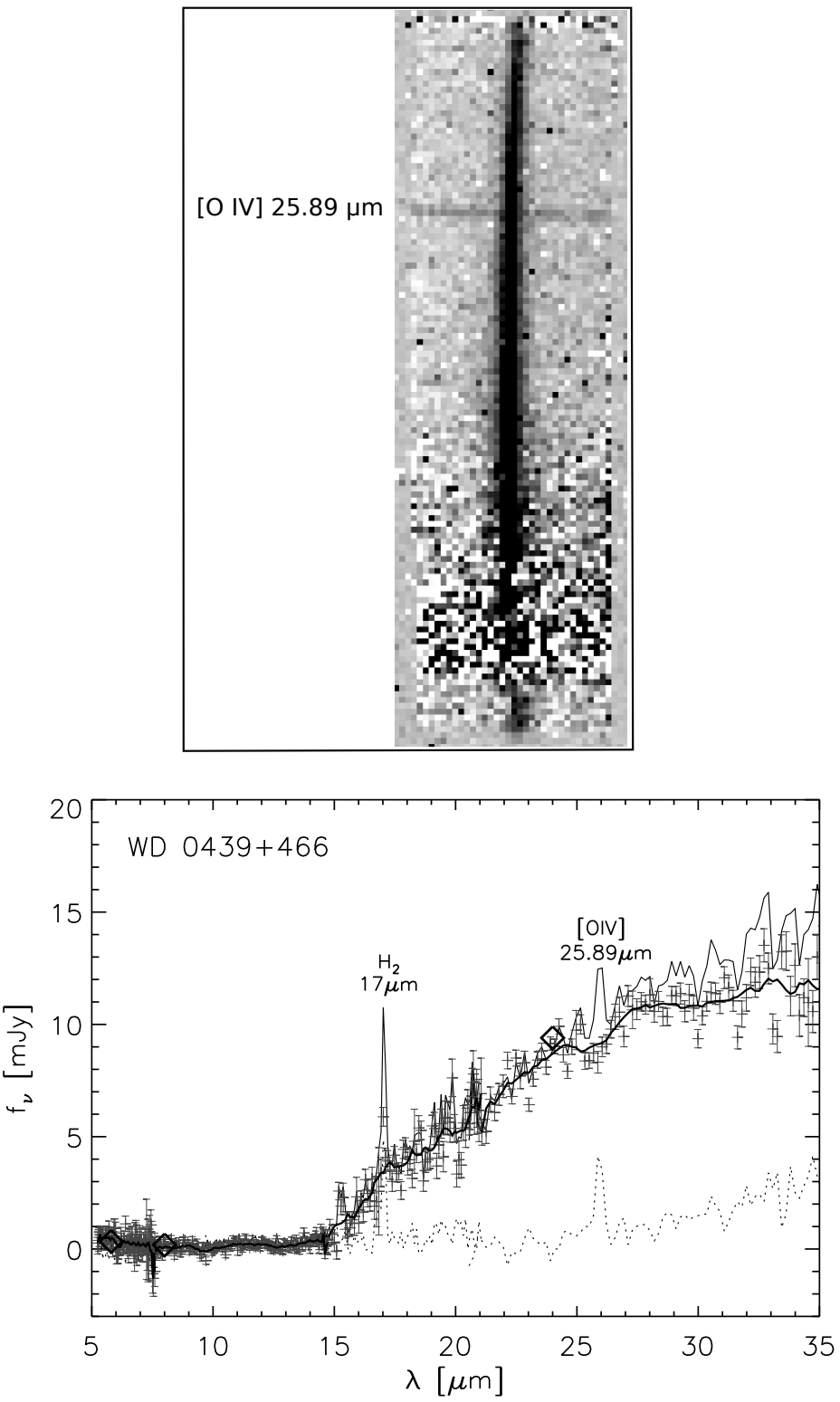

Figure 2.13: Raw spectral image (top) and the *Spitzer* IRS spectrum (bottom) of WD 0439+466. The spectrum extracted at WD 0439+466 is plotted in a thin solid line, the local background spectrum in a dotted line, the background-subtracted spectrum of WD 0439+466 in pixels with error bars, and the smoothed background-subtracted spectrum in a thick line.

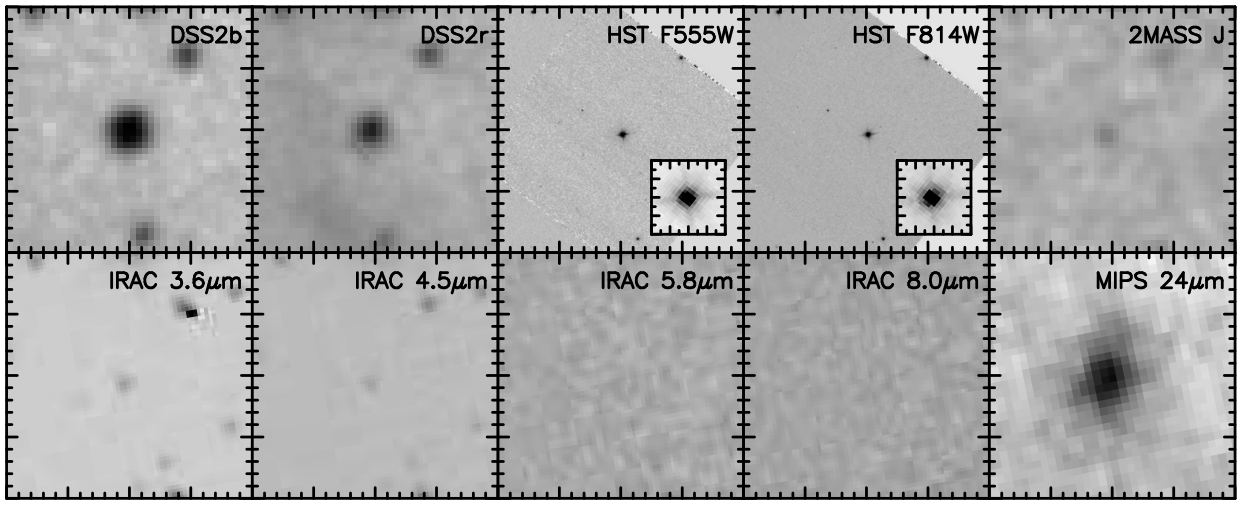

Figure 2.14: Optical and IR images of WD 0726+133. The field of view of each panel is $40'' \times 40''$. The inset in the *HST* images is $2'' \times 2''$.

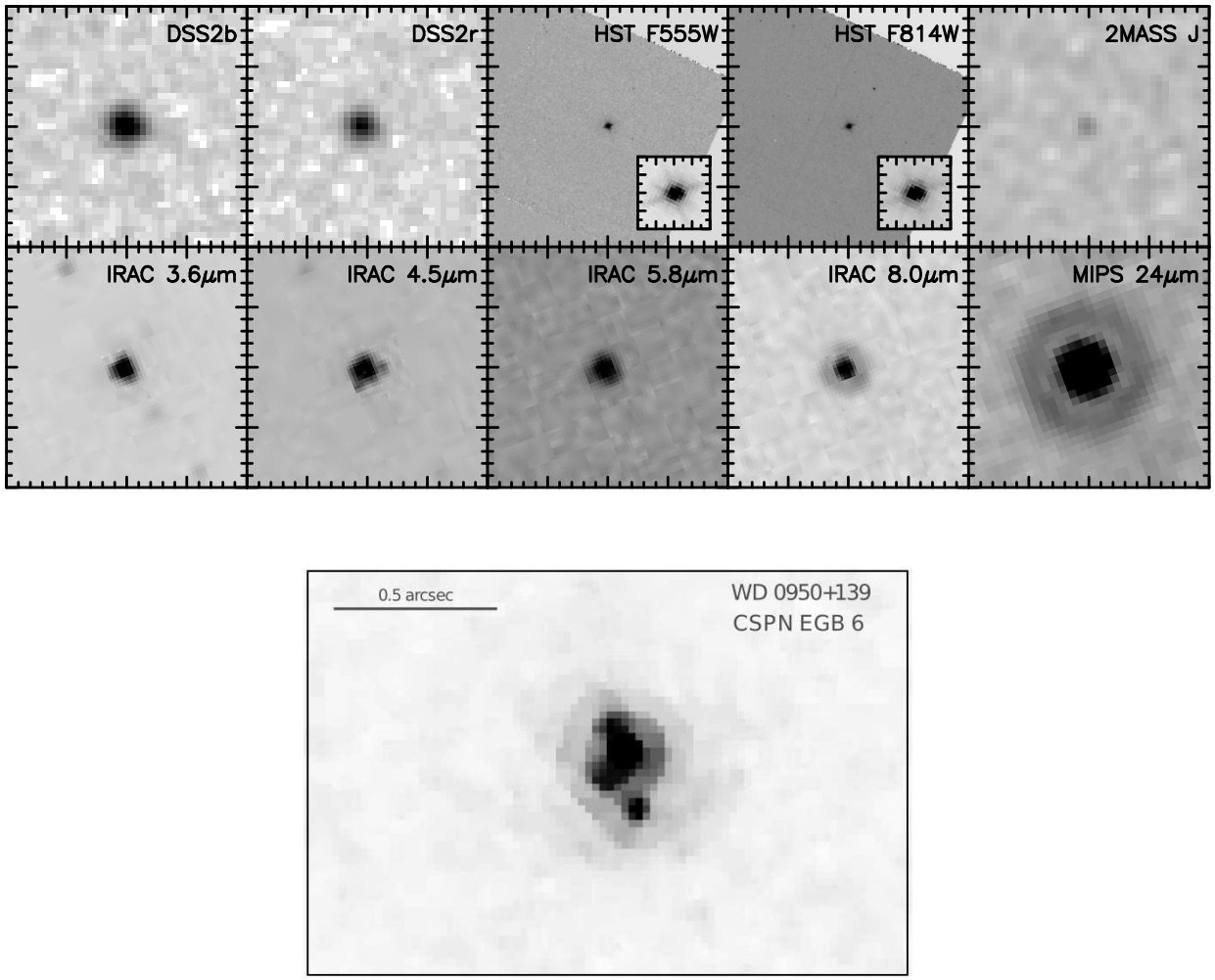

Figure 2.15: Top: Optical and IR images of WD 0950+139. The field of view of each panel is 40″×40″. The inset in the *HST* images is 2″×2″. Bottom: Narrow-band *HST* F501N ([OIII]) image of CSPN EGB 6.

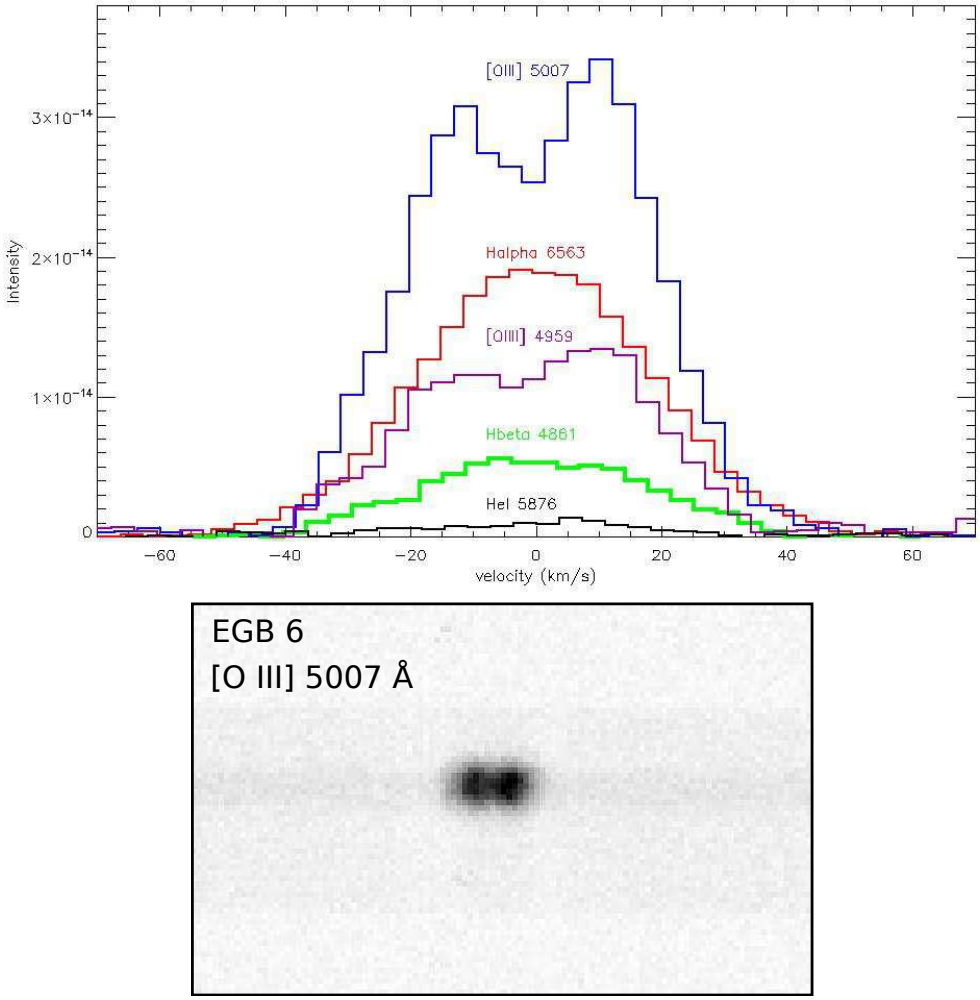

Figure 2.16: Top: Emission line profiles extracted from the echelle spectrum of WD 0950+139. Bottom: Raw spectral image of WD 0950+139 at the position of [O III] 5007 Å.

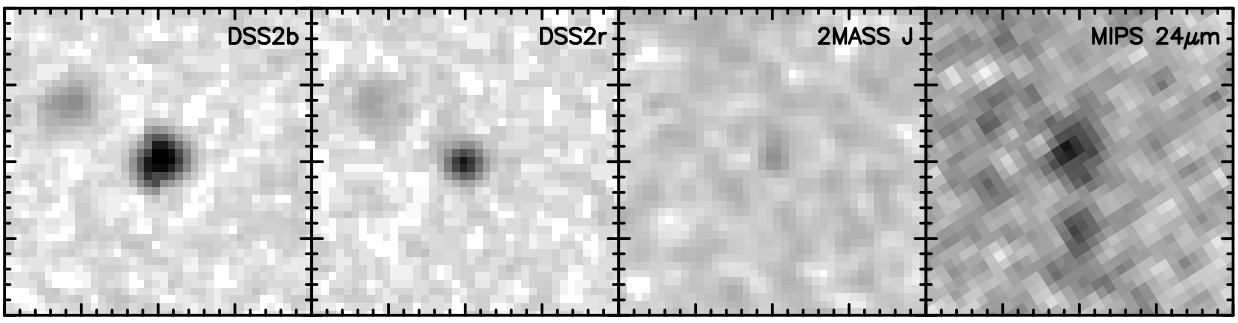

Figure 2.17: Optical and IR images of WD 1342+443. The field of view of each panel is $40'' \times 40''$.

Table 2.1. *Spitzer* Photometry of Hot White Dwarfs with 24 μm Excesses

WD Name	$f_{3.6\mu m}$ (μJy)	$f_{4.5\mu m}$ (μJy)	$f_{5.8\mu m}$ (μJy)	$f_{8.0\mu m}$ (μJy)	$f_{24\mu m}$ (μJy)	$f_{70\mu m}$ (μJy)
CSPN K 1-22	829±42	706±36	681±38	808±42	1,070±143	<12,000
CSPN NGC 2438	103±40	91±57	82±58	117±95	12,410±13,700[a]	...
WD 0103+732	88±15	71±19	58±20	132±35	2,760±141	<55,000
WD 0109+111	...	...	...	...	269±55	...
WD 0127+581	76±47	56±26	185±161	92±45	338±142	...
WD 0439+466	862±44	514±26	336±22	180±14	9,200±157	9,200 ±8,400
WD 0726+133	37.7±2.5	22.8±2.0	<19.8	<17.0	916±114	...
WD 0950+139	977±15[b]	1176±15[b]	1773±36[b]	3772±37[b]	11,740±66	...
WD 1342+443	...	...	...	...	218±41	...

[a]The photometric uncertainty is dominated by the bright nebular emission.

[b]Su et al. 2011, in preparation.

Table 2.2. Summary of the IRS Follow-up Observations

Star Name	Date Observed	IRS Mode	SL1 5.2–8.7 μm	SL2 7.4–14.5 μm	LL1 14.0–21.3 μm	LL2 19.5–38.0 μm
CSPN K1-22	2009 Feb 26	staring	7×60 s	7×60 s	8×120 s	8×120 s
WD 0103+732	2008 Sep 13	staring	8×60 s	8×60 s	4×120 s	8×120 s
WD 0127+581	2008 Oct 09	mapping[a]	2×60 s	2×60 s	2×120 s	2×120 s
WD 0439+466	2008 Sep 7	mapping[a]	8×60 s	16×60 s	4×120 s	4×120 s

[a]Exposure times given are for each pointing in the map.

Table 2.3. Source and Background Apertures for IRS Spectral Extractions

WD Name	LL1 & LL2 Aperture (arcsec^2)	SL1 & SL2 Aperture (arcsec^2)	LL1 & LL2 Offset (arcsec)	SL1 & SL2 Offset (arcsec)
CSPN K1-22	156	35	20	9.3
WD 0103+732	155	41	20	13.0
WD 0439+466	413	96	25.4	16.7

Table 2.4. $L_{\rm IR}/L_*$ of Hot White Dwarfs with 24 μm Excesses

WD Name	Spec Type	$T_{\rm eff}$ (K)	$E(B-V)$	Distance (pc)	R_* ($R_\oplus$)	$T_{\rm dust}$ (K)	$L_{\rm IR}/L_*$	SED Type[a]	References[b]
CSPN K 1-22	CSPN	141,000	0.076	1,330	3.3	700+150	1.1×10^{-4}	EGB 6-like	1, 2
CSPN NGC 2438	CSPN	114,000	0.25	1,200	4.1	1200+150	4.7×10^{-4}	EGB 6-like	1, 3
WD 0103+732 (CSPN EGB 1)	DA.34	150,000	0.58	650	3.7	190	1.4×10^{-5}	Helix-like	4, 5
WD 0109+111	DOZ.46	110,000	0.065	280	2.3	150	4.9×10^{-6}	Helix-like	6, 7, 8
WD 0127+581 (CSPN Sh 2-188)	DAO.49	102,000	0.27	600	1.7	900+150	6.6×10^{-5}	EGB 6-like	4, 9
WD 0439+466 (CSPN Sh 2-216)	DA.61	83,000	0.065	129	2.4	150	2.4×10^{-5}	Helix-like	10, 11
WD 0726+133 (CSPN Abell 21)	PG1159	130,000	0.13	541	2.0	150	1.6×10^{-5}	Helix-like	2, 11, 12
WD 0950+139 (CSPN EGB 6)	DA.46	110,000	0.21	645	3.0	500+150	4.7×10^{-4}	EGB 6-like	5, 13
WD 1342+443	DA.7	79,000	—	437	1.4	150	5.1×10^{-5}	Helix-like	13
WD 2226−210 (CSPN Helix)	DAO.49	110,000	0.03	210	2.6	120	2.5×10^{-4}	Helix-like	11, 14

[a]EGB 6-like SEDs show excesses in the IRAC bands as well as the MIPS 24 μm band. Helix-like SEDs show no excess emission at wavelengths shorter than $\sim$8 μm.

[b]References for stellar temperature, extinction, and distance: (1) Rauch et al. (1999), (2) Ciardullo et al. (1999), (3) Phillips (2004), (4) Napiwotzki (2001), (5) Tylenda et al. (1992), (6) Dreizler & Werner (1996), (7) Werner et al. (1997), (8) Wesemael et al. (1985), (9) Kwitter & Jacoby (1989), (10) Rauch et al. (2007), (11) Harris et al. (2007), (12) Phillips (2003), (13) Liebert et al. (2005), (14) Napiwotzki (1999).

Chapter 3

Spitzer Search for Dust Disks around Central Stars of Planetary Nebulae - Methods and Observations

3.1 Introduction

Debris disks have been detected around low- and intermediate-mass main sequence stars through their excess IR emission, but these dust disks dissipate and fade away before stars evolve off the main sequence (Rieke et al. 2005; Su et al. 2006; Carpenter et al. 2009; Trilling et al. 2008). As a star loses mass and evolves into a WD, its planetary system can become dynamically rejuvenated and increased collisions among subplanetary bodies may replenish the system with dust.

Indeed, two types of dust disks have been observed around WDs. Small (r<0.01 AU) dust disks were found around cool (T< 25,000 K) WDs, for example, G 29-38 (Reach et al. 2005a) and GD 362 (Becklin et al. 2005). These dust disks have been suggested to be produced by tidally disrupted asteroids, and the supporting evidence includes dust's location within the Roche limit, the silicate feature superposed on the dust continuum, and high metal content in WD atmospheres (Jura et al. 2007). Some dust disks are accompanied by metal-rich gaseous disks, for example SDSS 1228+1040 (Gänsicke et al. 2008).

A large dust disk was discovered around the hot (T=110,000 K) CSPN of the Helix nebula (Su et al. 2007). *Spitzer* observations of Helix CSPN detect dust continuum with a color temperature of 90–130 K at orbital distances of 35–150 AU. This location suggests that the dust is likely produced by collisions among Kuiper-Belt-like objects.

To search for more dust disks similar to that around Helix's CSPN, we have conducted a *Spitzer* MIPS 24 μm survey of 71 hot, young WDs and pre-WDs in Cycle 4 (PID 40953).

About 50% of these are still CSPNs, and are the closest analogs of the Helix Nebula and its central hot WD. Out of 71 targets observed, unresolved 24 μm emission coincident with the WD is convincingly detected in 9 cases, 7 of them still surrounded by PNe (Chu et al. 2011).

Inspired by the prevalence of PN environments for hot WDs showing mid-IR excesses, we have used archival *Spitzer* IRAC and MIPS observations of PNe to search for CSPNs with IR excesses and to investigate possible evolutionary effects. The following two chapters report the results of this archival survey.

3.2 Spitzer Archival Data and Flux Measurement

3.2.1 Archival Search

We have searched the *Spitzer* archive for programs that target PNe as of January 2011. The following nine programs contain imaging observations in IRAC (3.6, 4.5, 5.8 and 8.0 μm) and/or MIPS (24, 70 and 160 μm) bands, and have been selected for closer examination: programs 68 (PI: Fazio), 77 (PI: Rieke), 1052 (PI: Hora), 3362 (PI: Evans), 3668 (PI: Morris), 30285 (PI: Fazio), 40020 (PI: Fazio), 40115 (PI: Fazio), and 50530 (PI: Burleigh). In additon, program 50793 (PI: Bilikova) contains our follow-up MIPS observations of some PNe with IR excesses from this archival study; these observations are included in this paper.

We do not include programs 30029, 30036, 30077 and 40061 in this study, because the targets in these programs are either evolved stars surrounded by dusty stellar ejecta, such as R Coronae Borealis (RCrB) stars and post-AGB stars, or proto- and very young PNe that are not well resolved. Note that we may have missed some PNe observed in programs targeting WDs that are also CSPNs. We also do not include PNe serendipitously observed in surveys of the Galactic plane or high-latitude extragalactic surveys. We do not repeat the analysis of MIPS 24 μm observations of the 36 PNe from program 40953 (PI: Chu), a 24 μm survey of hot WDs for IR excesses, and follow-up IRS and IRAC observations from program 50629 (PI: Chu), as these have been reported by Chu et al. (2011). This paper and Chu

et al. (2011), together, represent a more complete *Spitzer* sample of CSPNs in well-resolved PNe.

We have examined the target lists of the nine selected programs, and further eliminated targets such as RCrB stars, proto-PNe, post-AGB stars, and supernova remnants. The remaining sample comprises imaging observations of 72 PNe in IRAC and/or MIPS bands. The full sample of PNe considered in this paper is presented in Table 3.1, along with the instruments and modes used for the observations, the observation IDs (AORs) and the program IDs.

We have retrieved all archival *Spitzer* images of PNe and identified their CSPNs by comparing their coordinates from the literature (Kerber et al. 2003) to those of the stars in the central region of each PN, as well as by visual comparison with images from Digitized Sky Survey (DSS), 2-Micron All Sky Survey (2MASS) and from the Planetary Nebula Image Catalogue[1]. CSPNs not suitable for photometric measurements are eliminated from further study. These include (1) small PNe in which the CSPNs were not resolved from the nebula, e.g., Hb 5, Hb 12, PB 6 and PB 8; (2) PNe whose nebular emission dominates the central region and overwhelms the stellar emission, e.g., NGC 6072 and NGC 6302; (3) PNe in which the CSPN is too faint and not detected, e.g., He 2-119 and NGC 2818. Remarks concerning the visual examination of the PNe are also given in Table 3.1. Out of the 72 PNe examined, 42 detected CSPNs were selected for photometric measurements.

For the 42 targets selected for photometry, we have searched the *Spitzer* archive again to find additional imaging observations from programs that did not specifically target PNe. One PN, DeHt 5, has additional IRAC images available from program 30432 (PI: Burleigh); these IRAC images have been included in our study. Seven PNe, A21, JnEr 1, NGC 246, NGC 1360, NGC 2438, NGC 2610, and NGC 3587, have MIPS 24 μm observations from program 40953; photometric measurements of these CSPNs have been reported by Chu et al. (2011), and only CSPNs of A21 and NGC 2438 are detected. The PN NGC 2346 has MIPS

[1]http://www.astro.washington.edu/users/balick/PNIC/

observations from a calibration campaign, program 715 (PI: Rieke); these data have been included in our photometric measurements. NGC 7354 has additional MIPS images available from program 50398 (PI: Carey), but they are not suited for photometric measurements because the CSPN is not visible against the very bright nebular emission. MIPS 24 μm images of NGC 6804 and NGC 7139 are from our follow-up program (see Section 3.1); of these, only CSPN NGC 6804 is detected and measured. These additional observations are also listed in Table 3.1.

In summary, we have selected 42 CSPNs for IRAC photometric measurements, and four CSPNs for MIPS 24 μm measurements (DeHt 5, NGC 2346, NGC 6804, and NGC 6853); we adopt the MIPS 24 μm fluxes or upper limits from Chu et al. (2011) for seven CSPNs. The CSPNs of NGC 7293, the Helix Nebula, and A21 have been analyzed by Su et al. (2007) and Chu et al. (2011) and will be included here for completeness, but will not be discussed in detail in this paper.

3.2.2 IRAC Photometry

For the 42 sources selected for IRAC photometry, we use the phot task in IRAF[2] to carry out aperture photometry on post-Basic Calibrated Data (post-BCD) files that were processed with pipeline version S18.18.0. The pixel size in the post-BCD data is $0\farcs6$, half the native IRAC pixel size. For images saturated at the CSPNs that were observed in the high dynamic range mode, we use the short-exposure images for photometric measurements.

We use the smallest aperture radius that encloses the central source but is sufficiently larger than the instrumental resolution (FWHM 1.5–2″ for IRAC), in order to minimize the nebular contamination in the aperture. As most sources are faint, a source aperture of 4-pixel (or $2\farcs4$) radius is used. For brighter CSPNs, NGC 1360 and NGC 6804, we use a 6-pixel (or $3\farcs6$) radius for the source aperture, and for the brightest sources, NGC 2346, M 2-9 and

[2]IRAF is distributed by the National Optical Astronomy Observatory, which is operated by the Association of Universities for Research in Astronomy (AURA) under cooperative agreement with the National Science Foundation.

Mz 3, we use a 10-pixel (or 6.″0) radius source aperture. The aperture was centered at the peak of CSPN emission by using a centering algorithm where possible; for faint sources or sources with nearby nebular background fluctuations, the source aperture was forced at the CSPN position established from the detection in the shorter-wavelength IRAC channels.

Estimating the background level for aperture photometry requires closer examination of each PN, because the nebular emission can be irregular, or vary radially outwards. To identify the PNe with radial variations in their emission, we have produced and examined radial profiles of central regions of all selected PNe. To construct the radial profiles, we use the median of the pixel flux densities for a succession of annuli with increasing radii and a width of 1 pixel.

For CSPNs with a uniform nebular background in the central region, we use annuli of radii 4−12 (2.″4−7.″2), 6−14 (3.″6−8.″4), and 10−20 (6″−12″) pixels for source apertures of 4, 6, and 10 pixels, respectively, to estimate the background level. After carrying out a 3σ trimming algorithm to reject the outlying pixel flux densities, such as those corresponding to stars within the background annulus, we adopt the median of the pixel flux densities as the background to calculate CSPN fluxes. Appropriate aperture corrections are applied using values provided in the IRAC data handbook (version 3.0), but no color correction is made. Photometric uncertainty is estimated using the prescription in Reach et al. (2005b), and an additional 5% of the CSPN flux is added in quadrature to account for random variations in the instruments and the errors resulting from calibration. For CSPNs with a background that does not have radial variations but is non-uniform and clumpy, we perform aperture photometry for a set of different sky annuli, and adopt the standard deviation in the measured flux densities as the measurement error, combined in quadrature with 5% of CSPN flux.

For non-detections, we perform 4-pixel-radius aperture photometry at the position of the CSPN established from detections in shorter-wavelength channels, and add 3σ to estimate upper limits on the CSPN fluxes, where σ is the estimated measurement error. For cases where background-subtracted flux inside the aperture is negative, the upper limits are equal

to 3σ.

In cases where strong radial variation is present, we use the radial profiles to estimate the background level. For a PN with a shell-like morphology, the nebular surface brightness is the lowest in the central region, and increases outward from the CSPN. The radial profile plots show the sum of the emission from the CSPN and from the nebular background. We adopt the local minimum value in the radial profile plot as the background level. Since not all of the CSPN emission is included in the aperture, and some of it contributes to the flux at the radial profile minimum, we apply the same aperture corrections as we do for the uniform background case. Since the adopted radial profile minimum is off-center from the CSPN, the central nebular background is still overestimated; however, the background is overestimated by no more than $\sim$10% for the range of observed shell thicknesses and the locations where the nebular backgrounds are sampled. To estimate the flux measurement error, we first subtract the median flux per pixel at each annulus, and estimate the errors using the formulae from Reach et al. (2005b) on the median-subtracted background pixels.

Two PNe, NGC 6629 and PMR 2 are centrally peaked; therefore, both techniques discussed above underestimate the background and overestimate the CSPN flux. For NGC 6629, we examine the radial profiles and assess conservative upper and lower limits to the nebular background to estimate the lower and upper limits to CSPN flux densities, respectively. The reported flux density is the average value, and the reported error is half the difference between upper and lower CSPN flux density estimates. The other centrally peaked PN, PMR 2, is very compact (diameter$<15''$ in IRAC images). For this CSPN, we carry out standard aperture photometry with 4-pixel aperture radius and 4-12 pixel background annulus, and report the resulting flux densities as upper limits.

For eight PNe, even though the CSPNs are seen, the nearby nebular or stellar emission is too bright, irregular, and/or blended with the CSPN, rendering the measured CSPN flux densities inaccurate. We do not report the flux densities for these CSPNs - A30, IC 4593, NGC 6153, NGC 6781, NGC 7009, NGC 7026, NGC 7048, NGC 7354. See section 3.4 for

further description.

Figure 3.1 illustrates the different background estimation techniques used for different PN morphologies. It shows images, histograms of pixel flux densities in the background annuli, and radial profiles for NGC 3587 and NGC 2392, and NGC 6629. For the case of NGC 3587, the nebular background is uniform, and the median flux density value of the pixels in the background annulus gives an accurate estimate of the background level. NGC 2392, on the other hand, has a shell-like morphology, and using the median value in the background annulus would over-estimate the background, and hence underestimate the CSPN flux. Using the background estimate from the radial profile, we are able to compute CSPN fluxes more accurately. For example, assuming a fractional shell thickness ($\Delta R/R$) of 0.3, the adopted nebular background at a distance $\sim$1/3 of the radius overestimates the central nebular background by $\sim$7%. NGC 6629 is centrally peaked, and both the histogram median and the minimum in the radial profile underestimate the nebular background. In this case, we estimate the limits to the nebular contamination using the range of values seen in the radial profile.

We have examined the radial profiles of all PNe, and, based on radial trends and stellar contamination, chosen the most reliable way to determine CSPN fluxes. A flux conversion error has been identified for data processed with the S18.18 pipeline, resulting in overestimate of the 5.8 and 8.0 μm fluxes. Our measured CSPN flux densities at 5.8 and 8.0 μm were thus multiplied by factors of 0.968 and 0.973, respectively, to account for this calibration error, as suggested by Spitzer Science User Support. The notes on individual objects, including a summary of the method used to estimate the background, are provided in section 3.4 .

The final fluxes and errors are listed in Table 3.2.

3.2.3 MIPS Photometry

Four targets are selected for photometric measurements in the MIPS 24 band: DeHt 5, NGC 2346, NGC 6804, and NGC 6853. At MIPS 70 and 160 μm, these sources are not

observed, undetected, or overwhelmed by the nebular emission; therefore, we only report the 24 μm fluxes. Our measured MIPS 24 μm fluxes, as well as those taken from Chu et al. (2011), are listed in Table 3.2.

We construct new 24 μm image mosaics with a pixel size of 1$''\!.$245 ($\sim$half the native pixel size) by combining the available BCD frames using the MOPEX[3] software. As in the case of IRAC observations, we construct the radial profiles of the central regions of these PNe. We examine the images and the radial profiles to select the appropriate photometry parameters. We apply the aperture corrections provided in the MIPS data handbook (version 3.3.1).

In the case of DeHt5, the nebular background is not uniform. The nebular emission is brighter on the east side of the CSPN, and is partially blended with the central source. A gaussian fit to the central source gives a FWHM of $\sim$6.5 pixels, slightly larger than that of the point source ($\sim$6$''$, or $\sim$5 pixels); however, this is likely due to the contamination by the nearby nebulosity, and the central source is likely a point source. To minimize the nebular contamination, we choose the smallest source aperture (3$''\!.$5 radius) and background annulus (6–8$''$ radii) combination for which aperture corrections are available.

The central sources of NGC 2346 and NGC 6853 are slightly extended, with FWHMs of $\sim$7.5 and $\sim$9 pixels, respectively. Su et al. (2004), indeed report that the central star of NGC 2346 is surrounded by extended dust emission, which is seen at 24 μm. To estimate the 24 μm flux of these two CSPNs, we again use a 3$''\!.$5 source aperture and a 6-8$''$ annular background. NGC 6853 is surrounded by centrally peaked nebular background which may be contributing to the CSPN flux. We estimate the error due to the nebular emission by performing aperture photometry for a set of diferent sky annuli, and adopt the standard deviation in the measured ux densities as the photometric error. For the above three CSPNs, we add 5% of the CSPN flux to the photometric errors in quadrature, to account for instrument and calibration inaccuracies.

The FWHM of the central source of NGC 6804 is $\sim$5 pixels, the same as that of a point

[3]http://irsa.ipac.caltech.edu/data/SPITZER/docs/dataanalysistools/tools/mopex/

source. The CSPN is surrounded by a bright nebular shell, the emission from which is enhanced in the southern portion of the shell. We therefore use the radial profile to estimate the background level (see Section 2.2). Despite the absence of background point sources, the background estimated from the average radial profile and that of the median radial profile differ considerably, likely due to the enhancement in the nebular emission toward the south. Since this southern enhancement contributes to the aperture contamination, we use background value from median as well as average radial profiles. We report the average of the computed fluxes as the final flux value, and use half the difference between these two flux estimates as our measurement error.

3.2.4 Spectral Energy Distributions

To assess the presence of mid-IR excesses, the measured fluxes in IRAC and MIPS bands need to be compared to those at shorter wavelengths. We have searched the literature for CSPN flux values shortward of the IRAC 3.6 μm band. Available $UBVRIJHK$ fluxes and extinction values are listed in Table 3.3, along with references. Some of the optical magnitudes that we found appear suspect, as they are inconsistent with other measurements or originate from astrometric catalogs that are not well calibrated photometrically. These are listed in parentheses in Table 3.3. The JHK fluxes are from the 2MASS catalog (Skrutskie et al. 2006), except for some CSPNs whose 2MASS photometry is evidently compromised by nebular emission. In these cases, we made our own JHK measurements using smaller source apertures to exclude the nebulae, these magnitudes are marked with an asterisk in Table 3.3, and the details of each photometric measurement are given in section 3.4 .

Supplemented by the optical and near-IR fluxes, we construct the spectral energy distributions (SEDs) for the 34 CSPNs with photometric measurements in the IRAC and MIPS bands. The fluxes are corrected for interstellar extinction based on the values from the literature. For cases that do not have an extinction value available in the literature, or where a different value gave a better fit to the optical fluxes, we list our adopted extinction correction

in Table 3.3 and mark it with a plus sign.

We approximate the photospheric emission of the CSPNs at IR wavelengths by the Rayleigh-Jeans tail of a blackbody function. Since the slope of this Rayleigh-Jeans approximation in a log-log plot is independent of temperature, we initially model the photospheric emission in all SEDs with a 100,000 K blackbody curve, normalized to the optical and/or near-IR fluxes.

We examine the SEDs and find that they can be divided into four categories:

(1) Clear IR excess. The CSPNs in this category have IR flux densities as well as their associated errors well above the expected photospheric emission. Nineteen CSPNs belong to this category: A21, A66, DeHt 5, He 2-99, M 2-9, Mz 3, NGC 1501, NGC 2346, NGC 2438, NGC 40, NGC 6369, NGC 650, NGC 6751, NGC 6804, NGC 6853, NGC 6905, NGC 7139, NGC 7293, and PMR 1. These will be further discussed in Section 4.

(2) Likely IR excess. Only one CSPN, that of PMR 2, belongs to this category. It is very likely that it does have an IR excess since it is well detected in all IRAC bands; however, it is difficult to establish accurate fluxes because the PN is very small. We only report the upper limits, but all of the upper limits lie well above the expected photospheric emission.

(3) Unlikely/uncertain IR excess. For CSPNs in this category, the IR data points are only slightly above the blackbody curve, and some error bars lie on the blackbody curve. For these CSPNs, there is a suspicion that the flux measurements may be contaminated by a nebular filament and/or a nearby star, or the lack/scatter of optical data points complicates the estimation of the expected photospheric emission. Three CSPNs belong to this category: NGC 246, NGC 2371 and NGC 6772.

(4) No IR excess. The data points closely follow the blackbody curve. Eleven CSPNs belong to this category: DS 2, IC 5148, JnEr 1, NGC 1360, NGC 2392, NGC 2610, NGC 3242, NGC 3587, NGC 6543, NGC 6629, and NGC 6720.

For a more detailed description of the SEDs of each CSPN, see section 3.4 . The SEDs with no or uncertain/unlikely IR excesses are presented in Figure 3.2, and the SEDs with

probable and clear IR excesses are presented in Figures 4.1-4.4.

3.3 New Follow-up Observations

3.3.1 *Spitzer* MIPS imaging

To extend the wavelength coverage of the SED, we have obtained follow-up 24 μm observations of NGC 7139 and NGC 6804 with the MIPS camera onboard *Spitzer* (Rieke et al. 2004) in our program 50793 (PI: Bilikova). Each target was observed in the small-field photometry mode, which obtained a sequence of 14 exposures dithered in a preset pattern (for details, see the *Spitzer Space Telescope* Observer's Manual). The observations used an exposure time of 10 s and cycled through the pattern 5 times, yielding a total exposure time of 700 s in the central $3\farcm2\times3\farcm2$ region. The BCD frames were combined using the MOPEX software and photometric measurements carried out as described in Section 2.3.

3.3.2 *Spitzer* IRS spectra

To assess the line and continuum contribution to the IR excesses, we have obtained follow-up *Spitzer* IRS spectra for CSPNs NGC 2438 and NGC 7139 in our program 50793. The sources were observed using the low-resolution short wavelength modules SL1 (7.4–14.5 μm) and SL2 (5.2–7.7 μm). See Houck et al. (2004) for a more detailed description of the IRS and its capabilities. Because both sources are faint, the observations were taken in the mapping mode where the source position is stepped along the slit to facilitate an improved background subtraction. For NGC 7139, we have obtained 2×60 s exposures at eight pointings with the CSPN stepping along the slit at $4''$ intervals. For NGC 2438, we have obtained 3×60 s exposures at eight pointings with successive of $4''$ offsets along the slit.

In addition to our follow-up observations, NGC 2346 has IRS spectral mapping observations available in the *Spitzer* archive, as part of the program 30482 (PI: Houck). The source

was observed in the low-resolution modules SL1 and SL2, and high-resolution modules SH (10-19.5 μm) and LH (19-37 μm). In the SL modules, 3×15 s exposures were taken at 17 positions, each successive position offset by 1.″85 in the direction perpendicular to the slit. In the SH module, 3×6 s exposures were taken at 114 positions, consisting of 6 steps parallel to the slit with 5″ step size, and 19 positions perpendicular to the slit with 2.″3 step size. In the LH module, 3×6 s exposures were taken at 32 positions, consisting of 4 steps along the slit with step size of 10″, and 8 steps perpendicular to the slit with a 4.″5 step size.

All spectra were reduced using the CUBISM software (Smith et al. 2007), with the latest pipeline processing of the data and the most recent calibration set (irs_2009_05_20-pb-pfc-trim-omeg-lhllbiasfork.cal). Each low-resolution module contains two subslits that are exposed at the same time, e.g., SL1 on-source and SL2 off-source, and vice versa.

For NGC 7139, all off-source frames appear free of any source contamination. We average these BCD records while trimming the maxima and minima at each pixel to produce a 2D background frame, which is then subtracted from all on-source frames in the corresponding module. Subtracting a 2D background frame of nearby sky from our target observations removes astronomical background and alleviates the bad pixels in the IRS data. After the 2D background subtraction, we flag the global and record-level bad pixels first using the default CUBISM parameters for automatic bad pixel detection, and then through manual inspection of each BCD record, as well as by backtracking the pixels contributing to a given cube pixel. The spectrum is then extracted with an aperture size 5.″5×3.″7, large enough to enclose the source. Two local background spectra on either side of the source offset by ∼7.″5 are extracted and averaged for 1D subtraction of the local background.

The background subtraction in the case of NGC 2438 is complicated by the fact that the off-source frames are still within the PN. Lacking a suitable local 2D background, it is recommended to use an observation that is close to the target's RA, DEC, and observation time. After experimenting with various backgrounds, the best results appear to be achieved by using the off-source frames of NGC 7139, which, albeit not close to NGC 2438 in position,

were observed in a similar setup within a day from NGC 2438's observations. This however causes over-subtraction in some emission lines that are present in the spectrum of NGC 7139 but not NGC 2438; however, this problem is alleviated after local 1D background subtraction.

In the SL2 (5.2–7.7 μm) module, the spectrum of the CSPN NGC 2438 is not detected in the background-subtracted frame; therefore, we do not extract the spectrum from this module. In SL1 (7.4–14.5 μm) module, the background-subtracted frame does show the CSPN spectrum, and we proceed with flagging the bad pixels and extracting the spectra in the same way as we did for NGC 7139. We extract the CSPN spectrum using an aperture area of $3\farcs7\times3\farcs7$, and two background spectra offset from the CSPN by $\sim5\farcs6$ on either side of the source, which are then averaged for 1D local background subtraction.

NGC 2346 has dedicated background observations in each module; we use these for the 2D background subtraction. In the SL modules, we extract the CSPN spectrum using a $11''\times13''$ aperture, and two local background spectra offset $15''$ from the CSPN. In the SH module, the CSPN spectrum is extracted using a $6\farcs8\times6\farcs8$ aperture, and two background spectra are extracted at two positions offset from the CSPN by $\sim11''$. In the LH module, the CSPN spectrum is extracted using a $13\farcs4\times8\farcs9$ rectangular aperture, and the background spectra are offset from the CSPN by $\sim18''$. The two background spectra extracted for each module are averaged for 1D local background subtraction. All *Spitzer* IRS spectra will be presented in Section 4.

3.3.3 Gemini - NIRI

We have obtained JHK $\sim$1–2.5 μm spectra for 5 CSPNs and LM $\sim$2.9–6 μm spectra for NGC 6804 using the NIRI instrument on the Gemini-North 8-m Telescope on Mauna Kea in Hawaii. The observations were carried out in the classical observing mode on UTC 2009 June 5-6 in our program GN-2009A-C-7.

In all cases but one we have used the f/6 camera ($0\farcs12$ pixel^{-1}) with a 4-pixel slit ($0\farcs47$), and the appropriate $JHKLM$ order-sorting filter (G0209, G0210, G0211, G0212, G0213)

and grism (G5202, G5203, G5204, G5205, G5206). The resolving powers are 610, 825, 780, 690, and 770; and the inverse dispersions are 3.625, 5.203, 7.064, 11.39, and 16.51 Å pixel^{-1} for the $JHKLM$ bands, respectively. NGC 7139, the only exception, was observed with the same setup but using a 6-pixel slit; the resolving powers are 460, 520 and 520 in the JHK bands, respectively.

To facilitate background subtraction, the targets were nodded along the slit, usually in 10 steps within 20–30″ from the central slit position. Flat-fields and Argon arcs were taken immediately after each science observation. For the L and M bands, the wavelength calibration is carried out using the sky lines. Telluric standards were taken before or after the observation of each target at a similar airmass. The observing conditions were photometric the first night and slightly less so the second night. The targets, exposure times, and telluric standard stars are summarized in Table 3.4.

The spectra were reduced using the tasks within the Gemini IRAF package developed for the reduction of NIRI and GNIRS slit spectra. Sky frames, generated by combining suitable frames from other nod positions, were subtracted from each image to remove the background and dark current. The frames were then flat-fielded and combined to produce a single spectral image. The spectral image was wavelength-calibrated using either an Argon arc (JHK) or sky lines (LM), traced, and extracted. The residual and local background was subtracted during the spectral extraction, using two background apertures on either side of the target.

Telluric corrections were performed with the general version of the IDL routine xtellcor (Vacca et al. 2003), using the spectra of telluric standard stars. This IDL routine in principle removes the hydrogen absorption lines present in the telluric standard's spectrum and then divides out the atmospheric and instrumental features from the target spectrum. The hydrogen line removal is complicated at wavelengths where the atmospheric transmission varies strongly, making it difficult to separate the hydrogen lines from the telluric absorption lines. Therefore, we check the spectral images to verify the presence of emission lines. The routine

also performs a rough flux calibration, based on the standard stars' B and V magnitudes, extrapolated to IR wavelengths using the model spectrum of Vega. Since our standard stars are not A0V-type stars like Vega, this method renders the flux calibration inaccurate. Thus, we normalize the final JHK spectra to the known JHK magnitudes, and LM spectra to IRAC 3.6 and 4.5 μm flux densities. The obtained spectra will be presented and described in Section 4.

3.3.4 Gemini - MICHELLE

We have obtained low-resolution N-band 8–14 μm spectroscopy for the CSPN of NGC 6804, using the Michelle spectrometer on the Gemini-North 8-m Telescope atop Mauna Kea, Hawaii. The observations were performed on UTC 2009 September 19 under our program GN-2009B-Q-74.

For this observation we use the 2-pixel ($0\farcs402$) wide slit in the focal plane and the Low Resolution 10 μm (lowN) grating, resulting in an inverse dispersion of 0.024 μm pixel^{-1} and a resolving power of R$\sim$200. A standard chop and nod technique was employed in order to reduce the time-variable sky background and telescope thermal emission. The slit was oriented N-S, and the chop throw was $6''$ in the direction 55° E of N. Two observations with 450 s on-source integration time were taken, but in one of these observations, the CSPN was not well-centered in the slit, and the observation was of lower quality. The mean airmass during the two observations was 1.035 and 1.018.

The acquisition images were taken through the Si-5 11.6 μm filter ($\Delta\lambda$=1.1 μm) with an on-source integration time of 1 s. The detector scale of Michelle is $0\farcs1005$ pixel^{-1} in imaging mode and $0\farcs201$ pixel^{-1} in spectroscopic mode. The weather was good and the FWHM of the standard star image was measured to be $\leq 0\farcs42$. The diffraction limit of the telescope is $0\farcs34$.

The data were reduced using the spectral reduction task msreduce in the Gemini midir package in IRAF. The reduction process in general involves bias subtraction and flat-fielding,

background frames subtraction, wavelength calibration using the sky lines in the spectrum, spectral extraction, and the application of the telluric correction. The telluric correction and flux calibration were carried out using the standard star HD 188310; this star was observed at a mean airmass of 1.054. The final Michelle spectrum of NGC 6804 will be presented and discussed in Section 4.

3.4 Notes on Individual targets

A21 – We use the B magnitude from Acker et al. (1992), VI and extinction from Ciardullo et al. (1999) and JHK magnitudes from 2MASS. The R magnitude listed in SIMBAD and shown in the SED as an open diamond is not from a photometric catalog, and is thus unreliable. We use standard aperture photometry for IRAC flux density measurement, since the background is uniform. The CSPN is detected in IRAC ch1 and ch2, but not ch3 and ch4, for which upper limits are determined. For MIPS 24 μm flux density we use the value from Chu et al. (2011). The optical and IR flux densities follow a blackbody curve up to 8 μm, but the CSPN has a significant 24 μm excess. For the SED image, as well as the discussion of the IR excess of A21, see Chu et al. (2011).

A30 – a born-again PN with dusty H-poor knots in the central region (Cohen & Barlow 1974; Jacoby & Ford 1983). The CSPN is detected in IRAC ch1 and ch2, but it is faint and blended with an irregularly varying background. In ch3 and ch4, the CSPN is not clearly seen against the bright nebular background. The inadequate spatial resolution precludes accurate flux measurement; high-resolution images are needed to establish accurate fluxes and to determine whether the CSPN has excess IR emission. No SED is constructed.

A66 – We use the UB magnitudes from Acker et al. (1992), and VI magnitudes from Ciardullo et al. (1999), who reported a nearby visual companion that is unlikely to be a physical binary companion. The CSPN is too faint to be detected in 2MASS. Since Ciardullo et al. (1999) did not provide an extinction value, we use an $E(B-V)$ of 0.2, so that UVI

flux densities lie on a blackbody curve. We use standard aperture photometry to measure IRAC fluxes in ch1 and ch2, since the background is uniform. The CSPN is not detected in ch3 and ch4; for these, we plot upper flux limits. Clear excess emission is seen in IRAC ch1 and ch2, and the upper flux limits in ch3 and ch4 also lie above the expected photospheric emission. The companion is responsible for the excess IR emission.

DeHt 5 – We use the B magnitude from Passy et al. (in preparation) and JHK magnitudes from 2MASS and the extinction $E(B-V)$=0.16 from Good et al. (2005a) to construct the SED. The V magnitude is from SIMBAD, but since the original reference is not provided, we plot it on the SED as an open diamond. The CSPN is detected in all IRAC bands and at MIPS 24 μm. We use standard aperture photometry for photometric measurements in the IRAC bands. Clear IR excess is seen at 8 and 24 μm. This object may be a mimic and not a true PN (Frew 2008).

DS 2 – The SED presents extinction-corrected UBV magnitudes from Acker et al. (1992) and JHK magnitudes from from 2MASS. We adopt an $E(B-V)$ of 0.25 to correct for extinction so that the optical data points follow the Rayleigh-Jeans tail. CSPN is seen in all IRAC bands, and we use standard aperture photometry for IRAC flux measurements. All data points follow the blackbody curve, no IR excess is seen in the SED.

He 2-99 – The SED uses the UBV magnitudes from Reed (2003), and JHK magnitudes from 2MASS. Acker et al. (1992) list fainter B and V magnitudes of 14.22 and 14.00, respectively; these are plotted as open diamonds for comparison. To correct for interstellar extinction, we use $E(B-V)$ value of 0.6, for which the $UBVJH$ flux densities lie along the Rayleigh-Jeans tail. The CSPN is detected in all IRAC channels, and we use standard aperture photometry to measure the CSPN fluxes. The CSPN shows excess emission starting at $\sim$2 μm, and it is a [WC]-type star.

IC 4593 – This PN is centrally peaked in IRAC images; the emission peak in IRAC ch4 is offset by $\sim$1$\farcs$5 from the emission peak in IRAC ch1-3. An Hα image (Manchado et al. 1996) reveals that the CSPN is surrounded by a shell with a diameter $<$5$''$. The emission from

this shell is blended with that of the CSPN. The off-center emission peak in ch4 indicates that the emission is dominated by the nebular shell. Due to the blending of the CSPN and nebular emission, accurate photometry cannot be carried out. No SED is constructed.

IC 5148 – We use the VI magnitudes from Ciardullo et al. (1999) to produce the SED. Note that Acker et al. (1992) gives a fainter V magnitude of 16.5, plotted as an open diamond. Standard aperture photometry is used to measure CSPN IRAC fluxes in ch1-3. The CSPN is not detected in ch4; thus, we plot the upper limit for this band. Ciardullo et al. (1999) give an extinction value of c=0.38 (or $E(B-V)\sim$0.26). This extinction appears too high, as both the I and the IRAC flux densities would lie below the expected photospheric emission. The optical and IR flux densities lie on the blackbody curve for an extinction of 0; we therefore adopt zero extinction in the SED construction. The CSPN of IC 5148 does not show any IR excess.

JnEr 1 – To construct the SED, we use the UB magnitudes from Acker et al. (1992), and VI and c=0 from Ciardullo et al. (1999). We use standard aperture photometry to measure IRAC fluxes in ch1 and ch2; in ch3 and ch4 the CSPN is not detected and we plot the upper flux limits. The CSPN is not detected at 24 μm and we plot the upper limit from Chu et al. (2011). The IRAC fluxes lie along the blackbody curve, no IR excess is detected. The CSPN is a PG1159 star.

M2-9 – To construct the SED, we use the VI magnitudes and extinction from Ciardullo et al. (1999), JHK magnitude from 2MASS. The B magnitude is from the Guide Star Catalog and is inaccurate; we plot it on the SED as an open diamond. The IRAC images are saturated at the CSPN; therefore, we use the short-exposure frames, and carry out standard aperture photometry. The SED also shows mid-IR fluxes from Smith & Gehrz (2005) as open black diamonds. Prominent IR excess is seen starting from the I band. The CSPN of M2-9 is a symbiotic star.

Mz 3 – We use the B magnitude from Acker et al. (1992), JHK magnitudes from 2MASS, and an extinction c = 2.11 from Tylenda et al. (1992). Standard aperture photometry is

carried out on the short-exposure frames for all four IRAC bands, as the long exposure frames are saturated at the CSPN. The SED also shows mid-IR fluxes from Smith & Gehrz (2005) as open black diamonds. Prominent and rising IR excess is seen starting from J band through all IRAC bands. The CSPN of Mz 3 is a symbiotic star.

NGC 40 – The SED is constructed using the UB magnitudes from Acker et al. (1992), VI magnitudes and extinction from Ciardullo et al. (1999), and JHK magnitudes from 2MASS. The CSPN is detected in all IRAC bands. Since the background varies radially outward, we use the radial profiles to measure the IRAC flux densities. Clear excess is seen from K band throughout all IRAC bands. CSPN NGC 40 is a [WC] star.

NGC 246 – We use the UBV magnitudes from Reed (2003) and JHK from 2MASS. The extinction toward the nebula is likely very low (Hoogerwerf et al. 2007); therefore, we do not correct our fluxes for extinction. This appears justified, as the flux densities follow the blackbody curve very closely. The CSPN is detected in all IRAC channels, we use standard aperture photometry to measure the fluxes. A small flux enhancement is seen in ch3 and ch4. NGC 246 has a K-dwarf $V\sim$14 visual companion $3\farcs8$ away (Cudworth 1973). In addition, the neighboring nebular emission is bright in ch3 and ch4. Both of these may be contaminating the CSPN flux. Higher resolution imaging is necessary to separate the nebular emission and the companion's emission for accurate photometric measurements in IRAC ch3 and ch4, although we do not see strong evidence for an IR excess.

NGC 650 – The SED uses VI magnitudes and extinction from Ciardullo et al. (1999). The B magnitude from SIMBAD appears inaccurate, we plot it on the SED as an open diamond. The CSPN is detected in IRAC ch1-3 and very faintly in ch4. We use standard aperture photometry for IRAC photometric measurements. A nebular clump near the CSPN becomes increasingly brighter at longer wavelengths and may be contaminating the source aperture in ch3 and ch4. To estimate the measurement error, we carry out aperture photometry with multiple sky annuli, and adopt the standard deviation of resulting CSPN flux densities as the uncertainty. Clear IR excess is seen in the IRAC channels. NGC 650 has a companion

which is itself a binary. The companion can account for the IR excess.

NGC 1360 – We use the UB magnitudes from Acker et al. (1992), VI and extinction ($c = 0$) from Ciardullo et al. (1999), and JHK from 2MASS to construct the SED. The CSPN is detected in all four IRAC bands, and we use standard aperture photometry to measure the IRAC flux densities. The star is not detected at 24 μm; the SED shows the upper limit from Chu et al. (2011). All data points closely follow the blackbody curve, no IR excess is detected.

NGC 1501 – We use the UB magnitudes from Acker et al. (1992), VI magnitudes and extinction from Ciardullo et al. (1999), and JHK from 2MASS. The R magnitude given in SIMBAD plotted as an open diamond, is not from a photometric catalog and appears too bright for the photospheric emission. This may be caused by the contribution of strong line emission in the R band, since CSPN NGC 1501 is a [WC]-type star. If the blackbody curve is normalized to the V magnitude, the UB flux densities would lie slightly below the blackbody curve. We choose to normalize to the brighter magnitudes in order to conservatively assess the presence of IR excess. The nebular background near the CSPN is uniform in IRAC ch1-ch3 images; thus, standard aperture photometry is used for these flux measurements. At 8.0 μm, the background is clumpy and shows slight radial variations in the central region but not a shell-like morphology. We report the 8 μm flux as an average of the two measurements from standard photometry and radial profile methods, and use half the difference between these two as the measurement error. Excess emission is seen starting from the J band and throughout all IRAC bands. The CSPN NGC 1501 is a [WC]-type star.

NGC 2346 – The SED is constructed using the B magnitude from Acker et al. (1992), VI magnitudes and extinction from Ciardullo et al. (1999), and JHK from 2MASS. NGC 2346 is a bipolar nebula, and the nebular background is not uniform, but the CSPN is much brighter than the nebular background, and standard aperture photometry is suitable for flux measurement. The image of the CSPN is saturated in long exposure frames, so we use the short-exposure images for flux measurement in all IRAC bands. Clear IR excess is seen

from J band, through all IRAC channels to the MIPS 24 μm band. The CSPN is a known spectroscopic binary.

NGC 2371 – The SED uses the UB magnitudes from Acker et al. (1992), VI magnitudes and extinction c=0.21 from Ciardullo et al. (1999), and JHK from 2MASS. The R magnitude given by SIMBAD is not from a photometric catalog and is plotted in the SED as an open diamond. The nebular background increases outward from the CSPN, but the morphology is not shell-like. In addition, the nebular emission toward the south is potentially included the aperture. We use the radial profile method to measure the CSPN IRAC fluxes, since the standard aperture photometry would overestimate the background at the CSPN. Despite the absence of background point sources, the background estimated from the average and the median radial profile differ, likely due to the enhancement in the nebular emission toward the south. Since this enhancement may be contaminating the aperture, we use background values from median as well as average radial profiles to measure the CSPN flux density. We report the average of the computed fluxes as the final flux value, and use errors to cover the whole range of possible flux density values. The IRAC data points lie close, but slightly above the expected photospheric emission. This is likely caused by nebular contamination in the aperture. The CSPN is a [WO]-type star; therefore, line emission may contribute to the IR photometry. Higher-resolution imaging is necessary to separate the extended nebular emission from the CSPN.

NGC 2392 – We construct the SED using the UB magnitudes from Acker et al. (1992), the VI magnitudes from Ciardullo et al. (1999), and $E(B-V)$=0.252 from Tylenda et al. (1992). Note that Ciardullo et al. (1999) give a lower extinction value of c=0.19 (or $E(B-V)\sim$0.13), but an $E(B-V)$ of 0.252 appears to better deredden the optical fluxes to fit a blackbody curve. The PN has a shell-like morphology, and we use the radial profiles to estimate the nebular background and the CSPN fluxes. All IRAC flux densities closely follow the blackbody curve, no IR excess is seen.

NGC 2438 – Few optical photometric measurements are available for this CSPN. SIMBAD

lists B and R magnitudes of 11.7 and 10.2, respectively, but these are too bright for the faint CSPN and likely correspond to a bright star that is projected near the CSPN. Gathier & Pottasch (1988) report their own V magnitude measurement of 17.22 and compare it to other measurements in the literature. We plot Gathier & Pottasch (1988) value as a filled diamond and others (e.g., Frew 2008) as open diamonds for comparison. We also use the B magnitude from Acker et al. (1992) in the SED, and 2MASS J magnitude, and HK upper limits. The extinction values are also varied, for example, Gathier & Pottasch (1988) lists $E(B-V)$=0.25, and Frew (2008) gives $E(B-V)$=0.46. The reported V magnitudes and extinctions are so varied that it is difficult to normalize the blackbody flux and estimate the expected photospheric emission in the IR portion of the SED. To conservatively assess the presence of IR excess, we normalize the blackbody emission to the brightest visual magnitude in Gathier & Pottasch (1988), and use the higher of the extinction values (0.46). The CSPN is detected in all IRAC bands as well as at MIPS 24 μm (Chu et al. 2011). The background estimation is complicated by a bright star that is projected close to the faint CSPN, which likely affects the median radial profile. We do see radial variation in the nebular background, however. We use both standard aperture photometry and radial profile method with their respective errors to estimate the CSPN fluxes, we report the average of these two results as the final CSPN flux, and give an uncertainty that covers the whole error range of both results. Despite the uncertainties in the optical and IR portions of the SED, all IRAC fluxes are above the expected photospheric emission, and we see a strong IR excess in the MIPS 24 μm band.

NGC 2610 – The SED is made using B from Acker et al. (1992), VI and extinction from Ciardullo et al. (1999), JH magnitude and K upper limit from 2MASS. The BR magnitudes listed in SIMBAD are from the Guide star Catalogue v.2.2 and are thus unreliable; they are not used for the SED construction. The CSPN is detected in IRAC ch1-ch3. The PN has a shell-like morphology, we therefore use radial profiles for flux measurements. The IRAC flux densities lie on the blackbody curve, and the CSPN is not detected at 24 μm (Chu et

al. 2011). No IR excess is seen.

NGC 3242 – We construct the SED using B from Acker et al. (1992) and VI and extinction from Ciardullo et al. (1999). The JHK magnitudes given in 2MASS are too bright, likely affected by the near nebular emission. We measure our own 2MASS fluxes via comparative photometry, using a 3″ aperture and 3-5″ background annulus on the CSPN, as well as a nearby star in the field of view, 2MASS J10245259-1837594, which is well-detected, not surrounded by a nebula, and appears similar in brightness to the CSPN. The background annulus is chosen to be close to the CSPN but still outside of the bright nebular shell. Our measured JHK fluxes listed in Table 3.3 are marked by an asterisk. The CSPN is detected in IRAC ch1-ch3; in ch4 the CSPN is not detected against the bright nebular background. The PN has a shell-like morphology; we therefore use the radial profile method to measure CSPN fluxes. The fluxes lie along the expected blackbody tail, no IR excess is seen.

NGC 3587 – We use UBV from Acker et al. (1992), and I and extinction from Ciardullo et al. (1999) to construct the SED. The CSPN is detected in IRAC ch1 and ch2, and standard aperture photometry is used to measure the flux densities. For IRAC ch3 and ch4, we give upper flux limits. The IRAC data points follow the blackbody curve. The CSPN is not detected at 24 μm (Chu et al. 2011). No IR excess is detected.

NGC 6153 – This CSPN is faintly seen in IRAC ch 1 and ch2, but the nebular background is bright and irregular. This precludes accurate photometry; high-resolution imaging is needed for flux measurement. No SED is constructed.

NGC 6369 – We use the V magnitude and extinction from Ciardullo et al. (1999), and JHK magnitudes from 2MASS to construct the SED. The B magnitude is from SIMBAD, but since the original reference is not provided, we plot in on the SED as an open diamond. The blackbody curve is normalized to the V magnitude. The CSPN is detected in all IRAC bands. The background varies radially outward, we therefore use the radial profiles to estimate the nebular background. At 8 μm we use the short-exposure frame to create radial profile, because the image is saturated at the bright PN shell. The measurement error in

ch4 is similar to the flux value, we therefore report the sum of the measured flux and the uncertainty as an upper limit at 8 μm. Clear IR excess is seen starting from J band through the IRAC channels. CSPN NGC 6369 is a [WC]-type star.

NGC 6543 – For the SED, we use the B magnitude from Acker et al. (1992), and VI magnitudes and extinction from Ciardullo et al. (1999). In the JHK bands, the bright nebula has compromised the automated 2MASS point-spread-function fitting and the 2MASS point source catalog lists fluxes for the CSPN that are too high. We carry out our own photometric measurements on the CSPN and a nearby star in the field of view, 2MASS J17591354+6636083, which is not surrounded by a nebula, and appears similar in brightness to the CSPN. We use a 3″-radius source aperture and a 3-5″annulus background annulus for both stars. A small background annulus is chosen in order to avoid the bright nebular shell. The JHK magnitudes for the CSPN are listed in Table 3.3, marked with an asterisk. We measure fluxes in IRAC ch1-3 using the radial profile method; in ch4 the nebular emission is too strong for photometric measurements. The fluxes follow the blackbody curve, no IR excess is seen.

NGC 6629 – We use the B magnitude from Acker et al. (1992), and VI magnitudes and extinction from Ciardullo et al. (1999) to construct the SED. The JHK magnitudes from 2MASS are compromised by the bright nebula, we therefore perform comparative photometry referencing to the star 2MASS J18253988-2312559. We perform the photometry on both the CSPN and the reference star using a 3″-radius source aperture and a 3-5″ annular background. The CSPN is detected in IRAC ch1-3; in ch4 the nebular emission is too strong for photometric measurements. The PN has a centrally peaked morphology; we therefore use the radial profiles to estimate lower and upper limits for the background emission, and use these values to estimate CSPN flux. The upper and lower flux limits are shown as the error bars, and the data points show the average flux for each band. The SED shows slight JHK excess, this is likely due to imperfect background subtraction, since using standard aperture photometry underestimates the background if the PN is centrally peaked. No IR

excess is seen in the IRAC bands.

NGC 6720 – The SED is constructed using the $BVRI$ magnitudes from Passy et al. (in preparation), and E(B-V)=0.04 from Frew (2008). The CSPN is detected only in IRAC ch1, we use the radial profile to estimate the background for flux measurement. For ch2-4, we report flux upper limits. The SED does not show any IR excess.

NGC 6751 – To construct the SED, we use the V magnitude and extinction from Acker & Neiner (2003). The magnitudes from SIMBAD and Acker et al. (1992), shown as open diamonds, are significantly fainter; therefore, the SED is difficult to constrain. To assess the IR excess conservatively, we normalize the blackbody curve to the highest optical magnitude. The JHK magnitudes from 2MASS are compromised by nebular emission, we therefore measure our own 2MASS fluxes by comparative photometry using the nearby star 2MASS J19055916-0559003 as a reference. We perform aperture photometry on both the CSPN and the reference star using a 3″-radius source aperture and a 3-5″ annular background. Our JHK fluxes are listed in Table 3.3, marked with an asterisk. The CSPN is detected in IRAC ch 1-3, but in ch4 the nebular emission is too bright for photometric measurements of the CSPN. Since the background varies radially outward, we use the radial profile method to measure IRAC fluxes. Regardless of the optical flux chosen to normalize the blackbody emission, there is IR excess present from the near-IR through all IRAC bands. The JHK images show a nearby star that might contaminate the JHK flux measurement slightly, this star is however much fainter than the CSPN and unlikely to be responsible for the entire IR excess. Furthermore, it fades at longer wavelengths and is not seen in any of the IRAC images. The CSPN is a [WC]-type star and the broad emission lines and free-free emission from the stellar wind are likely responsible for the observed IR excess.

NGC 6772 – The SED shows the B and V magnitudes from Acker et al. (1992), corrected for extinction using $E(B-V)$ from Gathier & Pottasch (1988), who also report V =18.63, 18.9, similar to V=18.68 listed in Acker et al. (1992). The B magnitude listed SIMBAD is from the Guide Star Catalog v.2.2 and is thus unreliable; we display it on the SED as an open

diamond. The CSPN is faintly detected in IRAC ch1 and ch2; for ch3 and ch4 we report the upper limits. The nebular background varies radially outward; therefore, we use the radial profile method to measure CSPN fluxes. The fluxes in IRAC ch1 and ch2 are slightly above the expected photospheric emission. The CSPN is faint and appears slightly elongated in the IRAC images. This elongation may be due to an underlying nebular emission or a faint not well resolved visual companion, either of which may contaminate the measured CSPN flux. There is no convincing evidence that the central star itself has an IR excess.

NGC 6781 – The CSPN is detected in IRAC ch1-2, but not in ch3-4. As it is very faint and blended with a much brighter nearby star and underlying nebular emission, the CSPN fluxes cannot be measured accurately. A higher resolution image with better signal to noise ratio is needed to measure the fluxes and assess the presence of IR excess. No SED is constructed.

NGC 6804 – To construct the SED, we use the B magnitude from Acker et al. (1992), VI magnitudes and extinction from Ciardullo et al. (1999), and JHK magnitudes from 2MASS. Note that the optical flux densities follow the blackbody curve better for a slightly higher extinction $E(B-V)\sim0.7$. The CSPN is bright and well detected in all IRAC bands. Even though the background does vary radially outward, the variation is insignificant compared to the brightness of the CSPN, and both standard aperture photometry and the radial profile technique give the same flux values. In ch4, the long exposure image is saturated at the CSPN; therefore, we use the short-exposure frame for flux measurement. The CSPN is also detected at 24 μm. Clear and rising excess emission is seen starting from the J band.

NGC 6853 – We use the U magnitude from Acker et al. (1992), $BVRI$ from Passy et al. (in preparation), JHK from 2MASS, and extinction E(B-V)=0.03 from Frew (2008) to construct the SED. The CSPN is detected in all IRAC bands. The nebular background gradually decreases outward, but it is clumpy, and there is a bright star near the CSPN which affects the radial profiles. We estimate the measurement error by carrying out aperture photometry with multiple sky annuli, and adopting the standard deviation of resulting CSPN flux densities as the uncertainty. The CSPN is also detected at 24 μm, and the measurement

error is estimated in a similar fashion as for the IRAC flux densities. The SED shows slight excess emission from J to IRAC 4.5 μm, and a strong IR excess from 5.8 μm band up to MIPS 24 μm. The near-IR excess up to 4.5 μm is due to a faint companion reported by Ciardullo et al. (1999), which cannot be resolved in IRAC images.

NGC 6905 – The SED is constructed using V from van Altena et al. (1995), and I and extinction from Ciardullo et al. (1999). The B magnitude from Acker et al. (1992) and R from Cutri et al. (2003) depart significantly from the blackbody curve and are likely affected by line emission, they are shown on the SED as open diamonds. The 2MASS JHK magnitudes are too bright, the flux measurement is likely compromised by the bright nebular emission. We therefore carry out comparative photometry referencing to the star 2MASS J20222230+2005127. We use a 3″ radius source aperture, and a 3-5″ annular background for both the CSPN and the reference star. The resulting 2MASS JHK magnitudes are listed in Table 3.3 and marked with an asterisk. The CSPN is detected in IRAC ch 1-3 and we use standard aperture photometry to measure the flux densities. A nearby nebular clump is seen in ch3, and may affect the photometry; therefore, we carry out aperture photometry with multiple sky annuli, and adopt the standard deviation of resulting CSPN flux densities as the measurement uncertainty. In ch4, the star is not detected against the bright nebular background. Clear excess emission is seen from near-IR through the IRAC wavelengths. CSPN NGC 6905 is a [WC]-type star, and the excess emission is likely caused by the free-free emission from the fast stellar wind, and broad emission lines.

NGC 7009 – The CSPN is detected in IRAC ch1-3, but is not seen in ch4 against the bright nebular background. The nebular emission is strong, nonuniform and blended with the CSPN emission, therefore, accurate fluxes cannot be measured. Higher resolution images are necessary to resolve the CSPN from the nebular emission and measure accurate fluxes. No SED is constructed.

NGC 7026 – The CSPN can be seen in IRAC ch1 and very faintly in ch2, but is not seen against the bright nebular emission in ch3 and ch4. NGC 7026 is bipolar and has a bright

waist whose emission is blended with the CSPN. Accurate fluxes cannot be measured with such bright and nonuniform nebular background. No SED is constructed.

NGC 7048 – The CSPN is seen only in IRAC ch1 and ch2, but it is very faint and blended with the surrounding nebular and stellar emission. Accurate fluxes cannot be measured. No SED is constructed.

NGC 7139 – Only the B and V magnitudes of this CSPN are found in the literature. Piliugin & Khromov (1979) report B of 18.3, while Jacoby & Kaler (1989) report 18.72, both of which are already extinction-corrected. For consistency, we report the uncorrected magnitudes in the Table 3.3, and list the extinction for c=0.76 (i.e., $E(B-V)\sim$0.521) given by Jacoby & Kaler (1989). The CSPN does not have magnitudes listed in 2MASS; however, the CSPN is faintly seen in 2MASS JHK images. We therefore carry out comparative photometry using nearby stars 2MASS J21461639+6347122 for measurements in J and H band, and 2MASS J21460448+6348299 for K band, using a 3″-radius source aperture and a 3-5″ annular background for photometry. The measurement uncertainty is estimated from the standard deviation of the pixels in the sky annulus multiplied by the source aperture area. In the J and K bands, CSPN NGC 7139 is detected at 1.4σ and 1.7σ level, respectively. In H band, the CSPN flux is below 1σ; we report the sum of background-subtracted flux in the aperture and 2σ as the H band flux upper limit. The JHK fluxes are listed in Table 3.3 and are marked with an asterisk. The CSPN is seen in all IRAC bands. The nebular background is uniform, and the flux densities are obtained via standard aperture photometry. The SED shows clear excess emission in all IRAC bands, and the excess may be starting from the J band.

NGC 7293 – The mid-IR excess of this CSPN has been analyzed in detail by Su et al. (2007).

NGC 7354 – The CSPN is detected only in IRAC ch1, but it is very faint and blended with the bright nebular background. Therefore, accurate flux measurements cannot be made. No SED is constructed.

PMR 1 – The VR magnitudes and the extinction are from Morgan et al. (2001). The CSPN is detected in all IRAC bands, and we use standard aperture photometry to make photometric measurements. Clear IR excess is seen in all IRAC channels. CSPN PMR 1 is a [WC]-type star with strong stellar wind, which is likely responsible for the IR excess.

PMR 2 – To construct the SED, we use optical magnitudes as well as the extinction correction of Morgan et al. (2001). PMR 2 is a small, centrally peaked nebula, and it is difficult to de-blend the stellar and nebular emission, even though the central source is clearly seen in all IRAC bands. We perform standard aperture photometry and report the measured fluxes as upper limits. All upper limits are well above the expected photospheric emission, and the CSPN likely does have IR excess since it is a [WC]-type star, but higher-resolution images are needed to separate the stellar and nebular emission and measure the CSPN fluxes accurately.

Table 3.1. Archive of *Spitzer* Observations of Planetary Nebulae

PN Name	Instr./Mode	AOR	PID(s)	Remarks	Phot.[a]
A21	IRAC Map	17595136	30285	CSPN detected in ch1-2, not ch3-4	phot
	MIPS Phot		40953	CSPN detected in ch1	Chu
A30	IRAC Map	21967616	40115	CSPN seen in ch1-2, in ch3-4 the nebula is too bright	phot:
A66	IRAC Map	17594624	30285	CSPN detected in ch1-4, has a visual companion	phot
A58	MIPS Scan	10838528	3362	nova	
A78	MIPS Scan	10838016	3362	not well resolved from the nebula	
DeHt 5	IRAC Map	18230272	30432	CSPN detected in ch1-4	phot
	MIPS Phot	26345728	50530	CSPN detected in ch1	phot
DS 2	IRAC Map	17593856	30285	CSPN detected in ch1-4, nearby visual comp	phot
Hb 5	IRAC Map	4413696	68	PN too small, CSPN not seen against the bright nebula	
Hb 12	IRAC Map	4413952	68	PN too small	
	MIPS Phot	4617728	77	PN too small	
He 2-119	IRAC Map	17594112	30285	CSPN not seen	
He 2-459	IRAC Map	21978880	40115	PN too small	
He 2-99	IRAC Map	21978112	40115	CSPN detected in ch1-4	phot
IC 4406	IRAC Map	4414208	68	CSPN not seen against the bright nebular background	
IC 4593	IRAC Map	21641472	40020	CSPN seen in ch1-3, emission peak offset in ch4	phot:
IC 5148	IRAC Map	4414464	68	CSPN detected in ch1-3, not in ch4	phot
JnEr 1	IRAC Map	17594880	30285	detected in ch1-2, barely seen in ch3, not in ch4	phot
	MIPS Phot		40953	CSPN not detected	Chu
M2-9	IRAC Map	4414720	68	CSPN detected in ch1-4, very bright, symbiotic	
M2-20	IRAC Map	21975040	40115	PN too small, crowded field	
M2-31	IRAC Map	21973248	40115	PN too small	
M4-18	IRAC Map	21979648	40115	PN too small	
Mz 1	IRAC Map	4414976	68	CSPN not detected	
Mz 3	IRAC Map	4415232	68	CSPN detected in ch1-4, very bright, symbiotic	phot
NGC 40	IRAC Map	21976576	40115	CSPN detected in ch1-4	phot
NGC 246	IRAC Map	4416256	68	CSPN detected in ch1-4	phot
	MIPS Phot		40953	CSPN not detected	Chu
NGC 650	IRAC Map	4421120	68	CSPN detected in ch1-4	phot
	MIPS Scan	9548032	77	CSPN not seen	
NGC 1360	IRAC Map	21641728	40020	CSPN detected in ch1-4, spectroscopic binary	phot
	MIPS Phot		40953	CSPN not detected	Chu
NGC 1501	IRAC Map	21971712	40115	CSPN detected in ch1-4	phot
NGC 2346	IRAC Map	4415488	68	CSPN detected in ch1-4	phot
NGC 2371	IRAC Map	17589760	30285	CSPN detected in ch1-4	phot
NGC 2392	IRAC Map	17589504	30285	CSPN detected in ch1-4	phot
NGC 2438	IRAC Map	4415744	68	CSPN detected in ch1-4	phot
	MIPS Phot		40953	CSPN detected in ch1	Chu
NGC 2440	IRAC Map	6621440	1052	CSPN not seen against the bright nebular background	
	MIPS Scan	4619264	77	CSPN not seen against the bright nebular background	
NGC 2610	IRAC Map	17590016	30285	CSPN detected in ch1-2, faintly in ch3, not in ch4	phot
	MIPS Phot		40953	CSPN not detected	Chu
NGC 2818	IRAC Map	4416512	68	CSPN not seen against the bright nebular background	
NGC 2867	IRAC Map	21969664	40115	CSPN not seen against the bright nebular background	
NGC 3132	IRAC Map	4416768	68	unresolved companion >5 mag brighter than the CSPN	
NGC 3195	IRAC Map	17590272	30285	CSPN not seen against the bright nebular background	
NGC 3242	IRAC Map	17590528	30285	CSPN detected in ch1-3, bright PN in ch4	phot
NGC 3587	IRAC Map	4417024	68	CSPN detected in ch1-2, not in ch3-4	phot
	MIPS Phot		40953	CSPN not detected	Chu
NGC 3699	IRAC Map	17594368	30285	CSPN not seen against the bright nebular background	
NGC 3918	IRAC Map	21639936	40020	CSPN not seen against the bright nebular background	
NGC 5315	IRAC Map	21972480	40115	PN too small	
NGC 6072	IRAC Map	4417280	68	CSPN not seen against the bright nebular background	
NGC 6153	IRAC Map	21640448	40020	CSPN seen very faintly in ch1-2, not ch3-4	phot:
NGC 6302	IRAC Map	4417536	68	CSPN not seen against the bright nebular background	
NGC 6309	IRAC Map	4417792	68	CSPN not seen against the bright nebular background	
NGC 6369	IRAC Map	4418048	68	CSPN detected in ch1-4	phot
NGC 6445	IRAC Map	4418304	68	CSPN not detected	
NGC 6537	IRAC Map	4418560	68	CSPN not seen against the bright nebular background	

Table 3.1 (cont'd)

PN Name	Instr./Mode	AOR	PID(s)	Remarks	Phot.[a]
NGC 6543	IRAC Map	4418816	68	CSPN detected in ch1-3, not in ch4, bright PN	phot
	MIPS Phot	11412736	3668	MIPS 1,3 observations, CSPN outside FOV	
	MIPS Phot	11412480	3668	MIPS 1,2 - CSPN unresolved from PN, or outside FOV	
NGC 6563	IRAC Map	4419072	68	CSPN not detected	
NGC 6572	IRAC Map	21640192	40020	PN too small	
NGC 6629	IRAC Map	4419328	68	CSPN seen in ch1-3, not in ch4, bright nebula	phot
NGC 6720	IRAC Map	4419584	68	CSPN detected in ch1, blended with PN/unseen in ch2-4	phot
	IRAC Map	21642496	40020		
	MIPS Scan	12646400	77	CSPN not seen against the bright nebular background	
NGC 6751	IRAC Map	4419840	68	CSPN detected in ch1-3, not in , bright nebula	phot
NGC 6772	IRAC Map	4420096	68	CSPN detected in ch1-2, not in ch3-4	phot
NGC 6781	IRAC Map	4420352	68	CSPN faintly seen in ch1-2, not in ch3-4	phot:
NGC 6804	IRAC Map	4420608	68	CSPN detected in ch1-4	phot
	MIPS Phot		50793[b]	CSPN detected	phot
NGC 6853	IRAC Map	4420864	68	CSPN detected in ch1-4	phot
	MIPS Scan	4620032	77	CSPN detected in m1, not in m2-3, bright nebula	phot
	MIPS Scan	4620288	77		
NGC 6905	IRAC Map	4421376	68	detected in ch1-3, in ch4 a nearby nebular bright clump	phot
NGC 7009	IRAC Map	4421632	68	CSPN detected in IRAC 1-3, strong nebular emission	phot:
NGC 7026	IRAC Map	21970432	40115	CSPN seen in ch1-2, not in ch3-4, bright nebula	phot:
NGC 7027	IRAC Map	4421888	68	PN too small, CSPN not seen against the bright nebula	
	IRAC Map	4422656	68		
	MIPS Phot	4618752	77	PN too small	
NGC 7048	IRAC Map	17592064	30285	faintly seen in ch1-2, not in ch3-4	phot:
NGC 7139	IRAC Map	4422144	68	CSPN detected in ch1-4	phot
	MIPS Phot		50793[b]	CSPN not seen against the bright nebular background	
NGC 7293	IRAC Map	4422400	68	CSPN detected in ch1-4, reported by Su et al. (2007)	Su
	IRAC Map	17591040	30285		
	IRAC Map	17591296	30285		
	IRAC Map	17591552	30285		
	IRAC Map	17591808	30285		
	IRAC Map	21641984	40020	halo	
	IRAC Map	21642240	40020	halo	
	MIPS Scan	4620544	77	CSPN detected in ch1-2	Su
	MIPS Scan	4620800	77		
	MIPS Scan	4621056	77		
NGC 7354	IRAC Map	17590784	30285	CSPN seen in ch1, not in ch2-4, bright nebula	phot:
	IRAC Map	28960512	50398		
	IRAC Map	28966656	50398		
	IRAC Map	28966912	50398		
	IRAC Map	28965120	50398		
	MIPS Scan	28079104	50398	CSPN not seen against bright nebular background	
	MIPS Scan	28090368	50398		
PB 6	IRAC Map	21968384	40115	PN too small	
PB 8	IRAC Map	21975808	40115	PN too small	
PM 1-310	IRAC Map	21980416	40115	PN too small	
PMR 1	IRAC Map	21974016	40115	CSPN seen in ch1-4, [WC]-type	phot
PMR 2	IRAC Map	21977344	40115	CSPN seen in ch1-4, [WC]-type, centrally peaked PN	phot

[a]phot=CSPN is selected for photometry, phot:=CSPN detected but photometry may be uncertain, Chu= we use flux densities or upper limits reported by Chu et al. (2011), Su= flux densities from Su et al. (2007) are used.

[b]Our follow-up program

Table 3.2. *Spitzer* Photometric Measurements of Resolved CSPNs

PN Name	IRAC 3.6 μm μJy	IRAC 4.5 μm μJy	IRAC 5.2 μm μJy	IRAC 8.0 μm μJy	MIPS 24 μm mJy
A21	36 ± 2	22 ± 1	< 37	<31	0.916 ± 0.114[a]
A66	79 ± 4	58 ± 3	<33	<49	...
DeHt 5	135 ± 7	87 ± 4	62 ± 4	84 ± 5	1.565 ± 0.093
DS2	1734 ± 87	1130 ± 57	633 ± 34	339 ± 19	...
He 2-99	6488 ± 327	7786 ± 392	7968 ± 432	9801 ± 857	...
IC 5148	33 ± 2	21 ± 1	15 ± 4	<16	...
JnEr 1	12 ± 1	7 ± 1	<10	<29	< 0.68[a]
M2-9	$9.2\times10^6 \pm 4.6\times10^5$	$1.6\times10^7 \pm 8.0\times10^5$	$2.6\times10^7 \pm 1.3\times10^6$	$3.9\times10^7 \pm 2.0\times10^6$	...
Mz 3	$2.0\times10^7 \pm 1.0\times10^6$	$2.9\times10^7 \pm 1.5\times10^6$	$3.4\times10^7 \pm 1.7\times10^6$	$5.1\times10^7 \pm 2.6\times10^6$	...
NGC 40	21853 ± 1095	19694 ± 988	16295 ± 833	15162 ± 940	...
NGC 246	1956 ± 98	1259 ± 63	956 ± 49	517 ± 32	< 26.25[a]
NGC 650	159 ± 9	103 ± 7	47 ± 8	38 ± 11	...
NGC 1360	2717 ± 136	1693 ± 85	1043 ± 53	558 ± 29	< 4.651[a]
NGC 1501	3435 ± 173	3036 ± 154	2113 ± 128	1711 ± 539	...
NGC 2346	344967 ± 17254	380063 ± 19009	378285 ± 18936	356819 ± 17849	170 ± 9
NGC 2371	241 ± 21	174 ± 100	100 ± 22	115 ± 52	...
NGC 2392	11241 ± 568	7320 ± 388	4922 ± 261	2198 ± 218	...
NGC 2438	111 ± 20	108 ± 23	100 ± 18	107 ± 12	12.4 ± 13.7[a]
NGC 2610	34 ± 2	19 ± 7	12 ± 6	...	<149.0[a]
NGC 3242	1238 ± 108	873 ± 198	374 ± 111	...	...
NGC 3587	42 ± 2	24 ± 2	<57	<21	< 6.15[a]
NGC 6369	10629 ± 816	10311 ± 839	4882 ± 1785	<8475	...
NGC 6543	3851 ± 472	1935 ± 760	1163 ± 475	...	...
NGC 6629	5494 ± 2600	2689 ± 1317	1960 ± 1380	...	...
NGC 6720	55 ± 9	< 130	<69	<66	...
NGC 6751	2202 ± 135	1799 ± 128	840 ± 317	...	...
NGC 6772	43 ± 5	30 ± 7	<27	<33	...
NGC 6804	38429 ± 1923	49567 ± 2480	69173 ± 3460	116539 ± 5836	170 ± 38
NGC 6853	376 ± 25	293 ± 28	363 ± 121	738 ± 181	23.1 ± 5.1
NGC 6905	869 ± 48	783 ± 57	755 ± 35	...	...
NGC 7139	299 ± 15	276 ± 14	240 ± 14	220 ± 14	...
NGC 7293[b]	374 ± 19	241 ± 24	171 ± 26	174 ± 17	48.4 ± 7.3
PMR 1	3008 ± 151	2933 ± 147	2299 ± 118	2185 ± 144	...
PMR 2	<4479	<4994	<6064	<17107	...

[a]From Chu et al. (2011)

[b]All values are from Su et al. (2007)

Table 3.3. Complementary Optical and Near-IR Photometry of CSPNs

PN Name	U	B	V	R	I	J	H	K	$E(B-V)$	Ref.[a]
A21	...	15.7	16.05	(17.4)	16.38	16.58	>17.21	>16.14	0.12	1,2,3
A66	16.8	17.7	18.17	...	18.29	...	...	...	0.2^{+}	1,2
DeHt 5	...	15.27	(15.5)	...	...	15.57	15.96	15.58	0.16	3,4,11
DS 2	11.3	12.4	12.4	...	...	12.68	12.797	12.93	0.25^{+}	2
He 2-99	12.57	13.26	13.18	...	...	12.63	12.55	12.10	0.6^{+}	3
IC 5148	...	...	16.16	...	16.59	...	...	...	0.0^{+}	1
JnEr 1	15.3	16.5	17.16	...	17.56	...	...	...	0.0	1,2
M2-9	...	...	14.45	...	13.16	11.20	9.18	7.00	0.76	1
Mz 3	...	17.6	...	...	...	9.35	7.36	5.61	2.11	2,5
NGC 40	11.1	11.8	11.55	...	11.28	10.89	10.80	10.38	0.55	1,2
NGC 246	10.15	11.43	11.78	...	...	12.61	12.80	12.87	0.0^{+}	3
NGC 650	...	(16.1)	17.57	...	17.73	...	...	...	0.13	1,3
NGC 1360	9.6	11.0	11.34	...	11.75	12.08	12.29	12.37	0.0	1,2
NGC 1501	14.3	15.2	14.36	(12)	13.80	13.20	12.92	12.79	0.76	1,2,3
NGC 2346	...	11.8	11.27	...	11.01	10.26	9.44	8.41	0.51	1,2
NGC 2371	13.3	14.5	14.85	(12)	15.16	15.21	15.50	15.49	0.14	1,2,3
NGC 2392	9.3	10.4	10.63	...	10.77	10.87	10.92	10.94	0.25	1,2,5
NGC 2438	...	(17.7)	17.22	...	...	17.02	>16.42	>16.56	0.25	2,6
NGC 2610	...	15.6	15.97	...	16.32	16.71	16.29	>15.94	0.07	1,2
NGC 3242	...	12.0	12.32	...	12.66	13.08*	13.29*	13.44*	0.08	1,2
NGC 3587	14.4	15.7	16.0	...	17.15	...	...	...	0.05	1,2
NGC 6369	...	(16.6)	15.13	...	...	12.45	11.87	11.48	1.33	1,3
NGC 6543	...	11.2	11.29	...	11.47	11.98*	11.97*	12.39*	0.08	1,2
NGC 6629	...	13.3	12.87	...	12.36	11.88*	11.88*	11.62*	0.62	1,2
NGC 6720	...	15.41	15.77	15.90	16.06	...	...	...	0.04	11,12
NGC 6751	...	(15.8)	14.6	...	...	13.55*	13.33*	12.95*	0.34	2,3,7
NGC 6772	...	19.0	18.7	...	...	...	...	...	0.75	2,6
NGC 6804	...	14.5	14.17	...	13.64	13.23	12.45	11.28	0.60	1,2
NGC 6853	12.4	13.75	14.09	14.25	14.41	14.75	14.70	14.61	0.03	2,11,12
NGC 6905	...	(16.3)	14.5	(11.8)	14.74	14.64*	14.63*	14.33*	0.13	1,2,3
NGC 7139	...	20.38	20.29	...	...	17.72*	>16.21*	15.54*	0.52	8
NGC 7293	11.894	13.158	13.524	13.689	14.03	14.33	14.49	14.55	0.0	3,9
PMR 1	...	...	18.80	17.94	...	...	...	...	1.3	10
PMR 2	...	13.48	13.30	13.12	...	...	...	...	0.5	10

[a] References: 1. Ciardullo et al. (1999), 2. Acker et al. (1992), 3. SIMBAD, 4. Good et al. (2005b), 5. Tylenda et al. (1992), 6. Gathier & Pottasch (1988), 7. Acker & Neiner (2003), 8. Jacoby & Kaler (1989) and references therein, 9. Su et al. (2007) and references therein, 10. Morgan et al. (2001), 11. Passy et al, in prep., 12. Frew (2008). Note that values in parentheses are unreliable (see section 3.4 for more details) and are displayed in SEDs as open diamonds.

*JHK magnitudes are from 2MASS catalog, those marked with asterisk denote our own measurements using comparative photometry (see section 3.4 for notes on individual targets).

$^{+}$Extinctions marked with a + are adopted based on the optical portion of the SED.

Table 3.4. Gemini Observations Summary

PN Name	Filter	Exp. Time	Coadds	Repeats	UT Date	Telluric Standard
NGC 6369	J	10	1	20	07/05/09	HIP 87003
	H	10	1	20	07/05/09	HIP 87003
	K	10	1	20	07/05/09	HIP 87003
NGC 6751	J	10	1	10	07/06/09	HIP 91038
	H	10	1	10	07/06/09	HIP 91038
	K	10	1	10	07/06/09	HIP 91038
NGC 6905	J	20	1	10	07/06/09	HIP 98428
	H	20	1	10	07/06/09	HIP 98428
	K	20	1	10	07/06/09	HIP 98428
NGC 6804	J	10	1	30	07/05/09	HIP 95002
	H	10	1	30	07/05/09	HIP 95002
	K	10	1	30	07/05/09	HIP 95002
	L	1	10	10	07/05/09	HIP 95002
	M	0.4,0.2	50,100	10,10	07/05/09	HIP 99742
NGC 7139	J	120	1	30	07/05/09	HIP 114309
	H	120	1	30	07/05/09	HIP 114309
	K	120	1	50	07/06/09	HIP 107276

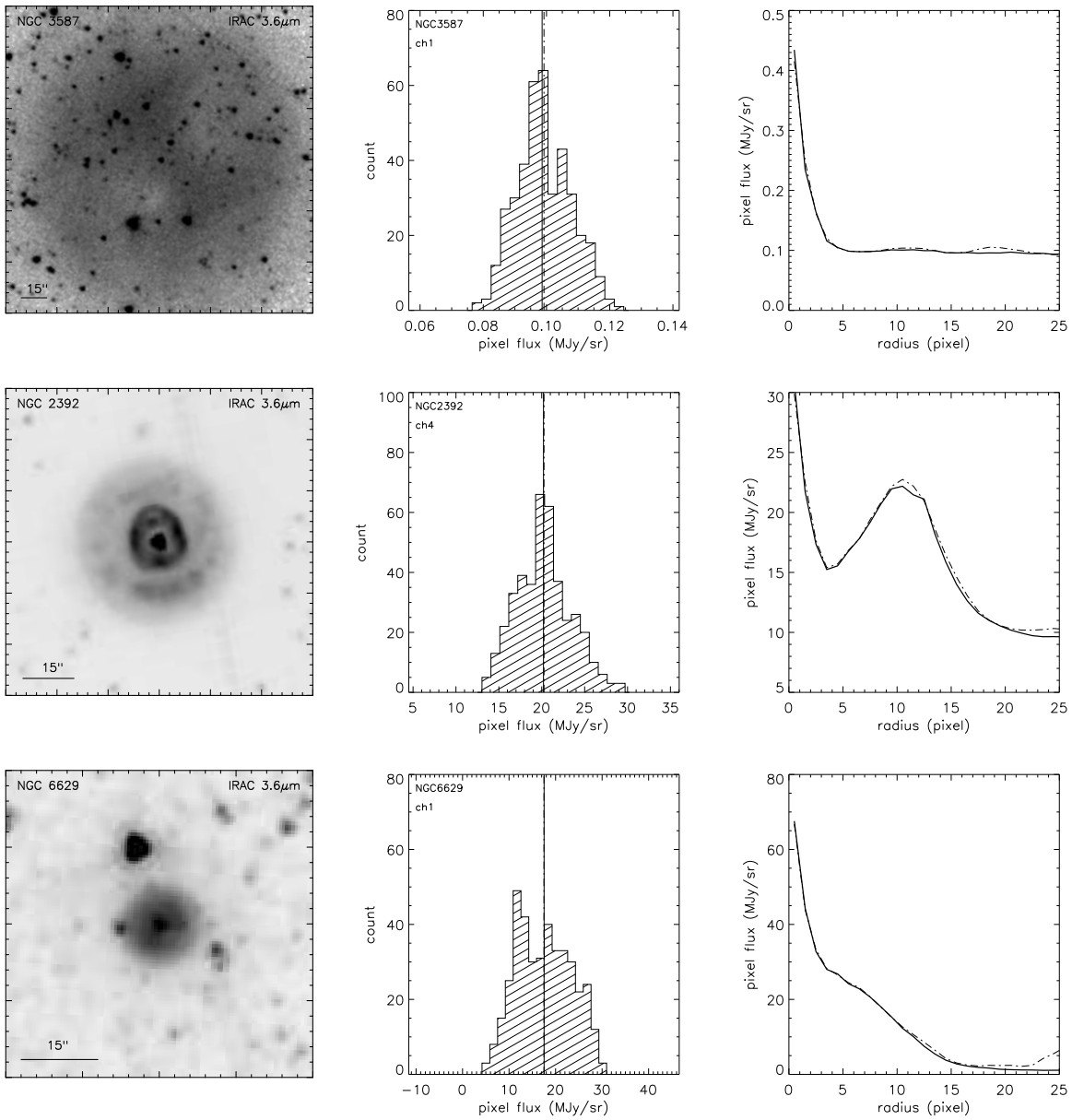

Figure 3.1: Images (left), histograms of pixel flux densities in the background annulus used for photometry (center), and radial profiles (right) of NGC 3587 (top) and NGC 2392 (bottom). The median of the pixel values is shown as a solid vertical line. The radial profiles show the median of the pixel fluxes as a thick solid curve, and the average value as a dot-dashed curve. For NGC 3587, the background is uniform, and the median in the background annulus gives a good estimate. On the other hand, for NGC 2392, the background increases radially outward from the CSPN Thus, using the median value from the histogram would result in over-subtraction of the background; using the minimum in the radial profiles gives a more accurate background level estimate. NGC 6629 is centrally peaked, and using the median value from the histogram would result in under-subtraction of the background; we estimate the range of background values based on the radial profile to find CSPN flux density. Note that using the median is better than using the average pixel fluxes for the radial profiles, because it avoids peaks caused by stars within the background annulus.

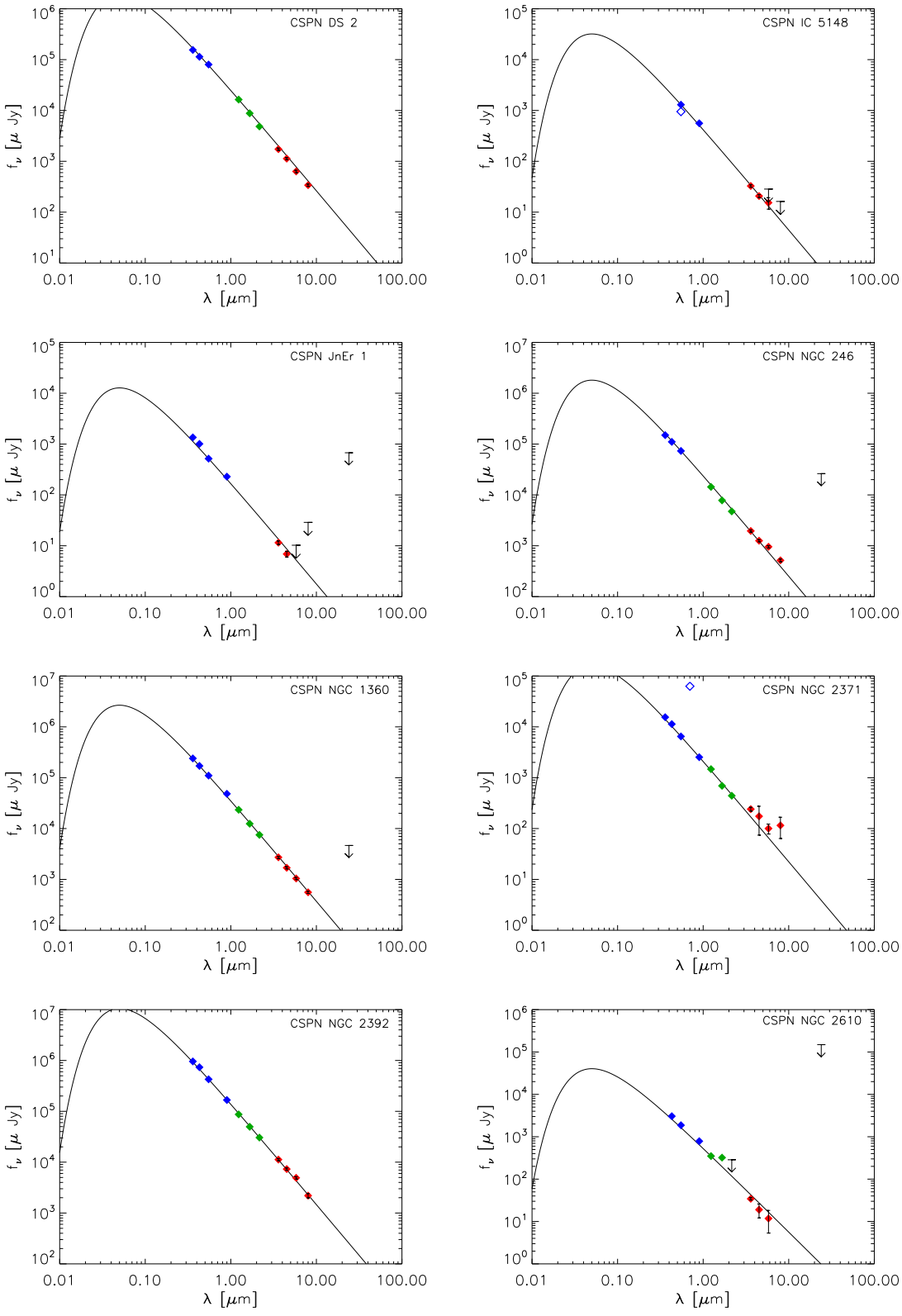

Figure 3.2: cont. on next page

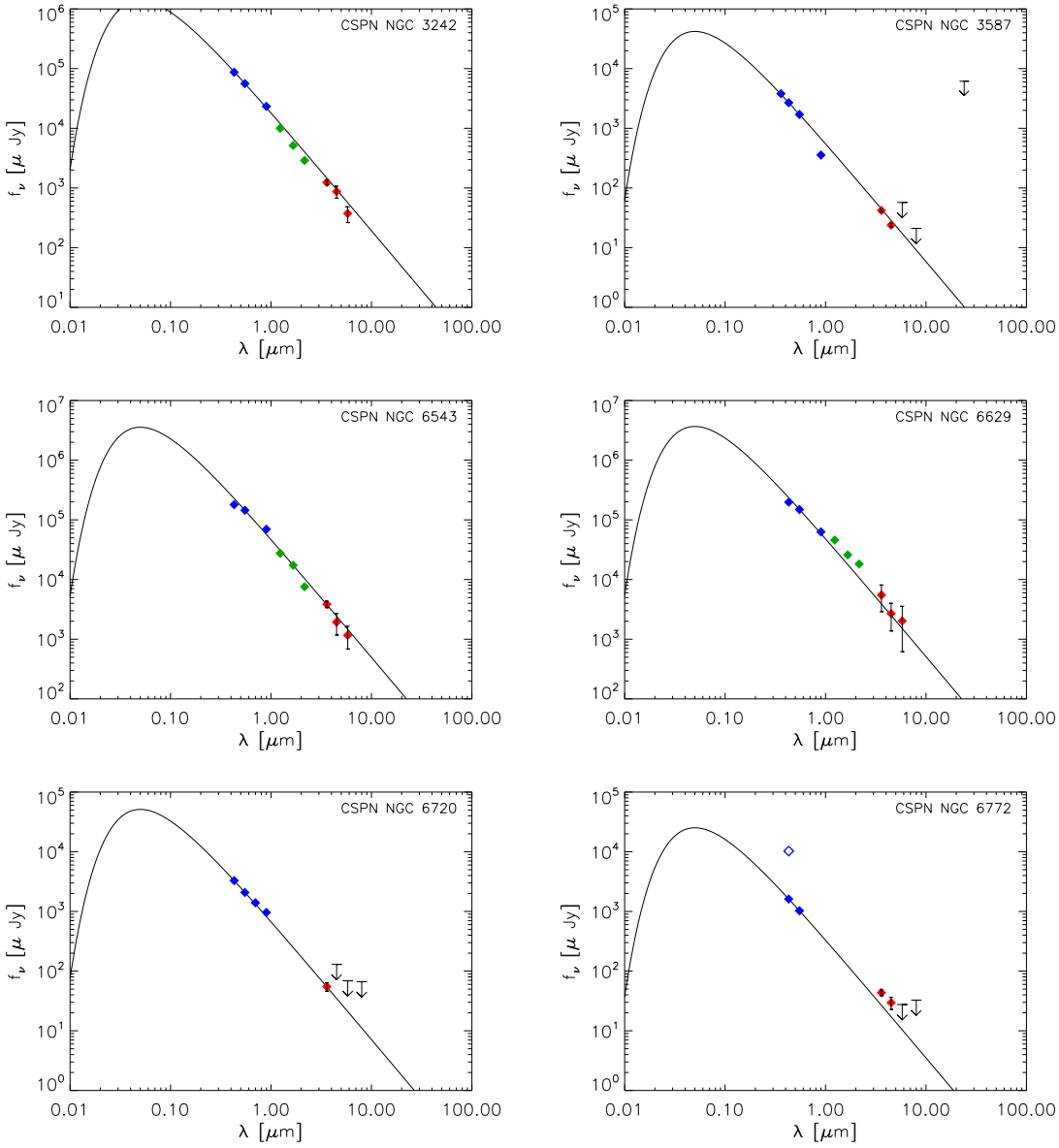

Figure 3.2: SEDs of CSPNs with no, unlikely, or uncertain IR excesses. The blue and green diamonds represent extinction-corrected optical and near-IR flux densities from literature and from the 2MASS catalog, which are listed in Table 3.3. IRAC and MIPS flux densities are shown as red diamonds, their values are listed in Table 3.2. Downward arrows represent the upper limits. A blackbody curve for the temperature of 100,000 K, normalized to optical or IR fluxes, is shown to guide the eye. For further details on each target, see section 3.4 .

Chapter 4

Spitzer Search for Dust Disks around Central Stars of Planetary Nebulae - Results and Discussion

4.1 CSPNs with IR Excesses

The CSPNs with IR excesses can be divided into four categories: (1) A companion accounts for all of the excess IR emission. (2) Free-free and line emission from stellar winds of [WC]-type CSPNs account for the IR excess, (3) The CSPN is a symbiotic star with a dusty disk, (4) An extended IR emitter, such as a dusty disk, is required to produce the observed excess emission. These four types will be described more closely in the following subsections.

4.1.1 Companions

Two CSPNs with IR excesses, A66 and NGC 650, have been previously reported to possess visual companions, and these companions can contribute to the excess IR emission. The visual companion of CSPN A66 was noted from ground-based observations, but Ciardullo et al. (1999) measured the surface density of field stars detected in their *HST* observation and concluded a rather high probability, 21%, for a random superposition of these two stars. The spectral type of the visual companion is unknown. To assess whether this companion can account for the observed excess, we estimate its V and I magnitudes from its $m_{\rm F555W}$ =18.424 and $m_{\rm F814W}$ =18.091 given in the Hubble Legacy Archive source catalog. The CSPN has V=18.17, I=18.29, $m_{\rm F555W}$ =18.287, and $m_{\rm F814W}$ =18.870. As the F555W and F814W bands are similar to V and I, respectively, we use $\Delta m_{\rm F555W}$ between the two stars to approximate the ΔV, and $\Delta m_{\rm F814W}$ to approximate the ΔI. Thus, the V and I magnitudes of the

companion are estimated to be V=18.3 and I=17.5.

Figure 4.1 shows the SED of CSPN A66. The extinction-corrected V and I magnitudes for the CSPN and its visual companion are plotted separately as filled diamonds and open triangles, respectively, and their sum is plotted as plus symbols. We have determined the extinction to the CSPN from the blackbody model fit to the SED (see section 3.4), and apply the same extinction correction for both sources[1]. A blackbody model of the CSPN's photospheric emission is shown in a black solid curve. We approximate the companion's photospheric emission with a T$\sim$7000 K blackbody, scaled to fit the V and I flux densities; shown in the SED as a dotted line. The sum of the CSPN's and companion's emission is plotted in a dashed curve. The combined SED fits the IRAC data points well; furthermore, the emission in IRAC bands is dominated by the companion.

The CSPN of NGC 650 has a visual companion which is itself a double. While the double might be a physical pair, it is unlikely to be associated with the CSPN (Ciardullo et al. 1999). The SED of CSPN NGC 650 is shown in Figure 4.1. The V and I magnitudes for the CSPN and its visual companions are plotted separately as filled diamonds and open triangles, respectively. A blackbody model of the CSPN's photospheric emission is shown in a black solid curve. As the spectral types, reddening, and the distance of the companion double are unknown, we model the SEDs of these two stars by blackbodies with a range of temperatures, and find that models with a temperature of $\sim$5800 K can simultaneously fit the V and I magnitudes of the companions. The blackbody curve for each companion is shown in the SED as a dotted curve. The sum of all three components, the CSPN and the binary companions, is shown as a dashed curve. It can be seen that the IRAC data points follow this dashed curve closely, suggesting that the excess IR emission can be accounted for by the photospheric emission of the CSPN's visual companions.

[1]The extinction of the companion is unknown. We have experimented with different extinction values and fitted a blackbody curve to the fluxes. In all cases, if we assume that the companion is a main-sequence star, the distance needed to produce the fluxes is always significantly higher than the CSPN distance. Therefore, the extinction is most likely similar to or higher than that of the CSPN A66.

4.1.2 [WC] Stars

Seven of our CSPNs with clear IR excesses (He 2-99, NGC 40, NGC 1501, NGC 6369, NGC 6751, NGC 6905, PMR 1) and one CSPN with probable IR excess (PMR 2) are [WC]-type stars (Fig. 4.2). They have prominent broad He and C emission lines in their optical spectra (e.g., Gorny & Stasińska 1995), which originate from the stars' strong, fast ($\sim 10^3$ km s^{-1}), optically thick stellar winds, which also give rise to free-free emission at IR wavelengths (Abbott & Conti 1987; Cohen et al. 1975). IR excesses of these stars are expected, as both the free-free emission and the strong emission lines contribute considerably to the emission at IR wavelengths. Furthermore, IR excesses due to circumstellar dust have been observed around late-type WC stars (Cohen et al. 1975). We expect the IR excesses of [WC]-type CSPNs to be combinations of free-free and line emission, and dust continuum.

Figure 4.5 shows Gemini near-IR (JHK) spectra of three [WC]-type CSPNs - NGC 6369, NGC 6751, and NGC 6905. The spectra show emission lines from, e.g., He II, C III, and C IV, many of which are blended together. The JHK bands contain many lines of these elements that are in common with those found in NIR line lists from Wolf-Rayet stars (e.g., Nishimaki et al. 2008). The most prominent lines in the three [WC] spectra in Figure 4.5 are at Si V 1.078 μm, He II 1.16 μm, C IV 1.19 μm, He II + C IV 1.736 μm, C IV 2.078 μm, C III 2.108 μm, and C IV 2.43 μm. In all three cases, a continuum component is clearly present. As these stars are not late-type WCs, this continuum is most likely dominated by free-free emission from the optically thick winds.

4.1.3 Symbiotic PNe

Two CSPNs from our archival study, M 2-9 and Mz 3, have very prominent IR excesses (Fig. 4.3). Corradi et al. (2010) characterize these as objects borderline between symbiotic stars and young PNe. They possess colors and some spectral features very similar to those of symbiotic stars, but lack others, preventing their classification as true symbiotics. Viironen

et al. (2009) characterize them as young PNe. We include these objects for comparisons of their IR excesses with those of other CSPNs.

Mz 3

Mz 3 is the Ant Nebula, a bipolar nebula known for its stunning and complex morphology, consisting of three pairs of nested bipolar lobes and an elliptical equatorial ring. Guerrero et al. (2004) have carried out a kinematical study of the different morphological components. The kinematics and morphology of Mz 3 is likely a result of recurrent outbursts, which can be produced in nova-like eruptions of symbiotic stars.

The high density of the nebular core, the IR colors and spectrum of the central star all suggest that Mz 3 is a symbiotic star (Zhang & Liu 2002; Schmeja & Kimeswenger 2001). Mid-IR observations of Mz 3 show an unresolved hot dust core component with a range of temperatures, likely originating from a circumstellar disk (Smith & Gehrz 2005); furthermore, silicate emission has been detected from this unresolved disk component (Chesneau et al. 2007). We approximate the central star with a blackbody of 35,000 K (Chesneau et al. 2007) normalized to the extinction-corrected B magnitude. The IR emission needs at least three blackbody components to reproduce the spectral shape. If we adopt the 360, 700 and 1400 K components, as plotted in Figure 5, the resulting luminosity fraction, $L_{\rm IR}/L_{\rm CSPN}$, is $\sim$0.55. The luminosity fraction is lower, $\sim$0.25, if we adopt the stellar luminosity of 10^4 $L_\odot$ and a distance of 1.4 kpc given by Chesneau et al. (2007).

M 2-9

M2-9, the Butterfly Nebula, is considered a spectroscopic twin of Mz 3 (Smith & Gehrz 2005). Both nebulae have a bipolar morphology with a dense core, and their SEDs are also very similar, with IR emission rising sharply from the near-IR. Lykou et al. (2011) report a disk inside this PN, similar to that in Mz 3.

The temperature of the CSPN is not well constrained, values between 15,000 and 42,000 K

have been reported (Gorny et al. 1997; Lykou et al. 2011). Furthermore, the distance to M2-9 is not well known, ranging from 0.65 to 3.7 kpc in the literature. We thus calculate only the luminosity fraction for comparison with other CSPNs with IR excesses, but do not report any distance-dependent parameters for M 2-9. Approximating the CSPN with a 35,000 K blackbody scaled to the V magnitude, we find a luminosity fraction of $\sim$4. If the IR emission is powered by stellar radiation, the IR luminosity clearly cannot exceed the stellar luminosity; thus there must be missing stellar flux unaccounted for by the small extinction reported by Ciardullo et al. (1999). Alternatively, if we adopt a central star temperature of 15,000 K, luminosity of 2500 $L_{\odot}$, and a distance of 1.2 kpc given by Lykou et al. (2011), the luminosity fraction becomes 0.33.

4.1.4 Dust Disks

Eight CSPNs, A21, DeHt 5, NGC 2346, NGC 2438, NGC 6804, NGC 6853, NGC 7139, and NGC 7293 have IR excesses that cannot be accounted for by a known or putative companion's photospheric emission (Fig. 4.4). An extended emitter, such as a dust disk, is required to account for the excess emission in the IR. While the SED does not provide constraints on the geometry of the IR emitter and a spherical dust shell can reproduce the SED as well as a dust disk, the small extinctions toward the majority of the CSPNs suggest that the dust is more likely to be distributed in a disk rather than a shell. Therefore, we assume that the IR emitters are all dust disks, and model their SEDs and determine their basic physical parameters.

For the CSPNs' photospheric emission, we use a blackbody model with observationally determined stellar effective temperatures from the literature. The normalization factor for matching the spectral model to optical and near-IR flux densities is (stellar radius/distance)^2. The stellar radii, determined from the normalization factors and distances reported in the literature, are mostly a few $R_{\oplus}$, consistent with the expectations for CSPNs. To match the excess emission in the IR SED, we use a single or multiple blackbody components (the

smallest number of components needed) with the dust temperatures ($T_{\rm d}$), emitting areas (A), and PN distances listed in Table 4.3. We further calculate the dust's equilibrium-temperature distance ($r_{\rm d}$) from the CSPN luminosity ($L_{\rm CSPN}$) and the dust temperature, and determine the fractional luminosity, $L_{IR}/L_{\rm CSPN}$, where L_{IR} is the luminosity of the IR emitter.

The following subsections discuss individual CSPNs in detail, except for NGC 7293, which has been reported by Su et al. (2007), and A21, which has been reported by Chu et al. (2011).

DeHt 5

DeHt 5 (Fig. 4.6) is an old PN that shows evidence of interaction with the ISM (Tweedy & Kwitter 1996). Its morphology is dominated by bright filaments toward the north of the CSPN, surrounded by fainter diffuse material. In the MIPS 24 μm image, the morphology is dominated by a bright filament near the central WD and extended diffuse material. Good et al. (2005b) carried out UV spectroscopy to search for radial velocity variations indicative of a companion, but none were found.

The SED (Fig. 4.4) shows excess IR emission at 8 and 24 μm. We approximate the WD photospheric emission by a blackbody with an effective temperature of 76,500 K (Napiwotzki 1999), at a distance of 345 pc (Benedict et al. 2009). The WD radius required for the emission to fit the optical and near-IR fluxes is $\sim$2.37 $R_{\oplus}$, within the range expected for WDs. The excess emission can be modeled with a single blackbody component with a temperature $T_{\rm d}$ of 190 K and an emitting area of 0.25 AU^2, and $r_{\rm d}$ of 8.2 AU. The temperature and the emitting area cannot be accounted for by any stellar or substellar object; therefore, an extended object, such as a dust disk, is required to produce the observed excess emission. The fractional luminosity, 7.3×10^{-5}, is similar to those of dust disks around hot WDs reported by Chu et al. (2011).

NGC 2346

NGC 2346 (Fig. 4.7) is a bipolar PN, well-known for harboring a single-line spectroscopic binary at its center (Mendez & Niemela 1981). The CSPN has also been observed to vary photometrically at optical (Mendez et al. 1982) and near-IR (JH) wavelengths (Roth et al. 1984). The IR excess of this CSPN in the 1–10 μm range has been reported by Cohen & Barlow (1975), and the MIPS 24 μm observations were presented by Su et al. (2004). The 24 μm image shows an unresolved hot dust component at the central source, and this hot dust cloud has been suggested to cause the fading events of the CSPN in 1981-1985 and 1996-1997 (Costero et al. 1986; Kato et al. 2001). In addition, Su et al. (2004) report a dusty torus-like structure, with r$\sim$20$''$, surrounding the central source.

Due to the changes in optical and IR fluxes, sometimes by almost $\sim$3 magnitudes (Mendez et al. 1982), the SED is complex and difficult to model. For comparison, we plot the lowest flux densities from Mendez et al. (1982) and Roth et al. (1984) as open diamonds in the SED (Figure 4.4). The SED is simulated with a blackbody curve for a hot subdwarf with an effective temperature of 100,000 K and a radius of 0.03 $R_{\odot}$ (or 3.3 $R_{\oplus}$) and an A-type main sequence companion with an effective temperature of 8200 K and radius of 1.9 $R_{\odot}$, at a distance of 800 pc (Acker et al. 1998; Su et al. 2004). The data points do not follow the combined curve well, but it is without doubt that the CSPN shows excess emission in the near-IR, in all IRAC bands, and at 24 μm.

We approximate the excess emission by two blackbody components at different temperatures. The warmer component has a $T_{\rm d}$ of $\sim$1000 K, A of 2.2 AU^2, and corresponding $r_{\rm d}$ of 0.7 AU. The cooler component has a temperature $T_{\rm d}$ of 250 , emitting area A of 37 AU^2, and $r_{\rm d}$ of 11 AU. The total luminosity fraction, calculated using both stellar components and both dust components, is $\sim$0.08, much higher than those of dust disks reported by Chu et al. (2011). The IR excess is likely due to the dust cloud proposed to have caused the fading of the CSPN, and the torus reported by Su et al. (2004). The separation of the binary is

small ($\sim$0.16 AU) compared to the dust's $r_{\rm d}$; therefore, the dust is likely circumbinary.

The IRS spectra of the CSPN is shown in Figure 4.8. The low-resolution spectra are multiplied by a factor of 1.15 to join smoothly the high-resolution spectra. This adjustment is necessary because the central source is slightly extended (Su et al. 2004), and the spectra in different modules are extracted with different aperture areas.

At wavelengths $\leq$15 μm, the background-subtracted spectrum is dominated by continuum, with some residual line emission. The spectral image in Figure 4.8b shows clearly that the continuum emission is dominant and that the line emission is more extended than the continuum emission. Figure 4.8c shows the surface brightness profiles of the continuum emission (8–13 μm), and at [S IV] 10.51 μm and [Ne II] 12.81 μm lines, extracted from the IRS SL1 data cube. Note that the surface brightness profiles at spectral lines also contain the underlying continuum emission at their respective wavelengths. The continuum emission in fact dominates the shapes of the surface brightness profiles at the spectral lines, and the diffuse nebular line emission is evident only in the extended wings of these profiles.

At wavelengths >15 μm, the background-subtracted spectrum shows a continuum weaker than that at shorter wavelengths, and very strong residual line emission of [Ne III] 15.55 μm and [O IV] 25.89 μm; and moderately strong residual line emission of [S III] 18.71 μm, [Ne V] 24.32 μm, and [S III] 33.48 μm. The raw spectral image, presented in Figure 4.8c, shows that the line emission is more extended than the continuum, with higher-ionization line emission more concentrated toward the center than the lower-ionization line emission. To illustrate the spatial distribution quantitatively, normalized surface brightness profiles of [S III] 33.48 μm, [O IV] 25.89 μm, [Ne V] 24.32 μm and continuum emission (20–35 μm) are shown in Figure 4.8d. This relative distribution of high- and low-ionization lines is expected in the ionization stratification of the PN.

NGC 2438

NGC 2438 (Fig. 4.9) is a multiple-shell PN superposed on the star cluster M46. The outer halo with angular diameter of $\sim 5'$ is clearly seen in the IRAC 8 μm image (Chu et al. 2009). It is difficult to assess whether the SED shows excess emission in the J band, because the optical data points reported in the literature are varied (see section 3.4). Furthermore, the CSPN is near a bright star, which may be contaminating the CSPN's J-band photometry. Excess emission in the IRAC bands is nevertheless evident, and the flux density at 24 μm is several orders of magnitude higher than the expected CSPN's contribution (Chu et al. 2011).

To assess the nature of the IR excess, we have obtained *Spitzer* IRS 7–14.5 μm spectrum of the PN. The IRS spectra extracted at the position of CSPN NGC 2438 and adjacent background regions are shown in Figure 4.10a,b. Both spectra are dominated by nebular emission lines of [Ar III] 8.99 μm, [S IV] 10.51 μm, [Ne II] 12.81 μm, [Ar V] 13.10 μm, and [Ne V] 14.32 μm. The background-subtracted spectrum shows weak but rising continuum emission, in addition to dips at the wavelengths of [Ar III], [S IV] and [Ne II], and residual line emission at [Ar V] and [Ne V]. These residual line features stem from imperfect background subtraction, as can be seen from the surface brightness profiles of the continuum and line emission along the slit (Fig. 4.10c). The emission line surface brightness profiles are consistent with the ionization stratification in the nebula: the high ionization lines such as [Ne V] and [Ar V] peak near the center of the nebula, and the lower ionization lines peak further away from the CSPN; thus, the high ionization lines are under-subtracted, while the low ionization lines are over-subtracted. The continuum emission peaks at the CSPN and is not extended (FWHM$\sim 5''$); therefore, it likely originates from an unresolved source. The surface brightness profiles thus suggest that the unresolved IR excess is continuum in nature, whereas the emission lines originate from the extended nebula. The surface brightness profiles do not reveal an unresolved emission-line source at the CSPN.

To estimate the physical parameters and the origin of the the IR emitter, we model the SED using the CSPN's effective temperature of 114,000 K (Rauch et al. 1999), and a distance of 1200 pc (Phillips 2004). For this blackbody emission to fit the V magnitude, the required radius of the CSPN is $\sim$4.5 $R_{\oplus}$; this is within the range of radii expected for CSPNs. The excess IR emission cannot be modeled by a single blackbody component; two temperature components are needed. The excess emission in the IRAC bands needs a warm component with a temperature of $\sim$1200 K, $r_{\rm d}$ of 0.9 AU, and an emitting area of $\sim 5\times10^{-4}$AU^2, or $\sim$24 $R_{\odot}^2$. Brown dwarfs may have such effective temperatures, but their surface areas are considerably smaller; therefore, an extended dust cloud or disk is needed to account for the excess emission seen in the IRAC bands. However, if we normalize the CSPN's photospheric emission to one of the fainter V magnitudes, then the excess emission in the J and IRAC 3.6 – 4.5 μm bands may be provided by a late M dwarf, but the excess in 5.8–8.0 μm would still persist. The excess emission from these wavelengths up to 24 μm requires a cooler component with a temperature of $\sim$150 K and an emitting area of $\sim$57 AU^2. Such temperature and area cannot be provided by any stellar or substellar object; only an extended emitter, such as a dust disk can produce this emission. The equilibrium-temperature distance $r_{\rm d}$ for 150 K is $\sim$56 AU from the CSPN. Note that the dust continuum at 24 μm may be overestimated because of the contamination of the [O IV] 25.89 μm line, in which case, the dust parameters need to be adjusted accordingly. The combined luminosity fraction, $\sim 3.7\times10^{-4}$, is slightly smaller than that of the IR emitter in the Helix Nebula.

While it is unclear whether the warm component originates from a stellar companion or a warm dust disk close to the CSPN, an extended disk of cooler dust is needed to explain the 24 μm emission. Better sampling of the fluxes at optical and near-IR wavelengths is needed to establish the CSPN's photospheric emission so that more accurate modeling of the SED can be performed.

NGC 6804

NGC 6804 (Fig. 4.11) is a multiple-shell PN with ansae protruding from the middle shell along the shell's major axis. Spatially resolved kinematic information suggests that the nebula is moving toward southwest, and is interacting with the ISM (Guerrero et al. 1998). Prominent IR excess is seen in the entire 1 – 8 μm JHK and IRAC range as well as in our follow-up MIPS 24 μm photometric measurements.

Our follow-up Gemini NIRI 1–5 μm and Michelle 7–14 μm spectra are shown in Fig 4.12. The spectra in individual bands are scaled so that the continuum varies smoothly across the different bands and follows the JHK and IRAC flux densities. The spectrum reveals a rising continuum, as well as emission lines from this compact source. In the J band, the most prominent line is a He I 1.08 μm line; we also detect He I + He II 1.09 μm line, He II 1.16 μm line, and H I + He II 1.28 μm line. The line emission in the H band is considerably weaker than that in the J band. The H band spectrum shows the H Brackett series, and the He I 1.701 μm line. The K band shows only one prominent emission line, H I 2.166 μm (Brγ). In the L band, we detect H I 3.74 μm (Pfγ) and H I 4.05 μm (Brα) line. The M band spectrum in Fig. 4.12 is smoothed; it only shows one emission line at $\sim$4.51 μm, probably corresponding to He II 4.508 μm line. This line is near the edge of the filter, where the transmission is lower and the noise is higher, however, the line appears weak but real in the raw image of the spectrum. The Michelle 7–14 μm spectrum is also smoothed, and exhibits a 10 μm silicate emission feature.

In Section 2.3, we have examined the FWHM of the central source in the MIPS 24 μm image and determined that it is an unresolved point source. This conclusion is supported by the Michelle acquisition images, in which the Gaussian fit to the CSPN's profile has a FWHM of $\sim$3.8 pixels ($\sim$0$''$.38), whereas the FWHM of the standard star is $\leq$0$''$.42, and the telescope diffraction limit 0$''$.34.

The CSPN's photospheric emission was modeled using a 86,000 K blackbody at a distance

of 1320 pc (Phillips 2003, 2004). The stellar radius required to fit the optical fluxes is ∼0.1 $R_{\odot}$ (or 28 $R_{\oplus}$), rather large, but within the range expected for CSPNs. Model fits of the IR excess require three components with $T_{\rm d}$ of ∼1400 K, ∼550 K, ∼250 K, A of 0.1, 6 and 155 AU^2, and $r_{\rm d}$ of 2.5, 16 and 77 AU, respectively. The need for multiple temperature components indicates that there is likely a range of dust temperatures present. The hottest of the three components reaches a temperature of a brown dwarf; however, the required emitting area corresponds to a spherical surface area for R ∼21 $R_{\odot}$, too large for a brown dwarf. Furthermore, *HST* imaging has not revealed any companion (Ciardullo et al. 1999).

NGC 6853

NGC 6853 (Fig. 4.13) is the well-known Dumbbell Nebula. Its 8 μm image shows an impressive morphology of radial spokes of molecular hydrogen emission (Manchado et al. 2007). Its CSPN is WD 1957+225. Cudworth (1973) has reported a faint visual companion at 6$\farcs$5 from the CSPN and suggested a physical association between them based on their common proper motion. The field of view towards NGC 6853 is crowded, and, based on star counts, Ciardullo et al. (1999) estimate a likelihood of 90% that a field star would be projected at that distance. In addition, Ciardullo et al. (1999) identify a V≈18.7 star 1$\farcs$1 from the CSPN to be a more likely candidate for a companion based on star counts, although the chance for a random superposition is still as high as 12%. The physical association between the CSPN and any stars projected in the vicinity has not been proven to date, and additional radial velocity observations are suggested to support the association of the two stars. Benedict et al. (2009) have analyzed the *HST* Fine Guider Sensor imaging fringes, but have not resolved any close companions.

The IR SED shows slight excess from 1–4.5 μm, and the flux densities rise sharply at 5.8 – 24 μm. The near-IR excess is due to the above-mentioned star 1$\farcs$1 from the CSPN (Ciardullo et al. 1999), which is not resolved by IRAC. We model the CSPN's photospheric emission by a blackbody with an effective temperature of 108,000 K (Napiwotzki 1999) at

a distance of 405 pc (Benedict et al. 2009). The IR emitter responsible for the emission longward of 4.8 μm has a temperature of 190 K and an emitting area of $\sim$5 AU^2. This area can only be provided by an extended object, such as a dust disk. The equilibrium distance is $\sim$25 AU, which corresponds to 0$''$.062 at the PN's distance and cannot be resolved by *Spitzer*. The central source appears to be slightly extended at 24 μm, with a FWHM of $\sim$11$''$.2, about twice the FWHM of a point source. At 70 μm, no point source at the CSPN can be recognized against the bright nebular background. High-resolution images at 24 μm are needed to determine whether the central source consists of an unresolved point source superposed on an extended component. Furthermore, spectral observations are needed to determine the relative contributions of line emission and continuum to the IR excess.

NGC 7139

NGC 7139 is a roughly spherical PN with an inner bipolar core (Stanghellini et al. 2002). As shown in Fig. 4.14, the round nebular rim has a fainter bipolar extension along the NE-SW direction. The MIPS 24 μm image shows clearly the bipolar structure in the core and two additional ansae. None of the axes of these bipolar features are aligned. The SED shows excess emission in all of the JHK and IRAC bands with a declining slope in the IRAC wavelengths. The CSPN is not detected at 24 μm, as the bipolar nebular emission by far dominates the flux in the central region.

We have obtained Gemini NIRI 1–2.5 μm spectra and *Spitzer* IRS 5–15 μm spectra of the PN in order to determine the nature of the IR emitter. The Gemini NIRI spectra of CSPN NGC 7139 are shown in Figure 4.15e. Note that the flux calibration of Gemini long-slit data is not absolute, and it is recommended to flux-calibrate the spectra using complementary photometric measurements. We use our own JHK measurements (see section 3.4) to perform flux calibration, but this calibration is rough, as the S/N ratio for 2MASS photometry is less than 3σ. The near-IR spectrum is dominated by continuum in all bands; the continuum rises in the J and H bands, and is flat in the K band. In the J band, He I 1.08 μm,

H I + He II 1.282 μm lines are detected; no emission lines are detected in the H band; and in the K band, a very weak line at 2.16 μm can be attributed to H I and He II emission.

The IRS spectra extracted from CSPN NGC 7139 and adjacent background regions are shown in Figures 4.15a,b. The most dominant features in all these spectra are the emission lines of [Ar III] 8.99 μm, [S IV] 10.51 μm, and [Ne II] 12.81 μm. The background-subtracted IRS spectrum of NGC 7139 shows a weak continuum component, and residual line emission in the [Ne II] 12.81 μm line.

To examine the nature of the residual line emission, we compare the spatial distribution of the continuum and line emission. Figure 4.15d shows surface brightness profiles along the slit for the continuum, [Ne II], [Ar III] and [S IV] lines. It is evident that the continuum originates from a point source, the CSPN. The line emission shows an extended component that originates from the PN, as well as a small peak near the CSPN. For the [Ar III] and [S IV] lines, the width of the small peaks is the same as the width of the continuum emission (FWHM$\sim$5$''$), and the height of the peaks above the underlying extended background is similar to that of the continuum component. It is probable that this small peak is caused by the continuum contribution at the wavelengths of the [Ar III] and [S IV] lines. The [Ne II] line also shows a centrally peaked component in addition to the extended PN emission, but its height and width (FWHM$\sim$10$''$) are greater than those of the continuum. In addition, the peak of the central [Ne II] emission appears slightly offset from the position of the CSPN. The [Ne II] residual emission is therefore due to a real enhancement near the CSPN, and not the result of imperfect background subtraction or from the continuum's contribution. The CSPN of NGC 7139 is a hot ($T_{eff}\sim$117,000 K, Gorny et al. 1997) star, and this low-ionization line emission is not expected to be detected so close to the CSPN. It is possible that the [Ne II] emission originates from the circumstellar material of a cooler companion. High-resolution images in continuum and low-ionization lines are needed to confirm the existence of this companion and determine the origin of the [Ne II] emission.

To model the SED, we adopt a distance of 2400 pc (Frew 2008) and a stellar effective

temperature of 117,000 K (Gorny et al. 1997). A ∼1650 K blackbody with emitting area of ∼0.004 AU^2, or 186 $R_\odot^2$, and $r_{\rm d}$ of 0.25 AU can fit the JHK and IRAC fluxes. While brown dwarfs may have such effective temperature, the required radius of the star is ∼4 $R_\odot$, much higher than the range expected for brown dwarfs. The temperature of 1650 K is near the dust sublimation temperature (∼1500–1700 K, depending on composition). It is possible that the excess is a combination of the emission from a companion and a dust disk near the sublimation temperature. No companion star of CSPN NGC 7139 has been reported to date.

4.2 Discussion

4.2.1 Statistical Properties

We have examined 72 PNe in this paper. Of these, 56 were extended enough to allow visual inspection whether the CSPN is detected against the nebular background. In 42 cases, the CSPN is visible and selected for photometric measurements. Therefore, we use the sample of 56 PNe to assess the IR excess detection rate. A summary of the statistics of our detections is presented in Table 4.1. Out of the 56 PNe, we find 19 cases, or 34%, with IR excess. Seven of these excesses are from [WC] CSPNs, six of which were observed in a single program targeting these stars. Two of the excesses were due to projected companions and were not physically associated with the CSPNs. Excluding the [WC] CSPNs from our sample, the detection rate of dusty IR excesses is 20% (=(8+2)/(56-7)). This rate includes the excesses of CSPNs Mz 3 and M2-9, whose status as PNe may be controversial. Without these two targets, the detection rate of dusty IR excesses is 17% (=8/(56-7-2)).

The detection rate of the IR excesses of CSPNs from Chu et al. (2011) is similar, 7 out of 35, or 20%, all of which are likely from dust disks. Table 4.1 also summarizes the statistics of the two surveys combined, taking into account the overlaps between the two samples. For the combined sample of 84 PNe (and excluding the [WC] stars), the total detection rate of

dusty IR excesses is 17–19%, depending on whether the two symbiotic PNe are included.

Figure 4.16 shows the distribution of the distances of CSPNs from this archival search with dusty IR excesses, [WC] CSPNs and the CSPNs without IR excesses. While equal numbers of dust disk excesses are found in each distance bin, the [WC]s and CSPNs without IR excesses are distributed at distances greater than 500 pc, almost half of them farther than 1500 pc. The median distance of CSPNs with IR excesses due to dust disks, ∼900 pc, is smaller than that of CSPNs without IR excesses, ∼1300 pc. The distribution of CSPNs with dusty IR excesses being closer compared to those without IR excesses may indicate that the detection of IR excesses at greater distances is limited by sensitivity.

4.2.2 Physical Parameters of CSPN with IR Excesses

The goal of our *Spitzer* archival survey of CSPNs is to search for dust disks that could potentially be formed through collisions, sublimation, or tidal disruption of subplanetary bodies. We therefore do not further discuss the IR excesses of [WC] CSPNs or the symbiotic CSPNs Mz 3 and M2-9, as the origins of these are known to be different. We also will not discuss the CSPNs A 66 and NGC 650 for which the IR excesses can be explained by visual companions. The remaining CSPNs with IR excesses are indicative of circumstellar dust emission. For completeness, we will discuss these objects in conjunction with those reported by Chu et al. (2011) and Su et al. (2007).

All of the above CSPNs with IR excesses originating from circumstellar dust are listed in Table 4.2, which summarizes their SED and spectral properties. Checkmarks in columns 2–7 indicate the presence of excess IR emission in any of the JHK bands, the four IRAC bands, and the MIPS 24 μm band. Columns 8–11 remark on the spectral features exhibited in four spectral ranges observed with different instruments. Column 12 notes known close or wide binary companions of the CSPNs. The SED characteristics of this group of CSPNs are varied. First, the onset of the excess can occur at different wavelengths, indicating different upper limits to the IR emitters' temperatures. For example, some SEDs display IR

excess starting from >5 μm (e.g., DeHt 5 and NGC 6853), while others show excess emission starting from shorter wavelengths, even from JHK bands (e.g., NGC 6804 and NGC 7139). Second, the IR excess may peak at different wavelengths, for instance, the IR emission of NGC 7139 peaks near 2–3 μm, and that of DeHt 5 peaks at wavelengths $\geq$24 μm. Third, the slope of the IR excess can vary continuously (e.g., NGC 6804), or abruptly, indicating the presence of more than one distinct IR emission component (e.g., NGC 2438).

Ten CSPNs with dusty IR excesses have spectra available, taken in one or more of the following wavelength bands: Gemini NIRI JHK 1–2.5 μm, LM 3–5.5 μm, Michelle N 7–14 μm, *Spitzer* IRS 5–15 μm, IRS 15–35 μm. In all cases, the spectrum is dominated by continuum emission. No unresolved circumstellar line emission is seen in the IRS spectra, except in the case of NGC 7139, where the slightly resolved [Ne II] line emission may contain a compact off-center circumstellar component. Unresolved H and He line emission is also seen in NIRI JHK and LM spectra of NGC 6804 and weakly in NGC 7139, in addition to the continuum emission. NGC 6804 exhibits a 10 μm silicate feature (which appears to be crystalline), but none of the other CSPNs exhibit any mineralogical features.

To investigate the origin of the IR excesses and possible relationship among IR excesses with varied SED shapes and spectral characteristics, we compare the physical characteristics of the CSPNs with the physical parameters of the IR emitters (see Table 4.3, which is ordered based on the luminosity fraction $L_{\rm IR}/L_{\rm CSPN}$). The effective temperatures, surface gravities, masses and distances are from literature, while the the stellar radii ($R_{\rm CSPN}$) are computed from the SEDs, based on the distances, effective temperatures and available optical flux densities. Stellar luminosities ($L_{\rm CSPN}$) are computed using distances, effective temperatures, and $R_{\rm CSPN}$, while $L_{\rm IR}$ values are derived from the IR flux densities and distances. The table also lists $L_{\rm IR}/L_{\rm CSPN}$, the luminosity fractions. Where available, we also list the dynamical and/or evolutionary ages of the PNe from the literature.

In Figure 4.17, the physical parameters of the CSPNs (temperature, dynamical age, luminosity) are plotted against the physical parameters of the IR excess emitters (luminosity

fraction, IR luminosity). We do not see any obvious correlations between the physical parameters of the CSPNs and the IR emitters. We do however see that NGC 6804 and NGC 2346, with their high IR luminosities, are outliers to the loci of the remaining CSPNs on the $L_{\rm IR}$ versus $L_{\rm CSPN}$ plot. Their luminosity fractions are still 1–3 orders of magnitude lower than those of the two symbiotic CSPNs. NGC 2346's central star is known to be a close binary and it also possesses a circumstellar dust cloud, and possibly a dust disk, which all contribute to the high IR excess. NGC 6804 is an outlier in many ways. First, unlike most of the CSPNs, it shows strong unresolved H and He lines coincident with the CSPN, and, unlike any of the CSPNs, its spectrum displays a 10 μm silicate dust feature. Its CSPN has the largest radius and the highest luminosity, and the lowest evolutionary age, $\sim$6200 years, among all CSPNs with IR excesses. Its $T_{\rm eff}$ and $L_{\rm CSPN}$ place it on the bend of the evolutionary track in the HR diagram, before the WD cooling track, unlike the remaining CSPNs, which are all on the WD cooling track.

NGC 6804 is clearly the least evolved CSPN in our sample, and it has the second highest luminosity fraction. It is worth noting that Chu et al. (2011) have detected 24 μm excesses of, in addition to CSPNs, two hot WDs that are not surrounded by known PNe, and are thus the most evolved. These were found to have the the lowest $L_{\rm IR}/L_{\rm WD}$ ratios in the sample. While these extreme cases suggest that the luminosity and luminosity fraction of the IR emitter decrease with age, there is no obvious correlation between ages and IR luminosities or luminosity fractions and the CSPN ages from the literature for the intermediate cases. It should be cautioned, however, that the age estimates may be quite uncertain because they require known distances.

The uncertainty in PN distances also affects the determination of CSPN's and IR emitter's physical characteristics. Distances derived from parallaxes are least controversial; thus, we adopt the parallax distances for A21, Sh 2-216, DeHt 5, NGC 6853, and NGC 7293. The remaining distances are derived from the following methods: statistical distance, spectroscopic distance of the CSPN, Shklovski method, interstellar NaD absorption and galactic

rotation, and spectroscopic parallax of a CSPN's main sequence companion. Each of these methods may have significant uncertainties and often the various reported values differ by a factor of 2 or more; furthermore, spectroscopic distances are known to be systematically greater than the parallax distances. For a discussion of distance measurements of PNe, see e.g. Napiwotzki (2001). The uncertainty in the distance is propagated into the calculation of radius and luminosity of the CSPN, as well as the luminosity of the IR emitter. The stellar mass determination depends on the quality of spectroscopic data and the accuracy of model atmosphere fits. The physical parameters listed in Table 4.3 are taken from various sources and are determined with different techniques and data sets. A set of physical parameters derived from a uniform data set and using a common method (see e.g., Frew 2008) would allow for a more meaningful comparison.

4.2.3 Origins of IR excesses

The IR excess of the Helix CSPN was suggested to originate from collisions among planetesimals (Su et al. 2007). With a larger sample of CSPN excesses and their varied characteristics, one needs to consider other possible mechanisms that could be responsible for producing the excess IR emission. It is unclear whether the observed differences in SED and spectral characteristics of CSPNs' IR excesses are due to different physical origins, different evolutionary stages, or a combination of both. We present two most likely scenarios for the origins of IR excesses in the following subsections.

Subplanetary Bodies

The destruction of subplanetary bodies has been proposed as dust generation mechanism for disks around old, cool WDs via tidal disruption of asteroids, and for the disk around the Helix Nebula's CSPN via collisions among KBOs (see Section 1). Tidally crushed asteroids are unlikely to have produced IR excesses of CSPNs. The Roche radii for a density of 2.5 g cm^{-3}, typical for asteroids, (e.g., Britt et al. 2005), are <0.01 AU for our stars, whereas the

equilibrium distances for the hottest temperature components are all greater than 0.25 AU (see Table 4.3). Furthermore, the effective temperatures of CSPNs are significantly higher (>80,000 K) than those of the cool WDs, and dust within the Roche limit would sublimate.

The fact that some very old WDs (age∼Gyr) have disks of tidally shredded asteroids does support the survival of planetesimal bodies, because a reservoir is needed to supply material that is eventually disrupted by tidal forces. While the presence of planetesimal bodies is likely, the question whether enough collisions occur to account for the observed dust and reproduce the observed SEDs is not yet fully answered.

Collisions among subplanetary objects provide a feasible mechanism to produce dust around CSPNs. Dusty debris disks have been observed around main sequence stars, and the dust was suggested to be produced by collisional cascades within planetesimal belts (e.g., Rieke et al. 2005). The mid-IR spectra of the majority of debris disks around main-sequence stars are featureless (Chen et al. 2006), similar to the mid-IR spectra of most CSPNs with IR excesses in our sample. Bonsor & Wyatt (2010) simulated the steady-state collisional evolution of a debris disk around a main-sequence A-type star into the late stages of stellar evolution, considering the effects of collisions, radiation pressure, stellar wind drag, sublimation, and Poynting-Robertson drag on the debris disk. In general, collisional lifetime increases as the star loses mass, and thus the dust generation rate, and consequently the detectability, decreases. They investigate the detectability of such disks and find that only the youngest WDs which are relatively close (∼200 pc) should have disks luminous enough to be detected. While their models are in line with the detection of the Helix CSPNs dust disk, most of our targets are much further than 200 pc. On the other hand, many of our targets are not yet WDs.

Dong et al. (2010) examine the dynamical evolution of a debris disk along with its parent star's evolution past the main sequence for a case in which the star also possesses a gas giant planet. According to their models, as the star loses mass, the planet's orbit expands, and it may sweep up sub-km-size planetesimals onto mean-motion resonance orbits, and

the planetesimal orbits become slightly eccentric. Disruptive collisions among planetesimals can then produce dust grains that may be observable in the IR. Their models are able to reproduce the amount of dust around the CSPN of the Helix Nebula.

To investigate the evolution of dust disks' frequency of occurence, better knowledge of CSPN's evolutionary status is necessary. Further modeling of the SEDs and better estimates of the disks' physical parameters, such as dust mass, grain sizes, and radial location will also be needed to compare to the model predictions. We defer this work to a later paper.

Binary Interactions

Another possible scenario is that the dust disks around CSPNs are associated with a binary companion. Many post-AGB stars exhibit IR excesses that imply the presence of hot, 500–1300 K dust, in addition to the cooler, 100–200 K, expanding dust shell (Trams et al. 1991; Waters 1993; Van Winckel et al. 1999). Radial velocity observations of these stars show that the presence of hot dust component is tightly correlated with the presence of a binary companion (Waters et al. 1997; Van Winckel et al. 1999), suggesting that hot dust disk remains in the system because it is trapped in a stable circumstellar or circumbinary orbit, and this dust disk was probably formed in binary interactions. Such stable Keplerian-rotating dust disks seem to be very common among binary post-AGB stars (de Ruyter et al. 2006).

It may be possible that the dust trapped in post-AGB binary system persists into the CSPN stage, which immediately follows the post-AGB. Interestingly, the 24 μm survey of Chu et al. (2011) targeted hot WDs with and without PNe, and they found that seven of the nine showing 24 μm excess are still in PNe, and two without PNe have the weakest 24 μm excess. Moreover, the IR emitter of CSPN NGC 2346, a known close binary, has the highest luminosity among our targets, and its luminosity fraction, $\sim$0.09, approaches that of post-AGB binaries of de Ruyter et al. (2006) and the symbiotic CSPNs. The CSPN with the second highest IR luminosity, NGC 6804, is the least evolved in our sample. Similar to those of post-AGB binaries, its disk is gas-rich, as evidenced by the near-IR spectra. The

10 μm silicate feature seen in its mid-IR spectrum is commonly seen in post-AGB binaries (Gielen et al. 2008).

It is thus possible that dust disks around CSPNs may be related to those around post-AGB stars, and the differences between post-AGB disks and those of CSPNs could be attributed to different evolutionary stages. However, it is not yet known how and whether the post-AGB binaries with dust disks evolve into the PN stage. Taam & Ricker (2010) model the common-envelope binary evolution, in which a circumbinary disk is indeed formed, but the evolution of the system into later stages has not yet been modeled. Passy et al. (2011) also carried out common envelope simulations and determined that the envelopes are not fully ejected. This sub-escape-velocity gas will return to the binary system, spin up, and form a rotating self-supported circumbinary disk. However, the central binary of these systems is a very close one (separation of a few solar radii) and not one of the typical post-AGB binaries observed in the middle of circumbinary disks which have periods of 100-2000 days (van Winckel 2003).

In the case of CSPN EGB 6 (WD 0950+139), a strong emission line component was found superposed on the stellar continuum emission (Liebert et al. 1989). High-resolution *HST* emission-line images revealed that the emission actually originates from a point-like source that is offset from the PN nucleus by 0.18″ (∼120 AU), and later continuum images confirmed the presence of a dM companion (Bond 1994). It has been suggested that the dM companion has accreted material from the progenitor of WD 0950+139 and that this accretion disk is responsible for the nebular line emission (Bond 2009). CSPN EGB 6 also shows dusty mid-IR excess. It is unclear whether this mid-IR excess is associated with the CSPN, or its companion (Chu et al. 2011). NGC 6804 is similar to EGB 6 in having an unresolved nebular emission component coincident with the CSPN. Such unresolved nebular emission has also been found in PNe M2-29 (Gesicki et al. 2010; Frew & Parker 2010), and JaFu 1 (De Marco et al. 2011) NGC 7139 also shows weak enhancement in emission lines at the CSPN. It is possible that these phenomena might be associated with an unresolved

companion.

The difficulty in confirming the association of dust disks with binary CSPNs is the fact that the binarity of a CSPN is difficult to verify. Close companions have been detected by photometric variability (Bond et al. 1992), and distant ones by direct imaging (e.g., Ciardullo et al. 1999). Companions at ∼0.1-10 AU can currently only be detected by radial velocity variations, but the detection is hampered by irregular spectral variations due to winds (de Marco et al. 2007). Near-IR excess could in principle reveal a companion at any separation, enabling us to find the elusive intermediate separation binaries. However, this is in practice a difficult task as the expected companions are faint: the spectral type distribution for companions of WDs, which should be representative of CSPNs, peaks at M3-4 (Farihi et al. 2005). Most of the systems in our sample, in particular those that have hot disks, would successfully hide such companions even with photometry more accurate than that collected for the current work. We leave the determination of companion mass limits implied by the non-detections to a future paper. If a dust disk trapped in a stable orbit around a binary system can persist throughout the PN phase, its presence could serve as a powerful diagnostic for the binarity of the CSPN.

Further theoretical studies are necessary to understand the evolution of post-AGB binaries and their disks into the PN stage. From the observational point of view, a search for companions (see e.g. De Marco 2009) would allow us to strengthen or weaken the link between dusty IR excesses and binary companions, and to help us distinguish between the two proposed origins. Better modeling of the SEDs that includes parameters such as dust distances, grain sizes, location, and dust mass, will also help us evaluate the likelihood of different possible origins. We defer the more detailed modeling for a future paper.

4.3 Summary

We have conducted a survey of 72 available resolved PNe in the *Spitzer* archive, 56 of which were large enough for CSPN photometric measurements, and 42 of which were detected in at least one *Spitzer* IRAC and/or MIPS band. We find 19 cases with clear IR excesses, of these, seven are [WC] stars, two have apparent visual companions that account for the observed excess emission, two are borderline between young PNe and symbiotic stars, and in eight cases, the IR excess originates from an extended emitter, likely a dust disk. Combined with the survey of Chu et al. (2011), the incidence of dust disks among CSPNs is $\gtrsim$17%.

The SEDs show a great diversity in the emission characteristics of the IR excesses. For some of the CSPNs, we have acquired follow-up spectra using *Spitzer* IRS, Gemini NIRI and Michelle spectrographs. For NGC 6804, a rising dust continuum is seen in addition to H and He lines, and a 10 μm silicate feature. For NGC 7139, the IRS spectra are dominated by continuum emission, but a small slightly resolved nebular emission is also seen. For NGC 2346, the continuum is dominant at wavelengths $\leq$15 μm; at longer wavelengths the continuum weakens and the line emission becomes prominent.

The varied SEDs and spectral properties of the IR emission may imply multiple mechanisms responsible for the IR excesses. We discuss two possible mechanisms for producing the observed dust emission. The first is the breakup of bodies in planetesimal belts, similar to the origin of dust disks observed in main sequence stars and proposed for the dusty disk of the Helix Nebula. The second possibility is that the dust disk is formed in binary interactions, and descends from the commonly-observed dust disks around post-AGB binaries.

Further understanding of post-AGB binary evolution as well as debris disk evolution along its parent star is needed to distinguish between these different origins. Spectroscopic observations for CSPNs lacking mid-IR spectra, and observations at longer wavelengths are needed to better constrain the extent and properties of the dust disks. A more detailed SED modeling will allow us to to derive physical properties of the dust disks and compare them to

the properties of disks arising from the different proposed scenarios. Finally, a careful search for companions will also help to discern between the possible dust production mechanisms.

Table 4.1. Detections of IR excesses of CSPNs

Survey	No. Targets	Total Excesses	Dust	Symbiotic	[WC]-type	Companions
This paper	56	19	8	2	7	2
Chu et al. (2011)	35	7	7	0	0	0
Combined[a]	84	24	13	2	7	2

[a]The combined sample takes into account the overlaps between the two samples.

Table 4.2. Summary of Observational Results of Dusty IR Excesses of CSPNs

CSPN name	EXCESSES						SPECTRUM[a]				Known Comp.[d]
	JHK 1–2.5 μm	I1 3.6 μm	I2 4.5 μm	I3 5.8 μm	I4 8.0 μm	M1 24 μm	JHK 1–2.5 μm	LM 2.5–5.5 μm	Mich/IRS[bc] ∼5–15 μm	IRS[c] 15–35 μm	
EGB 1					✓	✓	...	...	cont	cont	
A 21						✓	...	...	...	...	
Sh 2-216						✓	...	...	cont	cont	
DeHt 5					✓	✓	...	...	...	...	
Sh 2-188	✓	✓	✓	✓	✓	✓	...	...	cont[d]	cont[e]	
K1-22	✓	✓	✓	✓	✓	✓	...	...	cont	cont	W
NGC 6853				✓	✓	✓	...	...	...	...	
NGC 7293					✓	✓	...	...	cont	cont	
EGB 6	✓	✓	✓	✓	✓	✓	...	...	cont	cont	W
NGC 2438	✓[f]	✓	✓	✓	✓	✓	...	...	cont	...	
NGC 7139	✓	✓	✓	✓	✓	-	H I, He I+II, cont	...	cont, [Ne II]	...	
NGC 6804	✓	✓	✓	✓	✓	✓	H I, He I+II, cont	H I, He II, cont	cont, silicate	...	
NGC 2346	✓	✓	✓	✓	✓	✓	...	...	cont, lines?	...	C

[a]cont=continuum, silicate=silicate feature

[b]The spectrum of NGC 6804 was obtained with the Gemini Michelle, and the others were all obtained with the *Spitzer* IRS SL module.

[c]From our spectra, Chu et al. (2011), or Su et al., in preparation.

[d]W stands for a wide companion, C stands for a close companion

[e]CSPN near a bright star in the slit, spectral extraction is impossible but image shows a very weak continuum

[f]The optical SED is not certain, there may or may not be J-band excess, CSPN not detected in HK

Table 4.3. Physical Parameters

CSPN Name	Literature				SED							Dynam Age	Evol Age	
	$T_{\rm eff}$ (K)	log g (cm s^{-2})	M ($M_\odot$)	Dist (pc)	$R_{\rm cspn}$ ($R_\oplus$)	$L_{\rm cspn}$ ($L_\odot$)	$T_{\rm IR}$ (K)	$A_{\rm IR}$ (AU^2)	$r_{\rm d}$ (AU)	$L_{\rm IR}$ ($L_\odot$)	$L_{IR}/L_{\rm cspn}$	(10^3yr)	(10^3yr)	Ref[a]
EGB 1	147,000	7.34	0.65	650	3.68	479	190	1.55	25	0.0067	1.40×10^{-5}	20	...	1
A21	140,000	6.5	0.58	541	1.92	107	150	0.85	32	0.0014	1.33×10^{-5}	44,17.7	...	2,3,4
Sh 2-216	95,000	6.9	0.53	129	2.36	34	150	0.48	19	0.00081	2.37×10^{-5}	<460	...	6,4
DeHt 5	76,500	6.65*	0.44*	345	2.37	15	190	0.25	8.2	0.001	7.30×10^{-5}	130	...	1,7
Sh 2-188	102,000	6.82	0.56	800	2.26	42	900	0.0008	0.61	0.0017	4.02×10^{-5}	12.1, 22	...	1,5,18
							150	0.68	22	0.001	2.73×10^{-5}			
K 1-22	141,000	6.73	0.59	1330	3.29	325	700	0.034	2.7	0.027	8.29×10^{-5}	55	12	8,9
							150	5.92	58	0.0099	3.06×10^{-5}			
NGC 6853	108,600	6.72	0.56	405	3.64	140	190	5.33	28	0.023	1.65×10^{-4}	13	...	1,7
NGC 7293	110,000	7.0	0.58	216	2.50	69	100	105	57	0.0347	5.00×10^{-4}	...	22.2	1,7,10
EGB 6	108,400	7.39	0.64	645	3.04	97	500	0.12	1.7	0.025	2.60×10^{-5}	135	...	11
							150	15	19	0.026	2.68×10^{-4}			
NGC 2438	114,000	6.62	0.56	1200	4.52	260	1200	0.0005	0.87	0.0035	1.34×10^{-5}	110	20	8,12
							150	57	56	0.095	3.64×10^{-4}			
NGC 7139	117,200	7.46	0.642	2400	2.38	81	1650	0.004	0.25	0.1	1.22×10^{-3}	...	14.7	13,14,18
NGC 6804	90,000	5.37	0.596	1320	28	3885	1400	0.12	2.46	1.49	3.84×10^{-5}	7.9[b]	6.2	12,13,15
							550	6.2	16	1.87	4.84×10^{-4}			
							250	155	77	2.01	5.16×10^{-4}			
NGC 2346[c]	100,000	7.7	0.39	800	3.27	81	1000	2.2	0.7	7.31	9.0×10^{-2}	...	...	16,17
							250	37	11	0.48	5.9×10^{-3}			
M2-9	35,000[d]						1400+700+360				4.12[e]			
Mz 3	35,000[d]						1400+700+360				0.55[e]			

[a] References: 1. Napiwotzki (2001), 2. Werner et al. (2004), 3. Werner & Herwig (2006), 4. Harris et al. (2007), 5. Napiwotzki & Schoenberner (1995), 6. Rauch et al. (2007), 7. Benedict et al. (2009), 8. Rauch et al. (1999), 9. Ciardullo et al. (1999), 10. Su et al. (2007), 11. Liebert et al. (2005), 12. Phillips (2004), 13. Mal'Kov (1997), 14. Gorny et al. (1997), 15. Stanghellini et al. (2002), 16. Smalley (1997), 17. Su et al. (2004) 18. Frew (2008).

*Benedict et al. (2009) gives g=7.41, M=0.57 $M_\odot$

[b]Calculated using Table 4 of Stanghellini & Pasquali (1995)

[c]CSPN has a close companion; we model its emission using $T_{\rm eff}$=9520 K and R=1.9 $R_\odot$

[d]Assumed CSPN effective temperature.

[d]A 35,000 K blackbody model scaled to the optical fluxes of the CSPN is assumed for the stellar luminosity.

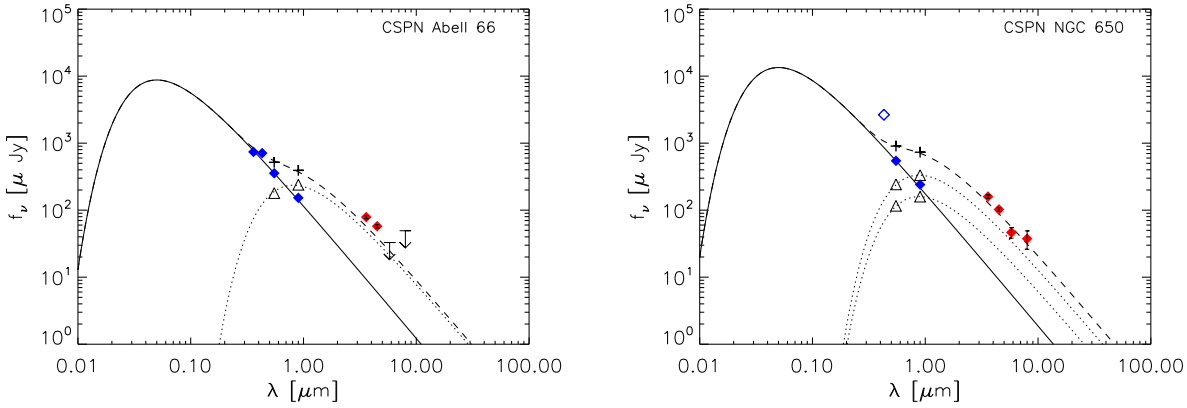

Figure 4.1: SEDs of CSPNs with IR excesses caused by companion's photospheric emission. The symbols are the same as in Figure 3.2, in addition, the triangles represent the flux densities of the companions, and the plus symbols show the sum of all components. The dotted blackbody curves approximate the companions' photospheric emission, and the dashed curves represent the sum of all emission components. For further details, see sections 4.1.1 and 3.4 .

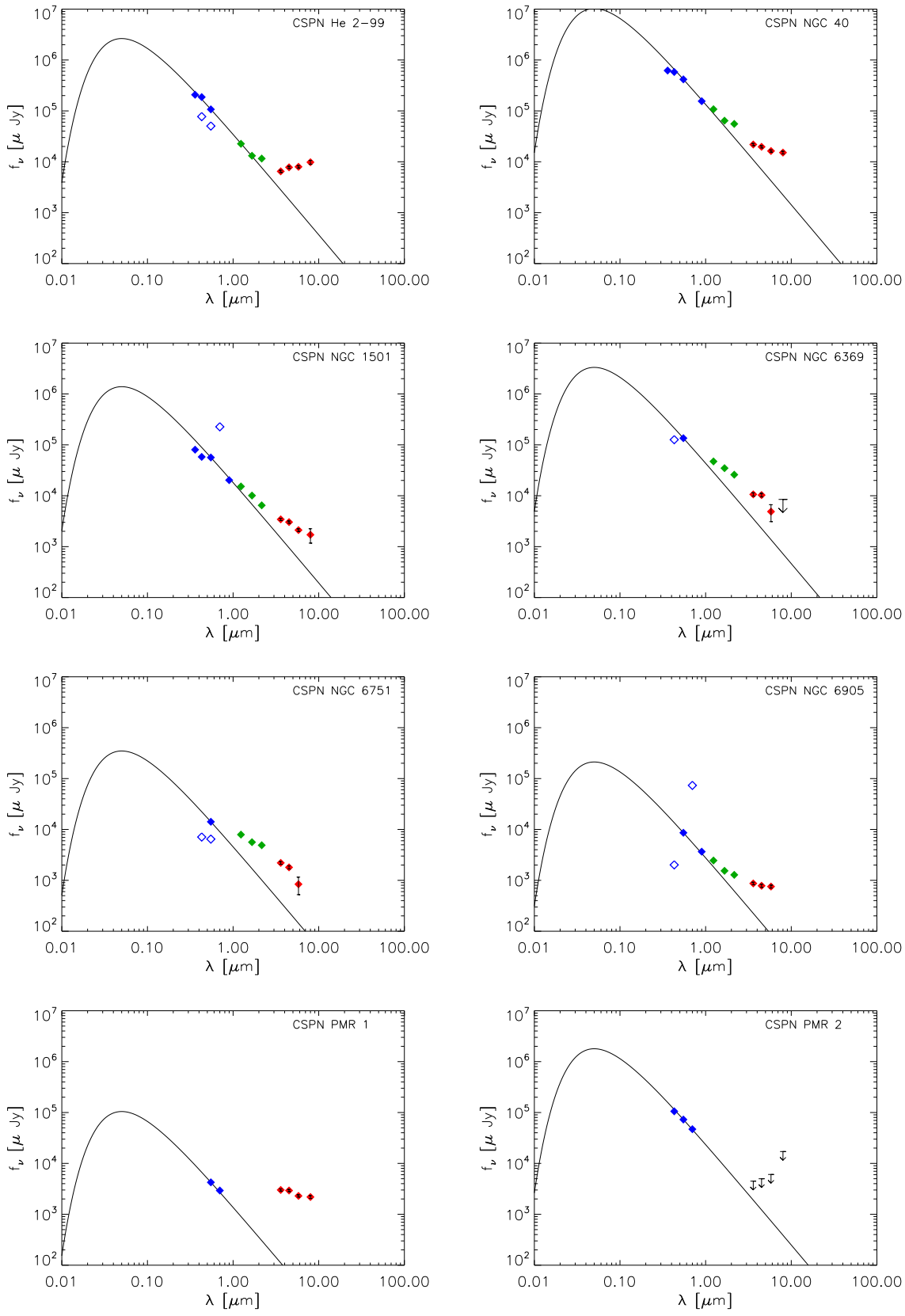

Figure 4.2: The SEDs of [WC]-type CSPNs. The symbols are the same as in Figure 3.2.

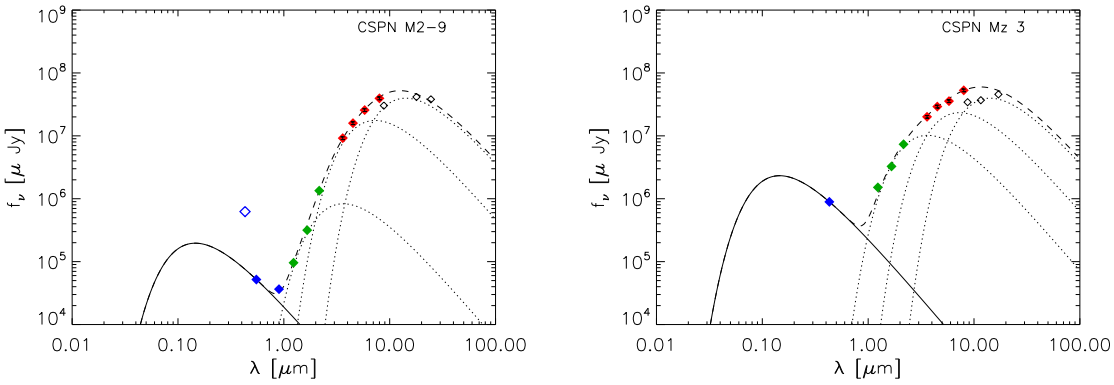

Figure 4.3: SEDs of CSPNs of symbiotic PNe. The symbols are the same as in Figure 3.2. In addition, the different components of model dust emission are shown as dotted curves, and the sum of all emission components is shown as a dashed curve.

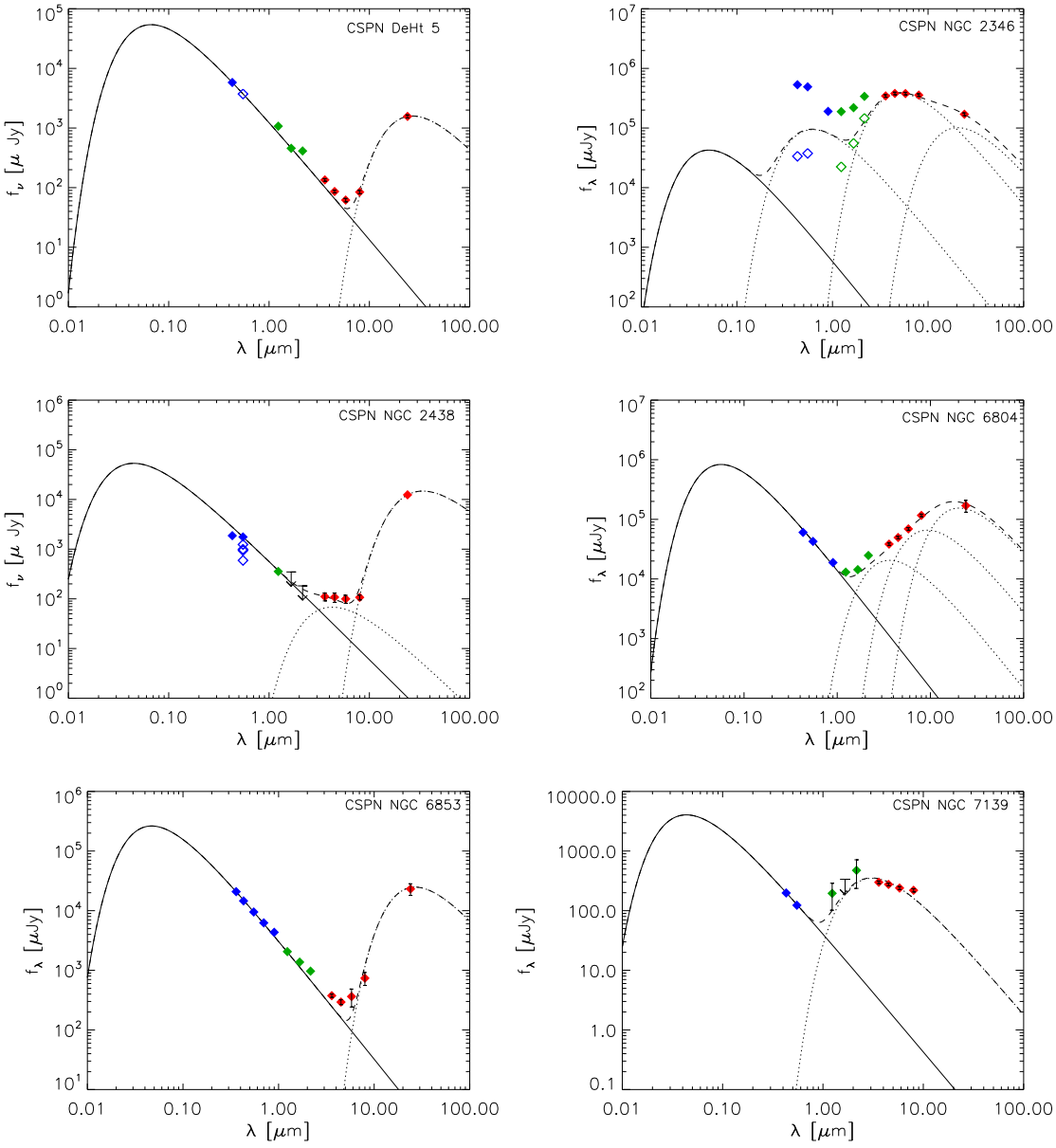

Figure 4.4: SEDs of CSPNs with IR excesses indicative of dust disks. The symbols are the same as in Figure 3.2. The CSPN's photospheres are approximated by a blackbodies with effective temperatures listed in Table 4.3. In addition, the different components of model dust emission are shown as dotted curves, and the sum of all emission component is shown as a dashed curve. For further details, see sections 4.1.4 and 3.4.

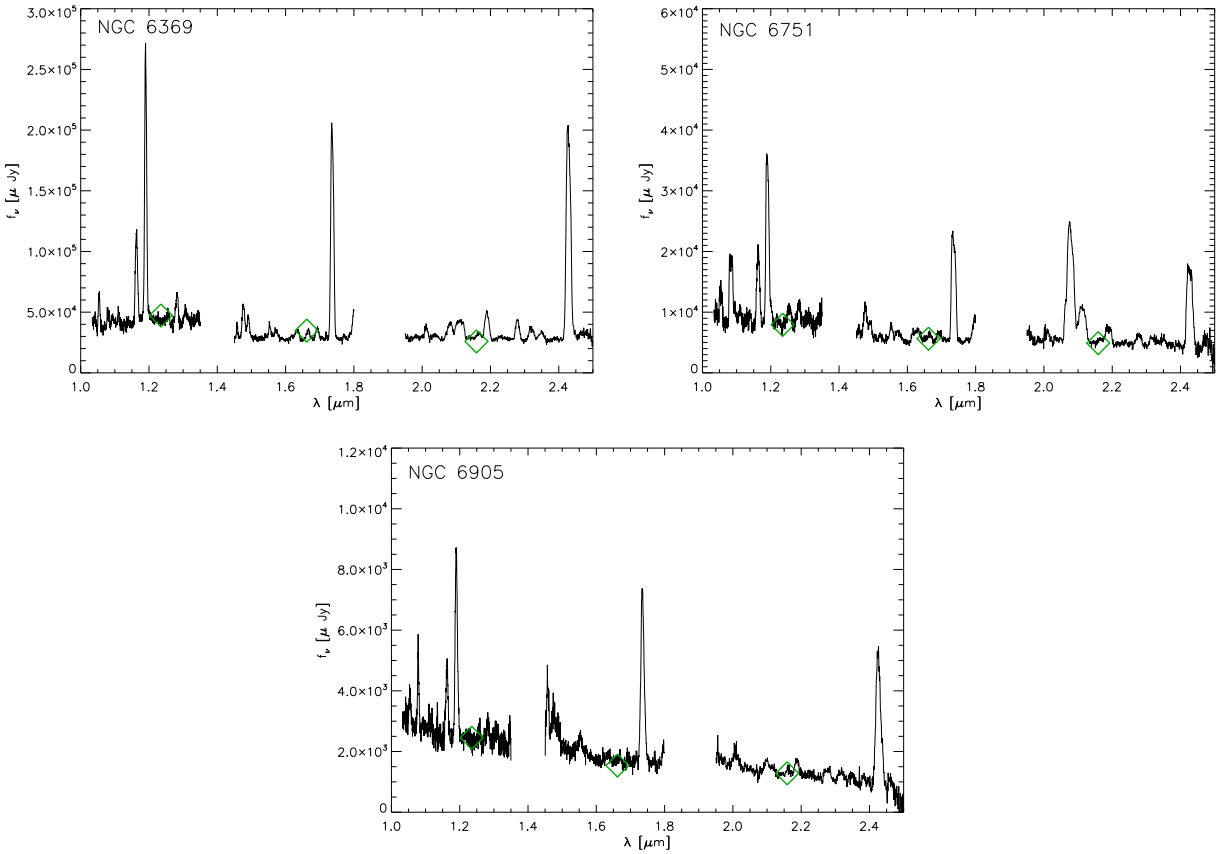

Figure 4.5: Gemini NIRI spectra of three [WC]-type CSPNs, NGC 6369, NGC 6751, and NGC 6905. The JHK flux densities are shown as open green diamonds.

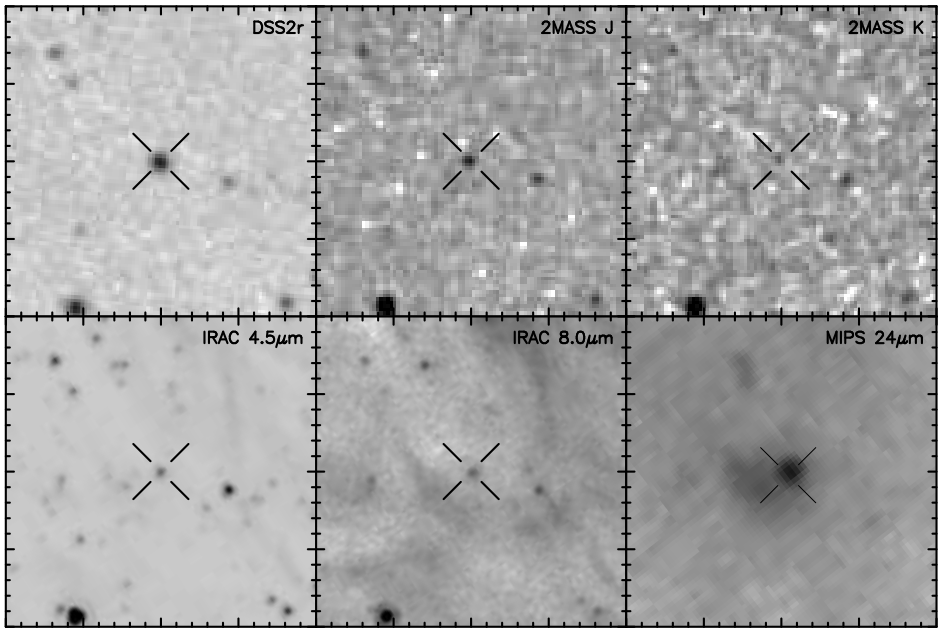

Figure 4.6: Optical and IR images of DeHt 5. The field of view of each panel is 90″×90″, with north at the top and east to the left.

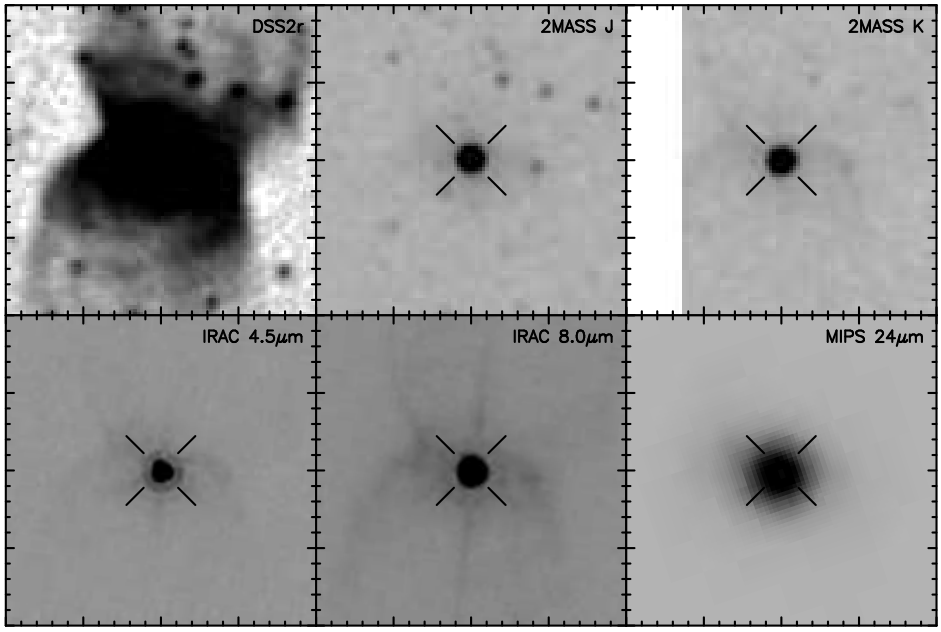

Figure 4.7: Optical and IR images of NGC 2346. The field of view of each panel is 90″×90″, with north at the top and east to the left.

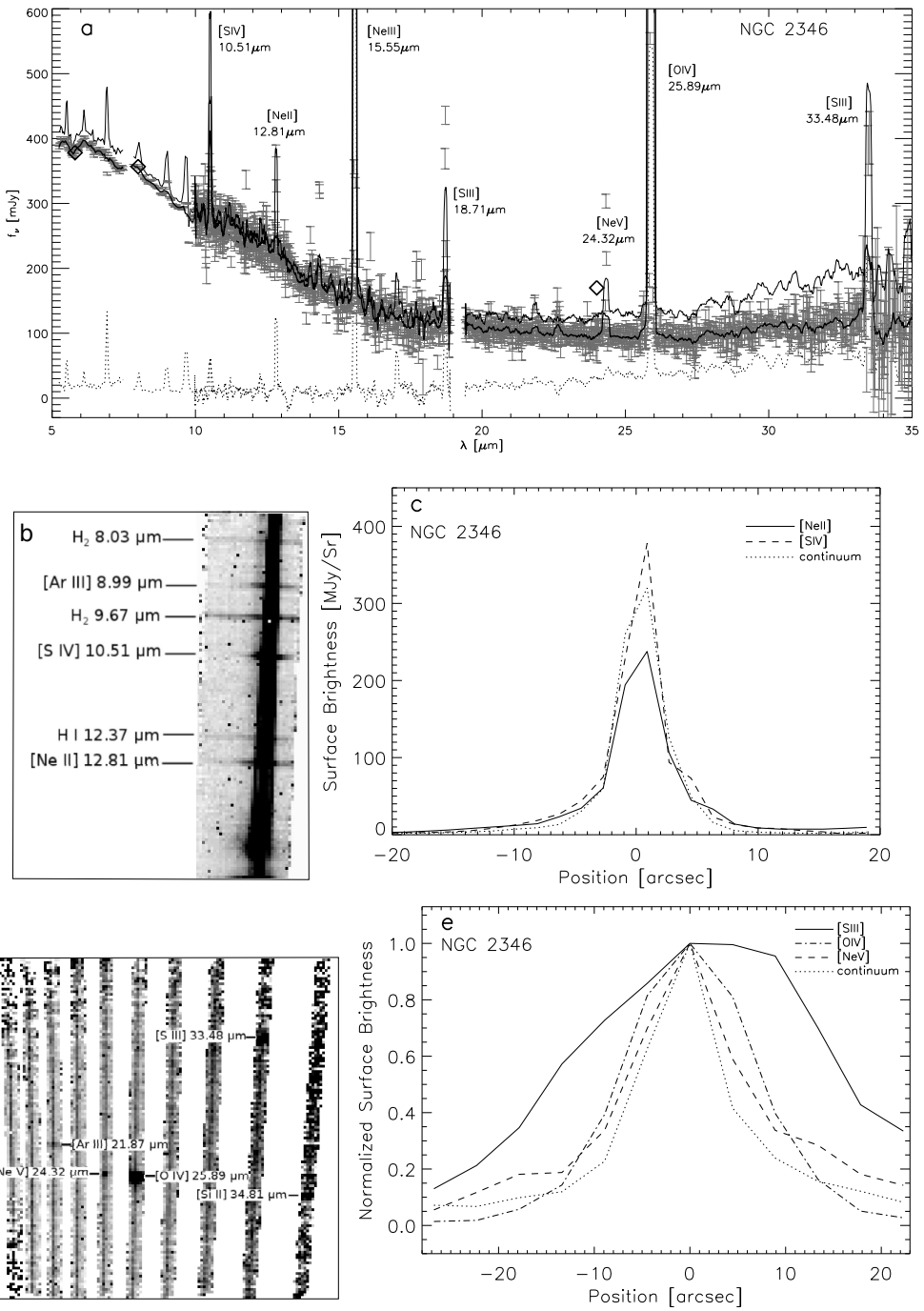

Figure 4.8: (a) *Spitzer* IRS spectrum of CSPN NGC 2346. The smoothed spectrum extracted at the CSPN is plotted in solid thin line, the smoothed local background in a dotted line, the background-subtracted spectrum in gray error bars, and the smoothed background-subtracted spectrum in a thick solid line. The IRAC and MIPS flux densities are shown as open diamonds. (b) The raw IRS spectral image in the SL1 (7.4 – 14.5 μm) module, with emission lines labeled. The spectrum is dominated by continuum emission. (c) Surface brightness profile plots extracted from the IRS SL1 module data cube in the continuum (dotted curve), at [S IV] 10.51 μm line (dashed curve) and at [Ne II] 12.81 μm line (solid curve). (d) The raw IRS spectral image extracted in the LH (19–37 μm) module, with emission lines labeled. (e) Normalized surface brightness profiles extracted from the LH module data cube of continuum (dotted curve), at [Ne V] 24.32 μm line (dashed curve), [O IV] 25.89 μm line (dash-dotted curve), and [S III] 33.48 μm line (solid curve). Note that all surface brightness profiles at spectral lines contain both the line and continuum emission.

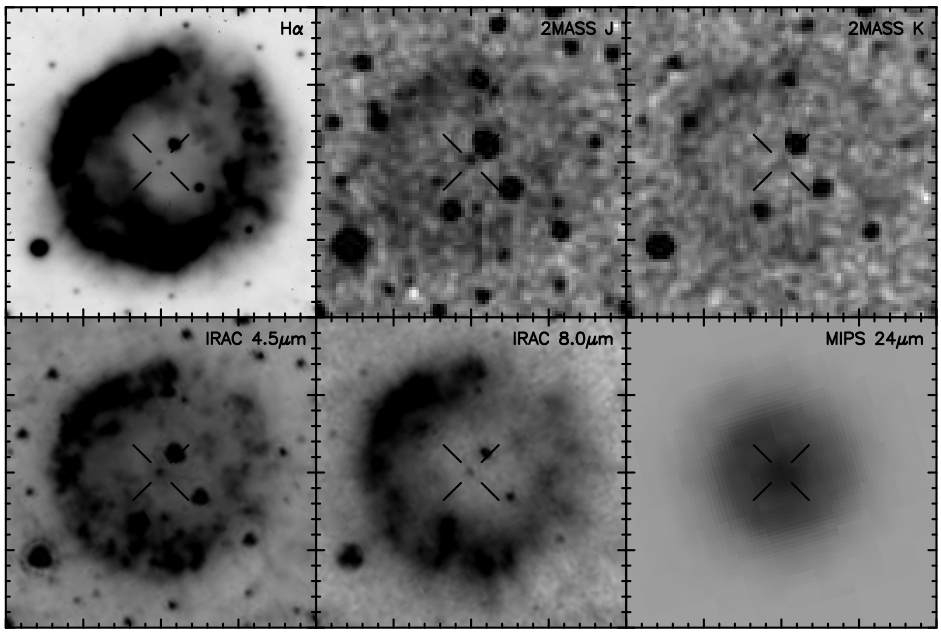

Figure 4.9: Optical and IR images of NGC 2438. The field of view of each panel is $90'' \times 90''$, with north at the top and east to the left.

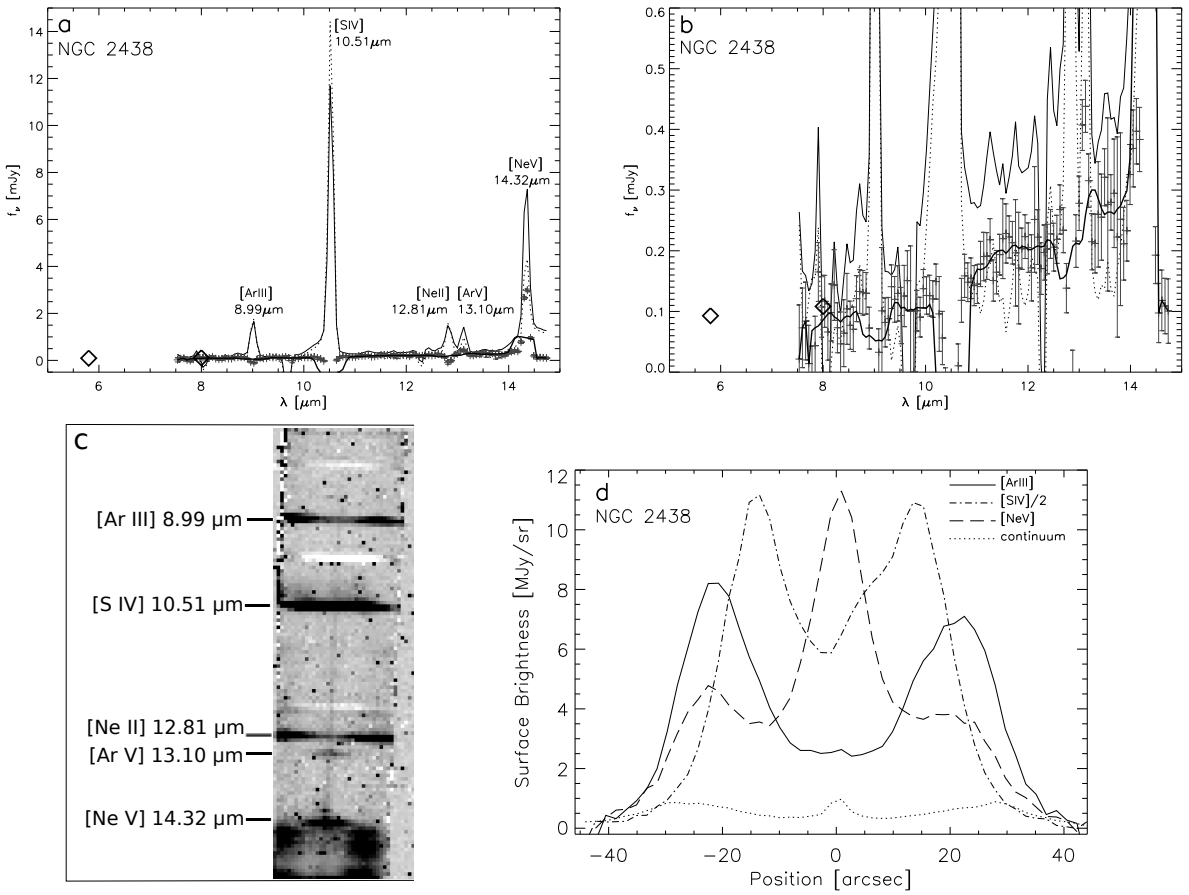

Figure 4.10: (a,b) *Spitzer* IRS spectrum of CSPN NGC 2438 plotted with different scales to illustrate the relative intensity of lines and continuum. The spectrum extracted at the CSPN is shown in solid thin line, the local background in a dotted line, the background-subtracted spectrum in gray pixels with error bars, and the smoothed background-subtracted spectrum in a thick solid line. The IRAC flux densities are shown as open diamonds. (c) The spectral image extracted in the SL1 (7.4 – 14.5 μm) module, with emission lines labeled. The slit length is 57″. (d) Surface brightness profile plots extracted from the IRS data cube in the continuum (dotted curve), [Ne V] 14.32 μm line (dashed curve), [S IV] 10.51 μm line (dash-dotted curve), and [Ar III] 8.99 μm line (solid curve).

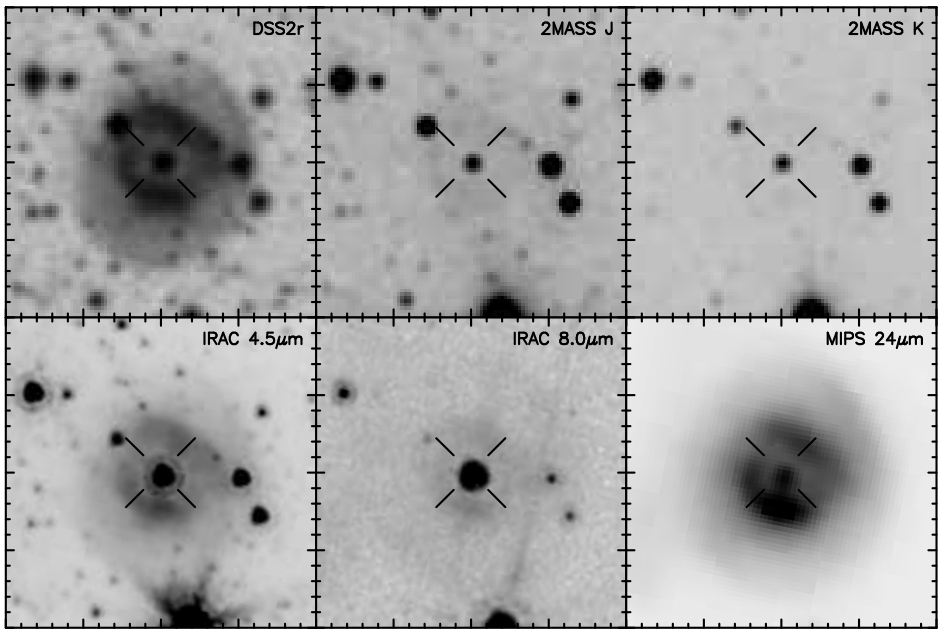

Figure 4.11: Optical and IR images of NGC 6804. The field of view of each panel is 90″×90″, with north at the top and east to the left.

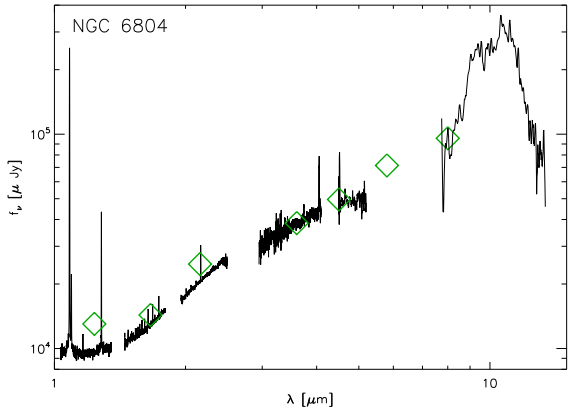

Figure 4.12: Gemini NIRI and Michelle spectra of CSPN NGC 6804. The JHK and IRAC flux densities are shown as green diamonds.

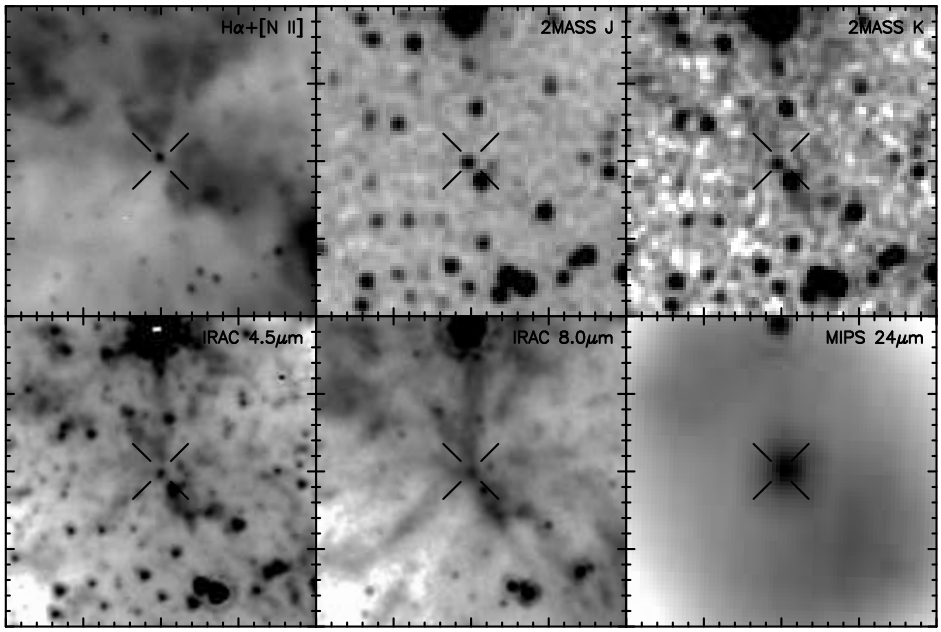

Figure 4.13: Optical and IR images of NGC 6853. The field of view of each panel is 90″×90″, with north at the top and east to the left. The Hα+[N II] image was taken from the The IAC morphological catalog of northern galactic planetary nebulae (Manchado et al. 1996).

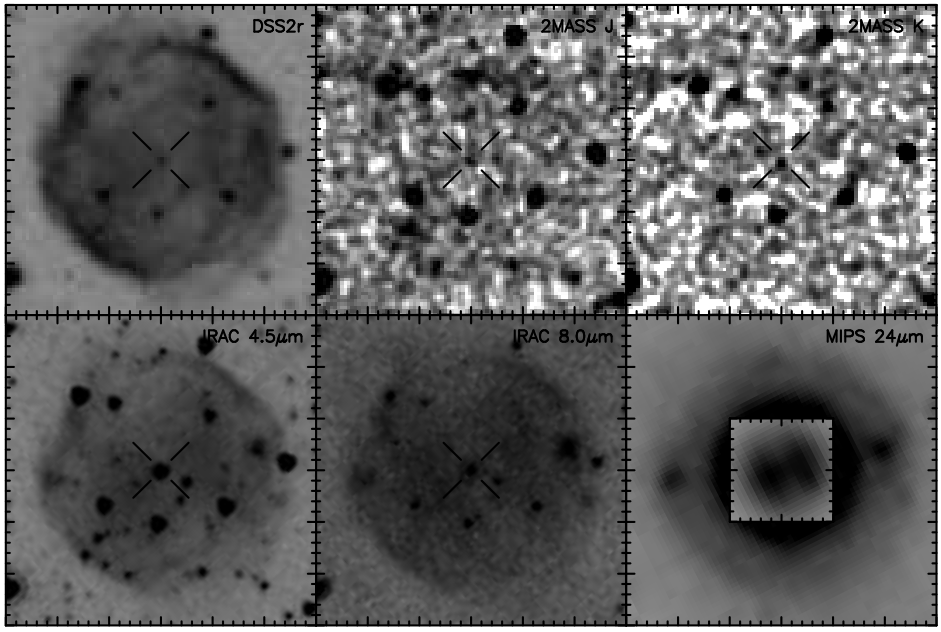

Figure 4.14: Optical and IR images of NGC 7139. The field of view of each panel is 90″×90″, with north at the top and east to the left. The inset in the 24 μm panel is made from the same image, using a different stretch to show the central torus.

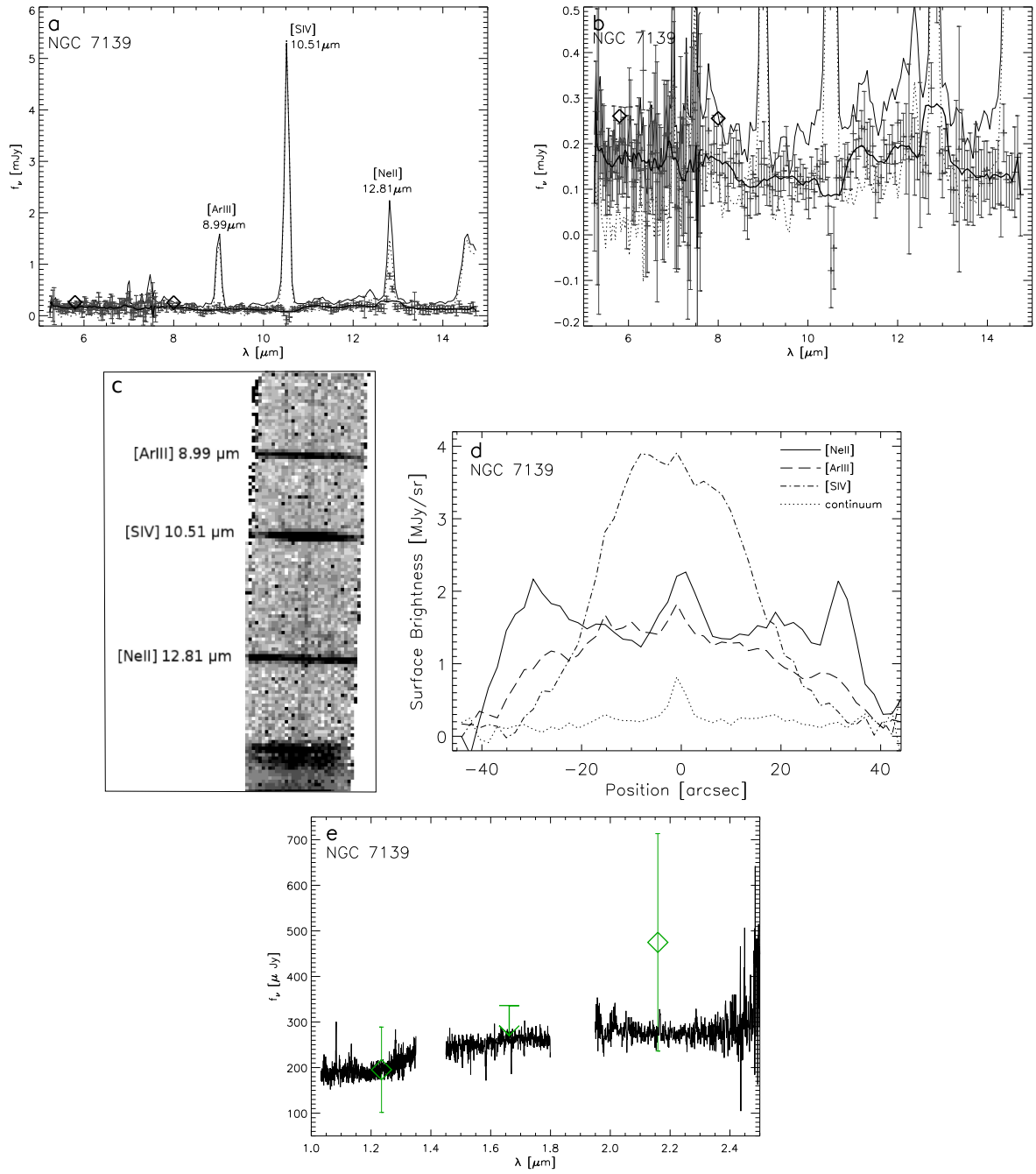

Figure 4.15: (a,b) *Spitzer* IRS spectrum of CSPN NGC 7139 plotted with different scales to illustrate the relative intensity of lines and continuum. The spectrum extracted at the CSPN is plotted in solid thin line, the local background in a dotted line, the background-subtracted spectrum in gray pixels with error bars, and the smoothed background-subtracted spectrum in a thick solid line. The IRAC flux densities are shown as open diamonds. (c) The spectral image extracted in the SL1 (7.4 – 14.5 μm) module, with emission lines labeled. (d) Surface brightness profile plots extracted from the IRS data cube in the continuum (dotted curve), [S IV] 10.51 μm line (dash-dotted curve), [Ar III] 8.99 μm line (dashed curve), and [Ne II] 12.81 μm line (solid curve). (e) Gemini NIRI JHK spectra of CSPN NGC 7139. The JK flux densities are shown as green open diamonds, and the H-band upper limit is plotted as a green downward arrow.

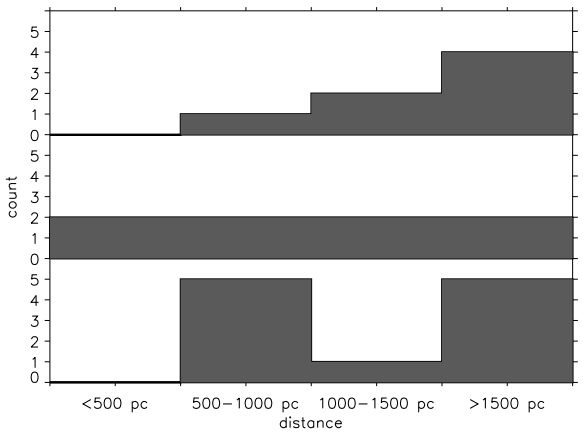

Figure 4.16: Distributions of distances of [WC] CSPNs (top), CSPNs with dusty IR excess (middle) and CSPNs without IR excess (bottom).

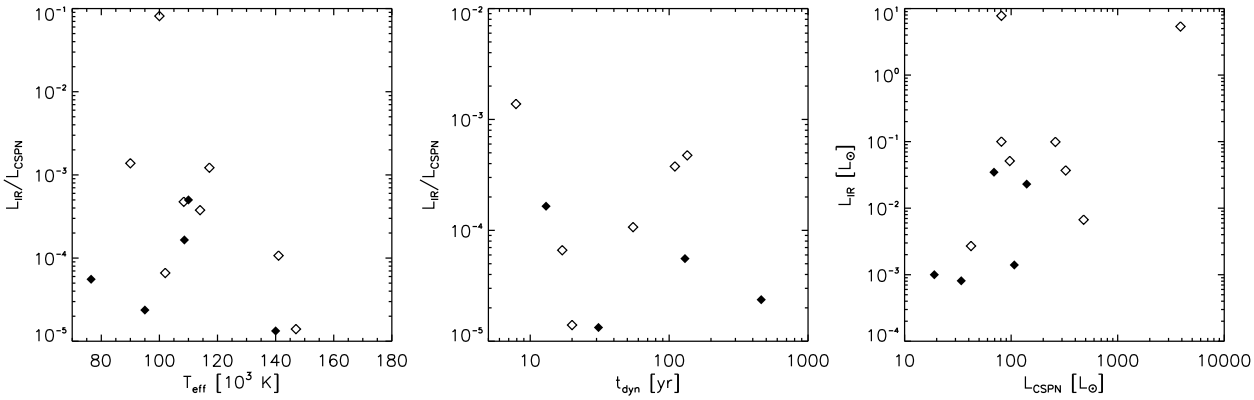

Figure 4.17: Relationships between physical parameters of the CSPNs and their IR excesses. $L_{IR}/L_{\rm CSPN}$ is shown as a sum of all temperature components used to fit the IR SED. The targets with parallax distances are shown as filled diamonds. The values used for construction of these plots are listed in Table 4.3.

Chapter 5

Dust Modeling

5.1 Introduction

The CSPN of the Helix Nebula exhibits excess IR emission at ∼8–70 μm that originates from a dust disk located between ∼35 and 150 AU from the central WD. It has been suggested that this dust disk was produced by collisions among KBOs that were dynamically rejuvenated during the post-AGB evolution (Su et al. 2007). To search for additional dust disks similar to that around the Helix CSPN, we have carried out a *Spitzer* MIPS 24 μm survey of hot WDs/pre-WDs, and discovered nine objects with 24 μm excesses that likely originate from dust disks (Chu et al. 2011). Interestingly, seven of these are still CSPNs. We have therefore examined the images of PNe in the *Spitzer* archive and analyzed the SEDs of their CSPNs to find five additional objects with IR excesses indicative of dusty disks. Together with the CSPN of the Helix Nebula, we have a sample of 15 WDs/CSPNs with excess IR emission likely originating from dust disks.

The SEDs of these objects are diverse. While some have excess emission only at wavelengths longer than 8 μm, others' IR excesses start in the near-IR. For some CSPNs, we have acquired follow-up *Spitzer* IRS, and Gemini NIRI and Michelle spectroscopic observations. All spectra indicate the presence of dust continuum, but they vary in the spectral shape and the strength of gas or dust emission features superposed on the continuum.

Unlike the dust disk around Helix's CSPN which has been suggested to be produced by collisions among surviving planetesimals, some of our disks may have formed through binary interactions, and are descendants of the dust disks observed around binary post-AGB stars

(de Ruyter et al. 2006).

To assess the origin of the excess IR emission, it is necessary to establish the physical parameters of these dust disks. For objects with few data points to constrain their mid-IR excesses, we use the blackbody models established in previous chapters to estimate the basic disk properties, such as masses, grain sizes, and lifetimes. For objects with adequate IR spectral coverage, we model the excess emission with a more realistic dust disk. We evaluate the properties of these disks against those of main-sequence debris disks produced by collisions among planetesimals and dust disks observed in binary post-AGB stars.

5.2 Simple Model

For the dust disks without available mid-IR spectra, we estimate the basic physical disk properties using simple blackbody approximations, assuming optically thin disks. The assumption of optical thinness is reasonable for stars with low internal extinction, but may not be appropriate if the extinction is high. Blackbody models of IR SEDs, combined with distances from the literature allow us to estimate the dust disks' emitting areas, and hence the areas of the disks intercepting the starlight. With assumptions on the size distribution and density of grains in the disk, we are able to estimate dust masses.

5.2.1 Grain Sizes and Distribution

For a collision-dominated disk, the grain size distribution is a power law with an index of -3.5, i.e., $n(a) \propto a^{-3.5}$ (Dohnanyi 1969). The minimum grain size in a disk is determined by β, the ratio of radiation pressure force ($F_{\rm rad}$) to the gravitational force ($F_{\rm g}$) exerted on the grain by the central WD. The radiation pressure force is given by

$$F_{\rm rad} = \frac{< S > \sigma_{\rm gr}}{c} = \frac{L_* \pi a^2}{4\pi r^2 c}, \tag{5.1}$$

where $< S >= \frac{L_*}{4\pi r^2}$ is the time-averaged Poynting vector, $\sigma_{\rm gr}$ is the dust grain cross-section, L_* is the WD luminosity, a is the dust grain radius, and r is the distance of the grain from the star, and c is the speed of light. The gravitational force exerted on the dust grain is

$$F_{\rm g} = \frac{GM_* m_{\rm grain}}{r^2} = \frac{GM_*}{r^2}\frac{4\pi a^3 \rho}{3}, \tag{5.2}$$

where M_* is the mass of the WD, $m_{\rm grain}$ is the mass of the dust grain, and ρ is the grain density. Thus,

$$\frac{F_{\rm rad}}{F_{\rm g}} = \beta = \frac{3L_*}{16\pi GM_* a\rho c}. \tag{5.3}$$

The parameter β determines the minimum grain size, $a_{\rm crit}$, below which the grains are blown out.

$$a_{\rm crit} = \frac{3L_*}{16\pi GM_*\rho c\beta}. \tag{5.4}$$

Artymowicz & Clampin (1997) show that for a dust grain produced by a collision, the daughter grain is at the periastron of an elliptic orbit with an eccentricity $e(\beta) = \beta/(1-\beta)$. For a $\beta = 0.5$, the eccentricity becomes 1, and the orbit becomes unbounded (parabolic). Therefore, dust grains with $\beta \geq 0.5$ wil escape the system.

Using equation 5.4 with $\beta = 0.5$, the luminosities of WDs determined from published distances and optical photometry, and WD masses from the literature, we calculate the blowout grain radius for each object. For our calculation, we adopt a dust grain density of 2.5 g cm^{-3}. The masses and luminosities of all WDs/CSPNs, along with the calculated minimum grain sizes, are presented in Table 5.1. For references for CSPN physical parameters, see Table 4.3. The maximum grain size within a dust disk is hard to determine, because the large grains' contribution to the IR emission is very small. For our models, we adopt a largest grain size of 1 mm.

5.2.2 Mass in a Disk

For a simplistic calculation of dust disk masses, we assume spherical dust grains with a power-law size distribution of $n(a) \propto a^{-3.5}$ between the minimum and maximum grain sizes $a_{\rm min}$ and $a_{\rm max}$, radiating as blackbodies at temperatures determined by the SED fits. The dust mass in the disk ($M_{\rm disk}$) is given by

$$M_{\rm disk} = \int_{a_{\rm min}}^{a_{\rm max}} \frac{4}{3}\pi a^3 \rho_{\rm g} N(a) da, \tag{5.5}$$

where $\rho_{\rm g}$ is the grain density and $N(a)$ is the total number of grains of size a within the disk. The sum of the grains' cross sections must add up to the total cross section ($\sigma_{\rm tot}$) determined from the SED fits:

$$\sigma_{\rm tot} = \int_{a_{\rm min}}^{a_{\rm max}} N(a)\pi a^2 da, \tag{5.6}$$

Since $n(a) \propto a^{-3.5}$, the same proportionality applies to $N(a)$. Calling the constant of proportionality η, we have

$$\sigma_{\rm tot} = \int_{a_{\rm min}}^{a_{\rm max}} \eta a^{-3.5}\pi a^2 da = \pi\eta \int_{a_{\rm min}}^{a_{\rm max}} a^{-1.5} da. \tag{5.7}$$

Hence,

$$\eta = \frac{\sigma_{\rm tot}}{2\pi(a_{\rm min}^{-0.5} - a_{\rm max}^{-0.5})}. \tag{5.8}$$

With a known $\sigma_{\rm tot}$, $a_{\rm min}$, and $a_{\rm max}$, we can evaluate η and use it to calculate the dust disk masses. We carry out this mass calculation for each of the hot WDs/pre-WDs with IR excesses, and list the results in Table 5.1.

5.2.3 Poynting-Robertson Lifetime

While the small grains in the disk will be blown out of the system due to radiation pressure, the larger grains will slowly spiral in toward the central star due to the Poynting-Robertson

effect. The star radiates energy isotropically outward, but in the moving particle's reference frame, the light is arriving slightly from the forward direction, thus acting as a damping force. The loss of angular momentum causes the particle's orbit to decay and spiral toward the star.

For a grain of size a orbiting at a distance r from the WD, the time $\tau_{\rm PR}$ it takes for the dust to spiral into its central star can be estimated by:

$$\tau_{\rm PR} \sim \frac{\pi m_{\rm gr} c^2}{\sigma_{\rm gr} L_*} r^2, \tag{5.9}$$

where $m_{\rm gr}$ is the grain mass, $\sigma_{\rm gr}$ is the grain cross-section, L_* is the star's luminosity, and r is the dust's orbital radius.

Since the smallest grains in the system dominate the IR emission, in order to assess the lifetimes of our dust disks, we calculate $\tau_{\rm PR}$ for the smallest grain sizes not blown out by radiation pressure, located at the blackbody equilibrium temperature distance. For the calculation of grain masses, we adopt a density of 2.5 g cm^{-3}.

The computed PR lifetimes are listed in Table 5.1. These values help us assess whether the dust in a given disk is likely to be optically thick or optically thin. If the PR lifetime of a disk around a very evolved object is short, the dust in the disk may be shielded from the stellar radiation to remain in the system for a long time, and the disk could be optically thick. On the other hand, long PR timescales are consistent with the assumption of optical thinness.

5.3 Simple Model Results

For objects without spectroscopic observations, there are not enough data points to trace the IR excess SED, and dust models with a greater number of free parameters would not be meaningful. Therefore, we only use the simple modeling to estimate the dust disk properties

of these WDs/pre-WDs. Generally, they can be separated into two categories: five CSPNs exhibit excess emission only at wavelengths longer than ~ 6 μm, and one CSPN shows excess emission starting from the near-IR. The physical parameters of these disks are summarized in Table 5.1.

For the 5 CSPNs with mid-IR excesses only, the disk masses are between $\sim 10^{-5}$ and 10^{-2} $M_{\oplus}$, in line with the observations of debris disks around main-sequence stars. The PR lifetimes are estimated to be between $\sim 10^5$ and 10^6 years. These timescales are greater or comparable to the age estimates of these objects, which are $\sim 10^4$ – 10^5 years. The equilibrium-temperature distances of these disks are between $\sim$10 – 30 AU. The $\sim$30 AU distance is consistent with distances of KBO objects in the Solar System or the main-sequence stars' debris disks. The $\sim$10 AU distances may correspond to asteroids' orbits expanded further from the central star due to its mass loss, or they may have been scattered inward during post-AGB and PN evolution. Alternatively, since the spectral coverage of the SEDs is low, the emission from these disks may be peaking at longer wavelengths that correspond to lower temperatures and greater equilibrium-temperature distances. A better SED coverage is necessary to establish firmer limits on the location of dust.

The results of these simple models for WDs/CSPNs with mid-IR excesses are consistent with the origin of collisionally disrupted planetesimals. However, spectroscopic observations to confirm the nature of the excess emission as dust continuum is needed, and better spectral coverage to constrain the extent and the temperatures within the disks are necessary to further examine this hypothesis.

One WD, CSPN Sh2-188, shows excess emission starting in the near-IR. Few data points exist to constrain the optical portion of the SED, the IRAC data points have large error bars, and the detection in IRAC 5.8 and 8.0 bands is questionable. It is thus difficult to constrain the origin of this near-IR excess. The CSPN may have an unresolved companion or a hot dust disk in addition to the cooler dust detected at 24 μm. This WD has been observed with *Spitzer's* IRS, but unfortunately a bright star within the slit precludes the

extraction of a meaningful spectrum. The simple SED modeling requires two temperature components, $\sim$ 150 and $\sim$ 900 K. The dust mass and the PR lifetime is computed for each component separately. The cooler $\sim$150 K component contains a dust mass of $\sim 10^{-4}$ $M_{\oplus}$ comparable to dust disks around main-sequence stars. The PR lifetime calculated for this component is $\sim 10^{6}$ yr, longer than the age of the nebula, $\sim 10^{4}$ years. The warmer 900 K component has a low dust mass $\sim 10^{-7}$ $M_{\oplus}$ and the PR lifetime of this dust is only $\sim$500 years, considerably shorter than the age of the PN. If the dust has remained in such warm disk around this CSPN throughout its PN evolution, the disk must be optically thick. More precise flux measurements and a better spectral coverage are necessary to model the IR excess of this WD, and to decipher its origin.

5.4 Optically Thin Dust Model

For WDs and CSPNs with available spectroscopic observations to constrain the IR emission, we assess whether their disks are likely optically thick or thin, and, where appropriate, model the IR emission with a more realistic dust model. The dust disk model and the modeling results of individual objects are described in the following sections. The modeling of disks that are likely optically thick is left for future work.

In our dust disk model, we discard the blackbody approximation for the disk, and calculate the grain temperatures based on their composition, sizes, and distances from the heating source. The dust temperature of a given grain is determined by the balance between the absorbed and emitted energy. The energy absorbed by a dust grain depends on the incident flux, grain cross section, and the absorption efficiency at a given wavelength, via

$$E_{\rm abs} = \int \frac{4\pi R_s^2 F_{s,\lambda}}{4\pi d^2} \pi a^2 Q_{{\rm abs},\lambda} d\lambda, \tag{5.10}$$

where R_s is parent star's radius, F_s is the flux from the parent star (in case of a blackbody

$\pi\times$ Planck function), d is the orbital distance of the dust, a is the radius of the dust grain, and $Q_{\rm abs}$ is the absorption coefficient of the dust grain with a given composition and size, at wavelength λ.

The energy emitted by a dust grain is a blackbody modified by the wavelength-dependent absorption coefficient $Q_{\rm abs}$:

$$E_{\rm em} = \int 4\pi a^2 Q_{{\rm abs},\lambda} F_{d,\lambda} d\lambda, \tag{5.11}$$

where F_d is the flux from the dust grain (i.e., $\pi\times$ Planck function), which is determined by the dust grain temperature. In thermal equilibrium, the energy absorbed by a dust grain is equal to the energy emitted by it. Therefore,

$$\frac{R_s^2}{4d^2} \int Q_{{\rm abs},\lambda} F_{s,\lambda,T} d\lambda = \int Q_{{\rm abs},\lambda} F_{d,\lambda,T} d\lambda. \tag{5.12}$$

The absorption coefficients for a given grain size and composition can be calculated or found in the literature (e.g., Draine & Lee 1984; Laor & Draine 1993). For known stellar parameters and a given orbital distance, the only remaining unknown is the dust temperature that enters into $F_{d,\lambda,T}$. The dust temperature can be found by numerically evaluating the right-hand side of equation 5.12 and adjusting the dust temperature, until both sides match. In our models, we have used $Q_{\rm abs}$ coefficients calculated for astronomical silicates and amorphous carbon grains with radii 0.1–1000 μm using Mie theory with additional modifications for large grain sizes (a >10 μm).

5.4.1 Dust Disk Parameters

A number of parameters are used as inputs into our disk models. Most of them are described in detail by Wolf & Hillenbrand (2003), and all are reviewed briefly below. Since there can be degeneracies in the disk models, we also discuss the constraints we place on some of these parameters, based on observations and our understanding of debris disks.

1. **Grain Composition:** The composition of the dust grains affects the absorption properties of the dust. The only CSPN whose mid-IR spectrum exhibits any dust features is NGC 6804, which has a 10 μm silicate feature. The spectra of dust disks detected in our *Spitzer* 24 μm survey are featureless; therefore, the dust composition is not known. We adopt the dust grain composition of either astronomical silicates or amorphous carbon.

2. **Minimum and Maximum Grain Size:** We assume that the grain sizes in the dust disks are between the blowout radius due to radiation pressure (see Section 5.2.1) and 1 mm. Note that grains larger than 1 mm are likely present, but they do not contribute significantly to IR emission.

3. **Grain Size Distribution:** For the distribution of grain sizes, we adopt a power-law, where $n(a) \propto a^p$. For an infinite collisional cascade, the power-law index is theoretically derived to be -3.5 (Dohnanyi 1969; Tanaka et al. 1996). This power-law index agrees well with the dust SED of, e.g., Formalhaut's disk (Wyatt & Dent 2002). Note that as smaller grains are depleted from the system, the index p may change with time (Wolf & Hillenbrand 2003).

4. **Surface Density Distribution:** The surface density distribution is a power law which can have a range of power-law indices. Various dust disk observations find an index ranging from 0 up to $\sim$2.5 (see e.g. Wolf & Hillenbrand 2003). For our models, since we do not have any observational constraints, we use a uniform surface brightness. Such distribution would be expected for tenuous PR drag-dominated disks (Wyatt 2005).

5. **Inner and Outer Disk Radius** The inner and outer radius of the disk determine the range of temperatures within it. The inner and outer radii are left as free parameters in our disk models, and will be determined for each system individually.

6. **Grain Density:** The density of the dust grains affects the mass of the dust disk, as well as the minimum grain size that remains around the WD. For our models, we use the dust grain density of 2.5 g cm^{-3}, which is within the range observed for asteroids in the Solar System (e.g., Britt et al. 2005).

7. **Stellar Properties:** The heating star clearly has a strong effect on the light detected from the debris disk surrounding it, since the luminosity of the star determines the temperatures of the dust grains. The mass and luminosity of the star also set the minimum grain size inside the disk, and since the greatest portion of the emission comes from the smaller grains, the minimum grain radius can have large effects on the resulting total disk mass. In general, the greater the stellar luminosity, the larger the minimum grain size, and the larger the derived dust mass.

   To find the luminosity of the star, one needs to know its distance. Unfortunately, distances are often very uncertain, and this uncertainty, propagated into the luminosity and minimum grain size values, can strongly affect the derived physical properties of the disk.

   The detailed spectral shape of the stellar radiation affects the grain temperatures. While the IR part of hot white dwarf spectra is very similar to that of a blackbody, the UV part differs from it greatly. The UV spectrum can vary with different effective temperatures and elemental abundances. Therefore, wherever possible, we use appropriate synthetic spectra for WDs' atmospheres. If these are not available, then we use blackbody approximations for WDs' atmospheres.

5.5 Individual Objects

5.5.1 CSPN Sh 2-216

Sh 2-216 is the closest PN to the Earth, at a distance of 129 pc. Its SED in Figure 5.1 shows optical and IR photometric measurements as filled diamonds. The *Spitzer* IRS spectrum is presented as open purple diamonds, and the the thick red line represents the smoothed IRS spectrum. The SED follows the expected WD's photospheric emission up to $\sim$10 μm. Beyond this wavelength, the SED rises, and peaks near $\sim$40 μm.

For the radiation from the WD, we adopt the synthetic spectral model from Rauch et al. (2007), the associated WD effective temperature of 95,000 K and log g of 6.9. The WD model spectrum was calculated using the Tuebingen non-Local Thermodynamic Equilibrium Model Atmosphere Package (TMAP, Werner et al. 2003; Rauch & Deetjen 2003), considering the atoms of H, He, C, N, O, Mg, Si, Ca, Sc, Ti, V, Cr, Mn, Fe, Co and Ni, based on observed UV spectra from the *Far Ultraviolet Spectroscopic Explorer (FUSE)* and the *HST*. The detailed model atmosphere of this WD is presented by Rauch et al. (2007), and it is displayed in the SED as a black solid curve.

We model the dust emission using the optically thin dust model and assume that the dust is heated only by the central WD. Since the spectrum does not show any mineralogical features, we consider composition of both astronomical silicates and amorphous carbon.

We calculate the total flux from the WD by integrating the synthetic spectrum normalized to the optical and near-IR photometry, and use a distance of 129 pc, derived from WD's parallax (Harris et al. 2007), to estimate the WD luminosity of $\sim$44 $L_{\odot}$. Note that this value is lower than that derived by Rauch et al. (2007), 158.5 $L_{\odot}$, because of their larger spectroscopic distance, 224 pc. Using the WD luminosity of 44 $L_{\odot}$, a mass of 0.55 $M_{\odot}$ (Rauch et al. 2007), and a dust grain density of 2.5 g cm^{-3}, we find the minimum grain size to be $\sim$35 μm. We adopt the maximum grain size of 1 mm. We also assume a power-law grain size distribution with a power index of -3.5, i.e., $n(a) \propto a^{-3.5}$, typical of collisionally

produced dust, and a uniform disk surface density.

The observed mid-IR fluxes and IRS spectrum can be approximated by emission from a dust disk at radii ∼30-35 AU, with a dust mass of ∼0.001 $M_{\oplus}$. For comparison, adopting a dust composition of amorphous carbon gives a best fit for a disk between 24 and 25 AU, and a dust mass of ∼0.001 $M_{\oplus}$.

The dust around this WD appears to originate from a narrow ring. This is consistent with the fact that the IR spectrum and SED can be very well approximated by a blackbody with a single T_{eff} of 120 K. Indeed, the ∼50 μm grains which dominate the IR emission have a temperature of 120 K at ∼33 AU for silicate and ∼25 AU for amorphous carbon composition.

The PR lifetime for 35 μm grains at ∼30 AU is $\sim 10^6$ yr, greater than the upper limit to the dynamical age of the nebula, 4.6×10^5 yr, or typical post-AGB timescales, $\sim 10^4$ yr. Therefore, collisionally produced dust can remain in the system on timescales similar to the PN age. The inner hole in the disk, whose presence is evidenced by lack of excess emission below 8 μm, may imply an object that is clearing the dust in the inner system.

5.5.2 CSPN EGB 1

The SED of CSPN EGB 1 (Figure 5.2) is similar to those of CSPN Sh 2-216 and Helix. The optical and IR data points are at or below expected photospheric emission for wavelengths up to ∼10 μm. The IRS spectrum, displayed in the SED as a thick purple line, is a featureless continuum that rises at wavelengths longer than ∼10 μm.

To model the emission from the WD itself, we use the synthetic TMAP spectrum provided by T. Rauch, scaled to the WD's optical photometric measurements. The model atmosphere calculation was carried out for an effective temperature of 147,000 K and $\log(g)$ of 7.34 (Napiwotzki 2001), and included the atoms of H, He, C, N, O, F, Ne, Mg, Ar, Ca, Fe and Ni. It is displayed in the SED as a thick solid curve.

Assuming a distance of 650^{+290}_{-210} pc (Napiwotzki 2001) and integrating the synthetic spec-

trum scaled to WD's photometric measurements yields a WD luminosity of 521 $L_\odot$. With the WD mass of 0.65 $M_\odot$ (Napiwotzki 2001), the calculated WD luminosity, and adopting a dust grain density of 2.5 g cm^{-3}, we find that dust grains smaller than ∼360 μm will be blown out. Therefore, for our modeling, we adopt the grain sizes between 360 and 1000 μm. We consider an optically thin dust disk, heated only by WD 0103+732, with a constant surface number density, and a power law grain size distribution, where $n(a) \propto a^{-3.5}$.

We use the 24 μm data point, the IRS spectrum, and the 70 μm upper limit to produce the best fit. Note that the portion of the IRS spectrum containing atomic line emission is excluded from the χ^2 calculation. The best χ^2 is achieved for a narrow dust disk between ∼170–173 AU with a mass of 0.05 $M_\oplus$ for grains composed of astronomical silicates, and ∼82-84 AU with a mass of ∼0.07 $M_\oplus$ for amorphous carbon grains. The disk around WD 0103+732 appears to be a narrow ring. The IRS spectrum can be well fit by a blackbody of ∼110 K, which is the temperature of ∼360 μm silicate grains at ∼170 AU, and carbonaceous grains at ∼80 AU. Note, however, that the outer radius of the disk is not well constrained. The IRS spectrum is rising, but beyond ∼35 μm, other than the 70 μm upper limit, no data point constrains the IR emission. Photometric and spectroscopic measurements at longer wavelengths would be useful in constraining the outer radius of the dust disk.

The distance estimate to the WD carries a large uncertainty, and this uncertainty has a significant effect on the estimation of dust disk parameters. To demonstrate the uncertainty resulting from the lack of precision in the distance measurement, we repeat the modeling for the lower and upper distance limits from Napiwotzki (2001). For a distance of 440 pc, the luminosity of the WD is 240 $L_\odot$, the minimum grain size is 168 μm, the dust disk is located near ∼100 AU, and the dust mass is 0.012 $M_\oplus$. On the other hand, if the distance is 940 AU, the WD luminosity is 1090 $L_\odot$ and the minimum grain size is 770 μm. The disk is located near ∼ 230 AU and has a mass of 0.12 $M_\oplus$.

Adopting the model for the distance of 650 pc, the PR lifetime for dust at 80 or 170 AU is on the order of 10^7 yr, a timescale much longer than the dynamical age of the nebula

(20,000 yr) or typical post-AGB evolutionary timescales ($\sim 10^4$ yr). Therefore, the scenario of collisionally produced dust is feasible. If the dust is slowly spiraling in due to PR drag, one would expect the disk to extend to the sublimation radius. The clear inner hole may be implying an object that truncates the dust's inspiral, such as a large planet. The presence of an unseen body near the WD is also supported by the periodic variability in optical magnitudes (T. Hillwig, personal communication), but the nature of this body is not yet well understood.

5.5.3 CSPN K 1-22

CSPN K 1-22 has a distant companion at a projected distance 0.″35, or 470 AU (Ciardullo et al. 1999). It is unclear whether the excess IR emission, starting at the J-band, is associated with the WD, or its distant companion; high-resolution IR observations are needed to verify the positional coincidence of the dust disk and the CSPN. For purposes of our modeling, we consider the case where the dust surrounds the CSPN. Since the companion is too far and too cool to contribute significantly to the heating of the dust around the CSPN, we consider the CSPN as the only heating source.

The SED in Figure 5.3 shows V and I magnitudes from each star individually (Ciardullo et al. 1999), the remaining magnitudes are for the two stars combined. For the atmospheric model of CSPN K 1-22, we adopt the synthetic spectrum provided by T. Rauch, scaled to the WD's optical photometric measurements. The model atmosphere was calculated using TMAP for a WD with an effective temperature of 140,000 K and log g of 6.70 (Rauch et al. 1999), considering the atoms of H, He, C, N, O, F, Ne, Mg, Ar, Ca, Fe and Ni. The emission from the companion is approximated by a Kurucz model for an M0V star. The two solid curves show contributions from the two components. The sum of these components and the best-fit dust model is plotted as a thin solid curve.

We adopt the CSPN distance of 1.33 kpc (Ciardullo et al. 1999), and integrate the synthetic spectrum scaled to optical magnitudes to find CSPN luminosity of $\sim$300 $L_\odot$. For

the stellar mass of 0.59 $M_\odot$ (Rauch et al. 1999) and grain density of 2.5 g cm^{-3}, all grains smaller than 210 μm will be blown out of the system. Thus, we carry out the dust modeling for grain sizes between 210 and 1000 μm, assuming constant surface number density and a power law ($n(a) \propto a^{-3.5}$) grain size distribution.

We use the IRS spectrum of CSPN K 1-22 to calculate χ^2, but exclude the portions that are affected by imperfect nebular subtraction. The best fit for silicate grain composition is achieved for a disk extending from sublimation temperature up to ∼43 AU, with a dust mass of 0.001 $M_\oplus$. For carbon grains, the best-fit disk also starts at sublimation radius, extends to ∼20 AU, and also has a mass of 0.001 $M_\oplus$. The SED of the best fit for silicate grains is presented in Figure 5.3.

The distance to CSPN K 1-22 has a large uncertainty, and different authors cite values between 1.33 and 3.43 kpc (e.g., Ciardullo et al. 1999; Rauch et al. 1999). This uncertainty can have a large impact on the derived disk parameters. Due to the near-IR excess, the model's inner radius will start at disk sublimation temperature, but the minimum grain sizes, outer radii and disk masses will be affected by the uncertain distance.

The PR lifetime for 210 μm dust grains at 40 AU is $\sim 3 \times 10^6$ yr. This is longer than the dynamical age of the nebula, ∼55,000 yr, or the timescale of post-AGB evolution, $\sim 10^4$ yr. Hence, it is feasible that dust produced in collisions that was not blown out of the system is now observed as the excess IR emission.

5.5.4 CSPN NGC 2438

SED modeling of CSPN NGC 2438 is complicated. First, the optical photometric measurements of the CSPN in the literature are varied, thus precluding a good grasp on the WD's photospheric contribution. The near-IR emission is not well constrained, with only the J measurement available, and both IRAC and MIPS data points have large uncertainties, especially the MIPS 24 μm flux density. Furthermore, the IR spectrum has low signal to noise ratio, and is affected by strong emission lines.

For the CSPN's photospheric emission, we use a blackbody approximation for an effective temperature of 114,000 K, a distance of 1200 pc, radius of 4.5 $R_{\oplus}$, luminosity of 260 $L_{\odot}$ and mass of 0.56 $M_{\odot}$. For this configuration, grains smaller than 213 μm will be blown out of the system by radiation pressure. To trace the shape of the excess emission, we use the IRAC data points, the MIPS data point, and three data points from the *Spitzer* IRS spectrum to capture the overall SED shape between 7.5 and 15 μm. These data points were chosen at portions of the spectrum not affected by line emission.

The SED of the excess emission is not well fit by a single disk component, even if we experiment with a non-uniform surface density distribution. In fact, there appear to be three distinct components in the spectrum - the flat component between 1 and 8 μm, the rising spectrum between 8 and 15 μm, and even more sharply rising emission between 15 and 24 μm. The 24 μm flux density is likely contaminated by emission lines, because the source is surrounded by diffuse nebulosity. A spectrum near 24 μm is necessary to assess the continuity of the 15–24 μm spectral shape.

The spectrum at 7–15 μm can be approximated by a dust disk between 10 and 90 AU, with a mass of $\sim$0.003 $M_{\oplus}$. The PR lifetime for dust at 10 and 90 AU is (0.14 – 11.6) $\times$ 10^6 yr, longer than the estimated age of the CSPN. The inner hot dust component can be approximated by a disk between the sublimation temperature and $\sim$2 AU with a mass of $\sim$ 10^{-6} $M_{\oplus}$. However, the PR lifetime for dust at such distances is $\sim 10^3$ yr, much less than the estimated age of the CSPN, (20–110) $\times$ 10^3 yr. Such a hot dust disk is therefore likely optically thick.

Note that these models are approximate, and that the total number of model parameters is greater than the number of data points. Therefore, there can be many degeneracies in the dust disk model. Better constraints on the optical WD spectrum and the spectral shape near 24 μm are needed to model the IR excess of CSPN NGC 2438 more accurately. Furthermore, a search for a companion would help decipher whether the IR excess around this CSPN originates from collisions, or is more likely to be associated with a binary phenomenon. In

addition, an optically thick model will be necessary for the modeling of the hot dust near the sublimation radius.

5.5.5 CSPN NGC 7139

CSPN NGC 7139 has an IR excess starting from the J band, but the signal to noise ratio in JK are below 3, and only an upper limit is established for the H band. The 7–15 μm spectrum in the IRAC bands is flat.

We approximate the CSPN's atmospheric emission by a blackbody with the parameters listed in Table 5.1: $T_{\rm eff}$ of 117,000 K, luminosity of 81 $L_{\odot}$, and mass of 0.64 $M_{\odot}$. For these parameters, dust grains with radii smaller than 57 μm will be blown out of the system by radiation pressure.

We trace the IR SED with 10 points chosen between 1 and 15 μm - four points in the JHK Gemini NIRI spectrum, four IRAC photometric measurements, and two points from the emission line-free portion of the IRS spectrum. A very narrow (<0.1 AU) disk at the sublimation temperature radius ∼0.3 AU can roughly approximate the IR excess SED, and it yields a dust mass of $\sim 10^{-6}$ $M_{\oplus}$. Note however that the PR lifetime for 57 μm dust around this CSPN is ∼110 yr, significantly shorter than the CSPN's evolutionary age, 14,700 yr. Therefore, the dust disk must be optically thick to remain around the CSPN for long periods. The optically thick nature of the disk is also supported by the high extinction toward the CSPN, $E(B-V)$∼0.52. Most likely, the observed near-IR emission comes from the inner optically thin sublimating layer of an optically thick disk, similar to the case of disks commonly seen around post-AGB binaries (de Ruyter et al. 2006). Future observations aiming to detect a binary companion of the CSPN are needed to strengthen or weaken the link between the disk near NGC 7139 and that of post-AGB binaries.

5.5.6 CSPN NGC 6804

NGC 6804 is the least evolved CSPN in our sample. We approximate the CSPN's atmosphere by a blackbody with $T_{\rm eff}$ of 90,000 K, luminosity of 3885 $L_{\odot}$, and mass of 0.6 $M_{\odot}$. For these CSPN parameters, all grains with radii smaller than ∼3 mm should be blown out of the system. For the ∼3 mm grains are to produce the observed IR emission, the dust mass in the disk must be ∼1.5 $M_{\oplus}$. This value is very high and not consistent with mass estimates for main-sequence stars' debris disks. Furthermore, the silicate spectral feature at 10 μm evidences the presence of small ∼μm-sized grains within the dust disk. The dust disk must be optically thick for such small grains to remain in the system with such a strong radiation field. An appropriate optically thick model is needed to simulate this dust disk.

The disk around NGC 6804 is very similar to those around post-AGB binaries. Unresolved emission-line source coincident with the CSPN implies that the disk is gas-rich, as are the circumbinary post-AGB dust disks. They also exhibit the 10 μm silicate emission, which has, like NGC 6804, features of crystalline silicates. The post-AGB dust disks are optically thick, with an optically thin inner layer, which is responsible for the silicate emission. Because the disk is optically thick, the grains inside are shielded from the strong radiation, and thus can be stable over longer periods of time.

The evolution of post-AGB dust disks into the PN stage is not well understood. The dust disk around NGC 6804 may be a glimpse into the future of post-AGB circumbinary disks. However, no binary companion of CSPN NGC 6804 has been reported to date. Future photometric or radial-velocity monitoring is necessary to examine the presence of a binary companion to this CSPN.

5.5.7 CSPN NGC 2346

CSPN NGC 2346 is a complex system that contains a close binary in which most light is provided by the main-sequence companion. It is a photometric and spectroscopic variable

with a period of ∼16 days (Mendez & Niemela 1981; Mendez et al. 1982). This system is surrounded by a dust disk and/or cloud, and the cloud was suggested to be responsible for CSPN fading in 1981-1985 and 1996-1997 (Costero et al. 1986; Kato et al. 2001). The short PR lifetime (1–100) × 10^3 yr (considering only the CSPN's radiation), the high extinction toward the CSPN, and the presence of gas in the disk all suggest that the dust surrounding the binary system is optically thick. Therefore, an optically thick dust model is needed to simulate the disk around CSPN NGC 2346.

5.5.8 CSPN EGB 6

As described in section 2.3.8, EGB 6 has a distant companion, surrounded by a dense gaseous disk. The IRS spectrum of CSPN EGB 6 shows rising continuum emission, but it is not clear whether this continuum is associated with the CSPN or its companion. The SED of the mid-IR excess can be approximated by two blackbody components with the temperatures of 500 and 150 K, respectively. For the WD parameters listed in Table 4.3 (0.64 $M_\odot$, 97 $L_\odot$ star), dust smaller than ∼70 μm will be blown out of the system. The PR lifetime for such dust grains is ∼10^3 and ∼10^5 yr for the equilibrium-temperature distances of the two temperature components. The dynamical age of the nebula, 135,000 yr, is between these two lifetime estimates. It is not clear whether the dust around CSPN EGB 6 is optically thick or thin. Detailed modeling of this dust disk is carried out by Su et al. (2012, in preparation).

5.6 Summary

We have constructed simple models of the dust disks surrounding hot WDs with excess IR emission. For WDs/CSPNs without spectroscopic observations, the basic disk parameters are derived based on blackbody approximations to the IR SEDs. For cases with available spectroscopic observations, where appropriate, we use optically thin dust disk models with realistic grain properties and distributions to match the IR spectral shapes and derive the

disk properties.

For cases with IR excesses at wavelengths longer than $\sim$6 μm (e.g., CSPN Sh 2-216, CSPN EGB 1), the dust is located a few tens of AUs from the central stars, consistent with the expected general location of planetesimals. The lack of near-IR excess does not lend support to the presence of a binary companion. The PR lifetimes for dust grains that dominate the emission are long enough for the dust to remain in the system for timescales comparable to the estimates of the WD/CSPN ages. In these cases, the origin of dust as collisionally disrupted planetesimals is consistent with the derived disk properties.

Some CSPNs exhibit not only mid-IR, but also near-IR excesses (e.g., CSPN NGC 6804, CSPN NGC 2438). While the dust disk around CSPN K 1-22 can be modeled by a single disk component extending from sublimation radius to $\sim$ 40 AU, in other cases, like that of NGC 2438, a single disk component is not sufficient to fit the data. Furthermore, short PR lifetimes imply that some of the disks must be optically thick, and further modeling with an appropriate disk model is needed. These optically thick disks may not originate from collisionally disrupted planetesimals, but may instead be remnants of circumbinary post-AGB dust disks (de Ruyter et al. 2006). The dust disk around CSPN NGC 6804 in particular resembles those around post-AGB stars. It is gas-rich, optically thick, and exhibits a 10 μm crystalline silicate feature, just like the dust disks around post-AGB binaries. However, only a few of these CSPNs are known to have binary companions, and except for NGC 2346, they are wide, separated by few hundred AU from the CSPN. Future photometric or RV monitoring, as well as high-resolution imaging is needed to search for binary companions of these CSPNs.

More data are needed to constrain the parameters of dust disks around these hot WDs. Wavelength coverage over a large range would help constrain the locations of the disks; observations at wavelengths $>$24 μm would be especially useful in constraining the disks' outer radii. IR spectra, especially for stars still surrounded by PNe, are necessary to measure the dust continuum level, assess the nebular contamination, and reveal mineralogical features of

the dust. Resolving the dust disk with interferometric observations and measuring the disks' surface brightnesses and outer radii would be very useful for constraining the parameters in the debris disk models. Better theoretical understanding of post-AGB binary dust disks, and their evolution into the PN stage, as well as debris disk evolution past the main sequence, would help us compare the derived disk properties to the theoretical predictions.

Table 5.1. Physical Parameters of Dust Disks

Name	L_* [$L_\odot$]	M_* [$M_\odot$]	$a_{\rm min}$ [μm]	$T_{\rm dust}$ [K]	EA [AU^2]	$r_{\rm dust}$ [AU]	$M_{\rm dust}$ [$M_\oplus$]	$\tau_{\rm PR,amin}$ [yr]
CSPN EGB 1	479	0.65	338	190	1.55	25	2.8×10^{-3}	7.7×10^{5}
CSPN A21	107	0.58	85	150	0.85	32	7.7×10^{-4}	1.4×10^{6}
CSPN Sh 2-216	34	0.53	29	150	0.48	19	2.6×10^{-4}	5.5×10^{5}
CSPN DeHt 5	15	0.44	16	190	0.25	8.2	9.8×10^{-5}	1.2×10^{5}
CSPN Sh 2-188	42	0.56	34	900	0.0008	0.6	4.6×10^{-7}	5.3×10^{2}
				150	0.68	22	3.9×10^{-4}	6.9×10^{5}
CSPN K 1-22	325	0.59	253	700	0.034	2.7	5.3×10^{-5}	9.9×10^{3}
				150	5.92	58	9.3×10^{-3}	4.6×10^{6}
CSPN NGC 6853	140	0.56	115	190	5.33	28	5.6×10^{-3}	1.1×10^{6}
CSPN NGC 7293	69	0.58	55	100	105	57	7.7×10^{-2}	4.5×10^{6}
CSPN EGB 6	97	0.64	70	500	0.12	1.7	9.9×10^{-5}	3.6×10^{3}
				150	15.	19	1.2×10^{-2}	4.5×10^{5}
CSPN NGC 2438	260	0.56	213	1200	0.0005	0.87	7.2×10^{-7}	1.1×10^{3}
				150	57	56	8.2×10^{-2}	4.5×10^{6}
CSPN NGC 7139	81	0.64	58	1650	0.004	0.3	3.0×10^{-6}	7.8×10^{1}
CSPN NGC 6804	3885	0.60	2994	1400	0.12	2.5	6.5×10^{-4}	8.1×10^{3}
				550	6.2	16	3.3×10^{-2}	3.4×10^{5}
				250	155	77	8.4×10^{-1}	8.0×10^{6}
CSPN NGC 2346	81	0.39	95	1000	2.2	0.7	2.1×10^{-3}	1.0×10^{3}
				250	37	11	3.6×10^{-2}	2.5×10^{5}
WD 0109+111	23	0.74	14	150	0.067	25	2.5×10^{-5}	6.9×10^{5}
WD 1342+443	6	0.69	4	150	0.13	13	2.5×10^{-5}	2.0×10^{5}

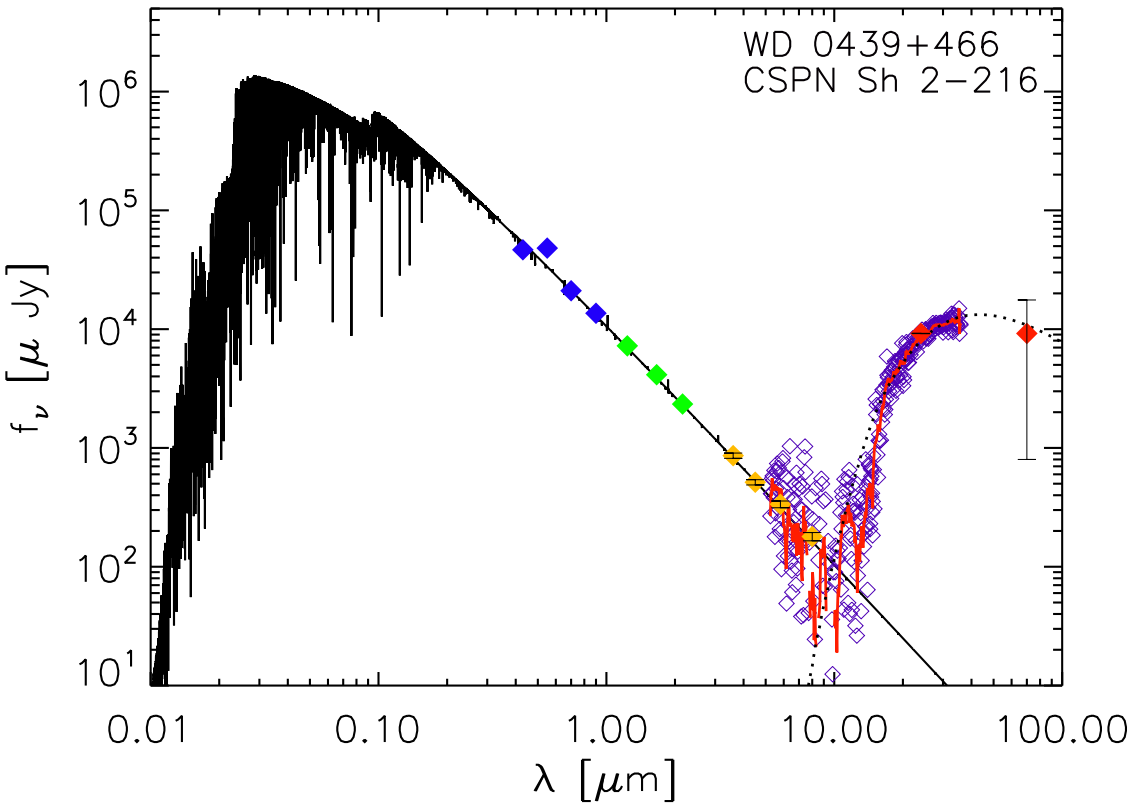

Figure 5.1: The SED and dust disk model for WD 0439+466. The SED is constructed with optical photometry from the literature, 2MASS JHK flux densities, our *Spitzer* IRAC and MIPS 24 and 70 μm photometric measurements, displayed as solid diamonds. The TMAP model atmosphere for the WD is displayed as black solid curve. The *Spitzer* IRS spectrum is shown in purple open diamonds, and the smoothed spectrum is shown in red solid line. The dotted curve represents the best-fit dust disk model for silicate grains located between $\sim$30 and 35 AU from the CSPN.

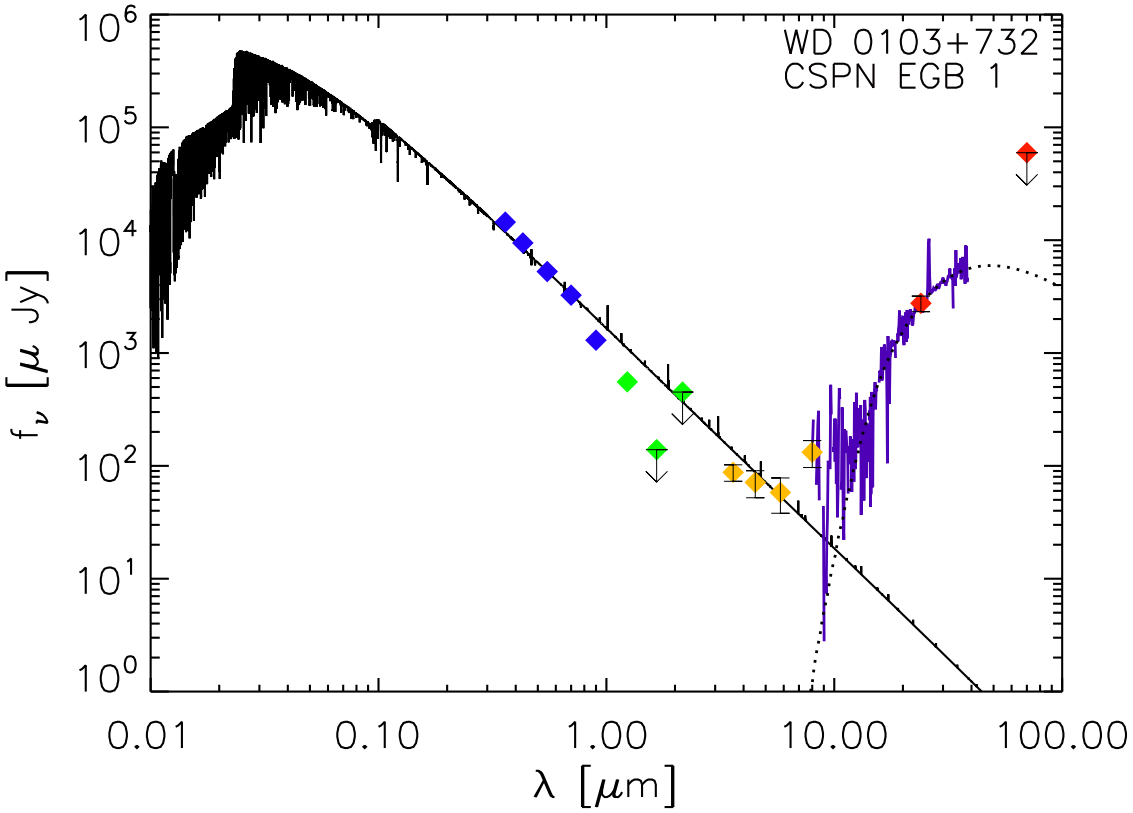

Figure 5.2: The SED and dust disk model for WD 0103+732. The SED is constructed with optical photometry from the literature, 2MASS JHK flux densities, our *Spitzer* IRAC and MIPS 24 μm photometric measurements, displayed as solid diamonds; the HK and 70 μm upper limit are displayed as downward arrows. The TMAP model atmosphere for the WD is presented as black solid curve. The smoothed *Spitzer* IRS spectrum is shown in purple thick line. The dotted curve represents the best-fit dust disk model for silicate grains located between $\sim$170 and 173 AU from the CSPN.

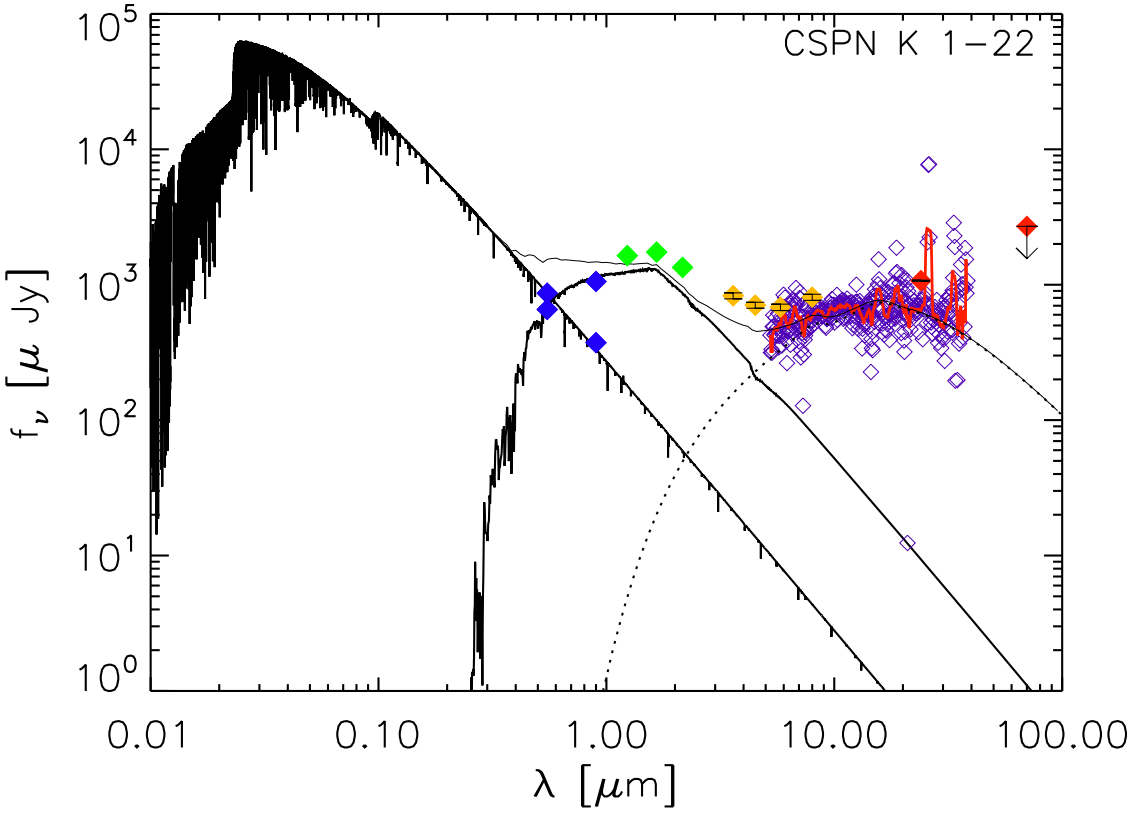

Figure 5.3: The SED and dust disk model for CSPN K1-22. The CSPN has a wide companion, and the VI photometric measurements are shown for each star individually as blue diamonds. The 2MASS JHK flux densities, our *Spitzer* IRAC and MIPS 24 μm photometric measurements, displayed as solid diamonds are for the two stars combined. The downward arrow represents the 70 μm upper limit. The TMAP model atmosphere for the WD and a Kurucz model for the companion's emission are displayed as black solid curve. The *Spitzer* IRS spectrum is shown in purple open diamonds, and the smoothed spectrum in red solid line. The dotted curve represents the best-fit dust disk model for silicate grains located between the sublimation radius and ∼40 AU from the CSPN. The sum of all emission components is displayed as a thin solid curve.

Chapter 6

Hard X-ray Emission Associated with White Dwarfs. III.

6.1 Introduction

White dwarfs (WDs) represent the final evolutionary stage of intermediate- and low-mass stars. Depending on their effective temperature ($T_{\rm eff}$) and composition, or opacity, their photospheric emission can be observed from near-infrared (IR) up to soft X-rays ($\lambda \gtrsim 25$ Å, $h\nu \lesssim 0.5$ keV), but no detectable hard X-ray emission (>0.5 keV) is expected from single WDs.

Many WDs are associated with hard X-ray emission. Almost all of them are in binary systems with a late-type companion, and the hard X-rays originate either from the companion's active corona, or from the accretion of the companion's material onto the WD's surface, as in a cataclysmic variable. Using the *ROSAT* All-Sky Survey, Fleming et al. (1996) found nine WDs with hard X-ray emission due to late-type companions. O'Dwyer et al. (2003, hereafter Paper I) and Chu et al. (2004b, hereafter Paper II) conducted systematic searches for hard X-ray emission from WDs in the McCook & Sion (1999) catalog, using *ROSAT* WGA point source catalog (WGACAT, White et al. 2000), and catalogs of *ROSAT* Results Archive Sources for the Position Sensitive Proportional Counter observed with and without the boron filter (ROSPSPCFCAT[1], and ROSPSPCCAT[2], respectively). They found 12 additional WDs in binary systems that are associated with hard X-ray emission.

Few apparently single WDs with hard X-ray emission are known. The soft X-ray emission

[1]Available at ftp://ftp.xray.mpe.mpg.de/rosat/catalogues/2rxf/pub/

[2]Available at ftp://ftp.xray.mpe.mpg.de/rosat/catalogues/2rxp/pub/, can be browsed at http://heasarc.gsfc.nasa.gov/docs/archive.html

of KPD 0005+5106 was detected in the *ROSAT* All-Sky Survey by Fleming et al. (1993), but an additional component of hard X-ray emission peaking near 1 keV was later detected in a pointed PSPC observation made with the boron filter (Paper I). For a canonical $L_{\rm X}/L_{\rm bol}$ of late-type coronal stars, the observed hard X-ray luminosity of KPD 0005+5106 requires a companion that is bright in the IR; the lack of IR excess thus excludes the existence of a coronal companion (Chu et al. 2004a). The origin of the hard X-ray emission of KPD 0005+5106 is still unknown. Another apparently single WD with hard X-ray emission is WD 2226−210, the central star of the Helix Nebula. Its hard X-ray emission peaks at 0.8-0.9 keV (Leahy et al. 1994) and appears unresolved in *Chandra* observations (Guerrero et al. 2001). Based on the hard X-ray luminosity and variations, as well as the variations in the stellar Hα line profile, it has been suggested that WD 2226−210 has a late-type companion (Guerrero et al. 2001; Gruendl et al. 2001); however, *HST* images do not show any companion (Ciardullo et al. 1999), and the near- to mid-IR photometry of WD 2226−210 excludes the existence of a companion down to brown dwarfs (Paper I; Su et al. 2007). A less publicized single WD with hard X-ray emission is WD 1159−034 (PG 1159); its hard X-ray emission is detected at a 3σ level (Paper I).

Since the systematic searches reported in Paper I and Paper II, the number of spectroscopically confirmed WDs in McCook & Sion's catalog has increased from 2,449 to 12,456 (as of September 2009), mainly due to the release of the Sloan Digital Sky Survey data (Eisenstein et al. 2006). In addition, the *XMM-Newton* satellite, launched in 1999, provided observations with much higher angular resolution (6″ on-axis) and ∼6 times higher effective area at 1 keV than *ROSAT*. The latest version of *XMM-Newton*'s Serendipitous Source Catalog (XMMSSC, or 2XMMi) as of September 2009 contains ∼290,000 X-ray sources. With a significantly larger number of known WDs as well as new X-ray data available, we have made another systematic search for hard X-ray emission from WDs, using the updated list of WDs from McCook & Sion (2006) and X-ray catalogs of ROSPSPCCAT, ROSPSPCFCAT, and XMMSSC. The aim is twofold: (1) to search for single WDs with hard X-ray emission

similar to WD 2226−210 in the Helix Nebula or KPD 0005+511, and (2) to diagnose WDs with late-type companions through hard X-ray emission. The results of these searches are reported in this paper. In Section 2, we describe the search for WDs with hard X-ray emission, in Section 3, we briefly describe the WDs with hard X-ray emission not previously reported in Papers I and II, and in Section 4, we present a summary and conclusions.

6.2 Search for Hard X-ray Sources associated with White Dwarfs

We use the J2000 coordinates from the latest text version of the McCook & Sion's WD catalog (McCook & Sion 2006) for WD coordinates. However, some WDs only have 1950 coordinates listed; for these WDs, we search for the coordinates in SIMBAD, or convert 1950 coordinates to J2000 values using the IRAF task precess. We adopt the positional uncertainty based on the given precision of the coordinates.

Next, we cross-correlate the WD coordinate list with ROSPSPCCAT, ROSPSPCFCAT, and XMMSSC catalogs. For WDs with positional uncertainty smaller than $1'$, we search for X-ray sources within $1'$ from the WD coordinates; for WDs with positional uncertainty greater than $1'$, we search for X-ray sources within $2'$. These search radii should sufficiently account for positional uncertainties and changes of WD coordinates due to high proper motions. Only 12 WDs in McCook & Sion (2006) are known to have proper motions that exceed $1''\mathrm{yr}^{-1}$; the WD with the highest proper motion, $\sim 4''\mathrm{yr}^{-1}$, is WD 0413-077. As we are searching for hard X-ray emission associated with WDs, we select only sources detected with $\geq 3\sigma$ significance at energies between 0.5 and 2 keV, i.e., band B for ROSPSPCCAT and ROSPSPCFCAT, and the sum of bands 2 (0.5-1 keV) and 3 (1-2 keV) for XMMSSC. XMMSSC reports source counts separately for the three detectors onboard *XMM-Newton*, i.e., European Photon Imaging Camera (EPIC) PN, MOS1 and MOS2. As long as a source is detected in hard X-rays by any one of these detectors, it is selected for further examination.

This initial search has yielded 72 WDs from XMMSSC, 48 WDs from ROSPSPCCAT, and 6 WDs from ROSPSPCFCAT.

Although our search included ∼10,000 more WDs than that of Papers I and II, no new hard X-ray sources associated with WDs are detected in ROSPSPCFCAT (i.e., observations made with the boron filter). The 6 candidate WDs with hard X-ray emission from ROSPSPCFCAT have been previously discussed in Paper I or Paper II. Among these, WD 0512+326, WD 1314+293 and WD 1631+781 are in binary systems with late-type coronal companions, WD 0005+511 (=KPD 0005+5106) and WD 2226−210 are apparently single, and WD 1821+643 is contaminated by an adjacent background source. These sources will not be further discussed in this paper.

For the candidate WDs with hard X-ray emission found in ROSPSPCCAT (i.e., observations made without the boron filter), we download data product images in the soft (0.11−0.41 keV) and hard (0.5−2.02 keV) bands. For XMMSSC sources, we download data product images in bands 2 (0.5−1 keV) and 3 (1−2 keV) for the EPIC MOS1, MOS2, and PN detectors, and spectra, when available. We supplement the X-ray images with the Digitized Sky Survey (DSS2) red and blue images, as well as the Two Micron All Sky Survey (2MASS) JHK images, to examine the positional coincidence between the X-ray sources and WDs. We use the coordinates supplied by McCook & Sion (2006) as well as the finding charts provided in the web version of the catalog to identify the WDs. We overlay gaussian-smoothed hard X-ray contours on the optical and near-IR images and examine the positional coincidence of the hard X-ray contours with the optical and near-IR images. We eliminate spurious detections of sources where (1) hard X-ray contours are coincident with an optical counterpart in the search cone that is not the WD; (2) the WD is in a crowded field (e.g., globular cluster), and the exact counterpart of the X-ray source cannot be identified; (3) X-ray source is offset from the WD by more than ∼40″; (4) the WD is near a very bright X-ray source, and the variations within the point-spread function (PSF) are misidentified as a separate point source; or (5) faint sources marginally identified in the catalog that are not

confirmed in the visual inspection.

Among the 48 ROSPSPCCAT sources, we find 22 hard X-ray sources associated with WDs; of these, 13 were reported in Papers I or II, but not the other 9. We also find 4 WDs with nearby (within $\sim$40″) hard X-ray sources that are not associated with the WDs, 3 of which were discussed in Paper I. The remaining 22 sources were spurious detections. Using XMMSSC, we find 20 hard X-ray sources associated with WDs; of these, 9 were reported in Papers I or II, but not the other 11. We also find 8 hard X-ray sources that are near (within $\sim$30″), but not associated with the WDs; of these, one has been discussed in Paper I. Another 44 sources were spurious detections.

The WDs coincident with hard X-ray sources detected in XMMSSC, ROSPSPCCAT, and ROSPSPCFCAT are listed in Tables 6.1−6.3. The previously reported cases are also included in the tables; spurious sources within $\sim$40″ are also included, but listed separately in the bottom sections. Columns (1)−(3) give the WD number, spectral type and common names; columns (4)−(6) give the X-ray source name, observation ID, and exposure time; column (7) describes the positional coincidence of the WD and hard X-ray source; columns (8)−(10) list the counts in the soft, medium, and hard energy bands, i.e., 0.2−0.5, 0.5−1.0, and 1.0−2.0 keV for XMMSSC, and 0.11−0.41, 0.52−0.9, and 0.9−2.01 keV for ROSPSPCCAT/ROSPSPCFCAT, respectively. The EPIC-PN counts are listed for the XMMSSC sources, unless noted in the remarks. Column (11) lists remarks on individual X-ray sources, where P1 marks sources discussed in Paper I, P2 marks sources discussed in Paper II, N marks the new sources, M1 and M2 label sources for which the table lists MOS1 and MOS2 fluxes, respectively, and EP indicates that the source is detected with 3σ significance only after summing all of *XMM-Newton*'s EPIC instruments.

To further examine the spectral properties of the *XMM-Newton* detections, we have obtained the preprocessed event files from the HEASARC archive. We have used XSELECT to extract the source and background spectra; the background spectra were taken from a blank sky region near the source. Each spectrum was then binned in GRPPHA so that each

energy bin has at least 25 photons over the whole energy range. Instrumental response and effective area were calculated using the rmfgen and arfgen commands in the *XMM-Newton* Science Analysis System suite. Spectral analysis was performed in XSPEC (v. 12.6.0). No single component model was sufficient to fit any of the WD spectra in our sample. All of the models presented are multi-component fits consisting of combinations of a Raymond & Smith (1977) thermal plasma (*raymond*) with solar abundances, and a power law photon spectrum (*powerlaw*). Fits were either a two temperature plasma, or a power law and plasma emission. The χ^2 fitting statistics were used to select the best fits.

Figures 6.1 and 6.2 show the X-ray spectra for WDs with hard X-ray emission in *XMM-Newton* that were sufficiently bright but not piled up. Figure 6.1 shows spectra for sources previously reported in Papers I or II, where the origin of the hard X-ray emission has been discussed. The spectral characteristics of these different sources help assess the nature of the new detections of WDs with hard X-ray emission. Figure 6.2 shows spectra and models for the new *XMM-Newton* detections of WDs not previously reported in Papers I and II.

6.3 Description of Individual white Dwarfs with Hard X-ray Emission

Here we describe individual WDs with hard X-ray emission that were not reported in Papers I and II. We also include descriptions of cases in which an X-ray source is near the WD, but is not associated with it.

6.3.1 XMM: Convincing Associations

WD 0232+035, also known as Feige 24, is a post-common envelope binary and a pre-cataclysmic variable (CV) with a period of 4.23 days (Vennes & Thorstensen 1994). The

effective temperature and mass of the WD are 57,000 K and 0.57 $M_{\odot}$, respectively, and the derived secondary mass of 0.39 $M_{\odot}$ corresponds to a dM1.5–2 spectral type (Vennes & Lanz 2001; Kawka et al. 2008). The X-ray spectrum cannot be fitted by a single blackbody model or a single thermal plasma model. Even a two-component model with a 57,000 K blackbody (representing the WD's photospheric emission) and a thermal plasma cannot fit the spectrum well. The best fits from the two-plasma model and the plasma + power law model are given in Table 6.4 and shown in Figure 6.2. The two-plasma model gives a better fit (reduced $\chi^2 = 1.5$), with plasma temperatures of 0.05 and 0.8 keV for the two components, respectively. The best-fit plasma + power law model gives a plasma temperature of 0.8 keV, similar to the hotter component of the two-plasma model. To assess whether the hard X-ray emission is attributed to the coronal emission of the dM companion, we have computed and listed in Table 6.5 the ratio of $L_{\rm X}/L_{\rm bol}$, where $L_{\rm X}$ is the X-ray luminosity in the 0.3-10.0 keV band derived from the best-fit 2-plasma model and a distance of 69 pc (Benedict et al. 2000), assuming no foreground absorption, and $L_{\rm bol}$ is the bolometric luminosity of a dM1.5–2 star. The computed $L_{\rm X}/L_{\rm bol}$, 2–2.5$\times10^{-4}$, is in the range expected for coronal emssion from dM stars (Fleming et al. 1995). It is thus likely that the hard X-ray emission associated with WD 0232+035 originates from its dM companian. The soft X-ray emission may consist of contributions from the dM companion's corona and the WD's photospheric emission. To further analyze the nature of WD 0232+035's X-ray emission, high-quality spectra at different orbital phases are needed in the future.

WD 0419−487, also known as RR Caeli, is a pre-CV and an eclipsing binary with an orbital period of ∼7.3 hours (Bruch & Diaz 1998; Bruch 1999). Maxted et al. (2007) analyzed the light curve and spectrum of this binary, and derived an effective temperature of 7,540 K and a mass of 0.44 $M_{\odot}$ for the WD, and a mass of 0.182-0.183 $M_{\odot}$ for the companion, corresponding to an M4 dwarf. The X-ray spectrum falls off more slowly on the high-energy side than those of the coronal emission from a dM companion. The spectrum is better fitted by a 0.35 keV thermal plasma + photon power law with photon power index

of 1.8 (reduced χ^2=1.017), than a two-plasma model with temperatures of 0.31 and 4.4 keV (reduced χ^2=1.17). Using these models and a distance of 11 pc (Bruch 1999) and an $L_{\rm bol}$ of a dM4 star, we calculate the $L_{\rm X}/L_{\rm bol}$ ratio to be 4.10 $\times 10^{-5}$. WD 0419−487 was also detected in ROSPSPCCAT. For comparison, we estimate $L_{\rm X}/L_{\rm bol}$ using observed PSPC count rates, the distance, and assuming a 0.3 keV plasma, yielding $L_{\rm X}/L_{\rm bol}$ of 6.41$\times 10^{-4}$. The two $L_{\rm X}/L_{\rm bol}$ differ by a factor of ∼4, partially caused by the more limited energy response of ROSAT PSPC, only up to 2.4 keV. Both $L_{\rm X}/L_{\rm bol}$ estimates are within the range expected for dM stars. Although the dMe companion may be able to account for the bulk of the hard X-ray emission, the high-energy tail and the short orbital period indicate that some accretion may be occurring.

WD 0905−724 is a binary companion to HR 3643 identified by Landsman et al. (1996). No evidence of radial velocity variation has been found, and the binary is not resolved by the *HST*, thus constraining the upper limit of the period to ∼21 years (Barstow et al. 2001). From the *International Ultraviolet Explorer* UV spectra, Holberg et al. (2003) derived the companion's spectral type of F9 II. The X-ray spectrum of this WD is severely piled up, so no spectral modeling could be carried out.

WD 1026+002 was discovered in the Palomar Green Survey (Green et al. 1986). This post-common envelope short-period (P≈0.597 days) binary consists of a DA WD with 17,600 K effective temperature and 0.65 $M_\odot$ mass, and a dM4e companion with a mass of 0.22 $M_\odot$ (Saffer et al. 1993). Too few counts are detected for a meaningful spectrum. We therefore estimate the $L_{\rm X}$ value with WebPIMMS[3], using the observed count rates, a distance of 38 pc (Liebert et al. 2005), and assuming a plasma temperature of 0.3 keV without foreground absorption. We find that $L_{\rm X}/L_{\rm bol} = 4.68\times 10^{-5}$, where $L_{\rm bol}$ is the expected bolometric luminosity of the dM4 companion. This $L_{\rm X}/L_{\rm bol}$ is within the range expected for coronal emission of a dM star. As coronal X-ray emission is commonly detected in dMe stars (Rucinski 1984), the dM4e companion is likely responsible for the observed hard X-ray

[3]http://heasarc.gsfc.nasa.gov/Tools/w3pimms.html

emission associated with this WD.

WD 1254+223 is a DA1.3 WD with $T_{\rm eff}$ of ∼40,000 K, mass of 0.6 $M_\odot$, and distance of 68 pc (Lajoie & Bergeron 2007). Near-IR photometry does not support the presence of a low-mass companion (Mullally et al. 2007). Hard X-ray emission is detected only in the *XMM* band 2 (0.5−1 keV), but not in band 3 (1−2 keV). The spectrum drops off monotonically and steeply towards 1 keV, and does not resemble spectra of late-type stars with coronal activity. This spectral shape is similar to that of WD 1234+481 (Paper I), which shows excess emission in $0.4 - 0.6$ keV, but not much beyond. Unlike WD 1254+223, WD 1234+481 does show IR excess, and follow-up spectroscopic observations suggest an L-type brown dwarf companion (Mullally et al. 2007; Steele et al. 2007). It is not clear whether the brown dwarf companion contributes to the hard X-ray shoulder of the WD's photospheric emission. The spectrum of WD 1254+223 cannot be fitted well by a blackbody model with the $T_{\rm eff}$ of the WD, or even higher temperatures. Furthermore, the observed X-ray flux by far exceeds that expected from the photospheric emission approximated by a blackbody model of ∼40,000 K with a radius of ∼1 $R_\oplus$ at a distance of 68 pc. Therefore, the WD photosphere alone cannot account for the X-ray emission. The spectrum can be modeled with a combination of a photon power law with photon power index of 6.9 and a solar-abundance 0.1 keV plasma (reduced $\chi^2 = 1.8$), but the physical significance of this model is unclear, and the origin of the X-ray emission is unknown.

WD 1310−230, or V396 Hya, is a double degenerate interacting binary, in which a 0.77 $M_\odot$ WD accretes material from a 0.17 $M_\odot$ helium degenerate donor through an accretion disk, indicated by triple-peaked He lines (Ruiz et al. 2001). The orbital period of this system is 65.1 minutes, and it is known to be a strong X-ray source. The X-ray emission, detected up to ∼7 keV, is powered by accretion. The X-ray spectra were modeled by Ramsay et al. (2006) with a multi-temperature plasma with maximum temperature of 5.5 keV, that was hydrogen-deficient but had an enhanced content of nitrogen and neon.

WD 1347−129 is an eclipsing binary, which has been analyzed in detail by O'Donoghue et al. (2003). It consists of a DA WD with a mass of 0.78 $M_\odot$ and an effective temperature of 14,220 K, and a 0.43 $M_\odot$ M3.5-M4 dwarf companion with an orbital period of 3 hr 37 min. O'Donoghue et al. (2003) argue that the the M dwarf just fills its Roche lobe, and that the rapid rotation of the WD ($v \sin i \approx 400$ km s^{-1}) indicates that the system has undergone mass transfer in the past, and is a hibernating CV. The hard X-ray emission is likely a combination of the dM companion's corona and the accretion of material onto the WD surface. This is further supported by the relatively high L_X/L_{bol}, 3–6×10^{-3}, where L_X was calculated using the observed count rates, a distance of 49 pc (Thorstensen et al. 2008), and assuming a plasma temperature of 0.3 keV without foreground absorption, and L_{bol} is the expected bolometric luminosity of the dM3.5-4 companion.

WD 1401+438 is a new WD spectroscopically identified in the SDSS (Eisenstein et al. 2006). The WD falls in a gap between the CCD chips in the EPIC PN observation. The total counts from PN and MOS detectors indicate a 3σ detection in the 0.5-2 keV band. This WD is faint (g=17.1) and is not detected in 2MASS. No fluxes beyond those in SDSS are yet available. Observations are needed to determine the X-ray spectral properties and to search for IR excess of this WD so that the origin of its hard X-ray emission can be assessed.

WD 1541−381, or LDS 539, is a DA4 WD (T_{eff} ∼12,600 K) with a near-IR excess, tentatively assigned a binary status with a dM3 or later companion by Hoard et al. (2007). The presence of the companion was later confirmed by high-resolution optical spectra taken with the Very Large Telescope (Koester et al. 2009). Too few counts are detected for a meaningful X-ray spectrum, and the distance of the WD is not known, therefore L_X/L_{bol} cannot be estimated. The WD is however too cool to generate X-rays, therefore, the dM companion is likely responsible for the observed hard X-ray emission.

WD 1734+742, or 29 Dra, is a CV of RS CVn type, consisting of a DA1.5 WD and a K0IV companion HD160538 (Holberg et al. 2003), with an orbital period of 903.8 days (Fekel et al. 1993). Zboril & Messina (2009) compiled a large set of observations of this

system and identified the companion to be a K0III star with an active chromosphere. The EPIC-MOS1 and MOS2 spectra were piled up, so we have used the EPIC PN observation to extract the spectrum; however, the source falls on the chip gap in PN images. The flux calibration is therefore compromised, and the detailed spectral shape will be affected, but the spectrum does show the presence of hard X-ray emission up to ∼4 keV. Due to the inaccurate flux calibration, the $L_{\rm X}/L_{\rm bol}$ value cannot be estimated from the *XMM-Newton* observations. WD 1734+742 has nevertheless been detected in our ROSPSPCCAT search, so we use the observed PSPC count rates and the distance of 88 pc (Strassmeier et al. 1993) to estimate $L_{\rm X}$, assuming a 0.3 keV solar-abundance plasma without foreground absorption. The estimated X-ray luminosity of $1.74{\times}10^{31}$ erg s^{-1} falls within the expected range of RS CVn stars ($\sim 10^{30}$–10^{31} ergs s^{-1}, Singh et al. 1996). $L_{\rm X}/L_{\rm bol}$, $8{\times}10^{-5}$ is above the value expected for normal K0III stars, with $M_{\rm bol}$=0.2, and extrapolating the $L_{\rm X}/L_{\rm bol}$ vs $M_{\rm bol}$ relationship reported by Caillault (1996). The hard X-ray emission originates from the greatly enhanced coronal activity due to large number of starspots of this companion.

WD 2128+469 is a CV, identified as the *ROSAT* X-ray source RX J2130.3+4709 (Motch et al. 1997). This eclipsing binary system was studied by Maxted et al. (2004) and was found to consist of a 0.554 $M_\odot$ WD and a 0.555 $M_\odot$ dMe 3.5-5 companion with an orbital period of ∼12 hrs. They further suggest that the WD's effective temperature of 18,000 K is too cool to contribute to the X-rays, and that the X-ray emission likely originates from the dMe companion. The X-ray spectrum can be modeled by a two-plasma model with 0.4 and 1 keV components, or by a combination of a photon power law with power index of 1.8 and a 0.7 keV solar-abundance plasma. The former model provides a better fit (reduced χ^2=0.918). The $L_{\rm X}/L_{\rm bol}$ is 0.9–$3.1{\times}10^{-3}$, where $L_{\rm X}$ is the X-ray luminosity in the 0.3-10.0 keV band derived from the best-fit 2-plasma model and a distance of 85 pc (Maxted et al. 2004), and $L_{\rm bol}$ is the bolometric luminosity of a dM3.5–5 star. WD 2128+469 was also detected in ROSPSPCCAT. For comparison, we use the observed PSPC count rates, the distance, and assume a 0.3 keV plasma to estimate the $L_{\rm X}$, which yields $L_{\rm X}/L_{\rm bol}$ of 1.4–$4.4{\times}10^{-3}$. Both

L_X/L_{bol} estimates are at the high end of expected coronal emission of dM stars.

6.3.2 XMM: Non-associations

WD 0046−297 has an X-ray source ∼30″ to the northwest. Although an optical counterpart to the X-ray source is not seen, the WD is too far to be associated with the X-ray source. Since the WD is superposed on a galaxy cluster, RXC J0049.4-2931, it is possible that the X-ray emission originates from a background galaxy.

WD 0836+197 is a member of Praesepe open cluster, NGC 2632. The X-ray source is seen 10″ to the west of the WD, and it is centered at another cluster member star, Cl* NGC 2632 KW 195. No X-ray source is associated with the WD.

WD 1307+577 is a new DA WD identified in the SDSS (Eisenstein et al. 2006). The X-ray source is ∼10″ southeast from the WD position. The SDSS image shows a very faint uncataloged red object about 4″ east of the WD. The X-ray source is not associated with the WD, but its association with the red object is unclear.

WD 1337−000 is a DA6.0 WD identified in the SDSS (Eisenstein et al. 2006; Kleinman et al. 2004). The faint X-ray source is located ∼10″ west of the WD. The WD is superposed on a galaxy cluster, with one galaxy projected as close as ∼15″ from the WD. The X-ray source is likely associated with a background extragalactic object rather than the WD.

WD 1449+168 is a DA WD, and has been reported to have a dM3 companion with an orbital semimajor axis of 78.″3 (Farihi et al. 2005). An X-ray source is detected near the WD, but the ∼12″ northeast offset makes it unlikely that they are associated. This X-ray source does not correspond to the dM3 companion, and does not have any obvious optical counterpart. The X-ray emission may originate from a background AGN, since the source is near a galaxy cluster, ACO 1983.

WD 2149+021, or GJ 838.4, has an X-ray source about 10″ to the west. An optical counterpart to this X-ray source is seen in the DSS2 red image, but not the blue image, indicating that the source is likely a background galaxy. This X-ray source is not associated

with the WD.

WD 2326+049, or G29-38, is a cool ($T_{\rm eff}$=11,700 K) DAZ WD and a ZZ Ceti variable with a mass of 0.62 $M_{\odot}$ (Farihi et al. 2009). It is the first WD known to have a dust disk created by tidal disruption of asteroids (Zuckerman & Becklin 1987). An X-ray source is detected near the WD, but it is $\sim$15″ southwest from the WD position; no source coincident with the WD itself was found (Jura et al. 2009). The nature of this background X-ray source is not known.

6.3.3 ROSAT PSPC Associations

The WDs reported in this section are all "new" and, unless otherwise noted, were not included in McCook & Sion Catalog when Papers I and II were completed.

WD 0121−756 is a hot PG1159 star discovered by Cowley et al. (1995), and it is one of the hottest known PG 1159 stars, with $T_{\rm eff}$ = 180,000 K (Werner et al. 1996). The WD was included in Paper I as a soft X-ray detection, but the WGACAT source was detected below 3σ (8±3 cts) in the 0.9-2 keV band and was thus dismissed. In ROSPSPCCAT, this X-ray source is reported with 3σ significance (9±3 cts) in the 0.9-2.01 keV band. The X-ray properties of this WD are similar to those of PG 1159 reported in Paper I. No companion to this WD has been reported, and the 2MASS photometry does not show any IR excess: V=15.4, J=16.229, H=16.164, and K=16.213.

WD 0331−356 is a new DA WD with $T_{\rm eff}$=31,372 K and has a dM companion (Koester et al. 2001). The light curve of this candidate pre-CV was studied by Tappert et al. (2004), but variability and orbital parameters could not be established due to poor data quality. The distance to the WD is not known, therefore $L_{\rm X}/L_{\rm bol}$ cannot be estimated. The hard X-ray emission is likely to originate from either the dM companion or the accretion of material onto the WD.

WD 0418+137 was detected by Böhm-Vitense (1993) as a companion to HR 1358 (HD 27483), which is itself a spectroscopic binary of two F6V stars that orbit each other with an

orbital period of 3.05 days. She estimates the period of the WD to be ∼16 yr. Burleigh et al. (1998) analyzed the *IUE* spectrum of the WD and derived an effective temperature of 22,000 K and a mass of 0.98 $M_{\odot}$. The *ROSAT* PSPC observation of X-ray emission from this WD is also discussed in Burleigh et al. (1998), who suggest that the hard X-ray emission could not originate from the WD, and that at least one of the F6V stars must therefore be active. We calculate the $L_{\rm X}/L_{\rm bol}$ (Table 6.6) to be 4.5–9$\times10^{-6}$, where $L_{\rm X}$ was calculated from the observed count rates, a distance of 46 pc derived from the parallax value listed in Perryman et al. (1997), and assuming a plasma temperature of 0.3 keV without foreground absorption. $L_{\rm bol}$ is the expected bolometric luminosity of the F6V companion with $M_{\rm bol}$ of 3.6. This value is within the range expected for a late-type companion (Caillault 1996).

WD 0419−487 is already described in section 6.3.1. The *ROSAT* detection of hard X-ray emission was dismissed in Paper II as unconvincing because it was faint and had a very broad point-spread function.

WD 0458−665 is a WD + red dwarf binary identified by *ROSAT* observations of its X-ray emission. The discovery and follow-up observations are reported in detail by Hutchings et al. (1995). Briefly, it is a post-common-envelope binary of a DA WD and an M2 star, with a period between ∼0.7 and several days. The WD temperature is ∼20,000 K. This binary system was not resolved in the *HST* images (Farihi et al. 2006). We calculate the $L_{\rm X}/L_{\rm bol}$ to be 1.5$\times10^{-3}$, where $L_{\rm X}$ was calculated from the observed count rates, a distance of 190 pc (Hutchings et al. 1995), and assuming a plasma temperature of 0.3 keV without foreground absorption. $L_{\rm bol}$ is the expected bolometric luinosity of the M2 companion. The $L_{\rm X}/L_{\rm bol}$ is at the high end of the range expected for coronal emission from late-type stars.

WD 0930+815 was detected serendipitously in the *IUE* spectrum of the hybrid K3III giant HD81817 (Reimers 1984). The WD effective temperature is ∼20,000 K. The X-ray emission has been reported by Ayres (2005). Hybrid red giants have a cold wind as well as hot high-ionization emission lines, and a number of them are detected in X-rays. We calculate the $L_{\rm X}/L_{\rm bol}$ to be 7.8$\times10^{-7}$, where $L_{\rm X}$ was calculated from the observed count

rates, a distance of 330 pc (Ayres 2005), and assuming a plasma temperature of 0.3 keV without foreground absorption, and $L_{\rm bol}$ is the expected bolometric luminosity of the K3III companion. The $L_{\rm X}/L_{\rm bol}$ falls within the range expected for a K3III star with $M_{\rm bol}$ of -0.5, if we extrapolate the trends in Caillault (1996) to lower $M_{\rm bol}$ values. The hard X-ray emission is likely associated with the hybrid K3III giant rather than the WD.

WD 1734+742 is already described in section 6.3.1.

WD 1803−482 is a RS CVn variable, consisting of a DA WD with a G8III companion, as seen in the *IUE* spectra (Holberg et al. 2003). The system's orbital period is 5200 days (Pourbaix et al. 2004). This object is categorized as a chromospherically active binary (Strassmeier et al. 1993), one of whose characteristics is coronal activity. $L_{\rm X}$ was calculated using the observed count rates, a distance range of 170 (Strassmeier et al. 1993) to 266 pc (Perryman et al. 1997), and a plasma temperature of 0.3 keV with no foreground absorption. The $L_{\rm X}$ value, $\sim 2.3\times10^{31}$, falls within the range expected for RS CVn stars. Using the bolometric luminosity of a G8III star, we find $L_{\rm X}/L_{\rm bol} = 4.8 \times 10^{-5}$ – 1.2×10^{-4}, which falls within the expected range for its $M_{\rm bol}$ of 8.4 (Caillault 1996). The X-ray emission is likely due to the coronal activity of the G8III companion.

WD 2128+469 is already described in section 6.3.1.

6.3.4 ROSAT PSPC Non-associations

WD 0157+004 has an X-ray source centered $\sim 35''$ northeast of the WD. The SDSS images show a faint background galaxy coincident with the X-ray source. The X-ray emission is not associated with the WD.

6.4 Summary and Conclusions

To extend the search for hard X-ray emission associated with WDs (Papers I and II), we have correlated XMMSSC, ROSPSPCCAT, and ROSPSPCFCAT point X-ray source catalogs

with the latest version of McCook & Sion (2006) WD catalog, which has been augmented with ∼10,000 new WDs, primarily from SDSS. Our new search yielded a total of 32 hard X-ray sources associated with WDs. Among these, 17 sources were not previously reported in Papers I or II.

Our current *ROSAT* search recovers all X-ray sources reported in Papers I and II, except four sources. As these searches used different *ROSAT* X-ray point source catalogs with different source detection algorithms, marginal sources may be detected in one catalog, but not the other. Indeed, all four sources not recovered in the current search are marginal due to low counts (WD 0339−451), or poor point-spread function at large off-axis angle (WD 1213+528, WD 1333+510, and WD 2154-512). On the other hand, WD 0419−487, discussed and dismissed in Paper II, is reported as a hard X-ray source in this paper. Three of these marginal sources, WD 0339−451, WD 1213+528, and WD 0419−487, were confirmed in XMMSSC.

The hard X-ray emission associated with WDs can be roughly divided into five categories:

(1) Binary WD: coronal companion.

The most common type of hard X-ray emission associated with WDs originates from the corona of a late-type binary companion, for example, WD 0232+035 and WD 1026+002. The coronal emission is the dominant source of hard X-rays in non-accreting binary systems. The hard X-ray emission usually diminishes below detection beyond ∼2 keV.

(2) Binary WD: mass transfer

The second most common type of hard X-ray emission from WDs is generated by accretion of material from a companion that has filled its Roche lobe, for example, WD 1310−230, WD 1944−421. Orbital periods of such binary systems are usually short (∼ few hours) and the X-ray spectral energy distribution is harder than that of stellar coronal emission, extending to several keV. Note that both the companion's corona and WD's accretion may contribute to the hard X-ray emission, so the resulting spectral energy distribution may have a wide range of properties.

(3) Single hot WD.

Two WDs belong to this category: WD 2226−210 and KPD 0005+511. Both appear single with no direct evidence of binary companions. Their X-ray spectra show a soft component of the photospheric emission and a hard component peaking near 1 keV, corresponding to plasma emission at temperatures of a few 10^6 K (Paper I; Leahy et al. 1994). The origin of the hard component is unknown.

(4) PG 1159.

ROSAT PSPC observations of two PG 1159 type WDs show very faint hard X-ray emission in the 0.9–2.0 keV band: WD 1159−034 and WD 0121−756. The former is the WD PG 1159 itself. In each case, only 9–12 counts were detected in the hard X-rays. It is not clear whether these sources are the fainter versions of the Single Hot WDs, and whether weak hard X-ray emission is intrinsic to the PG1159 spectral type.

(5) Hard shoulder of the soft component.

Two WDs show soft photospheric emission with appreciable emission in the 0.5–0.9 keV range: WD 1234+481(DA1) and WD 1254+223 (DA1.3). Their spectral shape does not show two distinct components as WD 2226−210 and KPD 0005+511. While WD 1254+223 shows no near- or mid-IR excesses indicative of a companion, WD 1234+481 has been shown to possess an L-type brown dwarf companion (Mullally et al. 2007; Steele et al. 2007). It is not clear whether the brown dwarf companion contributes to the hard X-ray shoulder of the WD's photospheric emission. It is also unclear whether the X-ray spectral model of WD 1254+223, a combination of 0.1 keV plasma and power law component, is physically meaningful.

Hard X-ray emission is a good diagnostic of coronal companions to WDs and of CVs. In six WDs, the hard X-ray emission cannot be explained by either of these scenarios. Five of these six WDs are apparently single; one has an L-type companion. The origin of hard X-ray emission from the single WDs is not understood, and it is not clear whether a brown dwarf companion can contribute to the 0.5-0.6 keV X-rays. Future observations are needed

to solve the mystery of hard X-ray emission from single WDs. Most importantly, deeper observations of the faint sources are needed to better specify the X-ray spectral properties. For the brightest source, WD 2226−210, high-dispersion X-ray spectra are needed so that plasma diagnostics can be used to determine the physical conditions of the plasma, such as temperature, density, and ionization state. Finally, it is also important to place limits on any binary companions to the single WDs by monitoring temporal variations of X-ray emission and the Hα line profile, and by acquiring IR photometry and spectra to search for signatures of companions.

Table 6.1. XMM Detections

WD Number (1)	WD Type (2)	Common Name (3)	XMM Src no. (4)	XMM Obs no. (5)	Exp (ks) (6)	Pos Coinc (7)	X-ray Counts Reported in XMMSSC (Counts)[a,b] 0.2−0.5 keV (8)	0.5−1.0 keV (9)	1.0−2.0 keV (10)	Remarks[c] (11)
0216−032	DA+M2III	Mira B	2XMM J021920.8−025840	0148500201	9.2	Good	15 ± 5	187 ± 14	224 ± 16	P1
0232+035	DA+dM1	Feige 024	2XMM J023507.6+034357	0305980101	6.1	Good	292 ± 18	96 ± 11	16 ± 6	N
0339−451	DA	QSF 1:02	2XMM J034125.1−450045	0045940301	6.7	Good	22 ± 6	14 ± 5	14 ± 5	P1
0347+171	DA1.5+K2	V471 TAURI	2XMM J035024.9+171447	0203260101	31.8	Good	4252 ± 67	14168 ± 122	9113 ± 98	P1, M2
0419−487	DAZ8.0+dM	LHS1660, LFT0349	2XMM J042105.5−483910	0305980301	7.5	Good	171 ± 14	393 ± 21	143 ± 13	N
0429+176	DA2.5+dM	HZ 09, EG038	2XMM J043223.7+174503	0094810301	3.5	Good	154 ± 13	304 ± 18	72 ± 9	P1
0736+053	DA4+F5IV	A CMI B, EG053	2XMMi J073917.7+051324	0415580101	30.7	Good	27915 ± 171	23059 ± 151	884 ± 32	P1
0905−724	DA1.5+F9	HD 78791B	2XMM J090508.2−723609	0164571401	16.7	Good	71366 ± 262	7441 ± 89	311 ± 20	N
1026+002	DAZ3.5+dM	...	2XMM J102834.9−000030	0305980401	9.6	Good	60 ± 9	100 ± 11	39 ± 7	N
1213+528	DAZ3.9+dM	C1, EG087, EG UMa	2XMM J121544.0+523100	0305980501	6.2	Good	1170 ± 35	2568 ± 52	943 ± 32	P1
1253+261[d]	PNN+G5III	WD1255+258J	2XMM J125533.7+255330	0012850201	14.7	Good	202 ± 15	438 ± 22	236 ± 16	P1
1254+223	DA1.3	GD 153, EG187	2XMM J125702.3+220151	0125910501	10.5	Good	13476 ± 117	372 ± 20	0 ± 1	N
1310−230	DD	V396 Hya, CE315	2XMM J131246.3−232132	0302160201	16.6	Good	2637 ± 53	2971 ± 56	2109 ± 47	N
1347−129	DA+dM	...	2XMM J134952.0−131336	0305310101	52.3	Good	1516 ± 40	4066 ± 65	5317 ± 75	N, M2
1401+438	DA	...	2XMM J140353.1+433457	0305360401	0.5	Good	1 ± 2	6 ± 6	14 ± 7	N, EP
1541−381	DA+dM	L0480-085, LDS 539	2XMM J154510.9-381850	0305980701	3.7	Good	66 ± 9	106 ± 12	50 ± 8	N
1631+781	DA1+dM4E	...	2XMM J162910.1+780441	0400920201	2.8	Good	577 ± 25	162 ± 14	59 ± 9	P1
1734+742	DA1.5+K0	29 Dra, HD160538	2XMM J173247.2+741403	0014150401	1.4	Good	59 ± 13	160 ± 22	86 ± 32	N, M2
2128+469	DA2.8+dM	...	2XMM J213018.4+471008	0307120101	4.5	Good	88 ± 11	249 ± 17	93 ± 11	N
2226−210	DAO.49	NGC 7293, PK 36-57	2XMM J222938.5−205014	0125911001	8.0	Good	75 ± 11	330 ± 22	129 ± 14	P2

Table 6.1 (cont'd)

WD Number (1)	WD Type (2)	Common Name (3)	XMM Src no. (4)	XMM Obs no. (5)	Exp (ks) (6)	Pos Coinc (7)	X-ray Counts Reported in XMMSSC (Counts)[a,b] 0.2−0.5 keV (8)	0.5−1.0 keV (9)	1.0−2.0 keV (10)	Remarks[c] (11)
				Non-associations						
0046−297	DA6.3	EIS	2XMM J004843.9−292944	0201900401	9.0	U(30″ NW)	7 ± 3	11 ± 4	23 ± 6	M2
0836+197	DA2.3	LB 5893	2XMM J083936.5+193027	0101440401	27.3	U(10″ W)	38 ± 8	44 ± 8	38 ± 8	
1307+577	DA	...	2XMMi J130920.7+572610	0301340501	9.1	U(10″ SE)	7 ± 4	22 ± 7	39 ± 8	
1337−000	DA6.0	...	2XMM J133946.7−002001	0211080701	5.0	U(10″ W)	10 ± 4	17 ± 5	11 ± 5	
1449+168	DA2+dM3	...	2XMM J145211.7+163815	0091140201	6.4	U(12″ NE)	10 ± 5	19 ± 7	14 ± 6	
1633+572	DQ8+2(dM4E)	G225-068, EG258	2XMM J163419.7+570948	0049540401	15.5	U	3077 ± 57	5491 ± 76	1418 ± 39	P1[e]
2149+021	DAZ2.9	G093-048, EG150	2XMM J215226.7+022318	0155560401	3.6	U(10″ W)	1 ± 1	6 ± 3	20 ± 5	
2326+049	DAZ4.3, DAV	G029-038, EG159	2XMM J232846.5+051447	0302820101	17.7	U(15″ SW)	19 ± 6	31 ± 7	24 ± 6	

[a]Counts are calculated using the count rates (ct/s) multiplied by the exposure times (s) listed in XMMSSC catalog.

[b]Unless otherwise noted, counts for PN detector are listed.

[c]Explanations of the terms in the Remarks column: EP: The source is detected with 3σ significance only after summing all EPIC instruments (MOS1, MOS2, PN). The counts given are for PN. M1: The best signal to noise ratio is in MOS1 instrument; values listed are catalog entries for MOS1. M2: The best signal to noise ratio is in MOS2 instrument; values listed are catalog entries for MOS2. N: New X-ray source associated with a WD, not reported in Papers I or II. P1: The X-ray source has been discussed in Paper I. P2: The X-ray source has been discussed in Paper II.

[d]The WD is listed as WD 1255+258J in Paper I.

[e]As discussed in Paper I, the hard X-ray emission comes from a nearby dM3-4e binary system and is not associated with the WD. For the discussion of positional coincidence, see Paper I.

Table 6.2. ROSAT PSPC Detections

WD Number (1)	WD Type (2)	Common Name (3)	ROSAT Src no (4)	ROSAT Obs no[a] (5)	Exp (ks) (6)	Pos Coinc (7)	X-ray Counts Reported in PSPC (Counts) 0.11−0.41 keV (8)	0.52−0.9 keV (9)	0.9−2.01 keV (10)	Remarks[b] (11)
0121−756	PG1159	WD0122−753J	2RXP J012253.2−752117	300369	5.4	Good	4530 ± 68	4 ± 2	9 ± 3	N
0216−032	DA+M2III	MIRA B	2RXP J021921.1−025841	201501	8.9	Good	2 ± 3	23 ± 5	35 ± 6	P1
0220+222	DA3.2	G094-B5B, EG018	2RXP J022334.0+222726	190230	0.9	Good	199 ± 15	100 ± 10	81 ± 9	P2
0331−356	DA1.6+dm	...	2RXP J033352.3−353118	800301	7.0	Good	86 ± 11	17 ± 4	14 ± 4	N
0347+171	DA1.5+K2	GH7-023, V471 TAURI	2RXP J035024.0+171457	200107	18.2	Good	29431 ± 174	2208 ± 51	2489 ± 52	P1
0418+137	DA3+F6V	HR1358, HD 27483	2RXP J042052.8+135150	200776	22.5	Good	1660 ± 42	416 ± 21	221 ± 15	N
0419−487	DAZ8.0+dM	LHS1660, LFT0349	2RXP J042104.8−483903	190090	0.2	Good	46 ± 7	15 ± 4	26 ± 5	N, P2
0429+176	DA2.5+dM	HZ 09, EG038	2RXP J043223.6+174505	200443	17.9	Good	504 ± 24	188 ± 15	148 ± 13	P1
0458−665	DA+dM	...	2RXP J045853.4−662815	900320	15.3	Good	10 ± 6	34 ± 8	34 ± 7	N
0736+053	DA4+F5IV	A CMI B, EG053	2RXP J073918.2+051334	200437	3.7	Good	9080 ± 96	332 ± 18	74 ± 9	P1
0930+815	DA3+K3	HD 81817B	2RXP J093708.8+811940	201223	8.5	Good	17 ± 6	5 ± 2	11 ± 4	N
1159−034	PG1159	GW Vir	2RXP J120146.4−034536	701202	13.1	Good	1280 ± 37	6 ± 3	12 ± 4	P1
1234+481	DA.92	...	2RXP J123645.2+475529	200578	2.4	Good	3280 ± 58	25 ± 5	-2 ± 4	P1
1253+261[c]	PNN	WD1255+258J	2RXP J125533.6+255333	201514	17.8	Good	254 ± 19	37 ± 6	39 ± 6	P1
1314+293	DA1+dM3e	EG098, HZ 43A	2RXP J131622.9+290551	100308	21.5	Good	1585270 ± 1260	7312 ± 86	120 ± 11	P1[d]
1631+781	DA1+dM4e	...	2RXP J162911.5+780434	170154	35.4	Good	131000 ± 1000	271 ± 51	236 ± 46	P1
1634−573	DOZ1+K0V	HD149499B	2RXP J163831.6−572810	200773	1.3	Good	322 ± 18	136 ± 12	121 ± 11	P1
1734+742	DA1.5+K0	29 Dra, HD160538	2RXP J173248.8+741320	701200	7.6	Good	9457 ± 99	4482 ± 67	6352 ± 80	N
1803−482	DA+G8III	V832 Ara, HD165141	2RXP J180700.3−481451	201178	1.6	Good	36 ± 6	142 ± 12	187 ± 14	N
1944−421	PEC	...	2RXP J194740.5−415934	300232	9.9	Good	463 ± 22	488 ± 22	614 ± 25	P1
2128+469	DA2.8+dM	...	2RXP J213018.4+471009	400363	28.4	Good	382 ± 22	228 ± 16	194 ± 15	N
2226−210	DAO.49	...	2RXP J222938.8−205015	900187	4.7	Good	232 ± 17	28 ± 5	25 ± 5	P2

Table 6.2 (cont'd)

WD Number (1)	WD Type (2)	Common Name (3)	ROSAT Src no (4)	ROSAT Obs no[a] (5)	Exp (ks) (6)	Pos Coinc (7)	X-ray Counts Reported in PSPC (Counts) 0.11−0.41 keV (8)	0.52−0.9 keV (9)	0.9−2.01 keV (10)	Remarks[b] (11)
				Non-associations						
0048−294	DA3.5	SGP 2:31	2RXP J005114.3−291022	700275	22.7	U	24 ± 8	5 ± 3	23 ± 5	P1[e]
0157+004	DZ	...	2RXP J020003.9+004025	700225	5.4	U(35″ NE)	25 ± 6	18 ± 5	15 ± 5	
1134+300	DA2.4+AGN	GD 140, EG184	2RXP J113705.1+294816	200091	32.5	U(41″ NW)	1360 ± 40	53 ± 8	54 ± 8	P1[f]
1633+572	DQ8+2(dM4E)	G225-068, EG258	2RXP J163421.3+570941	200721	44.9	U	2830 ± 55	1160 ± 34	895 ± 30	P1[g]

[a]For multiple observations of the same target, we give the values for the one withe the longest exposure time.

[b]Explanations of the terms in the Remarks column: P1: The X-ray source has been discussed in Paper I. P2: The X-ray source has been discussed in Paper II. N: New X-ray source associated with a WD, not reported in Papers I or II.

[c]The WD is listed as WD 1255+258J in Paper I.

[d]The values listed in *ROSAT* PSPC look suspect, therefore we cite the WGACAT values for this source.

[e]As discussed in Paper I, the hard X-ray source is not convincingly centered on the WD, and the X-ray source is occulted by the PSPC window support structure.

[f]As discussed in Paper I, the hard X-ray source is centered 41″ northwest of the WD and coincides with an AGN, which causes the hard X-ray emission.

[g]As discussed in Paper I, the hard X-ray emission comes from a nearby dM3-4e binary system and is not associated with the WD.

Table 6.3. ROSAT PSPCF Detections

WD Number (1)	WD Type (2)	Common Name (3)	ROSAT Src no (4)	ROSAT Obs no[a] (5)	Exp (ks) (6)	Pos Coinc (7)	X-ray Counts Reported in PSPCF (Counts) 0.11−0.41 keV (8)	0.52−0.9 keV (9)	0.9−2.01 keV (10)	Remarks[b] (11)
2226−210	DAO.49	CSPN NGC 7293	2RXF J222938.5−205012	900187	4.2	Good	26 ± 5	6 ± 3	24 ± 5	P2
0005+511	DOQZ.4	KPD 0005+5106	2RXF J000817.7+512315	200428	4.9	Good	172 ± 13	7 ± 3	18 ± 4	P2
0512+326	DA1.8	14 Aur C, HD33959C	2RXF J051523.5+324109	200815	2.3	Good	1130 ± 34	52 ± 7	44 ± 7	P2
1314+293	DA1+dM3.5e	HZ 43A	2RXF J131621.5+290558	200418	21.1	Good	26000 ± 870	82 ± 24	57 ± 20	P1
1631+781	DA1+dM4e	1ES 1631+78.1	2RXF J162907.8+780438	200821	2.7	Good	2190 ± 47	6 ± 3	11 ± 3	P1
			Non-associations							
1821+643	DOZ.4	DS Dra	2RXF J182152.3+642143	200429	8.0	U	175 ± 13	30 ± 6	126 ± 12	P1[c]

[a]For multiple observations of the same target, we give the values for the one with the longest exposure time.

[b]Explanations of the terms in the Remarks column: P1: The X-ray source has been discussed in Paper I. P2: The X-ray source has been discussed in Paper II.

[c]As mentioned in Paper I, the X-ray emission from this source is blended with an adjacent source.

Table 6.4. X-ray Spectra Model Parameters

WD Name	Component 1[a]	Component 2	χ^2_ν(d.o.f.)
WD 0232+035	power law	plasma	3.48 (10)
	Γ=6.526	kT=0.814 keV	
WD 0232+035	plasma	plasma	1.50 (10)
	kT=0.049 keV	kT=0.803 keV	
WD 0419-487	power law	plasma	1.017 (40)
	Γ=1.832	kT=0.348 keV	
WD 0419-487	plasma	plasma	1.171 (40)
	kT=0.308 keV	kT=4.438 keV	
WD 1254+223	power law	plasma	1.850 (77)
	Γ=6.890	kT=0.107 keV	
WD 2128+469	power law	plasma	1.513 (17)
	Γ=1.835	kT=0.678 keV	
WD 2128+469	plasma	plasma	0.918 (15)
	kT=0.361 keV	kT=1.096 keV	

[a]For the power law component, Γ denotes the power law index.

Table 6.5. XMM WDs with Known Companions

WD Name	Spec Type	Distance (pc)	Lx	Lx/Lbol
0232+035	dM1.5-2	69[a]	4.29×10^{28}	1.84×10^{-4} – 2.49E$\times10^{-4}$
0419-487	dM4	11[b]	2.98×10^{27}	4.10×10^{-5}
1026+002	dM4e	38[c]	3.40×10^{27}	4.68×10^{-5}
1310-230	DD	90[d]	3.88×10^{29}	...
1347-129	dM3.5-4	49[d]	3.40×10^{29}	2.47×10^{-3} – 4.67×10^{-3}
2128+469	dM3.5-5	85[e]	1.30×10^{29}	9.47×10^{-4} – 3.10×10^{-3}

[a]Benedict et al. (2000)

[b]Bruch (1999)

[c]Liebert et al. (2005)

[d]Thorstensen et al. (2008)

[e]Maxted et al. (2004)

Table 6.6. ROSAT WDs with Known Companions

WD Name	Spec Type	Distance (pc)	Lx	Lx/Lbol
0331-356	dM	...	...	
0418+137	2F6V	45.7[a]	9.33×10^{28}	4.52×10^{-6} – 9.04×10^{-6}
0419-487	dM4	11[b]	4.66×10^{28}	6.41×10^{-4}
0458-665	dM2	190[c]	2.51×10^{29}	1.46×10^{-3}
0930+815	K3III	330[d]	3.27×10^{29}	7.77×10^{-7}
1734+742	K0III	88[e]	1.74×10^{31}	7.60×10^{-5}
1803-482	G8III	170[e]266[a]	2.30×10^{31}	4.81×10^{-5} – 1.18×10^{-4}
2128+469	dM3.5-5	89[f]	1.86×10^{29}	1.35 – 4.43×10^{-3}

[a]distance calculated using the parallax value from Perryman et al. (1997)

[b]Bruch (1999)

[c]Hutchings et al. (1995)

[d]Ayres (2005)

[e]Strassmeier et al. (1993)

[f]Maxted et al. (2004)

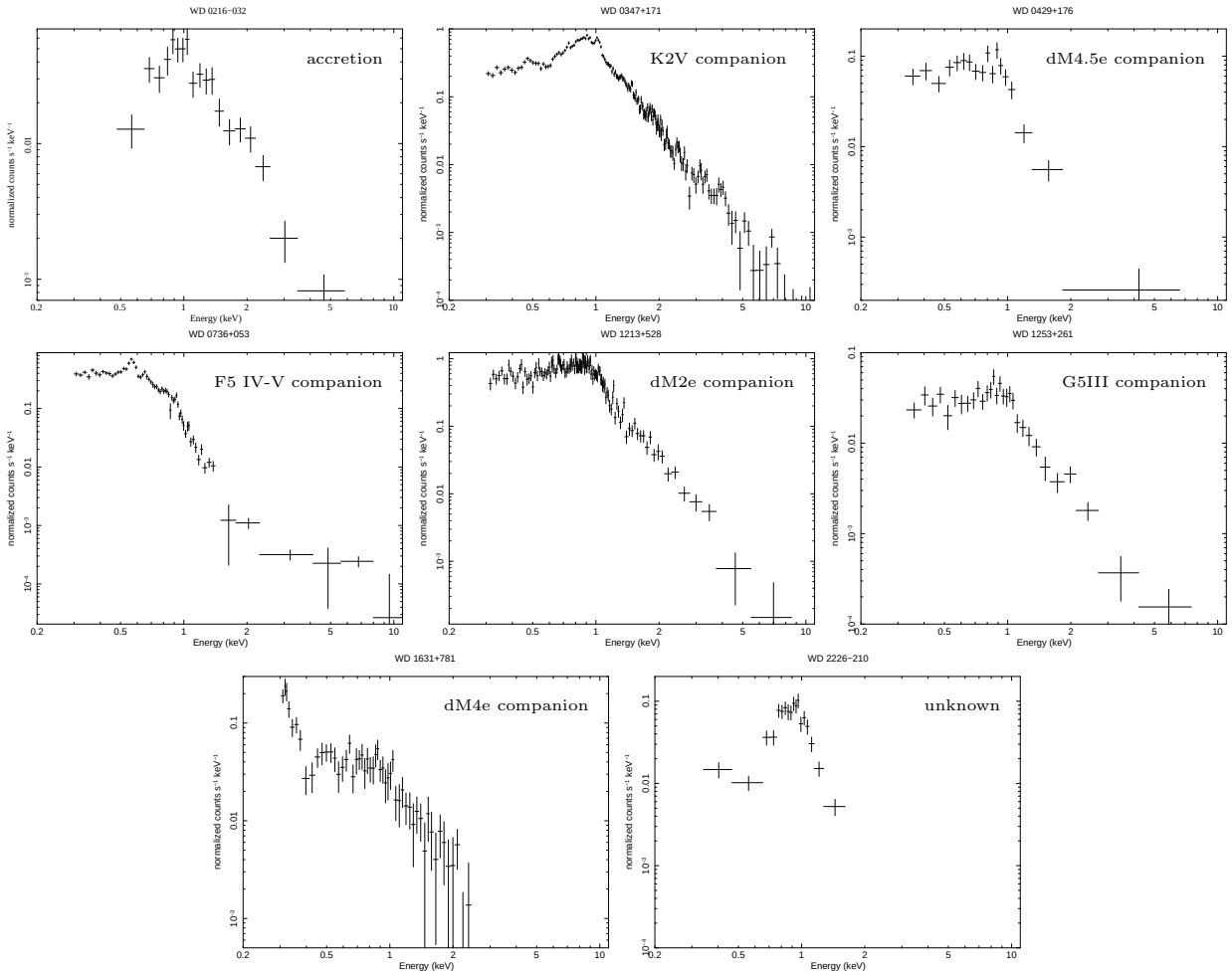

Figure 6.1: *XMM-Newton* spectra of WDs associated with hard X-ray emission reported in Papers I or II. Origin of the hard X-ray emission is noted in the upper right corner for each WD. row 1: WD0216−032, WD0347+171, WD0429+176, row 2: WD0736+053, WD1213+528, WD1253+261, row 3: WD1631+781, and WD2226−210.

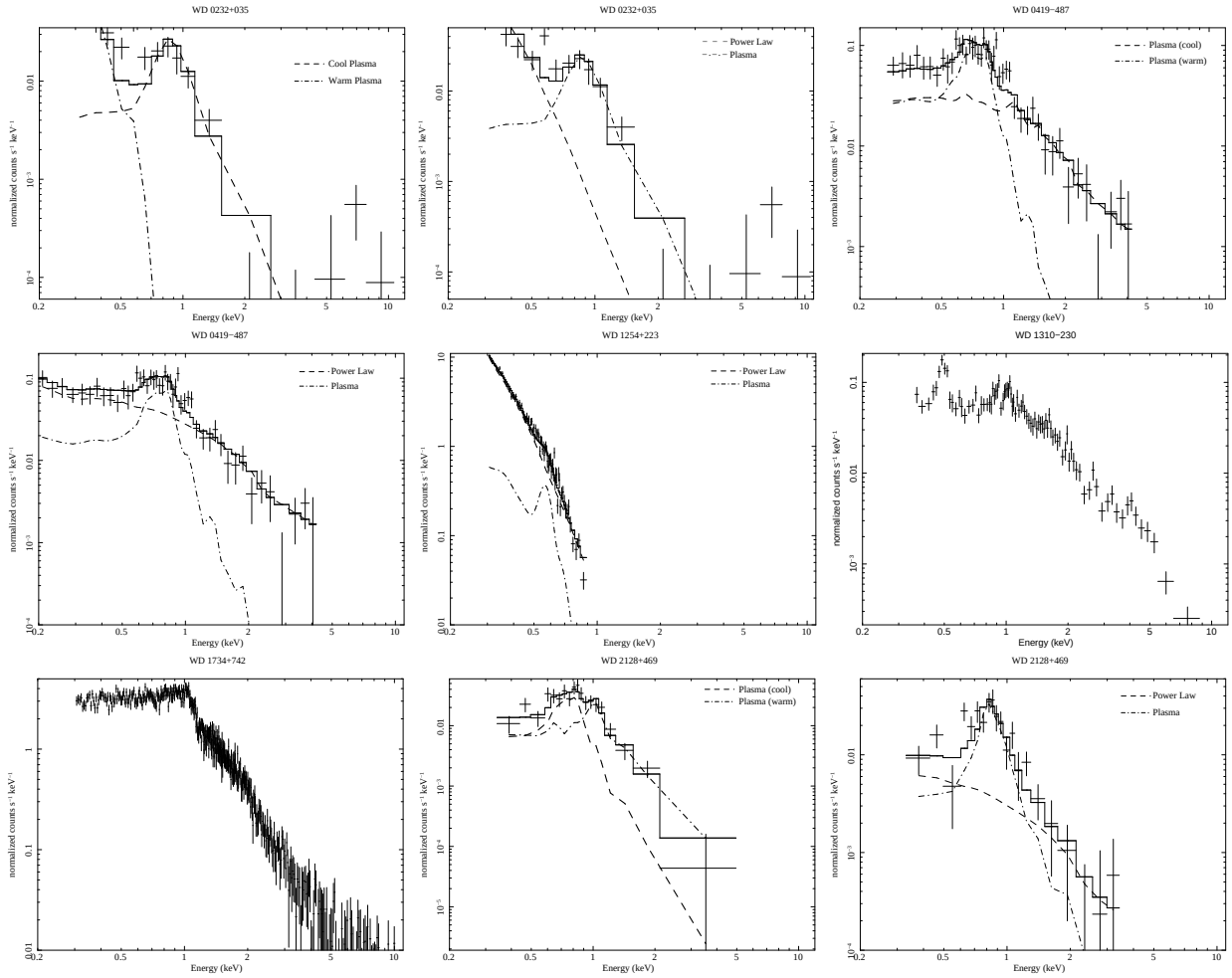

Figure 6.2: *XMM-Newton* spectra and models of WDs associated with hard X-ray emission not previously reported in Papers I or II. The dashed and dot-dashed lines show the model's components, labeled in the upper right corner. For WD 1310−230, we only present the X-ray spectrum; detailed modeling was carried out by Ramsay et al. (2006). The spectrum of WD 1734+742 is affected by chip gap, therefore, we do not model the X-ray emission.

Chapter 7

Summary and Future Work

The search for planetary systems around stars other than our Sun has yielded great results in recent years, with hundreds of planets discovered through RV variations (e.g. Butler et al. 2006) and, more recently, transits (Borucki et al. 2011). The evolution of planetary systems past the main sequence has been studied theoretically (Debes & Sigurdsson 2002; Villaver & Livio 2007, e.g.), and it is expected that planets massive and distant enough will survive through stellar evolution. Giant planets have been detected around red giants (e.g. Setiawan et al. 2005; Sato et al. 2007), but so far no planets around WDs have been confirmed.

Planetary systems also contain dust and debris, similar to asteroids or KBOs in our Solar System. Dust disks, thanks to their large emitting areas, are much easier to detect than planets. *Spitzer Space Telescope* observations have greatly improved our understanding of debris disks around main-sequence stars, and their evolution as the stars age on the main-sequence (Rieke et al. 2005; Su et al. 2006).

Interestingly, *Spitzer* has also enabled discoveries of dust disks around very old ($\sim$Gyr) WDs (Becklin et al. 2005; Kilic et al. 2005). These dust disks are around cool WDs whose atmospheres are polluted by metals, and the dust disks are all located within the WDs' Roche limits. These disks were produced by tidally disrupted asteroids that are accreted onto the WD's surface and contaminate its atmosphere with metals. The detection of asteroidal material around such old WDs provides the strongest observational evidence so far for the survival of planetary systems into late stages of stellar evolution.

An entirely different kind of disk has been discovered around Helix Nebula's CSPN. The dust disk around Helix's CSPN is detected as excess IR emission at 8, 24 and 70 μm. The

excess emission originates from a dust continuum, and is consistent with a dust disk located between 35 and 130 AU from the WD, containing $\sim$0.13 $M_{\oplus}$. It has been suggested that the dust was produced by collisions among KBOs that were dynamically rejuvenated during the post-AGB evolution (Su et al. 2007). Interestingly, X-ray observations of Helix have revealed a hard X-ray point source coincident with the CSPN. Hard X-ray emission is usually associated with companions, but the IR photometric measurements rule out companion as late as T dwarfs. We have searched the *XMM* and *ROSAT* archives for additional hard X-ray sources associated with single WDs, but none of them with IR observations show excess IR emission. The origin of the hard X-ray emission remains unclear.

To search for more dust disks similar to the one around the Helix CSPN, we have carried out a *Spitzer* MIPS 24 μm survey of hot WDs/pre-WDs (Chu et al. 2011). We have found 9 cases of excess 24 μm emission, and the spectra of four of these confirm that the excesses originate from a dust continuum. In eight cases, excess emission was seen only in 8–14 μm range, but a number of WDs/CSPNs also exhibit excesses at shorter wavelengths. Interestingly, 7 out of 9 hot WDs with 24 μm excesses were still surrounded by PNe.

Inspired by the fact that the majority and the strongest IR excesses were seen around WDs that are still CSPNs, we have searched the *Spitzer* archive for programs that include observations of PNe and examined their CSPNs. We have found 19 cases of IRAC and/or MIPS excesses, but these excesses have a variety of origins. Two stars have apparent visual companions which can account for all of the observed excess emission. Seven stars are [WC]-type CSPNs, which have strong stellar winds, and the IR excess is caused by dust and free-free emission from accelerating particles in the stellar winds. Two of the stars are borderline objects between young PNe and symbiotic stars. In eight cases, an extended emitter, such as a dust disk, is required to fit the IR SEDs. Combined with our 24 μm survey of hot WDs (Chu et al. 2011), the incidence of dust disks among CSPNs is $\gtrsim$17%.

The SEDs show a great diversity in the emission characteristics of the IR excesses. For some of the WDs/CSPNs, we have obtained follow-up spectroscopic observations with *Spitzer*

IRS, and Gemini NIRI and Michelle spectrographs. Each spectrum contains dust continuum emission, but the spectral shapes vary. In some cases, line emission coincident with the CSPN is seen in addition to the continuum emission (e.g., NGC 6804, NGC 7139). None of the spectra display any mineralogical features except for NGC 6804, which exhibits a crystalline silicate feature at 10 μm.

For WDs/CSPNs without spectroscopic observations, we derive basic disk parameters based on blackbody approximations to the excess emission. For cases with available spectroscopic observations, where appropriate, we use optically thin dust disk models and realistic grain parameters and distributions to model the dust emission and derive disk properties. In cases where excess is seen only at wavelengths longer than $\sim$5.8 μm, the dust is located a few tens of AUs from the central stars, and PR lifetimes are long enough for dust to have survived through a significant portion of the WD's/CSPNs age. These cases are consistent with the origin of collisionally disrupted subplanetary objects.

The cases that show near-IR excesses in addition to 24 μm excesses are more complicated. While the dust disk around CSPN K1-22 can be modeled by a single disk component extending from sublimation radius to $\sim$ 40 AU, in other cases, like that of NGC 2438, a single disk component is not sufficient to fit the data. Furthermore, short PR lifetimes imply that some of the disks must be optically thick, and further modeling with an appropriate disk model is needed.

The diverse SED and spectral characteristics of the IR excesses may imply different dust origins. We consider two mechanisms that can be responsible for the observed dust emission. The first one is the same mechanism suggested to produce the dust around main sequence stars as well as Helix's CSPN, the breakup of bodies in planetesimal belts due to collisions.

The second possibility is the formation of dust disks in binary interactions. Stable Keplerian-rotating disks are commonly observed around post-AGB binaries (de Ruyter et al. 2006), and some CSPNs with dusty disks may have descended from these objects. The disk around CSPN NGC 6804, is particularly similar to circumbinary post-AGB dust disks.

Its optical thickness, gas content, and the 10 μm crystalline silicate feature all resemble the features of post-AGB dust disks.

Much future work is necessary to understand the origins of these intriguing systems. On the theoretical side, better understanding of post-AGB binary evolution as well as debris disk evolution along its parent star is needed to compare the detection rate and properties of our disks to theoretical predictions.

Many observational ventures can be undertaken to probe these systems better. For objects without IR spectra, future spectroscopic observations will help assess the nebular contamination of the measured flux densities, and will help constrain the extent and properties of the dust disks. An appropriate instrument for this task would be the Mid-Infrared Instrument on the *James Webb Space Telescope*, with spectroscopic capabilities in the 5–28 μm range. Even objects with existing IRS spectra would benefit from both deeper exposures in cases where the signal to noise ratio is low, and coverage at longer wavelengths, because the constraints on outer disk radii are poor.

In optical wavelengths, a better sampling of the optical and near-IR SED would allow us to accurately model the WD atmospheres, which would be improved even further by constructing appropriate synthetic spectra for all WDs/CSPNs. Interferometric observations with EVLA or ALMA may spatially resolve the detected dust disk, and place better constraints on the parameters in the dust disk models.

In addition, to assess the link between CSPN dust disks and binarity, we need to carry out a thorough search for unresolved companions, especially for objects with near-IR excesses. High-resolution imaging with *HST* or adaptive optics can resolve wide companions, whereas photometric or RV monitoring may reveal close companions with short orbital periods.

Finally, surveys for additional dust disks around WDs and CSPNs may help us discover correlations between physical parameters of dust disks and their central stars, and possibly discern evolutionary trends.

References

Abbott, D. C., & Conti, P. S. 1987, ARA&A, 25, 113

Acker, A., Marcout, J., Ochsenbein, F., Stenholm, B., & Tylenda, R. 1992, Garching: European Southern Observatory, 1992,

Acker, A., Fresneau, A., Pottasch, S. R., & Jasniewicz, G. 1998, A&A, 337, 253

Acker, A., & Neiner, C. 2003, A&A, 403, 659

Artymowicz, P., & Clampin, M. 1997, ApJ, 490, 863

Ayres, T. R. 2005, ApJ, 618, 493

Baraffe, I., Chabrier, G., Barman, T. S., Allard, F., & Hauschildt, P. H. 2003, A&A, 402, 701

Barstow, M. A., Bond, H. E., Burleigh, M. R., & Holberg, J. B. 2001, MNRAS, 322, 891

Becklin, E. E., Farihi, J., Jura, M., Song, I., Weinberger, A. J., & Zuckerman, B. 2005, ApJ, 632, L119

Benedict, G. F., et al. 2000, AJ, 119, 2382

Benedict, G. F., McArthur, B. E., Napiwotzki, R., et al. 2009, AJ, 138, 1969

Bilíková, J., Chu, Y.-H., Gruendl, R. A., & Maddox, L. A. 2010, AJ, 140, 1433

Bilíková, J., Chu, Y.-H., Gruendl, R. A., Su, K. Y.-L., & DeMarco, O. 2012, ApJS, in press

Bleach, J. N., Wood, J. H., Catalán, M. S., Welsh, W. F., Robinson, E. L., & Skidmore, W. 2000, MNRAS, 312, 70

Böhm-Vitense, E. 1993, AJ, 106, 1113

Bond, H. E., Ciardullo, R., & Meakes, M. G. 1992, Evolutionary Processes in Interacting Binary Stars, 151, 517

Bond, H. E. 1994, Interacting Binary Stars, 56, 179

Bond, H. E. 2009, Journal of Physics Conference Series, 172, 012029

Bonsor, A., & Wyatt, M. 2010, MNRAS, 409, 1631

Borucki, W. J., Koch, D. G., Basri, G., et al. 2011, ApJ, 736, 19

Boss, A. P. 1996, ApJ, 469, 906

Brinkworth, C. S., Gänsicke, B. T., Marsh, T. R., Hoard, D. W., & Tappert, C. 2009, ApJ, 696, 1402

Britt, D. T., Yeomans, D., Housen, K., & Consolmagno, G. 2005, NASA Planetary Data System, EAR-A-5-DDR-ASTEROID-DENSITIES-V1.1, 25

Bruch, A., & Diaz, M. P. 1998, AJ, 116, 908

Bruch, A. 1999, AJ, 117, 3031

Burleigh, M. R., Barstow, M. A., & Holberg, J. B. 1998, MNRAS, 300, 511

Burleigh, M. R., et al. 2008, MNRAS, L35

Butler, R. P., et al. 2006, ApJ, 646, 505

Caillault, J.-P. 1996, Cool Stars, Stellar Systems, and the Sun, ASPC, 109, 325

Carpenter, J. M., et al. 2009, ApJS, 181, 197

Chen, C. H., Sargent, B. A., Bohac, C., et al. 2006, ApJS, 166, 351

Chesneau, O., Lykou, F., Balick, B., et al. 2007, A&A, 473, L29

Chu, Y.-H., Gruendl, R. A., Williams, R. M., Gull, T. R., & Werner, K. 2004a, AJ, 128, 2357

Chu, Y.-H., Guerrero, M. A., Gruendl, R. A., & Webbink, R. F. 2004b, AJ, 127, 477

Chu, Y.-H., et al. 2011, AJ, 142, 75

Chu, Y.-H., Gruendl, R. A., Guerrero, M. A., et al. 2009, AJ, 138, 691

Ciardullo, R., Bond, H. E., Sipior, M. S., Fullton, L. K., Zhang, C.-Y., & Schaefer, K. G. 1999, AJ, 118, 488

Cohen, M., & Barlow, M.J. 1974, ApJ, 213, 737

Cohen, M., & Barlow, M. J. 1975, Astrophys. Lett., 16, 165

Cohen, M., Kuhi, L. V., & Barlow, M. J. 1975, A&A, 40, 291

Corradi, R. L. M., Valentini, M., Munari, U., et al. 2010, A&A, 509, A41

Costero, R., Tapia, M., Méndez, R. H., et al. 1986, Rev. Mexicana Astron. Astrofis., 13, 149

Cowley, A. P., Schmidtke, P. C., Hutchings, J. B., & Crampton, D. 1995, PASP, 107, 927

Cudworth, K. M. 1973, PASP, 85, 401

Cutri, R. M., Skrutskie, M. F., van Dyk, S., et al. 2003, VizieR Online Data Catalog, 2246, 0

Debes, J. H., & Sigurdsson, S. 2002, ApJ, 572, 556

Debes, J. H., Hoard, D. W., Wachter, S., Leisawitz, D. T., & Cohen, M. 2011, arXiv:1110.6162

De Marco, O. 2009, PASP, 121, 316

de Marco, O., Wortel, S., Bond, H. E., & Harmer, D. 2007, Asymmetrical Planetary Nebulae IV,

De Marco, O., Jacoby, G. H., Davies, J., Bond, H. E., & Harrington, P. 2011, Bulletin of the American Astronomical Society, 43, #105.03

de Ruyter, S., van Winckel, H., Maas, T., Lloyd Evans, T., Waters, L. B. F. M., & Dejonghe, H. 2006, A&A, 448, 641

Dohnanyi, J. S. 1969, J. Geophys. Res., 74, 2531

Dong, R., Wang, Y., Lin, D. N. C., & Liu, X.-W. 2010, ApJ, 715, 1036

Draine, B. T., & Lee, H. M. 1984, ApJ, 285, 89

Dreizler, S., & Werner, K. 1996, A&A, 314, 217

Duncan, M. J., & Lissauer, J. J. 1998, Icarus, 134, 303

Eisenstein, D. J., et al. 2006, ApJS, 167, 40

Farihi, J., Barstow, M. A., Redfield, S., Dufour, P., & Hambly, N. C. 2010, MNRAS, 404, 2123

Farihi, J., Becklin, E. E., & Zuckerman, B. 2005, ApJS, 161, 394

Farihi, J., Hoard, D. W., & Wachter, S. 2006, ApJ, 646, 480

Farihi, J., Jura, M., Lee, J.-E., & Zuckerman, B. 2010, ApJ, 714, 1386

Farihi, J. 2011, in White Dwarf Atmospheres and Circumstellar Environments, ed. D. W. Hoard, 117, Weinheim, Germany:Wiley-VCH

Farihi, J., Jura, M., & Zuckerman, B. 2009, ApJ, 694, 805

Farihi, J., Burleigh, M. R., & Hoard, D. W. 2008, ApJ, 674, 421

Fazio, G. G., Hora, J. L., Allen, L. E., et al. 2004, ApJS, 154, 10

Fekel, F. C., Henry, G. W., Busby, M. R., & Eitter, J. J. 1993, AJ, 106, 2370

Fleming, T. A., Schmitt, J. H. M. M., & Giampapa, M. S. 1995, ApJ, 450, 401

Fleming, T. A., Snowden, S. L., Pfeffermann, E., Briel, U., & Greiner, J. 1996, A&A, 316, 147

Fleming, T. A., Werner, K., & Barstow, M. A. 1993, ApJ, 416, L79

Frew, D. J. 2008, Ph.D. Thesis

Frew, D. J., & Parker, Q. A. 2010, PASA, 27, 129

Fulbright, M. S., & Liebert, J. 1993, ApJ, 410, 275

Gänsicke, B. T., Marsh, T. R., Southworth, J., & Rebassa-Mansergas, A. 2008, Extreme Solar Systems, 398, 149

Gathier, R., & Pottasch, S. R. 1988, A&A, 197, 266

Gesicki, K., Zijlstra, A. A., Szyszka, C., et al. 2010, A&A, 514, A54

Gielen, C., van Winckel, H., Min, M., Waters, L. B. F. M., & Lloyd Evans, T. 2008, A&A, 490, 725

Good, S. A., Barstow, M. A., Burleigh, M. R., et al. 2005, MNRAS, 363, 183

Good, S. A., Barstow, M. A., Burleigh, M. R., Dobbie, P. D., & Holberg, J. B. 2005, MNRAS, 364, 1082

Gordon, K. D., et al. 2007, PASP, 119, 1019

Gorny, S. K., & Stasińska, G. 1995, A&A, 303, 893

Gorny, S. K., Stasińska, G., & Tylenda, R. 1997, A&A, 318, 256

Green, R. F., Schmidt, M., & Liebert, J. 1986, ApJS, 61, 305

Gruendl, R. A., Chu, Y.-H., O'Dwyer, I. J., & Guerrero, M. A. 2001, AJ, 122, 308

Guerrero, M. A., Villaver, E., & Manchado, A. 1998, ApJ, 507, 889

Guerrero, M.A., Chu, Y.-H., Gruendl, R.A., Williams, R.M., & Kaler, J.B. 2001, ApJL, 553, 55

Guerrero, M. A., Chu, Y.-H., & Miranda, L. F. 2004, AJ, 128, 1694

Hall, D. S., Henry, G. W., Louth, H., Renner, T. R., & Shore, S. N. 1982, Information Bulletin on Variable Stars, 2109, 1

Harris, H. C., Dahn, C. C., Canzian, B., et al. 2007, AJ, 133, 631

Hatzes, A. P., Guenther, E. W., Endl, M., Cochran, W. D., Döllinger, M. P., & Bedalov, A. 2005, A&A, 437, 743

Hoard, D. W., et al., 2007, AJ, 134, 26

Hogan, E., Burleigh, M. R., & Clarke, F. J. 2009, arXiv:0901.0532

Holberg, J. B., Barstow, M. A., & Burleigh, M. R. 2003, ApJS, 147, 145

Hoogerwerf, R., Szentgyorgyi, A., Raymond, J., Brickhouse, N. S., Slane, P. O., & Franco, J. 2007, ApJ, 670, 442

Houck, J. R., Roellig, T. L., van Cleve, J., et al. 2004, ApJS, 154, 18

Hutchings, J. B., Crampton, D., Cowley, A. P., Schmidtke, P. C., McGrath, T. K., & Chu, Y.-H. 1995, PASP, 107, 931

Jacoby, G.H., & Ford, H.C. 1983, ApJ, 266, 298

Jacoby, G. H., & Kaler, J. B. 1989, AJ, 98, 1662

Johnson, J. A., et al. 2007, ApJ, 665, 785

Jura, M. 2003, ApJ, 584, L91

Jura, M., Farihi, J., & Zuckerman, B. 2007, ApJ, 663, 1285

Jura, M., Muno, M. P., Farihi, J., & Zuckerman, B. 2009, ApJ, 699, 1473

Kato, T., Nogami, D., & Baba, H. 2001, PASJ, 53, 901

Kawka, A., Vennes, S., Dupuis, J., Chayer, P., & Lanz, T. 2008, ApJ, 675, 1518

Kerber, F., Mignani, R. P., Guglielmetti, F., & Wicenec, A. 2003, A&A, 408, 1029

Kilic, M., von Hippel, T., Leggett, S. K., & Winget, D. E. 2005, ApJ, 632, L115

Kilic, M., von Hippel, T., Leggett, S. K., & Winget, D. E. 2006, ApJ, 646, 474

Kilic, M., & Redfield, S. 2007, ApJ, 660, 641

Kilic, M., Gould, A., & Koester, D. 2009, ApJ, 705, 1219

Kilic, M., Brown, W. R., & McLeod, B. 2010, ApJ, 708, 411

Kilic, M., Patterson, A. J., Barber, S., Leggett, S. K., & Dufour, P. 2011, arXiv:1110.3799

Kleinman, S. J., et al. 2004, ApJ, 607, 426

Koester, D., et al. 2001, A&A, 378, 556

Koester, D.,et al. 2009, A&A, 505, 441

Kwitter, K. B., & Jacoby, G. H. 1989, AJ, 98, 2159

Lajoie, C.-P., & Bergeron, P. 2007, ApJ, 667, 1126

Landsman, W., Simon, T., & Bergeron, P. 1996, PASP, 108, 250

Laor, A., & Draine, B. T. 1993, ApJ, 402, 441

Leahy, D. A., Zhang, C. Y., & Kwok, S. 1994, ApJ, 422, 205

Leahy, D. A., Zhang, C. Y., Volk, K., & Kwok, S. 1996, ApJ, 466, 352

Liebert, J., Green, R., Bond, H. E., Holberg, J. B., Wesemael, F., Fleming, T. A., & Kidder, K. 1989, ApJ, 346, 251

Liebert, J., Bergeron, P., & Holberg, J. B. 2005, VizieR Online Data Catalog, 2156, 60047

Liu, Y.-J., et al. 2008, ApJ, 672, 553

Livio, M., & Soker, N. 1984, MNRAS, 208, 783

Lovis, C., & Mayor, M. 2007, A&A, 472, 657

Lykou, F., Chesneau, O., Zijlstra, A. A., et al. 2011, A&A, 527, A105

Mal'Kov, Y. F. 1997, Astronomy Reports, 41, 760

Manchado, A., Guerrero, M. A., Stanghellini, L., & Serra-Ricart, M. 1996, The IAC morphological catalog of northern Galactic planetary nebulae, Publisher: La Laguna, Spain: Instituto de Astrofisica de Canarias (IAC), 1996, Foreword by Stuart R. Pottasch, ISBN: 8492180609,

Manchado, A., Villaver, E., García-Segura, G., Acosta-Pulido, J.-A., & Barrena, R. 2007, Asymmetrical Planetary Nebulae IV,

Maxted, P. F. L., Marsh, T. R., Morales-Rueda, L., Barstow, M. A., Dobbie, P. D., Schreiber, M. R., Dhillon, V. S., & Brinkworth, C. S. 2004, MNRAS, 355, 1143

Maxted, P. F. L., O'Donoghue, D., Morales-Rueda, L., Napiwotzki, R., & Smalley, B. 2007, MNRAS, 376, 919

McCook, G. P., & Sion, E. M. 1999, ApJS, 121, 1

McCook, G. P., & Sion, E. M. 2006, VizieR Online Data Catalog, 3235, 0

Melis, C., Jura, M., Albert, L., Klein, B., & Zuckerman, B. 2010, ApJ, 722, 1078

Mendez, R. H., & Niemela, V. S. 1981, ApJ, 250, 240

Mendez, R. H., Gathier, R., & Niemela, V. S. 1982, A&A, 116, L5

Morgan, D. H., Parker, Q. A., & Russeil, D. 2001, MNRAS, 322, 877

Motch, C., Guillout, P., Haberl, F., Pakull, M., Pietsch, W., & Reinsch, K. 1997, A&A, 318, 111

Mullally, F., Kilic, M., Reach, W. T., Kuchner, M. J., von Hippel, T., Burrows, A., & Winget, D. E. 2007, ApJS, 171, 206

Mullally, F., Winget, D. E., Degennaro, S., Jeffery, E., Thompson, S. E., Chandler, D., & Kepler, S. O. 2008, ApJ, 676, 573

Mullally, F., Reach, W. T., De Gennaro, S., & Burrows, A. 2009, ApJ, 694, 327

Napiwotzki, R. 1999, A&A, 350, 101

Napiwotzki, R. 2001, A&A, 367, 973

Napiwotzki, R., & Schoenberner, D. 1995, A&A, 301, 545

Niedzielski, A., et al. 2007, ApJ, 669, 1354

Nishimaki, Y., Yamamuro, T., Motohara, K., Miyata, T., & Tanaka, M. 2008, PASJ, 60, 191

O'Donoghue, D., Koen, C., Kilkenny, D., Stobie, R. S., Koester, D., Bessell, M. S., Hambly, N., & MacGillivray, H. 2003, MNRAS, 345, 506

O'Dwyer, I.J., Chu, Y.-H., Gruendl, R.A., Guerrero, M.A., et al. 2003, AJ, 125, 2239

Passy, J.-C., De Marco, O., Fryer, C. L., et al. 2011, arXiv:1107.5072

Patten, B. M., et al. 2006, ApJ, 651, 502

Perryman, M. A. C., et al. 1997, A&A, 323, L49

Phillips, J. P. 2003, MNRAS, 344, 501

Phillips, J. P. 2004, MNRAS, 353, 589

Piliugin, L. S., & Khromov, G. S. 1979, Soviet Ast., 23, 425

Pourbaix, D., et al. 2004, A&A, 424, 727

Ramsay, G., Groot, P. J., Marsh, T., Nelemans, G., Steeghs, D., & Hakala, P. 2006, A&A, 457, 623

Rauch, T., Köppen, J., Napiwotzki, R., & Werner, K. 1999, A&A, 347, 169

Rauch, T., Ziegler, M., Werner, K., et al. 2007, A&A, 470, 317

Raymond, J. C., & Smith, B. W. 1977, ApJS, 35, 419

Reach, W. T., Kuchner, M. J., von Hippel, T., Burrows, A., Mullally, F., Kilic, M., & Winget, D. E. 2005, ApJ, 635, L161

Reach, W. T., Megeath, S. T., Cohen, M., et al. 2005, PASP, 117, 978

Reed, B. C. 2003, AJ, 125, 2531

Reimers, D. 1984, A&A, 136, L5

Rieke, G. H., Young, E. T., Engelbracht, C. W., et al. 2004, ApJS, 154, 25

Rieke, G. H., et al. 2005, ApJ, 620, 1010

Roth, M., Echevarria, J., Tapia, M., et al. 1984, A&A, 137, L9

Rucinski, S. M. 1984, A&A, 132, L9

Ruiz, M. T., Rojo, P. M., Garay, G., & Maza, J. 2001, ApJ, 552, 679

Sackmann, I.-J., Boothroyd, A. I., & Kraemer, K. E. 1993, ApJ, 418, 457

Saffer, R. A., Wade, R. A., Liebert, J., Green, R. F., Sion, E. M., Bechtold, J., Foss, D., & Kidder, K. 1993, AJ, 105, 1945

Sato, B., et al. 2007, ApJ, 661, 527

Setiawan, J., et al. 2005, A&A, 437, L31

Singh, K. P., Drake, S. A., & White, N. E. 1996, AJ, 111, 2415

Skrutskie, M. F., Cutri, R. M., Stiening, R., et al. 2006, AJ, 131, 1163

Smalley, B. 1997, The Observatory, 117, 338

Smith, J. D. T., et al. 2007, PASP, 119, 1133

Smith, N., & Gehrz, R. D. 2005, AJ, 129, 969

Schmeja, S., & Kimeswenger, S. 2001, A&A, 377, L18

Soker, N., & Kastner, J.H. 2002, ApJ, 570, 245

Stanghellini, L., & Pasquali, A. 1995, ApJ, 452, 286

Stanghellini, L., Villaver, E., Manchado, A., & Guerrero, M. A. 2002, ApJ, 576, 285

Steele, P. R., Burleigh, M. R., Dobbie, P. D., & Barstow, M. A. 2007, MNRAS, 382, 1804

Strassmeier, K. G., Hall, D. S., Fekel, F. C., & Scheck, M. 1993, A&AS, 100, 173

Su, K., Bilikova, J., Chu, Y.-H., et al. 2011, Asymmetric Planetary Nebulae 5 conference, held in Bowness-on-Windermere, U.K., 20 - 25 June 2010, A. A. Zijlstra, F. Lykou, I. McDonald, and E. Lagadec, eds. (2011) Jodrell Bank Centre for Astrophysics,

Su, K. Y. L., et al. 2007, ApJ, 657, L41

Su, K. Y. L., et al. 2006, ApJ, 653, 675

Su, K. Y. L., Kelly, D. M., Latter, W. B., et al. 2004, ApJS, 154, 302

Taam, R. E., & Ricker, P. M. 2010, New A Rev., 54, 65

Tanaka, H., Inaba, S., & Nakazawa, K. 1996, Icarus, 123, 450

Tappert, C., Gänsicke, B. T., & Mennickent, R. E. 2004, Revista Mexicana de Astronomia y Astrofisica Conference Series, 20, 245

Thorstensen, J. R., Lépine, S., & Shara, M. 2008, AJ, 136, 2107

Trams, N. R., Waters, L. B. F. M., Lamers, H. J. G. L. M., Waelkens, C., Geballe, T. R., & The, P. S. 1991, A&AS, 87, 361

Trilling, D. E., et al. 2008, ApJ, 674, 1086

Tweedy, R. W., & Kwitter, K. B. 1996, ApJS, 107, 255

Tylenda, R., Acker, A., Stenholm, B., & Koeppen, J. 1992, A&AS, 95, 337

Vacca, W. D., Cushing, M. C., & Rayner, J. T. 2003, PASP, 115, 389

van Altena, W. F., Lee, J. T., & Hoffleit, E. D. 1995, New Haven, CT: Yale University Observatory, —c1995, 4th ed., completely revised and enlarged

Van Winckel, H., Waelkens, C., Fernie, J. D., & Waters, L. B. F. M. 1999, A&A, 343, 202

van Winckel, H. 2003, Astronomical Society of the Pacific Conference Series, 303, 294

Vennes, S., & Lanz, T. 2001, ApJ, 553, 399

Vennes, S., & Thorstensen, J. R. 1994, ApJ, 433, L29

Viironen, K., Mampaso, A., Corradi, R. L. M., et al. 2009, A&A, 502, 113

Villaver, E., & Livio, M. 2007, ApJ, 661, 1192

von Hippel, T., Kuchner, M. J., Kilic, M., Mullally, F., & Reach, W. T. 2007, ApJ, 662, 544

Walton, N. A., Walsh, J. R., & Sahu, K. C. 1990, A&A, 230, 445

Wassermann, D., Werner, K., Rauch, T., & Kruk, J. W. 2010, A&A, 524, A9

Waters, L. B. F. M. 1993, Luminous High-Latitude Stars, 45, 409

Waters, L. B. F. M., Waelkens, C., & Van Winckel, H. 1997, Planetary Nebulae, 180, 313

Werner, M. W., Roellig, T. L., Low, F. J., et al. 2004, ApJS, 154, 1

Werner, K., & Herwig, F. 2006, PASP, 118, 183

Werner, K., Bagschik, K., Rauch, T., & Napiwotzki, R. 1997, A&A, 327, 721

Werner, K., Wolff, B., Pakull, M. W., Cowley, A. P., Schmidtke, P. C., Hutchings, J. B., & Crampton, D. 1996, Supersoft X-Ray Sources, 472, 131

Wesemael, F., Green, R. F., & Liebert, J. 1985, ApJS, 58, 379

White, N. E., Giommi, P., & Angelini, L. 2000, The WGA Catalogue of *ROSAT* Point Sources (Greenbelt: GSFC)

Wolf, S., & Hillenbrand, L. A. 2003, ApJ, 596, 603

Wyatt, M. C. 2005, A&A, 433, 1007

Wyatt, M. C., & Dent, W. R. F. 2002, MNRAS, 334, 589

Xu, S., & Jura, M. 2011, ApJ, in press (arXiv:1109.4207)

Zboril, M., & Messina, S. 2009, Astronomische Nachrichten, 330, 377

Zhang, Y., & Liu, X.-W. 2002, MNRAS, 337, 499

Zuckerman, B., & Becklin, E. E. 1987, Nature, 330, 138